

Abstract

Toward Understanding the Mechanism of Charge Transport in Protein Nanowires

Peter James Dahl

2023

The discovery of protein nanowires in soil microbes upended the field of biological electron transfer. Originally thought to be type IV pili, which lack metal-containing cofactors, recent studies have revealed that the nanowires are composed of polymerized multiheme cytochromes. Prior to the discovery of the structure of cytochrome nanowires, years of research were dedicated to understanding the mechanism of long-range charge transport in protein filaments. However, these efforts were not in vain. The hypotheses and models which emerged from studies of the hypothesized conductive pilus of *Geobacter sulfurreducens* inspired work, including my own, which ultimately revealed long-range charge transport in proteins to be a reality. In my dissertation research, I have evaluated the mechanisms of charge transport in both cytochrome nanowires as well as non-cytochrome protein nanowires. Through my work, I have identified several key mechanistic characteristics of charge transport in protein nanowires: Long-range charge transport occurs by a multistep hopping mechanism; the hopping rates are determined by the local protein environment; and protein conductivity is remarkably tunable. Fluctuations in the environment are strongly coupled to the structural factors which determine charge transfer rates. In particular, manipulation of hydrogen bonds gives rise to conductivity shifts spanning up to 3 orders of magnitude. In addition to the mechanistic details, I have contributed to discoveries of novel functions and applications of conductive proteins. These include bacterial pathogenicity and generation of electrical power from ambient humidity. I hope for my work to serve as a foundation for the future development of protein nanowire-based technologies.

Toward Understanding the Mechanism of Charge Transport in Protein Nanowires

A Dissertation
Presented to the Faculty of the Graduate School
of
Yale University
In Candidacy for the Degree of
Doctor of Philosophy

by
Peter James Dahl

Dissertation Director: Nikhil S. Malvankar

May 2023

Copyright © 2023 by Peter James Dahl
All rights reserved.

Table of Contents

ABSTRACT	I
TABLE OF CONTENTS	III
ACKNOWLEDGEMENTS	VII
ABBREVIATIONS	10
FIGURES AND TABLES	11
MAIN FIGURES	11
SUPPLEMENTAL FIGURES	12
MAIN TABLES	12
SUPPLEMENTAL TABLES	13
1. INTRODUCTION	1
1.1 BIOLOGICAL ELECTRON TRANSFER	1
1.2 HOW A CASE OF MISTAKEN IDENTITY FUELED THE SEARCH FOR A NEW MECHANISM OF PROTEIN CONDUCTIVITY	7
1.3 CYTOCHROME NANOWIRES	11
1.4 PROTEIN CONDUCTIVITY IN THE ABSENCE OF HEMES	13
2. COMPUTATIONAL METHODOLOGY	17
2.1 MOLECULAR DYNAMICS SIMULATIONS	17
2.2 QM/MM CALCULATIONS	20
2.2.1. <i>THEORY</i>	20
2.2.2. <i>PRACTICAL IMPLEMENTATION</i>	22
2.3 ELECTRON TRANSFER IN THE NON-ADIABATIC REGIME (MARCUS THEORY)	29
2.4 CALCULATING REDUCTION POTENTIAL USING <i>AB INITIO</i> COMPUTATIONAL METHODOLOGIES	29
2.4.1. <i>CALCULATING FREE ENERGIES WITHIN THE PERTURBATIVE REGIME</i>	30
2.4.2. <i>CALCULATING THE FREE ENERGY OF OXIDATION USING THE EXTENDED BORN-HABER METHOD</i>	32
2.4.3. <i>COMPARING COMPUTED FREE ENERGIES TO EXPERIMENT – GENERATING INTERPRETABLE DATA</i>	36
2.5 COMPUTING OUTER SPHERE REORGANIZATION ENERGY FROM MOLECULAR DYNAMICS	38
2.5.1. <i>THEORY</i>	38
2.5.2. <i>PRACTICAL IMPLEMENTATION</i>	41
2.6 CALCULATING ELECTRONIC COUPLING	45
2.7 KINETIC MONTE CARLO FOR SIMULATING CHARGE TRANSPORT	47

2.8	NORMAL COORDINATE STRUCTURAL DECOMPOSITION.....	49
3.	AN IMPROVED METHOD FOR CALCULATING REDUCTION POTENTIALS IN PROTEIN ENVIRONMENTS.....	52
3.1	SUMMARY	52
3.2	INTRODUCTION.....	52
3.3	THEORY	54
3.3.1.	<i>CALCULATING FREE ENERGIES USING VERTICAL ENERGY GAPS</i>	55
3.3.2.	<i>CALCULATING FREE ENERGY USING THE BORN-HABER CYCLE</i>	57
3.4	RESULTS	60
3.4.1.	<i>PROTON COUPLED REDUCTION POTENTIALS OF $\alpha 3X$</i>	60
3.4.2.	<i>REDUCTION POTENTIALS OF CYTOCHROME-C</i>	64
3.4.3.	<i>TRYPTOPHAN OXIDATION SIGNIFICANTLY DECREASES THE PK_A OF GLUTAMATE</i>	65
3.5	DISCUSSION	68
3.6	METHODS	69
3.6.1.	<i>MOLECULAR DYNAMICS</i>	69
3.6.2.	<i>QM/MM CALCULATIONS</i>	70
3.7	SUPPLEMENTARY INFORMATION.....	72
4.	MECHANISM OF CHARGE TRANSPORT IN OMCS NANOWIRES	76
4.1	AUTHOR CONTRIBUTIONS	76
4.2	SUMMARY	77
4.3	INTRODUCTION.....	77
4.4	RESULTS	79
4.4.1.	<i>CORRELATING NANOWIRE STRUCTURE WITH FUNCTION USING CONDUCTIVITY MEASUREMENTS UNDER CONDITIONS USED TO SOLVE THE ATOMIC STRUCTURE</i>	79
4.4.2.	<i>INTRINSIC CONDUCTIVITY MEASUREMENTS REVEAL HOPPING TRANSPORT WITH NEGLIGIBLE CARRIER LOSS</i>	80
4.4.3.	<i>A 300-FOLD INCREASE IN NANOWIRE CONDUCTIVITY UPON COOLING</i>	82
4.4.4.	<i>COMPUTATIONAL MODELLING CAPTURES EXPERIMENTALLY-MEASURED CONDUCTIVITY</i>	84
4.4.5.	<i>COOLING DECREASES HEME REDUCTION POTENTIALS WHICH COULD EXPLAIN INCREASED CONDUCTIVITY</i>	87
4.4.6.	<i>COOLING MASSIVELY RESTRUCTURES HYDROGEN BONDING NETWORK IN OMCS NANOWIRES</i>	88
4.4.7.	<i>COOLING MAKES HEMES MORE PLANAR, AS REVEALED BY RAMAN SPECTROSCOPY AND SIMULATIONS</i>	90
4.4.8.	<i>COOLING INCREASES THE ELECTRIC FIELD AT THE HEME IRON, LOWERING REDUCTION POTENTIAL</i>	93
4.5	DISCUSSION	93
4.6	MATERIALS AND METHODS	95
4.6.1.	<i>BACTERIAL STRAINS AND CULTURE CONDITIONS</i>	95

4.6.2.	<i>NANOELECTRODE DESIGN AND FABRICATION</i>	96
4.6.3.	<i>NANOWIRE SAMPLE PREPARATION</i>	96
4.6.4.	<i>DEUTERIUM EXCHANGE</i>	97
4.6.5.	<i>ELECTRICAL (DC) CONDUCTIVITY MEASUREMENTS</i>	97
4.6.6.	<i>CONDUCTING-PROBE ATOMIC FORCE MICROSCOPY (CP-AFM) MEASUREMENTS</i>	98
4.6.7.	<i>TEMPERATURE VARIATION CONDUCTIVITY EXPERIMENTS</i>	99
4.6.8.	<i>RAMAN SPECTROSCOPY</i>	100
4.6.9.	<i>UV-VISIBLE SPECTROSCOPY</i>	100
4.6.10.	<i>CALCULATION OF ELECTROSTATIC POTENTIAL AND ELECTRIC FIELD</i>	101
4.6.11.	<i>CALCULATION OF HYDROGEN BONDING STRUCTURE</i>	101
4.7	SUPPLEMENTARY INFORMATION	102
5.	HOMOGENOUS OMCZ FILMS CONDUCT VIA A MIXED IONIC-ELECTRONIC TRANSPORT MECHANISM	110
5.1	AUTHOR CONTRIBUTIONS	110
5.2	SUMMARY	110
5.3	INTRODUCTION	111
5.4	RESULTS	112
5.4.1.	<i>INCREASED HUMIDITY DRIVES A 30,000-FOLD INCREASE IN OMCZ CONDUCTIVITY</i>	112
5.4.2.	<i>OMCZ FILMS ARE MIXED IONIC-ELECTRONIC CONDUCTORS</i>	114
5.4.3.	<i>HIGH PROTON MOBILITY IS ASSOCIATED WITH A TRANSITION TO A GROTHUSS MECHANISM</i>	117
5.4.4.	<i>PROTON MOBILITY ENABLES POWER GENERATION FROM AMBIENT HUMIDITY</i>	118
5.5	MATERIALS AND METHODS	122
5.5.1.	<i>NANOWIRE SAMPLE PREPARATION</i>	122
5.5.2.	<i>ELECTRODE DESIGN AND FABRICATION</i>	123
5.5.3.	<i>HUMIDITY VARIATION</i>	123
5.5.4.	<i>ELECTRICAL (DC) CONDUCTIVITY MEASUREMENTS</i>	124
5.5.5.	<i>CHARGE MOBILITY MEASUREMENTS</i>	125
5.5.6.	<i>TEMPERATURE VARIATION CONDUCTIVITY MEASUREMENTS</i>	126
5.5.7.	<i>ELECTROCHEMICAL IMPEDANCE SPECTROSCOPY</i>	126
5.5.8.	<i>HYGROELECTRIC POWER EXPERIMENTS</i>	127
5.5.9.	<i>CALCULATION OF PROTON MOBILITY FROM HIGH SCAN RATE CURRENT-VOLTAGE RESPONSE</i>	127
5.5.10.	<i>CALCULATION OF CONSUMPTION RATE FOR O₂ AND H⁺</i>	130
5.6	SUPPLEMENTARY INFORMATION	131
6.	MECHANISM OF CHARGE TRANSPORT IN NON-CYTOCHROME PROTEINS	133
6.1	AMYLOID CRYSTALS WITH STACKED TYROSINES CONDUCT VIA HOLE HOPPING COUPLED TO PROTON ROCKING	133
6.1.1.	<i>AUTHOR CONTRIBUTIONS</i>	133
6.1.2.	<i>INTRODUCTION</i>	134
6.1.3.	<i>RESULTS</i>	134
6.1.4.	<i>DISCUSSION</i>	137
6.2	ELECTRONIC COUPLING IS ENHANCED BY THROUGH-BOND TUNNELLING PATHWAYS	138

6.2.1.	<i>INTRODUCTION</i>	138
6.2.2.	<i>RESULTS</i>	139
6.2.3.	<i>DISCUSSION</i>	144
7.	PROTEIN CONDUCTIVITY PROMOTES BACTERIAL ADHESION TO HOST-CELL SURFACES	146
7.1	AUTHOR CONTRIBUTIONS	146
7.2	SUMMARY	146
7.3	INTRODUCTION	147
7.4	RESULTS	148
7.4.1.	<i>PATHOGENS PERFORM EET IN HIGH FLUID FLOW</i>	148
7.4.2.	<i>PATHOGENS USE T4P TO DISSIPATE ELECTRONS</i>	150
7.4.3.	<i>EET VIA PILI ENHANCES BACTERIAL ADHESION</i>	152
7.4.4.	<i>PILI LOWER BARRIER FOR ELECTRON TRANSFER</i>	153
7.4.5.	<i>PATHOGENIC T4P ARE ELECTRICALLY CONDUCTIVE</i>	154
7.4.6.	<i>T4P CONDUCTIVITY CORRELATES WITH CELL ADHESION</i>	156
7.4.7.	<i>PH REGULATES CONDUCTIVITY AND ADHESION</i>	158
7.5	DISCUSSION	159
7.6	MATERIALS AND METHODS	162
7.6.1.	<i>BACTERIAL STRAINS AND CULTURE CONDITIONS</i>	162
7.6.2.	<i>N. GONORRHOEAE PILUS PURIFICATION</i>	162
7.6.3.	<i>N. MENINGITIDIS PILUS PURIFICATION</i>	163
7.6.4.	<i>P. AERUGINOSA PILUS PURIFICATION</i>	163
7.6.5.	<i>V. CHOLERAE PILUS PURIFICATION</i>	163
7.6.6.	<i>NANOELECTRODE DESIGN AND FABRICATION</i>	164
7.6.7.	<i>PREPARATION OF PILI FOR CONDUCTIVITY MEASUREMENTS</i>	164
7.6.8.	<i>ELECTRICAL (DC) CONDUCTIVITY MEASUREMENTS</i>	164
7.6.9.	<i>CONDUCTIVITY CALCULATIONS</i>	165
7.6.10.	<i>SINGLE CELL FORCE SPECTROSCOPY (SCFS)</i>	165
7.6.11.	<i>BACTERIAL ADHESION ASSAY</i>	166
7.6.12.	<i>ELECTROSTATIC FORCE MICROSCOPY (EFM) ON GRAPHENE OXIDE (GO)</i>	167
7.6.13.	<i>CURRENT GENERATION IN A MICROBIAL FUEL CELL (MFC)</i>	168
7.6.14.	<i>BACTERIAL BIOFILM VOLTAMMETRY</i>	169
7.6.15.	<i>MOLECULAR DYNAMICS (MD) SIMULATIONS</i>	170
7.6.16.	<i>ANALYSIS OF OPTIMAL CHARGE TRANSFER PATHWAYS</i>	170
7.7	SUPPLEMENTARY INFORMATION	171
8.	CONCLUSIONS AND FUTURE DIRECTIONS	175
9.	REFERENCES	178

Acknowledgements

Pursuing a PhD at one of the top research institutions in the world is an incredible yet challenging experience. I consider myself extremely lucky to have found myself surrounded by an incredible community of advisors, colleagues, and friends who helped me overcome the many difficulties along the way.

First and foremost, I need to thank my research advisor Dr. Nikhil Malvankar who provided an opportunity rich environment where I could grow as a scientist. I entered the Yale Molecular Biophysics and Biochemistry department with the intention of combining theoretical and experimental techniques in my research. Nikhil supported this endeavor from day one and allowed me the freedom to explore and apply computational and theoretical chemistry in my research. I am also incredibly thankful for my theory advisor Dr. Victor Batista. I must admit I was amazed when he and his group welcomed me and were so willing to donate their time toward teaching me the basics of computational chemistry. As I have transitioned into mentorship roles, I aspire to emulate the patient mentoring style of Victor, as well as that of Dr. Atanu Acharya and Dr. Uriel Morzan who were incredibly helpful at the beginning of my time at Yale.

I would also like to thank Dr. Gary Brudvig for serving on my thesis committee and for always providing constructive feedback. I also need to thank my external reader, Dmitry Matyushov for providing helpful feedback on this document.

I am also incredibly thankful to the many labmates I have had the privilege to consider my friends and colleagues. In particular, I would like to acknowledge Dr. Catharine Shipps and Dr. Vishok Srikanth who joined the Malvankar in the same year as myself. It was always comforting knowing that I had friends who could relate to the specific challenges related to our field of research.

I also need to note that without the research opportunities I had as an undergraduate student at Wayne State University, it is unlikely that I would have had the confidence to even apply to the Yale graduate school. I am incredibly thankful to Dr. Arun Anantharam, who gave me the

opportunity to work on my own research projects within his lab, and to connect me with the resources I needed to advance my work. This includes a collaboration with Dr. Jefferson Knight who treated me as a student of his own, despite about 1,200 miles separating our labs. It was actually Jeff who encouraged me to apply to Yale for which I am very grateful. I would also like to acknowledge Dr. Tejeshwar Rao and Mike Schmidtke, who were great labmates and friends. Our many conversations in the lab and at conferences showed me how enjoyable and exhilarating scientific discovery can be.

In my time at Yale I have met many wonderful people who have enhanced my life. I need to offer a very special thanks to Dr. Ekaterina Stroeva whose love and support has transformed my life. I am especially thankful for her willingness to be my sounding board for every challenge I have faced during my PhD, and for encouraging me to be the best version of myself. Also, through Kate I was fortunate to meet her lab mates in the Rothman lab who immediately welcomed me into their group of friends. While I am certainly thankful for their company and for being genuinely great people it is also notable that, without them, I would not have been able to experience so much delicious Indian cuisine.

When I was trying to decide where to go to graduate school, I attended a Biophysical Society conference. I had a very nice conversation with Dr. Daniel Axelrod who gave me very good advice. He told me to go to graduate school someplace that will make me happy. The logic was, research will often be frustrating, it is best to be in a location where you can occupy yourself with activities and surround yourself with people who give you fulfillment beyond science. This certainly was the case with New Haven. I was fortunate to have made many great friends in New Haven. In particular, I would like to acknowledge the New Haven Bicycling Club. Dozens of friends and thousands of miles of pedaling got me through some of the most challenging moments of my PhD. Also, I need to thank Phillips Hutchison who has been a great pal, for dragging me along on long rides and for waiting for me at the top of every hill.

And of course, I need to thank my family for being a constant source of support. My mom, Carol Dahl, my brother, Daniel Dahl, and my sister, Anne Dahl have been supporting me from day 1. Helping me move to New Haven and giving me a place to come home for holidays, I am eternally grateful. I also need to thank Dr. Elina Stroeve and Dr. Mikhail Stroeve for welcoming me into their lives. Having two families' support and love has been a great asset in my time at Yale.

Abbreviations

AFM	atomic force microscopy
Cryo-EM	cryo-electron microscopy
CV	cyclic voltammetry
DPV	differential pulse voltammetry
EET	extracellular electron transfer
ET	electron transfer
EET	extracellular electron transfer
FTO	fluorine doped tin oxide
G.s.	<i>Geobacter sulfurreducens</i> strain unspecific
I-V	current voltage
MD	molecular dynamics
CHARMM	<u>C</u> hemistry at <u>HAR</u> vard <u>M</u> olecular <u>M</u> echanics
QM/MM	quantum mechanics molecular mechanics
DFT	density functional theory
vdW	van der Waals
SHE	standard hydrogen electrode
SCE	standard calomel electrode
TEM	transmission electron microscopy
UV-Vis	ultraviolet visible spectroscopy
WT	wild type
KIE	kinetic isotope effect
PCET	proton coupled electron transfer
NSD	normal coordinate structural decomposition
T4P	Type IV pili

Figures and Tables

Main Figures

FIGURE 1.1: DISTINCT REDUCTION POTENTIALS DIRECT ELECTRON TRANSFER TOWARD THE ENZYME WITH THE HIGHEST POTENTIAL.	1
FIGURE 1.2: TUNNELING AND HOPPING IN BIOLOGICAL ELECTRON TRANSFER.	3
FIGURE 1.3: THE LOCAL ENVIRONMENT OF A COFACTOR DETERMINES ITS REDUCTION POTENTIAL.	6
FIGURE 1.4: POLYMERIZATION OF CYTOCHROME NANOWIRES ALIGNS HEMES IN STACKED CHAINS.	11
FIGURE 2.1: BORN-HABER THERMODYNAMIC CYCLE FOR COMPUTING OXIDATION FREE ENERGIES.	33
FIGURE 2.2: EXTENDED BORN-HABER CYCLE FOR CALCULATING OXIDATION FREE ENERGIES.	34
FIGURE 2.3: DEFINING REORGANIZATION ENERGY IN THE LINEAR RESPONSE REGIME.	40
FIGURE 3.1: EXTENDED BORN-HABER CYCLE FOR COMPUTING REDUCTION POTENTIALS IN PROTEIN ENVIRONMENTS.	58
FIGURE 3.2: PROTEIN SYSTEMS USED TO BENCHMARK THE METHODS INVESTIGATED IN THIS STUDY.	60
FIGURE 3.3: A HYDROGEN BONDING NETWORK CONNECTS TRYPTOPHAN 34 TO GLUTAMIC ACID 15 VIA A WATER BRIDGE.	63
FIGURE 3.4: PES TO DETERMINE BARRIER FOR PT TO E15.	66
FIGURE 3.5: THERMODYNAMIC CYCLE RELATING OXIDATION OF W34 TO PROTON DISSOCIATION FROM E15.	68
FIGURE 4.1: CLOSELY-STACKED HEMES IN OmcS NANOWIRES PROVIDE A CONTINUOUS PATH FOR EXTRACELLULAR ELECTRON TRANSPORT OVER MICROMETERS.	79
FIGURE 4.2: CORRELATING NANOWIRE STRUCTURE WITH CONDUCTIVITY BY MEASUREMENT UNDER CONDITIONS USED TO SOLVE THE ATOMIC STRUCTURE.	80
FIGURE 4.3: IDENTIFICATION OF HOPPING CONDUCTIVITY IN NANOWIRES.	81
FIGURE 4.4: OmcS DEMONSTRATES A NON-ARRHENIUS TEMPERATURE DEPENDENCE.	83
FIGURE 4.5: COMPUTATIONS AND EXPERIMENTS REVEAL FACILE HOLE TRANSPORT IN OmcS.	84
FIGURE 4.6: TEMPERATURE INDUCED INCREASE IN REDUCTION POTENTIALS ENHANCES NANOWIRE CONDUCTIVITY.	87
FIGURE 4.7: TEMPERATURE INDUCES RESTRUCTURING OF HYDROGEN BONDS.	89
FIGURE 4.8: HEMES BECOME MORE PLANAR UPON COOLING.	91
FIGURE 4.9: TEMPERATURE INDUCED CHANGES IN PROTEIN STRUCTURE ALTER THE ELECTRIC FIELD AT THE HEME IRON ATOMS.	92
FIGURE 5.1: CONDUCTIVITY OF OmcZ NANOWIRE FILMS INCREASED 30,000-FOLD WITH INCREASED HUMIDITY.	113
FIGURE 5.2: ELECTROCHEMICAL IMPEDANCE SPECTROSCOPY REVEALED A MIXED IONIC-ELECTRONIC AMBIPOLAR TRANSPORT MECHANISM.	115
FIGURE 5.3: A TRANSITION TO A GROTHUSS MECHANISM SUPPORTS HIGH PROTON MOBILITY.	117
FIGURE 5.4: CYTOCHROME NANOWIRE FILMS PRODUCE POWER BY USING A PROTON GRADIENT TO COUPLE ELECTRON TRANSFER TO OXYGEN REDUCTION.	120
FIGURE 6.1: STACKED TYROSINES AND COORDINATING Zn^{2+} IONS ARE REQUIRED FOR CONDUCTIVITY.	135
FIGURE 6.2: THE Zn^{2+} ION STABILIZES THE X1 STRUCTURE.	136
FIGURE 6.3: CONDUCTIVITY IN X1 IS LIMITED BY PROTON ACCEPTOR AVAILABILITY.	137
FIGURE 6.4: CTPR PROTEINS USE TYROSINE AND TRYPTOPHAN RESIDUES TO TRANSPORT CHARGE.	139
FIGURE 6.5: MIXING OF FRONTIER ORBITALS SUPPORTS HIGH ELECTRONIC COUPLING.	141
FIGURE 6.6: COMPUTED RESISTANCE OF CTPR PROTEINS.	142
FIGURE 6.7: FITTING REVEALS HOPPING MECHANISM WITH COMPETING CARRIER LOSS.	144
FIGURE 7.1: EET VIA DIRECT CONTACT ENABLES CHARGE REDISTRIBUTION ON HOST SURFACES.	149
FIGURE 7.2: <i>P. AERUGINOSA</i> USES T4P FOR DIRECT CONTACT EET.	151
FIGURE 7.3: PILI REDUCE THE BARRIER FOR DIRECT CONTACT EET.	154
FIGURE 7.4: ELECTRICAL CONDUCTIVITY OF PILI IN DIVERSE PATHOGENS CORRELATES WITH ABUNDANCE OF AROMATIC AMINO ACIDS IN $\alpha 1$ OF THE MAJOR PILIN PROTEIN.	155
FIGURE 7.5: BACTERIAL ADHESION INCREASES WITH HIGHER CONDUCTIVITY OF <i>N. MENINGITIDIS</i> T4P.	158
FIGURE 7.6: pH REGULATES <i>P. AERUGINOSA</i> PILI CONDUCTIVITY AND ADHESION.	159

Supplemental Figures

SUPPLEMENTARY FIGURE 3.1: CONVERGENCE OF REDUCTION POTENTIAL OF α_3Y COMPUTED WITH VERTICAL ENERGY GAPS.	74
SUPPLEMENTARY FIGURE 3.2: CONVERGENCE OF REDUCTION POTENTIAL OF α_3W COMPUTED WITH VERTICAL ENERGY GAPS.	75
SUPPLEMENTARY FIGURE 3.3: CONVERGENCE OF REDUCTION POTENTIAL OF CYTOCHROME-C COMPUTED WITH VERTICAL ENERGY GAPS.	75
SUPPLEMENTARY FIGURE 4.1: COMPUTATIONAL MODEL OF AN OMCS DIMER.	102
SUPPLEMENTARY FIGURE 4.2: FREE ENERGY LANDSCAPE OF OMCS IN A UNIFORM DIELECTRIC ENVIRONMENT.	102
SUPPLEMENTARY FIGURE 4.3: PROXIMITY OF CYSTEINE 12 TO HEME 2 CONTRIBUTES TO INCREASED COUPLING BETWEEN HEMES 1 AND 2.	103
SUPPLEMENTARY FIGURE 4.4: THE HYDROGEN BONDING NETWORK OF OMCS CHANGES SIGNIFICANTLY UPON COOLING.	103
SUPPLEMENTARY FIGURE 4.5: CONVERGENCE OF THE FREE ENERGY OF OXIDATION, REORGANIZATION ENERGY, AND ELECTRONIC COUPLING.	104
SUPPLEMENTARY FIGURE 4.6: QM REGION FOR ELECTRONIC STRUCTURE CALCULATIONS.	105
SUPPLEMENTARY FIGURE 4.7: BENCHMARKING NSD PROGRAM WITH ANALYSIS OF HEME DISTORTION IN HORSE HEART CYTOCHROME C.	105
SUPPLEMENTARY FIGURE 5.1: 4-PROBE EIS BODE PLOTS.	131
SUPPLEMENTARY FIGURE 5.2: FIELD-EFFECT BACK GATING REPEATS.	131
SUPPLEMENTARY FIGURE 5.3: HIGH SCAN-RATE CURRENT VOLTAGE RESPONSE.	132
SUPPLEMENTARY FIGURE 5.4: HYGROELECTRIC POWER DEVICE CHARACTERIZATION.	132
SUPPLEMENTARY FIGURE 7.1: EXAMPLE FORCE CURVES FROM SINGLE CELL FORCE SPECTROSCOPY.	171
SUPPLEMENTARY FIGURE 7.2: PILI REDUCE THE CHARGE TRANSFER RESISTANCE BETWEEN <i>PSEUDOMONAS AERUGINOSA</i> AND A PLANAR SURFACE.	171
SUPPLEMENTARY FIGURE 7.3: AROMATIC RESIDUES IN <i>VIBRIO CHOLERAE</i> T4BP ARE TOO FAR APART TO CONFER HIGH CONDUCTIVITY.	172
SUPPLEMENTARY FIGURE 7.4: CONDUCTIVITY OF <i>NEISSERIA MENINGITIDIS</i> T4P IS EXPONENTIALLY DEPENDENT ON DISTANCE.	172
SUPPLEMENTARY FIGURE 7.5: ADHESION OF <i>N. MENINGITIDIS</i> TO HUVEC CELLS INCREASES WITH THE CONDUCTIVITY OF THE PILUS EXPRESSED BY THE BACTERIA.	172
SUPPLEMENTARY FIGURE 7.6: LOWERING THE pH REDUCES THE DIAMETER OF <i>P. AERUGINOSA</i> PILI.	173
SUPPLEMENTARY FIGURE 7.7: THE LACK OF pH DEPENDENT CONDUCTIVITY INCREASE IN THE BUFFER AND <i>VIBRIO CHOLERAE</i> T4BP.	174
SUPPLEMENTARY FIGURE 7.8: PREDICTED STRUCTURE OF THE <i>B. ADOLESCENTIS</i> TYPE IVA PILUS.	174

Main Tables

TABLE 2.1: PARTIAL CHARGES FOR OXIDIZED DEPROTONATED TYROSINE (TYROSYL RADICAL)	19
TABLE 2.2: PARTIAL CHARGES FOR PROTONATED OXIDIZED TYROSINE (TYROSINE CATION RADICAL).....	19
TABLE 2.3: PARTIAL CHARGES FOR OXIDIZED DEPROTONATED TRYPTOPHAN	19
TABLE 2.4: PARTIAL CHARGES FOR OXIDIZED PROTONATED TRYPTOPHAN (TRYPTOPHAN CATION RADICAL)..	20
TABLE 2.5: CONTRIBUTION OF SOLVATION ENERGIES TO OXIDATION ENTROPY OF SUBSTITUTED ANILINES...	37
TABLE 3.1: COMPUTED REDUCTION POTENTIALS OF A3Y AND A3W AT pH 7.0.....	62
TABLE 3.2: COMPUTED REDUCTION POTENTIALS OF HORSE HEART CYTOCHROME-C	65
TABLE 3.3: POTENTIAL ENERGY BARRIERS TO PT FROM W34 TO E15	67
TABLE 6.1: HOLE TRANSFER PARAMETERS FOR CTPR8.....	142

Supplemental Tables

SUPPLEMENTARY TABLE 3.1: DFT BENCHMARKING FOR CALCULATIONS OF THE REDUCTION POTENTIAL OF α_3Y AND α_3W USING THE ZWANZIG EQUATION	72
SUPPLEMENTARY TABLE 3.2: DFT BENCHMARKING FOR CALCULATIONS OF THE REDUCTION POTENTIAL OF α_3Y AND α_3W USING THE EXTENDED BORN-HABER METHOD	72
SUPPLEMENTARY TABLE 3.3: DFT BENCHMARKING FOR CALCULATIONS OF THE REDUCTION POTENTIAL OF CYTOCHROME-C USING THE ZWANZIG EQUATION.....	73
SUPPLEMENTARY TABLE 3.4: DFT BENCHMARKING FOR CALCULATIONS OF THE REDUCTION POTENTIAL OF CYTOCHROME-C USING THE GAUSSIAN APPROXIMATION	73
SUPPLEMENTARY TABLE 3.5: DFT BENCHMARKING FOR THE CALCULATIONS OF THE REDUCTION POTENTIAL OF CYTOCHROME-C USING THE LINEAR RESPONSE APPROXIMATION.....	73
SUPPLEMENTARY TABLE 3.6: COMPUTED REDUCTION POTENTIAL OF α_3W FOR INCREASING SIZE OF QM LAYER	74
SUPPLEMENTARY TABLE 4.1: FREE ENERGIES OF OXIDATION AND REORGANIZATION ENERGIES FOR ELECTRON TRANSFER HALF REACTION AT 310 K.....	106
SUPPLEMENTARY TABLE 4.2: FREE ENERGIES OF OXIDATION AND REORGANIZATION ENERGIES FOR HOLE TRANSFER HALF REACTION AT 310 K	106
SUPPLEMENTARY TABLE 4.3: GIBBS FREE ENERGY, REACTION REORGANIZATION ENERGY, AND ELECTRONIC COUPLING FOR HEME-TO-HEME ELECTRON TRANSFER AT 310 K	106
SUPPLEMENTARY TABLE 4.4: GIBBS FREE ENERGY, REACTION REORGANIZATION ENERGY, AND ELECTRONIC COUPLING FOR HEME-TO-HEME HOLE TRANSFER AT 310 K.....	106
SUPPLEMENTARY TABLE 4.5: ELECTRON TRANSFER RATES AT 310 K.....	107
SUPPLEMENTARY TABLE 4.6: HOLE TRANSFER RATES AT 310 K.....	107
SUPPLEMENTARY TABLE 4.7: FREE ENERGIES OF OXIDATION AND REORGANIZATION ENERGIES FOR ELECTRON TRANSFER HALF REACTION AT 270 K	107
SUPPLEMENTARY TABLE 4.8: GIBBS FREE ENERGY, REACTION REORGANIZATION ENERGY, AND ELECTRONIC COUPLING FOR HEME-TO-HEME HOLE TRANSFER AT 270 K.....	108
SUPPLEMENTARY TABLE 4.9: ELECTRON TRANSFER RATES AT 270 K.....	108
SUPPLEMENTARY TABLE 4.10: MM REORGANIZATION ENERGY PARAMETERS FOR ELECTRON TRANSFER AT 310 K	108
SUPPLEMENTARY TABLE 4.11: MM REORGANIZATION ENERGIES FOR HOLE TRANSFER AT 310 K.....	108
SUPPLEMENTARY TABLE 4.12: MM REORGANIZATION ENERGIES FOR ELECTRON TRANSFER AT 270 K.....	109

1. Introduction

1.1 Biological electron transfer

Electron transfer (ET) between proteins is a fundamental process which is critical for life. Metabolic pathways across the domains of life utilize electron transfer along chains of redox active enzymes to catalyze the generation of chemical energy in the form of ATP. In the mitochondria of eukaryotes, chloroplasts of plants, or the inner membranes of prokaryotes, the enzymes which enable long-range ET bind cofactors such as quinones (organic redox mediators), copper atoms, or iron-containing hemes. These cofactors enable stable oxidation and reduction reactions without generating high potential radicals, which pose a threat to the organism via the production of reactive oxygen species (ROS). Furthermore, each enzyme has evolved to have a distinct reduction potential, which provides directionality for the electron transfer reactions along the electron transport chain (Figure 1.1).

Developing an understanding of biological redox reactions has been an ongoing pursuit for more than 100 years⁴. In an effort to create biofuels and artificial photosynthetic systems to solve the energy and climate problems facing the world today, interdisciplinary researchers have been spurred to further scrutinize the mechanisms of biological energy production. To understand these reactions, we must turn to the theory of electron transfer developed by Marcus⁵.

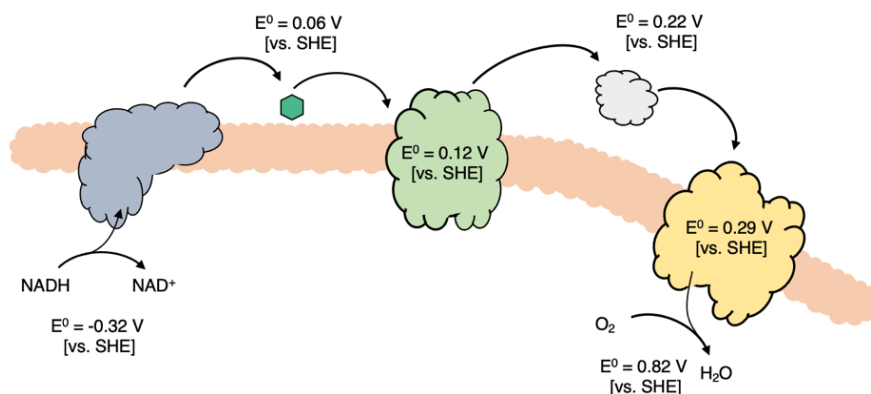


Figure 1.1: Distinct reduction potentials direct electron transfer toward the enzyme with the highest potential.

Tunneling models of electron transfer in proteins

Each pair of redox enzymes in the electron transport chain can be treated as separate donors and acceptors in an electron transfer reaction. Analogous to transition state theory, the rate of an electron transfer reaction is described by an equation of the form,

$$k \propto A e^{-E_A/k_B T} \quad (1.1)$$

Marcus demonstrated that this rate is determined by three parameters: the free energy difference between the donor and acceptor states, the coupling between the states, and an energy term, first introduced by Marcus, called the reorganization energy (see chapter 2.3-2.6 for detailed description of each term). The Gibbs free energy (ΔG^0) and the reorganization energy (λ) terms determine the activation energy of the reaction,

$$E_A = \frac{(\Delta G^0 + \lambda)^2}{4\lambda} \quad (1.2)$$

and the coupling contributes to the pre-exponential term,

$$A \propto |H_{AB}|^2 \quad (1.3)$$

In the 1990's models began to emerge which described biological electron transfer in terms of the coupling between cofactors, where the surrounding protein acts as an intervening medium⁶⁻⁹.

These models suggested that the protein surrounding the cofactors, mediates the electronic coupling by controlling the decay of the electron transfer rate. Beratan and Onuchic introduced separate decay constants for an electron tunneling through a covalent bond, a hydrogen bond, or through space⁸. Their model demonstrated a direct role of protein structural motifs such as alpha helices and beta sheets. By creating stable hydrogen bonding networks, these structural elements provide efficient pathways for tunneling electrons. However, electron transfer according to these models is still strongly limited to short distances (only a few nanometers). Therefore, many cofactors are required to enable electron transfer beyond a few nanometers.

These tunneling models have proven very useful in identifying the preferred pathways for electron transfer in protein environments, but they provide little information on the kinetics of the

reaction. Equation 1.1 and 1.3 show us that the rate of electron transfer depends quadratically on the coupling, and exponentially on the activation barrier. Therefore, models of biological electron transfer must move beyond tunneling and into the hopping regime.

From tunneling to hopping

Before moving on, I will take a moment to clarify the differences between the tunneling and hopping mechanisms. In many instances, these two terms have been used interchangeably. However, I would like to draw a distinction. Tunneling is a single-step process in which the electron goes through an energetic barrier (Figure 1.2). The rate of ET by tunneling decays exponentially with distance with the intervening medium determining the decay constant. In the last few paragraphs, we have discussed electron tunneling between cofactors, in which the distance separating the cofactors provides the energetic barrier, and the protein structure determines the decay. Notably, the rate of a pure tunneling process is independent of temperature.

In contrast, hopping is a process in which thermal energy propels the electron over the barrier in a single step. Within the Marcus theory of electron transfer, when an electron is exchanged between donor and acceptor, both hopping and tunneling are represented. The hopping contribution comes in the form of the free energy and reorganization energy, which together determine the activation barrier (Equation 1.2). The tunneling contribution comes from the coupling, which allows the electron to

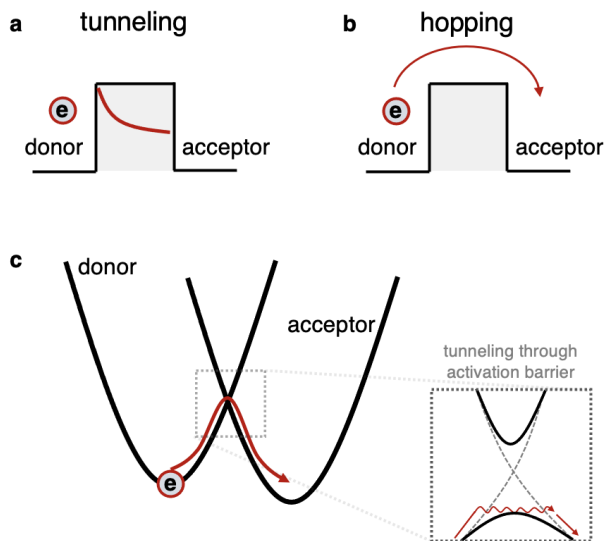


Figure 1.2: Tunneling and hopping in biological electron transfer.

(a) Depiction of electron tunneling through a rectangular barrier. (b) Depiction of electron hopping over a barrier. Hopping is driven by thermal energy. (c) Electron transfer between molecules requires energy to get over a barrier. When the barrier is small enough, tunneling takes over. This results in an effectively smaller barrier.

tunnel through the activation barrier (Figure 1.2). However, a multistep tunneling process in which the electron transiently occupies intermediate cofactors between initial and final states is referred to as hopping. Unlike a single step, for which the dependence on length is exponential, hopping has a linear length dependence.

For a molecule between two electrodes, the transition from single step tunneling to hopping is dependent on molecular length. Work from the group of Daniel Friesbie has demonstrated, using molecular wires, that ET across molecules less than 4 nm in length occurs by tunneling, whereas for molecules greater than 4 nm in length, ET occurs by hopping¹⁰. In the context of biological electron transfer, an individual electron exchange between enzymes occurs on the tunneling length scale, but the transport across multiple sites spans greater distances and is best characterized by hopping.

Reorganization energy sets the speed limit

Proteins are composed of flexible polypeptide chains folded into higher order structures. While the folds are incredibly reproducible, the resulting structures are dynamic, resulting in fluctuating conformations which can respond to changes in environment. Proteins are also charged (i.e. polar) molecules, submerged in an aqueous solution. Therefore, fluctuations in the positions of the charged amino acids or bound cofactors induce a response from the surrounding water. When an electron is transferred to a protein, its charge is altered, and the protein and surrounding water molecules must relax to a new minimum energy conformation. The energy required for the system to reach its new minimum energy state is quantified by the reorganization energy.

In polar solvents, such as water, reorganization energies can reach values as high as 1 eV. For reference, the free energy change for each step in the mitochondrial electron transport chain is approximately -0.1 eV. Therefore, the activation barrier (Equation 1.2), determined by the square of the sum of the Gibbs free energy change and the reorganization energy, is heavily dominated

by the reorganization energy. However, the structure of proteins can also restrain, or dampen conformational relaxation such that the time required for the protein to fully sample the available energetic states is much slower than the electron transfer reaction. This pushes the ET reaction out of equilibrium and into the non-ergodic regime.

This scenario has been explored extensively by Matyushov¹¹⁻¹⁵. His work has demonstrated that ergodicity breaking dynamics give rise to large variance reorganization energies. This occurs because the polarizability of the active site (cofactor) couples to the fluctuations of the protein and the solvent, giving rise to large potential energy fluctuations. Therefore, the potential energy surfaces of the donor and acceptor states get wider, and their crossing point lowers. In this regime, reorganization energies can be as low as 0.3 V¹². This mechanism has been the subject of debate^{16,17}. However, measured kinetics of electron transfer reactions strongly suggest there is a mechanism by which enzymes decrease reorganization energies^{18,19}.

Protein environments tune reduction potentials

Thus far, we have established that the protein surrounding electron transfer cofactors provides an efficient pathway for electron tunneling, and its dynamics determine reorganization energies. Therefore, it may not be surprising that protein environments are also responsible for tuning reduction potentials and thus setting the Gibbs free energy difference for an ET reaction. Reduction potentials are determined by the relative stabilities of the charged and uncharged states of the cofactor. Cytochrome c, for example, which contains an iron-containing heme molecule, can exist either in an oxidized Fe(III) state or a reduced Fe(II) state.

The protein sets the reduction potential of the heme through three interactions. The first is through the primary coordination sphere of the iron atom (Figure 1.3). Iron containing hemes in c-type cytochromes exist in an octahedral geometry, meaning that they have 6 separate bonds to the iron (4 in plane from porphyrin, 2 out-of-plane from protein or solvent). By altering the ligand strength of the bonds donated from the protein, the oxidized or reduced state can be preferentially

stabilized. For example, replacing the distal methionine ligand of cytochrome c with a histidine, such that both axial and distal ligands are histidine, stabilizes the oxidized state, shifting the redox potential by more than 300 mV²⁰.

The second interaction is often referred to as the secondary coordination sphere. This includes protein residues which form hydrogen bonds with the cofactor (Figure 1.3) or distort its geometry. For hemes, hydrogen bonds with propionic acid sidechains stabilize the reduced state. Deletion of hydrogen bond donors near the active site can lead to shifts in reduction potential of about -20 mV to -70 mV²¹. A similar range can be achieved by influencing heme geometry, and in particular out-of-plane distortions²²⁻²⁴. These distortions shift the energy levels of the orbitals responsible for bonding with the protein, thus altering ligand strengths. While this does not lead to shifts in redox potential as large as when swapping the ligand identity, it has been linked to the large range of potentials found in hemes²².

Geometrical distortions are particularly limited to large cofactors such as hemes. However, regulation of redox potentials through the hydrogen bonding interactions is ubiquitous across hemes, flavins, quinones, and amino acids^{3,21,25}. In fact, the role of hydrogen bonds in determining reduction potentials and thus ET rates is a theme in my dissertation. You will find that this topic is revisited in Chapters 3, 4, and 6.

The final protein interactions which influence reduction potential are electrostatics. The charges surrounding the active site create a Coulomb potential which can polarize the active site (Figure 1.3), preferentially stabilizing the oxidized or reduced state. The reduction potential of

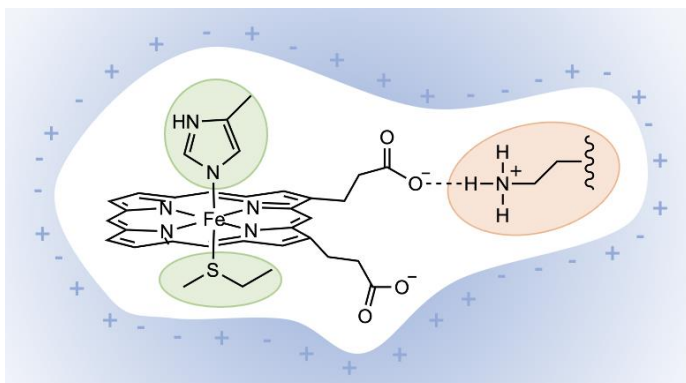


Figure 1.3: The local environment of a cofactor determines its reduction potential.

The reduction potentials of cofactors such as hemes are determined by a set of primary secondary and tertiary interactions with the protein environment. The primary coordination sphere includes the amino acids directly bound to the iron atom (green). The secondary interactions include hydrogen bonds (orange) and distortions of the cofactor. The tertiary interactions are long range electrostatics (blue continuum).

the copper atom in plastocyanin was tuned over 50 mV by altering the distribution of charged amino acids²⁶. A similar result was observed for an artificial heme protein maquette in which alterations to charge placements resulted in shifts in potential up to 100 mV²⁷. In these studies, we can view the protein as a complex solvent with a macroscopic dipole, which pushes and pulls on electrons placed on the cofactor. In chapters 3 and 4, I present data for which I used quantum mechanical/molecular mechanics models to explicitly describe these effects on hemes as well as the amino acids tyrosine and tryptophan. I demonstrate that polarizability must be incorporated to accurately determine the reduction potentials in proteins.

Together, the primary and secondary sphere interactions as well as electrostatics give rise to a highly tunable arsenal of redox active enzymes, enabling functions ranging from energy production²⁸ to signaling²⁹ and DNA synthesis³⁰. It seemed clear that biology used enzymes with distinct redox potentials to direct electron flow toward terminal electron acceptors such as molecular oxygen. However, the discovery of *Geobacter sulfurreducens*, an anaerobic soil bacterium challenged this understanding, ultimately leading to a new branch of the biological electron transfer field of research: the study of protein nanowires.

1.2 How a case of mistaken identity fueled the search for a new mechanism of protein conductivity

G. sulfurreducens is an obligate anaerobic (cannot grow using oxygen or fermentation) bacterium isolated from surface sediments³¹. Interest in this bacterium focused on its ability to respire using insoluble iron oxide as the terminal electron acceptor³². Reduction of transition metal complexes by microbes in the soil has an incredible impact on the stability of the geochemical cycling of iron, manganese, and uranium, among others³³. The ability to reduce toxic metals such as chromium and uranium inspired efforts to cultivate these organisms, to be applied toward bioremediation efforts^{33,34}.

Efforts to understand the respiratory mechanisms of *G. sulfurreducens* led to the discovery that the mechanisms that enable iron oxide reduction also allow the bacterium to generate current

in microbial fuel cells³⁵. In these experiments, *G. sulfurreducens* was cultured in a sealed chamber in which it was provided a graphite electrode as the only electron acceptor. Through metabolism of acetate, it converted chemical energy into an electrical current. Later experiments demonstrated that maximal current output could be sustained under a steady flow of nutrient rich medium³⁶. This experiment demonstrated that the bacterium makes a direct electrical contact with the electrode. This result was consistent with the observation that *Geobacter* species were incapable of producing soluble redox shuttles such as flavins³⁷.

The process by which microbial organisms transfer respiratory electrons to insoluble electron acceptors beyond their outer membrane is known as extracellular electron transfer (EET). EET can occur by two modes: diffusive redox shuttles and direct electrical contact^{38,39}. At the time when *G. sulfurreducens* was shown to reduce extracellular iron oxide and transfer electrons to graphite electrodes, it was known that several bacterial species were capable of EET via diffusive redox shuttles, however it was unclear how a bacterium would achieve EET through direct electrical contact. Ultimately, it was determined that type IV pili, a class of protein filaments which mediate contact and adhesion between bacteria and their surroundings⁴⁰, were critical to the mechanism of EET in *G. sulfurreducens*.

More specifically, experiments demonstrated the necessity of the *pilA* gene for iron oxide reduction and current production⁴¹. When the *pilA* gene was knocked out ($\Delta pilA$) cells could not reduce iron oxide. Furthermore, filaments observed to project out from the bacterium under iron reducing conditions were not observed in the $\Delta pilA$ strain. This led to the conclusion that the filaments that were observed were type IV pili composed of the PilA protein and that the pili themselves were the electrical conduit through which *G. sulfurreducens* transferred respiratory electrons.

The model of ET along pili implies that electrons could be transported over micrometer distances along a homopolymer composed entirely of protein. This conclusion challenged the

biological electron transfer paradigm. At the time, it was thought that long-range electron transfer required multiple steps between distinct enzymes containing cofactors with progressively more positive reduction potentials. A homopolymer is necessarily an equipotential surface, and the only redox active amino acids found in natural proteins are tyrosine and tryptophan, both of which have large reduction potentials close to 1 V vs SHE. Under these conditions, electron hopping seemed unlikely to support high enough electron flux to support respiration, and the distance was much too large for single step tunneling. This left room for new hypotheses for the mechanism of direct-contact EET.

Models of protein nanowire conductivity

The hypothesis that *G. sulfurreducens* uses type IV pili for direct-contact EET, while interesting, has since been disproved. *Geobacter* does not produce T4P, rather it produces novel split pili made up of PilA-N and PilA-C proteins that fuse together to form pili that show low stability. These split pili are required for EET, but they appear to serve a secretory role⁴², while conductive protein filaments (i.e. protein nanowires) composed of multiheme cytochromes OmcS^{43,44} and OmcZ⁴⁵ provide the path for electron transport. While wrong, the pili hypothesis shaped the electron transfer field for 15 years and contributed to models which largely motivated my thesis project.

Measurements of the electrical conductivity of the extracellular filaments from *G. sulfurreducens* confirmed their intrinsic ability to transport charge⁴⁶. This study also probed the mechanism of charge transport by measuring how the conductivity changed as the temperature was lowered. For a thermally activated process like an electron hopping mechanism, the conductivity is expected to follow an Arrhenius dependence (Equation 1.1), where, E_A is the activation energy and $k_B T$ is the thermal energy. Therefore, as temperature is lowered the conductivity would be expected to decrease. Tunneling, unlike hopping, is temperature

independent. However, rather than an Arrhenius dependence, or a lack of a temperature dependence, the conductivity of the filaments increased exponentially (Chapter 4).

An exponential increase in conductivity upon cooling suggests that the transport of electrons through the nanowires is inhibited by molecular vibrations. This is what happens in metals, where the only barrier faced by electrons are collisions with quantized vibrations called phonons. The similarities between the temperature dependence of metallic charge transport and that of the nanowires led to the hypothesis that aromatic amino acids such as tyrosine, phenylalanine, and tryptophan were stacked along the core of the pilus filaments resulting in a delocalized cloud of electrons along the entire length of the nanowire. This hypothesis was supported by measurements which demonstrated that nanowires produced by cells in which point mutations were introduced to remove aromatic amino acids were incapable of iron reduction or current production in fuel cells⁴⁷.

A static model of the putative *G. sulfurreducens* pilus was built in which the aromatic residues in the helical N-terminal pilin (PilA-N) were positioned within van der Waals contact of each other to maximize molecular orbital overlap⁴⁸. Homology models, based on the structure of the type IV pili of *Pseudomonas aeruginosa* and *Neisseria gonorrhoeae*, were also constructed. However, when calculations of coherent electron transfer through delocalized molecular orbitals were performed on any of these models, they were unable to account for the experimentally determined conductivity⁴⁹. Alternative mechanisms, such as electron hopping along tyrosine and tryptophan redox centers were also considered. However, theoretical estimates of hopping conductivity in pili also came up short^{49,50}.

The failure of theoretical models of the putative *G. sulfurreducens* pilus was not due to poor construction of the aromatic amino acid hypothesis, as aromatics can indeed support charge transfer in proteins, both over short (~ 3.5 nm)⁵¹ and long (>100 nm) distances^{3,52}. Rather, the models could never have succeeded as the nanowires were misidentified. This statement may seem obvious, but I make this point because it is important that the work on conductivity in pili

not be rejected but rather cautiously reinterpreted. The models may be wrong, but it spawned a new branch of a century-old field of research and inspired discoveries and inventions that may not otherwise have been.

1.3 Cytochrome nanowires

The failure of computational models of hypothetical conductive pili highlighted the need for experimentally determined, high resolution structures of the extracellular filaments of *G. sulfurreducens*. However, solving the structure of thin (~4 nm) helical protein filaments posed several technical challenges. Micrometer long filaments are not amenable to x-ray crystallography, necessitating the use of cryo-electron microscopy (Cryo-EM). But even with Cryo-EM, standard single-particle techniques are inappropriate for reconstructing the three-dimensional structure of a helical filament. Fortunately, the development of methods for helical

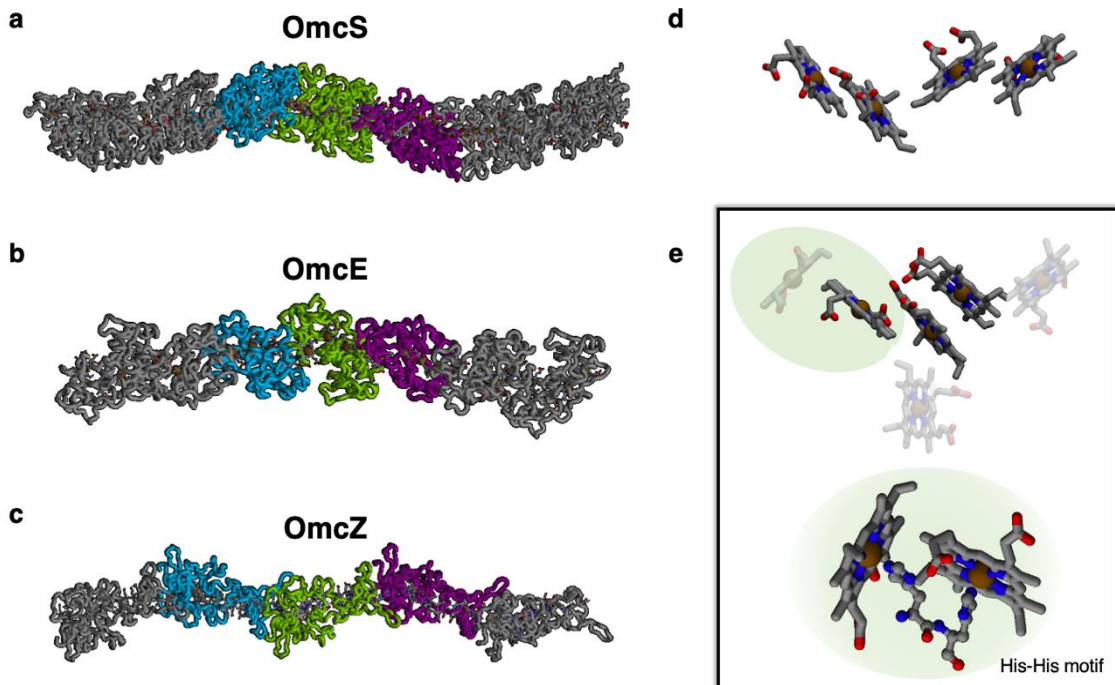


Figure 1.4: Polymerization of cytochrome nanowires aligns hemes in stacked chains.

(a-c) Structure of the (a) OmcS, (b) OmcE, and (c) OmcZ cytochrome nanowires. The central three protein chains of the homopolymers are colored in cyan, green and purple. (d) Alternating parallel/perpendicular heme arrangement which characterizes the electron transport pathway in OmcS and OmcE. (e) Distinct features of the heme arrangements in the OmcZ cytochrome nanowire. The central six hemes of each subunit include a set of three parallel hemes, flanked by perpendicular hemes which are held together by a di-histidine (his-his) peptide motif.

reconstruction⁵³ and the so-called Cryo-EM “resolution revolution”⁵⁴ enabled five research groups (collaboration 1: Malvankar, Hochbaum, and Egelman labs; collaboration 2: Lovley and Strauss labs) to obtain two independent structures the *G. sulfurreducens* filaments within 2 months of each other^{43,55}.

These structures revealed a homopolymer of hexa-heme cytochrome OmcS in which the hemes were arranged in an alternating parallel-perpendicular stacking arrangement. In hindsight, this result was not surprising, as OmcS had previously been demonstrated to be required for iron reduction⁵⁶, and was localized along the length of the extracellular filaments⁵⁷. However, the lack of precedent for polymeric cytochromes and the indirect evidence identifying pili as the electrical conduit kept the field from reaching this conclusion prior to the presentation of the structure.

Since the publication of the structure of the OmcS nanowire, the structures of two more cytochrome filaments have been published. OmcE is a tetraheme cytochrome that was produced when the *omcS* gene was mutated⁵⁸, and OmcZ is an octaheme cytochrome which is upregulated in response to an applied electric field^{45,59,60}. While each has a unique structure, the heme arrangements are very similar, with alternating parallel and perpendicular configurations. OmcZ, which has a 1000-fold higher conductivity than OmcS⁴⁵, has the most distinct heme arrangement. The hemes are aligned linearly with sets of three parallel hemes and pairs of perpendicular hemes connected by a dihistidine peptide.

The existence of cytochrome filaments seemed to some to be an answer to the question of how *G. sulfurreducens* achieves ET to electron acceptors more than a micrometer away⁶¹. In part, this is true. After all, cytochrome nanowires contain heme cofactors. Therefore, from a structural point of view, they fit within the biological ET paradigm. However, the nanowire is still an equipotential surface, and is therefore lacking a driving force to direct electrons within the wire. This is most clearly demonstrated by the reversibility of the experimentally determined current-voltage response of OmcS and OmcZ nanowires (current-voltage response of OmcE has not been

determined). Therefore, the difference in potential between the bacterium and the electron acceptor (iron-oxide or electrode) ($100 - 200 \text{ mV}^{62}$) must be sufficient to drive electron transfer.

This analysis implies that ET along cytochrome nanowires is characterized by a low activation barrier. Experimental evidence strongly suggests that both OmcS and OmcZ conduct via a multistep hopping mechanism of charge transport^{44,45}. Therefore, the activation barrier is described by Equation 1.2. Several groups, including myself, have attempted to compute the activation barrier using Marcus theory, but to date, computational estimates of cytochrome nanowire conductivity have been low^{44,63} likely due to overestimation of the reorganization energy. The modeling I present in Chapter 4, suggests reorganization energies are approximately 0.8 eV. However, theoretical analyses of hopping conductivity in extended one-dimensional wires suggests that reorganization energies as low as 0.2 eV are required to explain the charge transport rates measured in OmcS⁶⁴. Future efforts will be required to explain this discrepancy.

One of the key conclusions of my thesis is that cytochrome nanowires are highly tunable, functional materials. The existence of two nanowires with conductivities spanning three orders of magnitude is remarkable enough ($\sigma(\text{OmcS}) = 30 \text{ mS/cm}$; $\sigma(\text{OmcZ}) = 30 \text{ S/cm}$)⁴⁵, but in my work, I have demonstrated that through environmental perturbations, I could increase OmcS conductivity 300-fold (Chapter 4) and OmcZ conductivity 30,000-fold (Chapter 5). This has clear implications regarding the adaptability of *G. sulfurreducens* in its environment, but also presents cytochrome nanowires as promising candidates for bioelectronic devices.

1.4 Protein conductivity in the absence of hemes

Even before the discovery of cytochrome nanowires, non-cytochrome proteins have been of interest for applications in bioelectronic devices. Protein-based electronics have several benefits over traditional silicon-based electronics. Proteins are flexible, biocompatible, and easily tuned using site-directed mutagenesis. However, proteins are large band-gap materials, meaning that it takes a large amount of energy to inject mobile electrons, and resulting currents are very small

(~1 nA). Despite its limitations, the application of proteins in bioelectronics has had success in biosensing, where the detection of a biomolecule is converted into an electrical signal⁶⁵.

The first section of this introduction discussed the evolution of the view of the role of protein in biological ET reactions. In contrast to the view that protein serves as a dielectric medium to enable efficient ET between cofactors, the last 25 years have demonstrated that protein can be an active participant in redox biochemistry. It has been demonstrated that enzymes such as ribonucleotide reductase^{51,66} or the BLUF photoreceptor⁶⁷ use chains of tyrosines and tryptophans to guide electrons through a proton environment. However, these natural reactions occur over short distances of a few nanometers and leverage high potentials to oxidize the tyrosine and tryptophan residues. The last few years have demonstrated that stacked aromatic amino acids can extend these reactions over tens to hundreds of nanometers in both natural and synthetic systems^{1,3,12,52}. Most importantly, these studies have uncovered key mechanistic details which enable efficient charge transport in the absence of cofactors.

When lacking cofactors such as hemes, the amino acids tyrosine and tryptophan must serve as redox centers. When oxidized, both of these residues undergo a large shift in pKa. This means that upon oxidation, their protons become destabilized and are more likely to dissociate. Therefore, their oxidation most often occurs in a proton coupled electron transfer (PCET) reaction, in which ET reaction is paired with proton dissociation. This is very important to keep in mind when studying ET in proteins as the efficiency of PCET reactions are often determined by the proton dissociation pathway⁶⁷⁻⁶⁹. Work that I performed in collaboration with my colleague Catharine Shippy, demonstrated that stable hydrogen bonds with tyrosine residues enable proteins to perform ET over distances greater than 100 nm by reducing the barrier for proton transfer (Chapter 6)³.

In the context of the ET mechanisms introduced earlier, PCET qualifies as hopping conductivity. Like hopping in other systems, the rate will depend on the free energy difference and electronic coupling between donor and acceptor as well as the reorganization energy

determined by the environment. As the reduction potentials of tyrosine and tryptophan residues are similar, it is plausible that ET barriers between residues can be small. However there still exist large barriers for injection of charges into protein. In fact, the contact resistance of a protein-electrode interface can be as large as 10-100 G Ω , comparable to the resistance of protein itself³. Contact resistance is influenced by both the coupling of the protein to the electrode surface as well as the reorganization energy of the protein and solvent at the electrode interface. This is detrimental for biosensing applications, in which fluctuations in the intrinsic resistance must be measured.

The group of Stuart Lindsay has made significant progress in overcoming contact limitations. By creating a direct link between the electrode and the molecule, the measured contact resistance can be reduced by 4 orders of magnitude⁷⁰. For proteins, a this can be achieved by injecting charge through specific contacts, such as those formed from specific binding interactions⁷¹. Analysis of conductance through specific contacts has enabled several mechanistic studies which have revealed remarkably efficient transport through a variety of proteins^{1,65,71,72}. These observations are consistent with the models of Beratan and Onuchic⁹ which predict more efficient electron tunneling through covalent and hydrogen bonds.

It is important to note that this discovery is not without controversy. Attempts to reproduce efficient ET through proteins forming specific contacts were unsuccessful, leading Bera et al. to conclude that specific contacts do not provide a more efficient ET path⁷³. While I do not want this introduction to devolve into a nuanced point-by-point analysis comparing two studies, I will point out one key difference between the experiments. The experiments performed by Zhang et al., which demonstrated efficient ET through specific contacts, were performed under fully solvated conditions, whereas those performed by Bera et al. were performed after the protein had been air dried. This is very important as the most recent models of protein conductivity have suggested that the most important determinant of the ET rate between tyrosine and tryptophan residues is the reorganization energy¹², which is heavily influenced by the solvation environment. In the

absence of water, it appears that the ET reaction switches to a single-step tunneling mechanism⁷³, which can support ET over small gaps of about 3 nm, but would fail for greater distances.

My work on ET in proteins is focused on the long-distance regime, which appears to occur by hopping with a low activation barrier. Throughout my thesis work I have studied several natural and synthetic protein systems (Chapters 6 & 7), all of which are consistent with the idea that aromatic amino acids can enable long-range ET. Remarkably, my thesis culminates with work which demonstrates EET performed by the pathogens *P. aeruginosa*, *N. meningitidis*, and *N. gonorrhoeae* is assisted by conductive type IV pili (Chapter 7). This is somewhat ironic, given that the project was inspired by the now disproved hypothesis of conductive pili in *G. sulfurreducens*. However, conductivity in proteins appears to be a widespread phenomenon, with real biological significance.

2. Computational Methodology

In this chapter I will describe the computational methods I have used to study charge transport in protein systems. While most are implementations of previously developed methods, sections 2.1.4 and 2.1.11 describe methods I have developed in my time at Yale. Every section will describe the theory behind the method as well as specific settings I have used to obtain my data. Several sections (2.1.4 and 2.1.5) also include a “Practical Implementation” tutorial in which I include step-by-step instructions for performing the calculations described.

2.1 Molecular dynamics simulations

Biological electron transfer occurs in flexible protein scaffolds at finite temperature. This means that the environment surrounding the active sites of these reactions is dynamic⁷⁴. Therefore, to accurately model these reactions, we need to sample fluctuations in the structure to account for all accessible distances between donor and acceptor and well as variations in the environment which occur in response to a change in charge. To do this, I have used molecular dynamics simulations.

For all of my simulations, I used NAMD to implement dynamics according to the CHARMM⁷⁵ force field, with periodic boundary conditions and the particle-mesh Ewald (PME) method to describe long-range electrostatics. All standard amino acid residues were parameterized with the CHARMM36 force field parameters. For the c-type hemes in the OmcS and OmcZ nanowires, the force field parameters were obtained from Autenrieth et al⁷⁶.

For simulations of oxidized tyrosine, for which CHARMM parameters did not exist, I adapted the topology assigned to the phenoxide residue. Specifically, I altered the MM partial charges to reproduce the difference in electronic dipole between oxidized and reduced phenol, as evaluated by DFT at the B3LYP / cc-pVDZ level of theory. The partial charges used in the simulations can be found in Table 2.1.1. For the oxidized tryptophan residue, I used a similar approach, in which I adjusted the MM partial charges to reproduce a change in dipole between

the oxidized and reduced species of the tryptophan residue determined at the B3LYP / cc-pVDZ level of theory. The partial charges used in the simulations can be found in Table 2.1.2.

Once the topology of the protein was defined, each system was solvated in a rectangular water box using the TIP3P model, such that the edge of the water box was at least 12 Å from any protein atoms. The total charge of the system was neutralized using Na⁺ or Cl⁻ ions using the VMD ionization protocol.

The fully solvated and ionized systems were initially minimized for 5,000 – 10,000 steps followed by a 2.5 ns relaxation of the solvation water box under constant atom count, pressure, and temperature (NPT) conditions. Temperature and pressure were maintained using the Langevin thermostat and barostat, respectively. The systems were then equilibrated to the temperature at which we wished to run the production run. Most simulations were run at 310 K (37 °C); however, for my work on the temperature dependence of OmcS conductivity, I also ran a simulation at 270 K (-3 °C).

Equilibration was performed under constant atom count, volume, and temperature (NVT) conditions, with the temperature increased from 0 K to the final temperature in 10 K increments with 100 fs of simulation at each temperature. Once the final temperature was reached the system was allowed to simulate for 3.5 ns. The equilibration was performed under harmonic restraints with a force constant of 0.1 kcal/mol applied to the amino acid sidechains and a force constant of 1.0 kcal/mol applied to the protein backbone and any non-protein ligands (e.g. hemes). Production runs were performed in an NPT ensemble. For most projects, production simulations were run for at least 100 ns. However, for the more computationally expensive simulations of OmcS dimers, simulations were run for at least 50 ns. Frames were written every 2.5 ps. Thermal equilibration was assessed by a stable protein backbone RMSD, or by analyzing the distribution of atomic velocities.

Table 2.1: Partial charges for oxidized deprotonated tyrosine (tyrosyl radical)

Atom Name	Atom Type	Partial charge (e-)
CE1	CA	-0.524
HE1	HP	0.396
CE2	CA	-0.524
HE2	HP	0.396
CD1	CA	-0.078
CD2	CA	-0.078
HD1	HP	0.223
HD2	HP	0.223
CG	CA	0.106
CZ	CA	0.392
OH	OC	-0.532

TOTAL RESIDUE CHARGE = 0.00

Table 2.2: Partial charges for protonated oxidized tyrosine (tyrosine cation radical)

Atom Name	Atom Type	Partial charge (e-)
CE1	CA	-0.069
HE1	HP	0.212
CE2	CA	-0.069
HE2	HP	0.212
CD1	CA	-0.073
CD2	CA	-0.073
HD1	HP	0.208
HD2	HP	0.208
CG	CA	0.025
CZ	CA	0.156
OH	OC	-0.405
HH	H	0.49

TOTAL RESIDUE CHARGE = 1.00

Table 2.3: Partial charges for oxidized deprotonated tryptophan

Atom Name	Atom Type	Partial charge (e-)
CB	CT2	-0.189
HB1	HA2	0.129
HB2	HA2	0.129
CG	CY	-0.02
CD1	CA	-0.102
HD1	HP	0.234
NE1	HY	-0.472
CE2	CPT	0.216
CD2	CPT	0.110
CE3	CAI	-0.224
HE3	HP	0.185
CZ3	CA	-0.184
HZ3	HP	0.175
CZ2	CAI	-0.221
HZ2	HP	0.196
CH2	CA	-0.112
HH2	HP	0.170

TOTAL RESIDUE CHARGE = 0.00

Table 2.4: Partial charges for oxidized protonated tryptophan (tryptophan cation radical)

Atom Name	Atom Type	Partial charge (e-)
CB	CT2	-0.2
HB1	HA2	0.18
HB2	HA2	0.18
CG	CY	-0.024
CD1	CA	-0.04
HD1	HP	0.32
NE1	HY	-0.446
HE1	H	0.435
CE2	CPT	0.244
CD2	CPT	0.133
CE3	CAI	-0.194
HE3	HP	0.247
CZ3	CA	-0.181
HZ3	HP	0.221
CZ2	CAI	-0.238
HZ2	HP	0.243
CH2	CA	-0.106
HH2	HP	0.225

TOTAL RESIDUE CHARGE = 1.00

2.2 QM/MM calculations

2.2.1. Theory

For reactions, such as electron transfer, which require a quantum mechanical description, but are much too large to fully describe using density functional theory (DFT), I used hybrid quantum mechanics / molecular mechanics (QM/MM) calculations. QM/MM methods allow for large molecular systems to be partitioned into layers which can be described at different levels of theory. This allows a user to simulate processes, such as charge transfer or the breaking and formation of bonds, which cannot be described by standard molecular mechanics force fields, using methods such as Hartree-Fock (HF), DFT, or density functional tight binding (DFTB), while describing the remainder of the system using a less computationally demanding level of theory.

In my work, I have used a few QM/MM schemes to describe electron transfer reactions. The first is an electrostatic embedding scheme, in which the active site of the reaction (heme, tyrosine, or tryptophan) is described with DFT, while the remainder of the system is simplified to a

collection of point charges, with charge values determined by the partial charges defined in the CHARMM force field. Electrostatic embedding as implemented in the Q-Chem⁷⁷ software package defines the system energy as the sum of the self-consistent field (SCF) energy and the electrostatic potential energy of the point charges.

$$E_{total} = E_{QM} + E_{MM} \quad (2.1)$$

where,

$$E_{MM} = \sum_i \sum_j \frac{q_i q_j}{r_{ij}} \quad (2.2)$$

where, q_i and q_j are the partial charges of atoms i and j , and r_{ij} is the distance between atoms i and j . Notably, when computing the SCF energy, the electron density is allowed to be polarized by the electric field imposed by the point charges. This is a very important point, as external electric fields can significantly impact the computed wavefunction energy (see Figure 3.6). However, it is important to note that, when implementing electrostatic embedding using the Q-Chem `$external_charges` module, E_{QM} and E_{MM} are not reported separately. Rather, the software returns one SCF energy containing both the MM and QM contributions.

The Q-Chem Janus model is another QM/MM module which allows for electrostatic embedding. The benefit of the Janus model is the additional ability to include van der Waals (vdW) and bonding contributions to the MM layer. Additionally, the energetic contributions are reported separately, providing an advantage over the `$external_charges` approach. The Janus model defines the total energy using the additive scheme defined by Equation 2.1. However, in these calculations E_{QM} is further partitioned into the QM SCF energy and the QM/MM interaction energy, which includes the vdW interaction, and E_{MM} is defined by an MM force field. For my calculations, I used the CHARMM force field.

These two methods contrast with the ONIOM method, a subtractive scheme, which defines the total system energy as follows.

$$E_{Total} = E_{total}^{MM} - E_{QM}^{MM} + E_{QM}^{QM} \quad (2.3)$$

where E_l^a is the energy of the l layer at the a level of theory. This method is widely used, but it is important to note that ONIOM does not allow for accurate electrostatic embedding calculations due to a mismatch between the electrostatic interaction energies computed at the QM and MM levels.

The details regarding the DFT methods used for each project are specified in the methods section of each relevant chapter.

2.2.2. Practical Implementation

Required software

- Python3
- Q-Chem

Required files (scripts and input files)

- build_qmmm_struct_v11.py
- run_janus_noopt.py
- average_energies.py
- janus.rem

You can download these files from Github: <https://github.com/dahlpete/qmmm-qchem-setup>

Setting up QM/MM calculations can be a daunting task. To alleviate the difficulty, I wrote a Python script which uses the MDAnalysis package in Python3 to generate QM/MM input files for the Q-Chem software package. This tutorial will walk you through installing the MDAnalysis module and setting up a QM/MM optimization of a tryptophan using the Janus model.

Step1: Install MDAnalysis

MDAnalysis can be easily installed using conda. If you are working off of a local machine use the following commands:

```
conda config --add channels conda-forge
```

```
conda --install mdanalysis
```

If you are running your code on a computing cluster, install MDAnalysis using a conda environment:

```
module load miniconda  
conda create -n mdanalysis python=3.7  
source activate mdanalysis  
conda install -c conda-forge mdanalysis
```

Once installed, you can operate python with MDAnalysis within the conda environment you have just created. When you log back into the cluster, you will need to reload the conda environment:

```
module load miniconda  
source activate mdanalysis
```

Alternatively, you can include the path to the Python3 executable in the header of the Python scripts and compile them using the `chmod` command. To do this, first determine the location of the Python executable in your MDAnalysis conda environment. Load the environment using the commands above then type,

```
which python
```

This will return the fully path to the Python executable. Copy the path and paste it into the header of your Python scripts. For example,

```
#!/[my_path]/python
```

where, [my_path] is the directory that was returned in your last command.

Step 2: Choose the level of theory for your calculation

Open the file janus.rem

```
$comment
QMMM Janus Model for Tryptophan
QM : Tryptophan residue
MM : All atoms not in the QM layer
$end

$rem
QM_MM_INTERFACE      JANUS
FORCE_FIELD          CHARMM27
USER_CONNECT         TRUE
JOBTYPE              opt
EXCHANGE             b3lyp
BASIS                cc-pVDZ
SCF_CONVERGENCE      6
SCF_GUESS            CORE
MAX_SCF_CYCLES       200
MODEL_SYSTEM_CHARGE  0
MODEL_SYSTEM_MULT    1
THRESH               12
VARTHRESH            FALSE
INCDFT               FALSE
$end
```

This file is formatted to be directly copied and pasted into the Q-Chem input file. In this file, you choose the method you wish to use for the QM/MM calculation. Notice that the variable QM_MM_INTERFACE is set to JANUS, indicating that the Janus model will be used to partition the QM and MM layers. The variable FORCE_FIELD sets the level of theory for the MM layer. In this tutorial, we will use the CHARMM27 force field, but Q-Chem also supports the AMBER and OPLSAA force fields. The variable USER_CONNECT determines whether we will explicitly define all bonding interactions. This should be set to TRUE.

The next variables determine the level of theory to be used for the QM layer. JOBTYPE is set to opt, indicating that we are performing an optimization. Next, the variables EXCHANGE and BASIS set the functional and basis set we wish to use for the calculation on the QM layer. The variables SCF_CONVERGENCE, SCF_GUESS, and MAX_SCF_CYCLES are details

regarding the method by which the wavefunction is iteratively solved. Note that when using the Janus model, SCF_GUESS must be set to CORE unless you are reading in a guess from a prior calculation. The final two variables which define the QM layer are MODEL_SYSTEM_CHARGE and MODEL_SYSTEM_MULT. These variables indicate the charge and multiplicity of the QM layer, independent from the full system. My recommendation is to always set these variables. Otherwise, the calculations may crash prior to performing the SCF cycles.

Step 3: Select your QM layer

I designed this step to be excruciatingly simple. Create a text file called qm.txt and add one line per residue you would like in your QM layer. It should be formatted as follows:

```
resname      resid      chain      segment
```

Great! Moving on.

Step 4: set up the Q-Chem input file

Open the file run_janus_setup.py

The setup is split into two steps.

- 1) Generate a string formatted as MDAnalysis selection text
- 2) Build the input file

```
mypsfsf = '../system_1.psf'  
mypdb = '../system_1_min.pdb'  
  
filename = 'qm.txt'  
  
ofilename = 'reduced/system_1_opt'  
  
qlist = build.text2list(filename2)  
seltext,caplist,zcharge = build.selection_text(qlist,mode='sc')  
caplist = []
```

Define the `mypsf` and `mypdb` variables to match the names of your structure and coordinate files; the variable `filename` is the file you wrote in the last step; and `ofilename` is the base name you wish to use for your Q-Chem input file. Then the only variable you need to set is `mode`. In the screenshot above, `mode` is set to `'sc'`. This indicates that the QM layer will be separated from the MM layer by breaking a bond between the protein backbone and the sidechain (hence `'sc'`) of the residues in the QM layer. This code also also allows for cuts at the peptide bond (using `mode='nc'`) the backbone carbon-carbon bond (using `mode='cc'`). Unless you are including successive residues in the QM layer, I recommend the `'sc'` cut.

The `selection_text` function outputs the selection text for the QM layer (`seltext`), as well as the variables `caplist` and `zcharge`. These variables are used to add capping hydrogens to the QM layer at the sites where the bond linking the QM and MM layers was cut. However, since we are performing an optimization, we will neglect these variables. When not specified, Q-Chem will introduce a Ying-Yang atom to serve as the cap and apply a potential to reduce electrostatic repulsion between the QM and MM layers. You can read more about this function on the Q-Chem website (<https://manual.q-chem.com/4.3/sec-QMMM.html>).

The input file is built using the `struct_generator` function. I have built many options into this function, each specified by an input variable which can be set in the `run_janus_setup.py` script.

```
build.struct_generator( mypsf,
                       mypdb,
                       seltext,
                       caplist,
                       ofile      = ofilename,
                       ftype      = 'qchem',
                       rem        = 'janus.rem',
                       charge     = 'read',
                       mult       = 1,
                       mm         = True,
                       wat_thresh = 15,
                       wat_layer  = 'QM',
                       qmmm_mode  = 'janus',
                       bonded     = True,
                       fixed      = 'CA',
                       zerocharge = zcharge,
                       params     = ['/home/pd455/parameters/updated/par_all36_prot.prm',
                                   '/home/pd455/parameters/updated/toppar_water_ions_modified.prm'])
```

The first few variables specify the variables we obtained from the `selection_text` function. The `rem` variable specifies the `janus.rem` file where we have specified the type of calculation we wish to perform (see Step 2 above). The `charge` variable specifies the total charge of both the QM and MM layers of the calculation. If unknown or if you are applying a selection which may alter the total system charge, this variable can be set to 'read' and the program will determine the charge from the provided psf file. The `mult` variable is the spin multiplicity of the total system. In my experience, this should always be set to a singlet. Setting the QM layer to have a non-singlet multiplicity using `MODEL_SYSTEM_MULT` in the rem file is sufficient to specify that there are unpaired electrons in the calculation. The `mm` variable specifies whether an MM layer should be added to the calculation.

The next two variables are only used if you wish to manipulate the selection of waters in the calculation. The variable `wat_thresh` indicates how many waters you wish to include and the variable `wat_layer` indicates whether those waters should be added to the QM or MM layer. In the screenshot above, the values of these variables indicate that the 15 water molecules closest to the QM selection should be added to the QM layer. All other water molecules will be treated at an MM level of theory. If `wat_layer` is set to MM, the waters will be added to the MM layer and all other waters will be excluded.

The `qmmm_mode` variable, in the current state of the program, takes values of `janus` or `None`. This will determine whether the Janus formatting is used or if the MM layer will be added to the `$external_charges` section of the Q-Chem input file. Finally, the program allows user specified MM parameters to be included via specification of a list of CHARMM parameter files. The program will write all necessary parameters for the system in the `$force_field_params` section of the input file.

To run the program, load the MDAnalysis environment and run the script with python:

```
python run_janus_setup.py
```

This will generate your input file. Now you just need to run Q-Chem.

Step 5: Run Q-Chem and obtain the results

Run Q-Chem using the following command in an input script.

```
qchem -nt 12 myinputfile.inp myoutputfile.out
```

Once run, you can extract the energies using the following command:

```
grep "E(Tot)" myoutputfile.out
```

This command will return a line that looks like

```
E(QM + QM/MM): -1818.0091463694 E(MM): 44347.1827651 E(Tot): 42529.173618769448
```

which specifies the energies of each partition as well as the total energy of the system.

Or if you have run a series of calculations which output file names formatted like **base_n.out**, where **base** is a name common to all files in the directory and **n** is a number specifying which calculation, then you can use the `average_energies.py` script to compile all energies of the QM subsystem using the following command:

```
python average_energies.py (min) (max) janus (T/F)
```

Here, `min` is the smallest `n` value, `max` is the largest `n` value, and `(T/F)` is either `True` if you want to print a list of all energies, or `False` if you only want the average printed to the terminal.

2.3 Electron transfer in the non-adiabatic regime (Marcus theory)

Electron transfer in molecular systems occurs between discrete molecular orbitals and depends on the energetics of the molecules involved as well as the coupling between the donor and acceptor orbitals. Such a reaction can be expressed as a chemical equation,



where, `D` and `A` represent the donor and acceptor molecules, respectively, and the `(-)` sign indicates the location of the electron. In the non-adiabatic regime, the electronic coupling between donor and acceptor is small, and the electron transfer reaction can be described by Marcus theory⁷⁸. Within the framework of Marcus theory, the rate of electron transfer is described by the following expression:

$$k_{ij} = \frac{2\pi}{\hbar} |H_{AB}|^2 \frac{1}{\sqrt{4\pi\lambda_{ij}k_B T}} \exp\left(-\frac{(\Delta G_{ij}^0 + \lambda_{ij})^2}{4\lambda_{ij}k_B T}\right) \quad (2.5)$$

where, H_{AB} is the electronic coupling between the donor and acceptor orbitals, λ_{ij} is the reorganization energy, ΔG_{ij}^0 is the free energy for the reaction, \hbar is the reduced Planck constant, k_B is the Boltzmann constant, and T is the temperature. The only three free parameters are the coupling, reorganization energy, and the free energy, all of which can be computed using *ab initio* methods. Therefore, the electron transfer rate is uniquely defined by the structure and environment of the donor-acceptor system. In the next three sections, I will describe the computational methods I have used to compute these parameters.

2.4 Calculating reduction potential using *ab initio* computational methodologies

The free energy of an electron transfer reaction is equal to the difference in free energies for the oxidation of the donor and acceptor molecules. Therefore, by computing the free energy of

oxidation for each molecule separately, we can determine the free energy for the exchange of charge between donor and acceptor.

$$\Delta G^0 = \Delta\Delta G_{OX} = \Delta G_{OX}^{\text{Acceptor}} - \Delta G_{OX}^{\text{Donor}} \quad (2.6)$$

I have computed free energies for three classes of reactions:

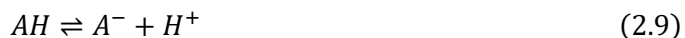
1. electron transfer (ET) reactions,



2. proton coupled electron transfer (PCET) reactions



3. and, proton dissociation reactions



For ET and PCET reactions, the free energy of oxidation (ΔG_{OX}) determines the potential of the oxidation reaction according to Nernst's equation:

$$E^0 = -\Delta G_{OX} / nF \quad (2.10)$$

where, n is the number of electrons transferred and F is Faraday's constant. For proton dissociation reactions the standard free energy of dissociation (ΔG_a^0) determines the pKa of the molecule according to the following equation:

$$pKa = \frac{\log_{10}(e)}{k_B T} \Delta G_a^0 \quad (2.11)$$

In the following sections, I will outline two computational approaches to computing free energies using QM/MM calculations.

2.4.1. Calculating free energies within the perturbative regime

To compute the free energy of a system, we must use the framework of statistical thermodynamics, where the free energy is defined in terms of the partition function,

$$Z_A = \exp(-\beta G_A) = \int_{\nu} \exp(-\beta U_{\nu}) d\nu$$

$$\beta \equiv \frac{1}{k_B T}$$
(2.12)

where, Z_A is the partition function of system A, G_A is the Gibbs free energy of system A, U_{ν} is the potential energy of state ν , k_B is the Boltzmann constant, and T is the temperature.

Within the framework of the vertical energy gap, energetic states are sampled along the partition function of a single system. For example, for an ET reaction, one may sample configurations of the reduced molecule using molecular dynamics or Monte Carlo sampling. Once configurations are selected, the products state of the reaction (e.g. oxidized) is imposed without changing the system's conformation. In 1954, Zwanzig demonstrated that when using this scheme, the free energy of the reaction can be computed according to the following equation⁷⁹:

$$\Delta G_A = -k_B T \ln \langle \exp(-\beta \Delta U) \rangle_A$$
(2.13)

where, ΔG_A is the free energy change obtained from sampling on system A. The exponential expectation values can then be expanded via a cumulant expansion. This is a power series expansion which results in the linear response approximation (LRA), which defines the free energy change of the reaction as the expectation value of the energy differences sampled over states A and B.

$$\Delta G = \frac{1}{2} (\langle \Delta U \rangle_A + \langle \Delta U \rangle_B)$$
(2.14)

Often, the details of the cumulant expansion are omitted from papers which apply the LRA. As an exercise, I have worked through the process below:

Starting from equation 2.13, we can extract the expectation value of the exponential function and redefine it via a Taylor series expansion,

$$\langle \exp(-\beta \Delta U) \rangle_A = \sum_{n=0}^{\infty} \frac{(-\beta)^n}{n!} \langle \Delta U^n \rangle_A \quad (2.15)$$

Therefore, using the first three terms, we can redefine the reaction free energy change,

$$\Delta G_A \approx -k_B T \ln \left(1 - \beta \langle \Delta U \rangle_A + \frac{\beta^2}{2} \langle \Delta U^2 \rangle_A - \frac{\beta^3}{3!} \langle \Delta U^3 \rangle_A + \dots \right) \quad (2.16)$$

Now we use the Taylor series expansion for $\ln(1 - x)$ to simplify the expression:

$$\ln(1 - x) = \sum_{\ell=1}^{\infty} (-1) \frac{x^\ell}{\ell} \quad (2.17)$$

where,

$$x = \sum_{n=1}^{\infty} (-1) \frac{(-\beta)^n}{n!} \langle \Delta U^n \rangle_A \approx \beta \langle \Delta U \rangle_A - \frac{\beta^2}{2} \langle \Delta U^2 \rangle_A + \frac{\beta^3}{3!} \langle \Delta U^3 \rangle_A \quad (2.18)$$

Therefore, the reaction free energy change is redefined to be the following:

$$\Delta G_A = -k_B T \sum_{\ell=1}^{\infty} \frac{1}{\ell} \left[\sum_{n=1}^{\infty} \frac{(-\beta)^n}{n!} \langle \Delta U^n \rangle \right]^\ell \quad (2.19)$$

When expanded to third order terms in β , we can approximate the free energy to be

$$\begin{aligned} \Delta G_A \approx & \langle \Delta U \rangle_A - \frac{\beta}{2} (\langle \Delta U^2 \rangle_A - \langle \Delta U \rangle_A^2) + \frac{\beta^2}{3!} (\langle \Delta U^3 \rangle_A - 3 \langle \Delta U \rangle_A \langle \Delta U^2 \rangle_A + 2 \langle \Delta U \rangle_A^3) \\ & - \frac{\beta^3}{4!} (\langle \Delta U^4 \rangle_A - 3 \langle \Delta U^2 \rangle_A^2 - 4 \langle \Delta U \rangle_A \langle \Delta U^3 \rangle_A + 12 \langle \Delta U \rangle_A^2 \langle \Delta U^2 \rangle_A - 6 \langle \Delta U \rangle_A^4) \end{aligned} \quad (2.20)$$

Truncating this expression after the first term, we see that we obtain the LRA from Equation 2.14.

One benefit of the LRA is cancellation of all energies that are not involved in the vertical energy gap. Within the context of a redox reaction, this is the addition or removal of an electron. Therefore, the calculation of ΔU isolates the change in the electrostatic interaction energy. In section 2.5, this will be leveraged for the calculation of reorganization energies from molecular dynamics simulations.

2.4.2. Calculating the free energy of oxidation using the extended Born-Haber method

DFT solutions for the wavefunction of a molecule are inherently approximate, and therefore, are subject to errors. These errors can be limited by using a functional which has been extensively benchmarked for molecules similar to your molecule of interest. The best results often result from a combination of benchmarking and subtractive schemes which cancel systematic error. For the calculation of Gibbs free energy change for a reaction, the Born-Haber thermodynamic cycle defines the solution phase free energy change ($\Delta G_{(soln)}$) in terms of the gas phase free energy ($\Delta G_{(g)}$) and the solvation free energies of the reactants (ΔG_{solv}^R) and the products (ΔG_{solv}^P).

$$\Delta G_{(soln)} = \Delta G_{(g)} + \Delta G_{solv}^P - \Delta G_{solv}^R \quad (2.21)$$

In Figure 2.1, I depict this thermodynamic cycle for the oxidation of tyrosine, the reaction I used to benchmark this method (see Chapter 3).

The gas-phase free energy is computed on DFT optimized configurations of the reactant and product states of the molecule. The free energy of the molecule is given by,

$$G = E(SCF) + H_{corr} - TS_{tot} \quad (2.22)$$

where, $E(SCF)$ is the electronic energy obtained from the SCF calculation on the optimized configuration of the molecule, H is the enthalpy correction, S is the total entropy, and T is the temperature. The enthalpy and entropy contributions to the free energy of the molecule are obtained via a vibrational frequency calculation performed on the optimized geometry of the molecule.

The solvation free energies of the reactants and products are often taken to be the difference in energy of the SCF energies calculated in solvent and in the gas phase. This approach makes two assumptions: 1) solvation of the molecule does not significantly alter the configuration of the molecule, and 2) solvation does not affect the enthalpy nor the entropy. These two assumptions must be considered on a system-to-system basis. For molecules which undergo a significant

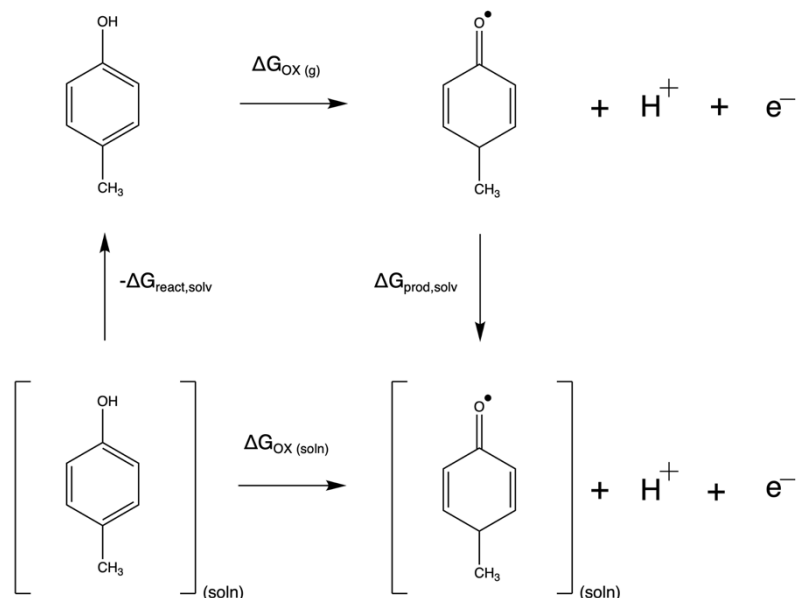


Figure 2.1: Born-Haber thermodynamic cycle for computing oxidation free energies.

conformational transition upon solvation, a direct calculation of the free energy may be more appropriate⁸⁰.

The goal of my work was to devise a method for calculating Gibbs free energy changes in complex solvation environments such as proteins. Within such an environment, redox cofactors such as tyrosine, tryptophan, and hemes are subject to fluctuations which can significantly alter their conformation. In fact, for hemes in particular, regulation of cofactor conformation is known to tune their reduction potential. Therefore, we cannot assume that the molecule maintains its gas-phase optimized geometry upon solvation. To address this, I introduced an extended Born-Haber cycle, which accounts for the solvation-induced distortion of the molecule by adding a conformational free energy term (Figure 2.2). The conformational free energy is computed as the difference in gas-phase SCF energies of the solution-phase configuration of the molecule and its gas-phase optimized configuration. It is easy to prove that the conformational free energy can be combined into the solvation free energy, thus demonstrating that one need not assume a lack of conformational change upon solvation to use the Born-Haber cycle. However, this scheme also

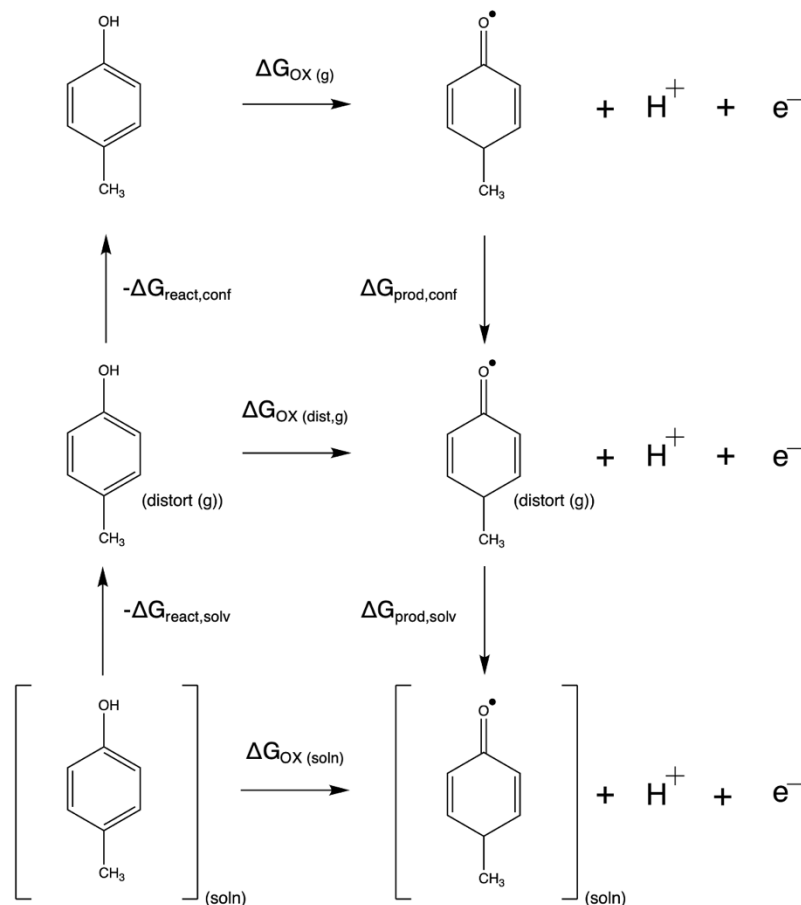


Figure 2.2: Extended Born-Haber cycle for calculating oxidation free energies

allows for decomposition of the contributions of conformation and solvation to the free energy change.

Computing accurate solvation free energies in complex environments requires extensive sampling of both solute and solvent configurations. For protein systems, I used molecular dynamics, from which I chose configurations upon which I could compute QM/MM energies. The framework of the extended Born-Haber cycle defines the free energy of oxidation of the solute in the solvent environment to be,

$$\Delta G_{OX,(soln)} = \Delta G_{OX,(g)} + \Delta G_{prod,conf} + \Delta G_{prod,solv} - \Delta G_{reac,solv} - \Delta G_{reac,conf} \quad (2.23)$$

where, the subscript *conf* indicates the conformational free energy change. Since we want to use this scheme to compute reduction potentials in protein environments, it is important to recognize

that once the redox center is distorted by the protein away from its minimum energy configuration, we cannot use DFT to compute the entropy. However, in an NPT ensemble, we can use thermal sampling of the internal energy of the system to obtain the enthalpy. We can then rewrite Equation 2.23, where we approximate the solution-phase free energy of oxidation using the conformational and solvation enthalpy changes,

$$\Delta G_{OX,(soln)} \approx \Delta G_{OX,(g)} + \Delta H_{prod,conf} + \Delta H_{prod,solv} - \Delta H_{react,solv} - \Delta H_{react,conf} \quad (2.24)$$

The solvation enthalpy change is computed by taking the difference between the expectation values of the energies of the sampled configurations evaluated in the solvent environment and in the gas-phase,

$$\Delta H_{A,solv} = \langle U_A \rangle_{A,solv} - \langle U_A \rangle_{A,dist(g)} \quad (2.25)$$

where, $\langle U_A \rangle_{A,solv}$ is the average of the combined energy of solvent and solute averaged over the configurations of the solvated system. $\langle U_A \rangle_{A,dist(g)}$ is the average of the gas-phase potential energy of solute A, sampled over the configurations obtained from the simulation of the solvated system. Note that this calculation assumes that the solvent for both reactant and product states is the same. Therefore, the contribution of the solvation energy from the solute prior to polarization by the solute is cancelled when summing around the thermodynamic cycle. The conformational free energy is given by,

$$\Delta H_{A,conf} = \langle U_A \rangle_{A,dist(g)} - (E(SCF) + H_{corr})_{A,(g)} \quad (2.26)$$

This scheme assumes that the contributions of the solvation entropies of reactant and product to the solution-phase free energy of oxidation cancel each other. This assumption is supported by an analysis of computed oxidation and solvation entropies for a set of substituted aniline derivatives (Table 2.5). This analysis used an SMD solvation model of water to determine the solvation entropies. It demonstrated that in most cases, the contribution of the solvation entropy to the oxidation entropy of the solvated system ($\Delta(T\Delta S_{solv}) = (T\Delta S_{solv})_{prod} - (T\Delta S_{solv})_{react}$) was small ($< k_B T$). Of course, the balance of the contributions of solvation and gas-phase

Table 2.1: Contribution of solvation entropes to oxidation entropy of substituted anilines

molecule	$(T\Delta S_{OX})_{(solv)}$ (meV)	$(T\Delta S_{OX})_{(g)}$ (meV)	$\Delta(T\Delta S_{solv})$ (meV)
aniline	-1.74	-2.32	0.58
2-methylaniline	10.83	11.76	-0.93
3-methylaniline	-1.18	6.97	-8.15
4-methylaniline	-75.81	10.38	-86.19
2-methoxyaniline	-0.83	7.28	-8.11
3-methoxyaniline	10.34	11.89	-1.55
4-methoxyaniline	-10.74	4.88	-15.62
2-nitroaniline	2.32	23.97	-21.66
3-nitroaniline	-0.79	9.75	-10.5
4-nitroaniline	-94.61	-42.67	-51.94
2-chloroaniline	-0.58	7.68	-8.25
3-chloroaniline	-2.31	6.36	-8.66
4-chloroaniline	-4.02	-14.81	10.79
4-methyl-3-nitroaniline	6.01	13.02	-7.02
2-methoxy-5-nitroaniline	10.06	17.07	-7.02

$$\langle \Delta(T\Delta S_{solv}) \rangle = -14.95 \text{ meV}$$

oxidation entropy is unique to each molecule. Therefore, this assumption should be examined for each system.

2.4.3. Comparing computed free energies to experiment – generating interpretable data

Once a Gibbs free energy change has been determined, we can use Equation 2.10 to convert the free energy to a reduction potential. However, a reduction potential is difficult to interpret without a reference. Most experiments are performed against a silver / silver chloride (Ag/AgCl) reference electrode or the standard calomel electrode (SCE), but by convention the values are often presented vs the standard hydrogen electrode (SHE).

Shifting the computed reduction potential vs. the standard hydrogen electrode is done differently, depending on the reaction type. For an ET reaction (Equation 2.7), this is done by subtracting the empirically determined absolute potential of the standard hydrogen electrode from the computed potential for your molecule of interest. Values ranging from 4.24 – 4.44 V have been reported⁸¹⁻⁸³, but the values most common in recent literature include that of Trasatti⁸¹ (4.44 V) and that of Isse and Gennaro⁸³ (4.281 V). For my calculations on hemes, I have used the latter, as shifting by the former resulted in computed potentials that were unrealistically low.

For PCET reactions (Equation 2.8), both an electron and a proton are lost from the molecule, in a manner similar to the reaction of the standard hydrogen electrode itself.



Therefore, the computational hydrogen electrode (CHE) method can be used to provide an internal reference for the standard hydrogen electrode^{84,85}. This method equates the proton and electron lost from the PCET reaction to $1/2 H_2^{(g)}$, an equivalence which holds true at pH 0.0, when the SHE is in equilibrium. Therefore, the chemical equation for the PCET reaction can be rewritten to be,



and the standard Gibbs free energy change, at pH 0.0, is given by,

$$\Delta G_{PCET}^0 = G(A') + \frac{1}{2} G(H_2^{(g)}) - G(AH) \quad (2.29)$$

Then, after converting to potential using Equation 2.10, the Nernst equation can be used to adjust the value according to the pH.

$$E = E^0 + \frac{RT}{nF} \log([H^+]) = E^0 - 0.059 \text{ pH} \quad (2.30)$$

where, R is the molar gas constant, n is the number of electrons, and F is the Faraday constant.

For proton dissociation reactions, it is best to use an internal reference molecule which has a known pKa value. Then the proton dissociation reaction can be recast as a proton exchange reaction. In this case, Equation 2.9 can be rewritten to be,



where, B is a base which acts as a proton acceptor for acid A. In this scheme, the free energy of dissociation for the acid can be rewritten to be,

$$\Delta G_a = \Delta G_{exch} - \frac{k_B T}{\log_{10}(e)} pKa(B) \quad (2.32)$$

where, ΔG_{exch} is the free energy for the proton exchange reaction and $pKa(B)$ is the known pKa for the base.

2.5 Computing outer sphere reorganization energy from molecular dynamics

2.5.1. Theory

Computing reorganization energy from the electronic energy gap

The reorganization energy is the energetic displacement experienced by a system when it undergoes a change in its electronic state. In a polarizable environment, this is the result of the rearrangement of surrounding charges to accommodate the change in the electronic state. In a simple solute/solution model, we can split this energy into two components: the inner sphere reorganization energy (λ_i) and the outer sphere reorganization energy (λ_o). Then the total reorganization energy is the sum of the inner and outer sphere contributions.

$$\lambda_{\text{tot}} = \lambda_i + \lambda_o \quad (2.33)$$

Generally, the inner sphere contribution is much less than the outer sphere contribution. This is especially true in a protein environment^{63,86}. Therefore, we will make an approximation that the total reorganization is equal to the outer sphere component:

$$\lambda_{\text{tot}} \cong \lambda_o \quad (2.34)$$

To compute this parameter, all we need to know is the electronic energy difference between the oxidized and reduced states of the redox active species in our simulation. For our work, this is the heme. This can be accomplished by computing the difference in electrostatic energy for each frame of our molecular dynamics simulation as follows:

$$\delta\epsilon(t) = \frac{1}{4\pi\epsilon_0\epsilon_D} \sum_i \sum_K \frac{\delta Z_i Z_K}{|r_i(t) - R_K(t)|} \quad (2.35)$$

Here, i is each solute atom (our heme) and K is each solvent atom (protein environment, water, and ions); δZ_i is the difference in partial charge between the oxidized and reduced states of solute atom i , Z_K is the partial charge of each solvent atom K , $r_i(t)$ is the position of solute atom i at time t , and $R_K(t)$ is the position of solvent atom K at time t . This parameter describes a vertical energetic displacement from the potential energy surface of one charge state to the other.

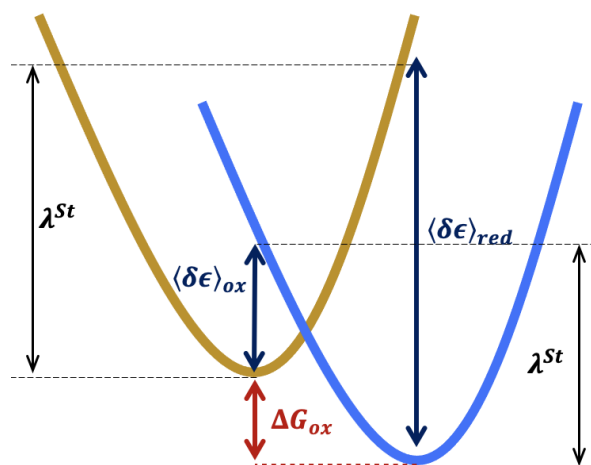


Figure 2.3: Defining reorganization energy in the linear response regime.

Defining the reorganization energy with the energy gap between oxidized and reduced states. Both the reorganization energy as well as the free energy of oxidation can be defined using the difference in energy between the oxidized (gold) and reduced (blue) states of the solute molecule (heme). This definition assumes that the free energy landscape is a quadratic. This comes from the Taylor expansion of a Gaussian, truncated after the second term. This truncation results in an approximation known as the linear response approximation (LRA).

We compute this energy gap ($\delta\epsilon$) for the simulation when the heme is oxidized ($\delta\epsilon_{OX}$) as well as the simulation when the heme is reduced ($\delta\epsilon_{RED}$). We can then define the Stokes shift reorganization energy:

$$\lambda^{St} = \frac{1}{2} (\langle \delta\epsilon \rangle_{RED} - \langle \delta\epsilon \rangle_{OX}) \quad (2.36)$$

In many instances, this value represents the final outer sphere reorganization energy. However, this is not the case for systems which do not obey Boltzmann thermodynamics. For such systems, we must extend this theory to accommodate extended sampling of the conformational landscape⁸⁷.

Computing reorganization energy for non-ergodic protein systems

Since the charges in the interior of a protein are positioned according to the protein's tertiary structure, the reorganization energy for proteinaceous systems is strongly influenced by the structural fluctuations. Protein structures fluctuate, sampling conformational space according to the free energy landscape dictated by their tertiary structures and their amino acid compositions. For many proteins, this sampling can occur on timescales ranging from 100s of nanoseconds (10^{-7} s) to several microseconds (10^{-5} s). Electron transfer reactions occur on timescales ranging from picoseconds (10^{-12} s) to microseconds (10^{-6} s). The mismatch of the

timescales required for electron transfer and protein structural sampling can result in non-ergodic behavior. This is because electrons can be transferred before the protein scaffold has enough time to rearrange in response to the additional charge. Alternatively, differences in the polarizability of the oxidized and reduced states of the active site can give rise to dynamics which do not follow Boltzmann thermodynamics (*Note: If dynamics do not obey Boltzmann thermodynamics, the distribution of energies will not be gaussian and the LRA will not hold*).

To address this, Matyushov and coworkers have introduced a variance reorganization energy^{15,87}:

$$\lambda_{RED/OX}^{var} = \frac{var(\delta\epsilon_{RED/OX})}{2k_B T} \quad (2.37)$$

This term accounts for increased variance of the electronic energy gap resulting from non-ergodic dynamics. We then compute the reaction reorganization energy as follows:

$$\lambda^r = \frac{(\lambda^{St})^2}{\frac{1}{2}(\lambda_{RED}^{var} + \lambda_{OX}^{var})} \quad (2.38)$$

This formalism is a generalization of the simple LRA definition. When $\lambda_{RED}^{var} = \lambda_{OX}^{var} = \lambda^{St}$, then λ^r is equal to λ^{St} as assumed by the LRA. To quantify the deviation from Marcus ET, we can use the following ratio:

$$\kappa_G = \frac{\lambda^{var}}{\lambda^{St}} \quad (2.39)$$

A value of κ_G greater than 1 indicates the breaking of ergodicity or altered polarizability of the active site. For example, Matyushov showed a value of $\kappa_G = 2.26$. In contrast, the values of κ_G I observed for the hemes in OmcS fell on the range [0.8, 1.34].

2.5.2. Practical implementation

Required software

- VMD
- NAMD

- Python3

Required files (scripts and input files)

- write_deltaQ.tcl
- omcs_pair_interaction_ox.conf
- omcs_pair_interaction_red.conf
- omcs_fully_ox.sb
- omcs_hred.sb
- namddat
- reorg_energy.py

You can download these files from Github: https://github.com/dahlpete/NAMD_reorg_energy

Step1: Set up pair interaction files

To compute the electrostatic energy gap we will produce a structure file (.psf) which sets the heme partial charges equal to the difference in partial charges for the oxidized and reduced hemes. We must also write a coordinate file (.pdb) which defines the solute and solvent groups.

This is achieved with the write_deltaQ.tcl script. This script must be updated to specify

1. the heme number (This is for the input and output file names)
2. the base molecule (fully oxidized system)
3. The charged molecule (heme reduced on an oxidized background)
4. The selection text specifying the solute (heme and bound residues)

```

# Write a psf file specifying the heme atom differences in charge for Reduced and Oxidized states
package require psfgen

#####          ADJUST THE LINES IN THIS SECTION          #####
set heme_num 1
mol new omcs_2chains_ox_wb_ionized.psf
mol addfile omcs_2chains_ox_wb_ionized-c.pdb
mol new omcs_2chains_h${heme_num}red_wb_ionized.psf
mol addfile omcs_2chains_h${heme_num}red_wb_ionized-c.pdb
#)
# Use the following line if you do not want to include propionates
#set selection_text "{resid 412 and chain Z and not name CAA HAA1 HAA2 CBA HBA1 HBA2 CGA O2A O1A CAD HAD1 HAD2 CBD HBD1 HBD2 CGD O2D O1D}
2 CD2) and chain B}"
# This next line includes propionates
set selection_text "{resid 412 and chain Z} or {(resid 9 12 and name SG or resid 147 13 and name CB ND1 CE1 NE2 CD2) and chain B}"
#or (resid 16 and name CB ND1 CE1 NE2 CD2 and chain B)"
#####          STOP ADJUSTING          #####

```

Run this script with VMD

```
vmd -dispdev text -e write_deltaQ.tcl
```

The script will return the following files:

- hemeN_ox_deltaQ.psf
- hemeN_ox_beta.pdb
- hemeN_red_deltaQ.psf
- hemeN_red_beta.pdb

where N is the heme_num parameter you set at the top of the script.

The files labeled *_ox_* are built on the fully oxidized base molecule whereas the *_red_* files are built on the charged molecule. The *_deltaQ.psf files specify the charge difference between the two input systems for the solute molecule, and the *_beta.pdb files specify the solute (1 in beta column) and the solvent (2 in the beta column).

Step 2: Compute the pair interaction energy

Next we perform a pair interaction calculation using NAMD. This is an adaptation of the calculation described in the NAMD electron transfer tutorial (<https://www.ks.uiuc.edu/Training/SumSchool/materials/sources/tutorials/10-electron-transfer/html/node3.html>). This is achieved using the NAMD configuration files. The only adjustable parameters are specified in the top section of the files. Be sure to update the path to the

CHARMM parameter files. If you require additional parameters, you will need to add the parameter files in the parameters section.

This script will cycle through each frame of the specified trajectory file, computing the interaction energy between the solute and solvent using the specified force field. This calculation is described by the following equation:

$$\delta\epsilon = \sum_j \Delta z_j \phi_j^{EW} \quad (2.40)$$

where Δz_j is the difference in partial charges for the solute in oxidized and reduced states and ϕ_j^{EW} is the Ewald lattice sum electrostatic potential of the solvent or thermal bath.

This calculation is very similar to that which is described by equation (2.36). However, the sum over the solvent atom charges is replaced with an Ewald sum, which accounts for periodic boundary conditions.

Depending on the length of the trajectory, this can become very computationally expensive. The attached submission scripts will allow for submission of the job to a computing cluster which uses the Slurm scheduler.

This calculation will return a NAMD .log file, where the interaction energies are printed for each frame of the simulation with the format

```
ETITLE:  TS      BOND      ANGLE      DIHED      IMPRP      ELECT ...
```

Step 3: Extract the electrostatic energy and compute reorganization energy

To compute the reorganization energy, we need the electrostatic interaction energy. To extract only this energy we use the `namddat` script. This is a shell script and must be compiled into an executable to run. This can be done with the `chmod` command:

```
chmod +x namddat
```

Then you can execute the script as follows:

```
./namddat ELECT omcs_pair_interaction_ox.log
```

This will return a file `data.dat`. For the calculation performed on the fully oxidized system, rename this file to `data_ox.txt`. Rename the file for the other simulation to `data_red.txt`.

Potential error: The energies in these text files should be positive. If they are negative, the base molecule and charged molecule were incorrectly assigned in the `write_deltaQ.tcl` script. However, since equation 2.39 uses the square of the Stokes shift reorganization energy, the resulting reaction reorganization energy is unaffected by this mistake.

Put these two text files into a directory with the `reorg_energy.py` script. The only adjustable parameter in this script is the temperature. By default, the temperature is 310 K. If you ran your simulation at a different temperature, you will need to update this parameter (see variable `T` under the defined functions).

Run this script with python3:

```
python3 reorg_energy.py
```

This will print the Stokes shift reorganization energy, oxidized variance reorganization energy, reduced variance reorganization energy, and the reaction reorganization energy.

```
r_st = 0.782 eV
r_ox = 1.012 eV
r_red = 1.078 eV

-----

lambda_r = 0.586 eV

lambda_r_err = 0.308 eV

-----
```

The reaction reorganization energy (`lambda_r`) is the outer sphere reorganization energy.

2.6 Calculating electronic coupling

The electronic couplings for electron transfer and hole transfer were calculated using either the ADF⁸⁸ or Q-Chem package which implement the charge transfer integral (CTI) method⁸⁹. The calculations were performed at a PBE0/DZ level of theory. This combination of functional and basis set consistently produced stable wavefunctions whose frontier orbitals contained the d-orbitals of the heme iron.

Using the fragment orbital approach, we split each pair of hemes into two fragments. Each fragment was equal in size to the QM region we defined for the QM/MM electronic structure calculations. As in our electronic structure calculations the coupling calculations were performed in the presence of external point charges corresponding to the surrounding protein and solvent. Prior work has suggested the protein environment and solvent have a negligible effect on electronic coupling values⁹⁰, however we found that their presence greatly influenced the energetic ordering of the molecular orbitals and the stability of the occupied orbitals. Initially, we ran a single point calculation on each fragment, followed by the charge transfer integral calculation to get the coupling. In brief, the CTI method defines the coupling as follows⁸⁹:

$$H_{AD} = \frac{J_{AD} - 0.5 \cdot S_{AD}(e_D + e_A)}{1 - S_{AD}^2} \quad (2.41)$$

Here, J_{AD} is the off-diagonal element of the Fock matrix corresponding to the donor and acceptor orbitals (charge transfer integral); S_{AD} is the overlap integral of the donor and acceptor orbitals; and e_D and e_A are the energies of the sites occupied by the charge on the donor and acceptor orbitals, respectively. We used this equation to compute the coupling between all pairs of frontier orbitals (HOMO – 2 to HOMO) containing substantial d_{xz} or d_{yz} character. These are denoted the d_π orbitals. The total coupling between a pair of hemes was calculated as a combination of the individual couplings between d_π containing orbitals as described previously⁹⁰:

$$|H_{AB}| = c_{corr} \cdot \sqrt{\frac{1}{N} \sum_{i,j=1}^N \langle d_{\pi,i}^A | h_b^{KS} | d_{\pi,j}^D \rangle^2} \quad (2.42)$$

where $\langle d_{\pi,i}^A | h_b^{KS} | d_{\pi,j}^D \rangle$ denotes the electronic coupling between the i-th and j-th d_{π} -containing molecular orbitals of the donor (D) and acceptor (A) fragments. c_{corr} is a correction factor which corrects for the lack of polarization in FODFT calculations. Prior work has calculated c_{corr} by taking the ratio of the coupling values obtained using constrained DFT (CDFT) and FODFT. Previous studies have used values of 1.75⁹⁰ and 1.38⁹¹. We used CDFT as implemented in Q-Chem to compute coupling for a subset of our MD snapshots, and we obtained a value of 1.70 for c_{corr} . This value was used to scale our FODFT coupling values. Note that we computed coupling using CDFT for only a subset of MD snapshots as many of the snapshots did not converge. FODFT allowed for better sampling and thus proved to be the most feasible technique.

For calculations of electron transfer couplings, snapshots were selected from the fully oxidized MD trajectory, and for hole transfer couplings, snapshots were obtained from the fully reduced MD trajectory.

2.7 Kinetic Monte Carlo for simulating charge transport

The kinetic Monte Carlo scheme employed to compute the charge flux has been previously described by Byun et al.⁹² to compute charge flux in the multiheme cytochrome MtrF. The scheme is designed such that the probability of a charge transfer event occurring during a given time step is proportional to the rate of that event. The probability of an event is also directly dependent on the charge population (redox state) of the hemes at a given timepoint. This is best expressed by the following master equation:

$$J_{ij} = k_{ij}P_i(1 - P_j) - k_{ji}P_j(1 - P_i) \quad (2.43)$$

where k_{ij} is the rate of charge transfer from heme i to heme j, k_{ji} is the rate of the reverse reaction, P_i is the population of heme i, and P_j is the population of heme j. The population can take values

of either 0 or 1 corresponding to the presence or absence of a charge. What this says is that for a charge transfer event from heme i to heme j to be possible, there must be a charge on heme i , and there must not be a charge on heme j .

Selection of a charge transfer event during the simulation is determined through satisfaction of the following condition:

$$\sum_{i=1}^{m-1} k_i < \xi_1 k_{total} < \sum_{i=1}^m k_i \quad (2.44)$$

where ξ_1 is a uniformly distributed number on the range $[0,1]$, and k_{total} is defined as the sum of rates for all the possible events at the given point in time. Possible events include injection of charge into the first heme, ejection of charge from the last heme, charge transfer from one heme to the next heme, or charge transfer from one heme to the previous heme. Alternatively, it is possible that the condition is never met. In this case, no event occurs for that timestep. While we allow charge transfer to occur bidirectionally, injection and ejection of charge is biased along one direction. This is achieved by setting the input and output rates to be larger than any of the heme-to-heme charge transfer rates, and their corresponding reverse rates are set to 0. For a long chain of hemes, there may be many possible charge transfer events. However, in this KMC scheme, only one event can occur during each iteration. To account for the effect this has on the timespan of the simulation, the time elapsed per iteration is defined as follows:

$$\tau(t) = \frac{-\ln(\xi_2)}{k_{total}} \quad (2.45)$$

where τ is the time elapsed for a given iteration of the simulations, and ξ_2 is another uniformly distributed random number on the range $[0,1]$.

From this simulation we get two outputs: charge flux and average occupancy. The charge flux is defined as the total number of charges ejected from the system in the timeframe of the simulation:

$$J = \frac{N_{eject}}{\sum_{t=1}^T \tau(t)} \quad (2.46)$$

We then converted the flux into current by multiplying by the elementary charge ($I = e \cdot J$). Using this approach, it is possible that we have neglected potential effects of voltage drops over each heme pair, resulting from application of an external bias. However, due to the length of the nanowires, and the magnitude of the intrinsic redox potentials, physiologically relevant external biases have minute effects on heme-to-heme charge transfer rates.

The average occupancy of the hemes in OmcS are determined by taking the mean of the heme occupancy, which takes values of 1 or 0 depending on whether the heme is occupied or unoccupied by a charge, over all time points:

$$\langle n_i \rangle_t = \frac{\sum_{t=1}^T n_i(t) \tau(t)}{\sum_{t=1}^T \tau(t)} \quad (2.47)$$

This metric was revealing in the analysis of the temperature dependence of OmcS charge transport (Fig 3). The marginal shifts in heme-to-heme charge transfer rates caused a drastic shift in heme occupancy. For both electron and hole transport, the OmcS heme chain underwent a transition from mostly occupied by a carrier at 300 K to almost entirely unoccupied by a carrier at 260 K. In the state where all hemes are unoccupied, carriers that are injected into the system are allowed to flow without encountering occupied hemes, which would serve as a roadblock, impeding charge transport. The temperature dependence KMC simulations were all performed on OmcS trimer systems (18 hemes total). The occupancy analysis was restricted to the central subunit since the injection and ejection rates increase the propensity for the edge hemes to be occupied or unoccupied, respectively.

For single particle dynamics, we adapted from the scheme described above. We initialized a reduced state on heme 1 of a 6-site model with periodic boundary conditions. The system was allowed to evolve for 100,000 iterations with the electron changing sites according to Equation 10. As there is only one electron in the system, k_{total} is the sum of $k_{i+1,i}$ and $k_{i-1,i}$, the forward rate

and reverse rate for electron transfer to the hemes adjacent to site i . Additionally, m is always equal to 2.

The mobility was determined by recording the mean squared displacement of the electron as a function of the simulation time. The distance per step was determined by the average iron-to-iron distances obtained from our molecular dynamics simulation. The mean squared displacement was fit to the expression

$$\langle d^2 \rangle = 2Dt^\alpha \quad (2.48)$$

to extract the diffusion coefficient (D). This value was divided by thermal energy giving mobility.

2.8 Normal coordinate structural decomposition

Work from the group of John Shelnut, Kara Bren, and Paul Champion has demonstrated a correlation between the out-of-plane distortions of c-type hemes and their reduction potential⁹³⁻⁹⁶. Therefore, given a structure of a heme, it is possible to learn information about its reduction potential by quantifying the out-of-plane distortions. This can be done via a normal coordinate structural decomposition (NSD), in which the structure of the heme is projected onto the normal modes of a reference state.

This projection is performed by computing a mass-weighted difference vector (\vec{d}) which quantifies the total displacement of the heme atoms from the reference state,

$$\vec{d} = \sqrt{m} \cdot \vec{x} \quad (2.49)$$

where,

$$\vec{x} = \vec{x}_m - \vec{x}_{ref} \quad (2.50)$$

and, \vec{x}_m is a vector composed of the coordinates of the molecule of interest (distorted heme), and \vec{x}_{ref} is a vector composed of the coordinates of the reference state. To decompose the distortions the difference vector is then projected onto the normal modes,

$$\vec{q} = M^T \vec{d} \quad (2.51)$$

where, M is a matrix of the normal modes, and \vec{q} is the vector containing the magnitudes of the projections along each mode.

In our implementation of NSD analysis, I used an unsubstituted planar copper (II) porphine with D4h symmetry as the reference structure. In the first implementation of NSD, a copper (II) porphine was used as the Cu(II) metal minimizes internal strains which lead to in-plane and out-of-plane distortions of the optimized structure⁹⁷. I optimized the geometry of our reference structure and computed its normal modes with DFT using Gaussian 16. I used a B3LYP functional, a 6-31G(d) basis set for the H, C, and N atoms, and a LANL2DZ basis set with an effective core potential for the Cu atom.

I used a custom Tcl script, executed with VMD⁹⁸, to compute a mass-weighted difference vector ($x_{diff} = x_{obs} - x_{ref}$) which describes the displacement of each cartesian coordinate of each atom in the heme macrocycle, including the metal, from the optimized reference structure. I then used the same script to compute the absolute value of the scalar product of the difference vector with the mass weighted unit vectors (q) describing the normal modes of the reference structure ($x_{diff} \cdot q$). We restricted our analysis to the normal modes belonging to the following classes of symmetry: B2u, B1u, A2u, Eg, and A1u. These symmetry groups correspond to the saddling, ruffling, doming, waving, and propeller distortions, respectively. To benchmark the ability of our program to capture these distortions, we compared the results of NSD analysis of the heme in horse heart cytochrome c (PDB ID: 1HRC) using our program to the results given by the publicly available NSD program described by Graves et al. (2016)². Both programs gave similar results (Supplementary Figure 4.7), demonstrating that our program can capture the relative contributions of each of the porphyrin distortions. To determine the total out-of-plane displacement, we computed the root mean square of a modified mass-weighted difference vector composed only of the displacements that lie along the unit normal vector (\hat{n}) of the porphyrin plane. This was achieved by multiplying the x, y, and z components of \hat{n} with the corresponding entries in x_{diff} for each atom.

3. An improved method for calculating reduction potentials in protein environments

An extended Born-Haber cycle for the calculation of reduction potentials in protein environments

Peter J. Dahl, Nikhil S. Malvankar, and Victor S. Batista

This chapter contains unpublished results.

3.1 Summary

Theoretical studies of electron transfer reactions in proteins rely on computational estimates of reduction potentials. These estimates are often inaccurate, with errors as large as 0.1 to 0.3 V. Subtractive schemes which cancel systematic error can improve accuracy. Here, we evaluate subtractive schemes using vertical energy gaps and thermodynamic cycles for electron transfer (ET) and proton coupled electron transfer (PCET) reactions. We find that an extended Born-Haber thermodynamic cycle provides reduction potential estimates for PCET reactions involving tyrosine and tryptophan with errors less than 10 meV. However, this method fails when there is poor agreement between the MM force field and the QM level of theory, and vertical energy gap methods must be used. We apply this method to two benchmark systems and uncover conditions under which a tryptophan and glutamic acid residue participate in a one electron 2 proton (E2PT) mechanism.

3.2 Introduction

Electron transfer reactions are critical for many biological functions including energy harvesting, signaling, and nucleic acid synthesis. Proteins often utilize transition metal complexes such as iron containing hemes, iron sulfur clusters, or copper ions to enable reversible oxidation and reduction reactions without introducing high potential radicals. However, in several systems,

including photosystem II, the BLUF photoreceptor, and ribonucleotide reductase, the amino acids tyrosine and tryptophan are known to undergo one electron oxidation via a proton coupled electron transfer (PCET) reaction. The PCET reaction enables the transient formation of a radical intermediate to direct high potential electrons through a protein environment.

Synthetic protein nanowires composed of chains of tyrosine or tryptophan residues^{1,3,52}, and natural nanowires composed of polymerized cytochromes^{44,58,60} have demonstrated that biological ET reactions can occur over surprisingly long distances (> 100 nm). These discoveries have generated much interest in applying protein nanowires in bioelectronic circuits and have shown some early success in the field of nucleic acid sequencing⁶⁵. Often cited benefits of protein-based electronics, are their flexibility, biocompatibility, and tunability using site-directed mutagenesis. Computational prediction of the reduction potentials of ET enzymes is a useful tool in understanding biological function as well as directing rational design efforts. However, calculations of reduction potentials in protein environments are often challenging and, in many cases, result in large errors relative to experiment (~0.1 V).

Errors in reduction potential calculations result from systematic errors associated with the methods employed as well as approximations of the physical description of the reaction. Systematic errors can be limited by using subtractive schemes or internal references. A common strategy is to calculate potentials based on vertical energy gaps rather than absolute energies. Computational tools such as density functional theory (DFT) compute energy differences to a higher accuracy than absolute energies⁹⁹. This strategy limits error contributed by the choice of functional and basis set, and eliminates error associated with explicit solvent descriptions, isolating the internal energy of the solute and the solute-solvent interaction energy. This is particularly useful when using QM/MM models, as the energetic contributions from the low level of theory can be canceled.

When applied, this method often employs the linear response approximation (LRA) to extract free energies from vertical energy gaps¹⁰⁰. This approximation assumes that the

probability distribution of the energy gaps of both reactant and product are gaussian with equal variance. For proteins, this is not always true, and results in error proportional to the difference in the variance.

Beyond vertical energy gaps, thermodynamic cycles, such as the Born-Haber cycle, partition free energies into the gas phase free energy and the solvation energies of reactant and product. Our group has used the Born-Haber cycle to successfully compute reduction potentials of transition metal complexes with good agreement with experiment^{101,102}. However, this approach assumes that both reactant and product respond similarly to solvation (i.e. there is minimal conformational change, and the enthalpic and entropic contributions to the solvation free energy are comparable). When applied in this manner, this approximation needs to be separately evaluated for each system. For protein environments, this approximation is invalid. The reduction potentials of redox enzymes are known to be influenced by protein induced conformational changes²²⁻²⁴.

Here, we reevaluate the methods used to compute reduction potentials in protein environments. We start with the definition of free energy from Zwanzig⁷⁹ and increase the degree of approximation until we reach the LRA. We also describe a novel extended Born-Haber cycle (BH^{ext}) which accounts for protein-induced distortions in the calculation of reduction potentials. We have benchmarked each method on three protein systems: α_3Y , a synthetic protein designed for the study of PCET reactions involving tyrosine; α_3W , a variant of α_3Y in which the tyrosine was replaced with tryptophan; and cytochrome c. We find that with proper benchmarking, we can predict the potential of each system within an error of 17 mV. Our BH^{ext} method performs best for proton coupled reduction potentials, but fails for the reduction potential of cytochrome c.

3.3 Theory

Under standard biological conditions (i.e. neutral pH), the oxidization of tyrosine and tryptophan occurs via PCET. This is because the oxidation of tyrosine and tryptophan results in a

large shift in their pKa of about 12 units, destabilizing their proton promoting dissociation. The PCET reaction we wish to model is described by the following chemical equation:



Here, we use Y to represent tyrosine, but the same equation describes the oxidation of tryptophan (W). The oxidation of cytochrome c as an ET reaction resulting the loss of an electron, converting the iron atom in the heme to Fe(III) from Fe(II):



The reactants and products for both reactions are both described by diabatic free energy curves, and the reaction coordinate is given by the vertical energy gap between the product and reactant states.

3.3.1. Calculating free energies using vertical energy gaps

The free energy difference between reactant and product can be defined in terms of the vertical energy gap and is given by the Zwanzig equation:

$$\Delta G = -k_B T \ln \langle \exp(-\beta \Delta U) \rangle_R \quad (3.3.1)$$

$$= k_B T \ln \langle \exp(\beta \Delta U) \rangle_O \quad (3.3.2)$$

where $\beta \equiv 1/k_B T$ and,

$$\Delta E = E_O - E_R \quad (3.4)$$

The angled brackets $\langle \dots \rangle_{O/R}$ represent the expectation value of the exponential sampled over configurations of the oxidized (O) or reduced (R) state of the system. Adding both sides of Equation 3.3 and dividing by 2, we get the following definition for the free energy difference:

$$\Delta G = -\frac{k_B T}{2} \ln \frac{\langle \exp(-\beta \Delta U) \rangle_R}{\langle \exp(\beta \Delta U) \rangle_O} \quad (3.5)$$

Equations 3.3 and 3.5 are exact expressions based on the partition functions of the reactants and products. Therefore, with sufficient sampling of the partition functions, these equations should provide very accurate estimations of the free energy of oxidation, from which the reduction

potential can be computed using the Nernst equation. However, in practice, convergence of the free energy can be difficult to ascertain. Furthermore, due to the exponential term, large fluctuations in the energy gap can amplify the energetic contributions of statistically unlikely configurations.

This problem can be addressed by expressing Equation 3.3 as a cumulant expansion. When the distribution of energy gaps is gaussian, all terms of order greater than 2 are zero, and we get the following definition for the free energy difference, which we will refer to as the gaussian approximation (GA),

$$\Delta G = \langle \Delta U \rangle_R - \frac{\beta}{2} (\langle \Delta U^2 \rangle_R - \langle \Delta U \rangle_R^2) \quad (3.6.1)$$

$$= \langle \Delta U \rangle_O + \frac{\beta}{2} (\langle \Delta U^2 \rangle_O - \langle \Delta U \rangle_O^2) \quad (3.6.2)$$

Then Equation 3.5 becomes,

$$\Delta G = \frac{1}{2} (\langle \Delta U \rangle_R + \langle \Delta U \rangle_O) - \frac{\beta}{4} (\sigma_R^2 - \sigma_O^2) \quad (3.7)$$

where, $\sigma_{R/O}^2$ is the variance of the distribution of energy gaps for the oxidized (O) or reduced (R) state of the system. Often, the variance of the distributions of energy gaps for both reactants and products are assumed to be equal, and Equation 3.7 reduces to the linear response approximation (LRA):

$$\Delta G \approx \frac{1}{2} (\langle \Delta U \rangle_R + \langle \Delta U \rangle_O) \quad (3.8)$$

Note that in this regime we can apply Jarzynski's inequality to give the following relation between the vertical energy gap and the free energy¹⁰³:

$$\langle \Delta U \rangle_{R/O} \geq \Delta G \quad (3.9)$$

The difference $\langle \Delta E \rangle_{R/O} - \Delta G$ gives the work dissipated due to an increase in entropy¹⁰³.

Therefore, at finite temperature, the linear response approximation is a limiting case in which the

entropy change associated with the oxidation reaction is zero. This definition also allows us to equate the second order term from the cumulant expansion to the entropic contribution to the free energy,

$$T\Delta S = \frac{\beta}{4}(\sigma_R^2 - \sigma_O^2) \quad (3.10)$$

Neglecting this term can result in large errors. At room temperature $\beta/4 = 10 \text{ eV}^{-1}$. Therefore, even when the difference in the variance of the energy gap distributions is small, this term can provide significant contributions to free energy.

3.3.2. Calculating free energy using the Born-Haber cycle

The Born-Haber cycle allows for estimation of thermodynamic quantities through partitioning the free energy into the gas phase free energy and the solvation energies of the reactants and products. Previous implementations of the Born-Haber cycle have computed solvation energies under the assumption that solvation does not significantly alter the molecular geometry from the gas-phase optimized geometry. This approximation fails in a protein environment, as collections of covalent bonds, hydrogen bonds, and steric clashes can significantly displace molecular geometries. We define an extended Born-Haber cycle (Figure 3.1) which accounts for solvation-induced distortions of the molecular geometry. Within this scheme the free energy of oxidation of the solution-phase system is given by,

$$\Delta G_{OX,(soln)} = \Delta G_{OX,(g)} + \Delta G_{prod,conf} + \Delta G_{prod,solv} - \Delta G_{reac,solv} - \Delta G_{react,conf} \quad (3.11)$$

where, the subscript *conf* indicates the conformational free energy change in response to solvation, which can be calculated by performing a gas-phase single point calculation on the molecular geometry obtained from the solution-phase simulation. It is straightforward to show that the free energies of the distorted molecules in the gas phase cancel and the solvation free energy change can be computed by taking the difference in the free energy of the solution-phase molecule and the free energy of the gas-phase molecule. Therefore, we need not assume that the

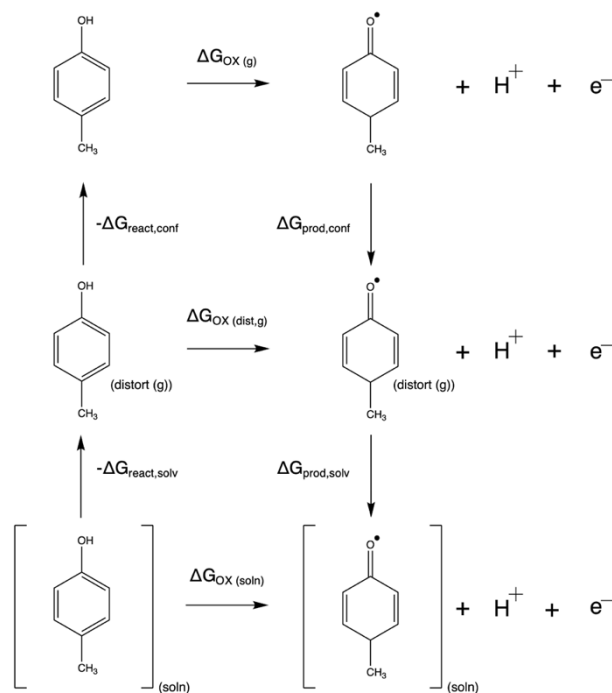


Figure 3.1: Extended Born-Haber cycle for computing reduction potentials in protein environments

geometry is unchanged upon solvation. Nonetheless, the extended Born-Haber cycle provides a framework for decomposing the conformational and solvation induced contributions to oxidation free energies.

For oxidation reactions in protein environments, we defined the solute to be the redox center and the solvent to be the surrounding protein, water, and ions. As protein structures are flexible and dynamic, we used molecular dynamics to sample conformational space. Once displaced from its minimum energy structure, we cannot directly compute entropy. However, in an NPT ensemble, we can use thermal sampling internal energies to obtain enthalpy. Therefore, we approximate the solution-phase oxidation free energy using the conformation and solvation enthalpy changes,

$$\Delta G_{OX,(soln)} \approx \Delta G_{OX,(g)} + \Delta H_{prod,conf} + \Delta H_{prod,solv} - \Delta H_{react,solv} - \Delta H_{react,conf} \quad (3.12)$$

This approximation holds so long as the conformational and solvation entropy changes of reactant and product are similar.

We define the conformational enthalpy change to be the difference between the expectation value of the electronic energies of the solute evaluated in the gas-phase and the gas-phase optimized electronic energy with the enthalpy correction obtained from vibrational analysis,

$$\Delta H_{M,conf} = \langle U_{solute} \rangle_{R/O}^{(g)} - (E(SCF)^{(g)} + H_{corr}) \quad (3.13)$$

Computing the solvation enthalpy change is more complicated. We use all-atom explicit solvent simulations to achieve thermal sampling of conformational space. The contribution of the solute to the solvation enthalpy change be the difference between the expectation values of the internal energies of the solute evaluated in the protein environment (i.e. solution-phase) and the gas-phase,

$$\Delta H_{M,solv}^{solute} = \langle U_{solute} \rangle_{R/O}^{(soln)} - \langle U_{solute} \rangle_{R/O}^{(g)} \quad (3.14)$$

However, we also need to include the solvation enthalpy change of the solvent. The total solvation enthalpy change can be described by the sum of the contributions from the enthalpy change of the solute and the enthalpy change of the solvent,

$$\Delta H_{solv} = (H_{solute}^{(solv)} - H_{solute}^{(g)}) + (H_{solvent}^{(occ)} - H_{solvent}^{(P)}) \quad (3.15)$$

where, the superscripts (occ) and (P) signify that the solvent is occupied by solute or pristine, respectively. When the charge of reactant and product remain the same, such as during PCET, both reactant and product simulations can be built with identical solvent and summation around the thermodynamic cycle will eliminate $H_{solvent}^{(P)}$. When the charge is different, and additional ions must be added to neutralize the simulation box, this term must be explicitly evaluated. Schemes to do this are described in the Methods.

When the solvent is identical for both reactant and product, summation around the thermodynamic cycle simplifies Equation 3.12 to

$$\Delta G \approx \langle U \rangle_O - \langle U \rangle_R - T\Delta S_{OX}^{(g)} \quad (3.16)$$

This equation is similar to the equation used for estimation of binding free energies using the MM/GBSA theoretical framework¹⁰⁴. Therefore, like the MM/GBSA method, our extended Born-Haber method is likely sensitive to the quality of the force fields used for conformational sampling, and the DFT methods used to obtain the energies of the system.

3.4 Results

3.4.1. Proton coupled reduction potentials of α_3X

We have benchmarked our proton coupled reduction potential calculations on the α_3X protein system. α_3X is a triple α -helix motif with a single tyrosine (α_3Y) or tryptophan (α_3W) residue positioned at residue 34, putting them between the helices^{105,106} (Figure 3.2a-c). This is a synthetic protein, which was designed for the purpose of studying the oxidation of tyrosine and tryptophan residues within a protein environment. The reduction potentials of both the tyrosine¹⁰⁶ and tryptophan¹⁰⁵ variant have been well characterized, and experimentally measured Pourbaix

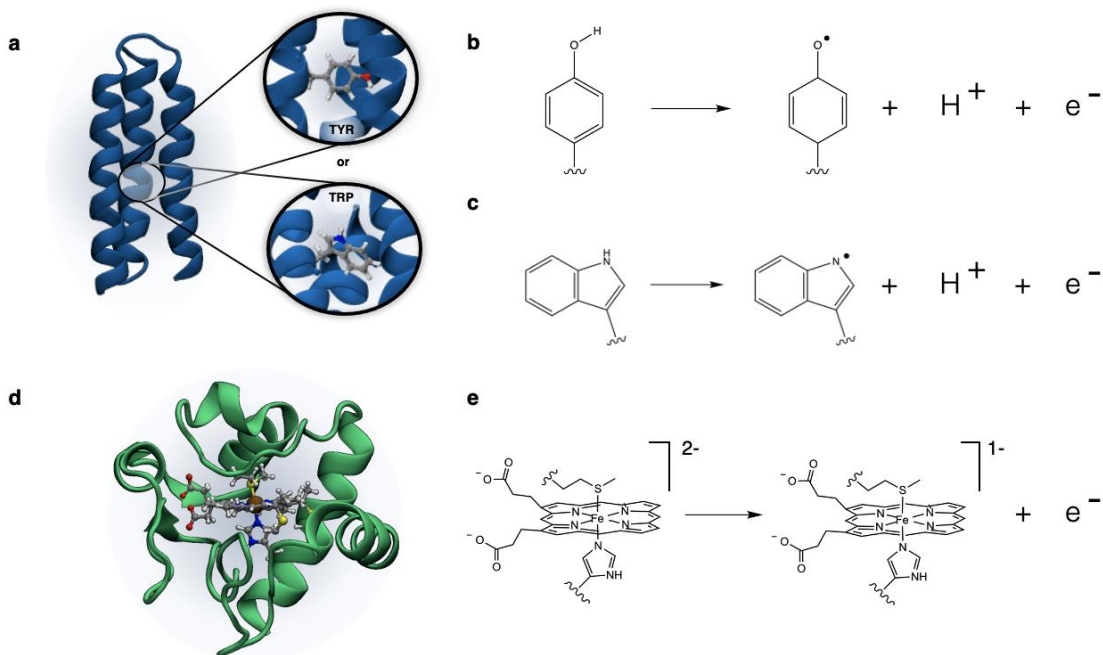


Figure 3.2: Protein systems used to benchmark the methods investigated in this study.

(a) Structure of the α_3X protein system. Either a tyrosine (TYR) or tryptophan (TRP) residue is found in the center of a 3-helix bundle. **(b)** PCET reaction scheme for the oxidation of tyrosine. **(c)** PCET reaction scheme for the oxidation of tryptophan. **(d)** Structure of horse heart cytochrome c. **(e)** ET reaction scheme for the oxidation of the heme in cytochrome c.

diagrams have demonstrated that their oxidation occurs via a PCET reaction. Kinetics measurements¹⁰⁵ and computational studies¹⁰⁷ indicate that upon oxidation, the proton is dissociated to water. Therefore, we modeled product state of the PCET reaction as the neutral radical species and the dissociated proton was excluded from the simulation. We ran molecular dynamics of both the reactant and product states of the protein system using the CHARMM36⁷⁵ force field. We selected snapshots from our production trajectory and performed single point QM/MM calculations to obtain the energy of the system. We described the redox center (tyrosine or tryptophan) with DFT using the B3LYP functional and the Dunning correlation-consistent double zeta basis set with polarization functions (cc-pVDZ). The rest of the protein and the surrounding water and ions were described at the MM level with the CHARMM36 force field.

To compute the reduction potential using vertical energy gaps, we needed to impose the electronic structure of both reactant and product on each of the configurations obtained from our molecular dynamics simulations. For reduced configurations, this required the deletion of the hydroxyl proton from tyrosine or the indole N-H proton from tryptophan and adjusting the spin multiplicity to a doublet state. For the oxidized configurations, the spin multiplicity needed to be adjusted to a singlet, and a proton needed to be added. While relatively straightforward for the indole group of the tryptophan residue, the hydroxyl proton on tyrosine has more degrees of freedom. To avoid introducing bias on the results, we elected to restrict our calculations to sampling performed on the reduced structures.

We computed the free energy of oxidation using vertical energy gaps (Equation 3.3) and our extended Born-Haber cycle. When using vertical energy gaps, we computed free energies using the Zwanzig equation (Equation 3.3), the LRA (Equation 3.8), and the GA (Equation 3.6). Our computed free energies were converted to reduction potentials using the Nernst equation,

$$E_{1/2} = \frac{\Delta G_{ox}}{nF} \quad (3.17)$$

Table 3.1: Computed reduction potentials of a3Y and a3W at pH 7.0

	Reduction potential (V vs. SHE)				
	Ref 104	Zwanzig	LRA	GA	BH ^{ext}
$\alpha_3\text{Y}^*/\alpha_3\text{Y}$	0.986	0.918	1.226	0.797	1.000
$\alpha_3\text{Y}^{*+}/\alpha_3\text{Y}$	1.510	1.866	1.728	2.069	0.807
$\alpha_3\text{W}^*/\alpha_3\text{W}$ (QM1)	1.095	1.191	1.611	0.707	1.289
$\alpha_3\text{W}^*/\alpha_3\text{W}$ (QM2)		1.238	1.690	0.817	1.090

where, F is the Faraday constant and n is the number of moles involved in the redox reaction (here, $n=1$). We used the computational hydrogen electrode (CHE) method^{84,85} to convert our computed potentials to the standard hydrogen electrode (SHE) scale, and then used the Nernst equation to adjust our proton coupled reduction potential to a pH of 7.0,

$$E = E^0 + \frac{RT}{nF} \log([H^+]) = E^0 - 0.059 \text{ pH} \quad (3.18)$$

where, R is the universal gas constant, E^0 is the standard cell potential, and $[H^+]$ indicates the concentration of protons in solution.

The extended Born-Haber method predicted the potential of $\alpha_3\text{Y}$ within 14 mV but overestimated the potential of $\alpha_3\text{W}$ by 194 mV (Table 3.1). Of the vertical energy gap methods, the Zwanzig equation performed best. The LRA grossly overestimated the potentials of both proteins, and the GA grossly underestimated the potentials. Notably, all methods, except for the GA which failed to capture the correct scaling, overestimated the difference in potential between the two proteins. Closer inspection of our simulations revealed that, while the tyrosine is largely occluded from water, the tryptophan is solvent exposed. In fact, a network of hydrogen bonds connects tryptophan 34 (W34) to glutamic acid 15 (E15) via a water bridge (Figure 3.3). We hypothesized that the poor scaling of our reduction potential calculations was the result of an MM description of the hydrogen bonding network. Hydrogen bonds can influence the polarization of the electronic wavefunction, but this effect is diminished when the hydrogen bonding network is partially described by a MM forcefield with fixed point charges.

To test the role of the hydrogen bonds in setting the reduction potential of α_3W , we expanded the QM layer of our QM/MM calculations to include E15 as well as a set of the water molecules between the two residues (QM2). When treating the hydrogen bonding network at the QM level, the extended Born-Haber method was able to predict the α_3W reduction potential within 5 mV. Notably, this improvement was only observed when both E15 and the surrounding waters were added to the QM layer. The addition on only E15 or the water molecules did not improve the results (Supplementary Table 3.6). In contrast, the vertical energy gap methods still performed poorly for all QM/MM models (Table 3.1, Supplementary Table 3.6). In fact, the overestimates of the α_3W potential given by the Zwanzig and LRA methods increased upon the addition of E15 and the water.

These results suggest that vertical energy gap methods failed to capture the full extent of the effects of active site polarization. Intuitively, this makes sense.

The calculation of the electronic energy gap isolates the energetic contributions which most strongly respond to the electronic perturbation. For the PCET reaction, there is no change in charge. Therefore, the effect of the change in charge on the polarization of the surroundings is minimal, and the corresponding energetic contributions are canceled. The BH^{ext} improves on this by explicitly accounting for the relaxation of the hydrogen bonding network around the loss of the indole N-H proton.

We also computed the reduction potential of the tyrosine cation radical. Since this reaction is not proton coupled, we could not use the CHE to convert our computed potential to the SHE scale. Therefore, we adjusted our value by the empirically determined absolute potential of the SHE determined by Trasatti⁸¹. Using this value, the vertical energy gap methods

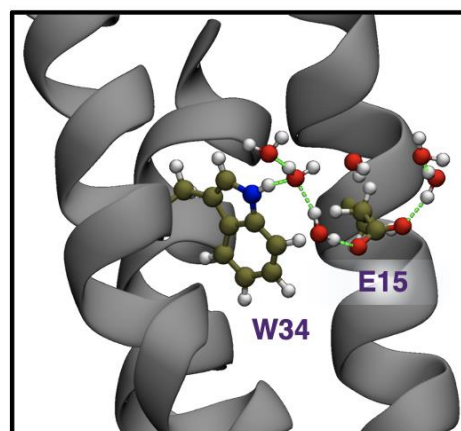


Figure 3.3: A hydrogen bonding network connects tryptophan 34 to glutamic acid 15 via a water bridge.

overestimated the potential and the BH^{ext} method underestimated the value estimated by Glover et al¹⁰⁵. This is likely because we did not alter the protonation states of the 17 glutamic acid residues to account for the drop to pH < 0. However, the use of empirical values of the absolute potential of the SHE is also known to introduce errors, which can be corrected using an internal reference¹⁰⁷.

3.4.2. Reduction potentials of cytochrome-c

Heme-containing metalloenzymes are some of the most widespread and important ET proteins in the biology. While much is known about the interactions which influence their reduction potentials, predicting their potentials using *ab initio* computational chemistry techniques is still challenging. We used horse-heart cytochrome c as a model system to evaluate the ability of the Zwanzig, LRA, GA, and BH^{ext} models to correctly predict its potential. Horse-heart cytochrome-c is a well-characterized cytochrome with a single heme (Figure 3.1d). The iron atom is coordinated in an octahedral geometry by the porphyrin ring, a histidine residue, and a methionine residue. Oxidation of cytochrome-c occurs via ET with a potential of 0.255 V vs. SHE¹⁰⁸, changing the formal charge of the iron atom from Fe(II) to Fe(III) (Figure 3.1e).

We computed the reduction potential of cytochrome c after sampling configurations using molecular dynamics. Since oxidation of cytochrome c is an ET reaction and no protons are dissociated, we used the Trasatti value for the absolute potential of the SHE⁸¹ to shift our computed potentials. Additionally, since the transition from oxidized to reduce does not require the addition of a proton, we could compute the reduction potential using configurations sampled from both the reduced and oxidized simulations. This significantly increased the accuracy of the vertical energy gap methods. Unlike the proton-coupled reduction potentials of α_3Y and α_3W , the vertical energy gap methods outperformed our BH^{ext} method (Table 3.2). The Zwanzig equation gave us the best agreement, estimating the potential within 17 mV. The LRA resulted in an underestimate which was partially corrected using the GA.

Table 3.2: Computed reduction potentials of horse heart cytochrome-c

	Reduction potential (V vs. SHE)				
	Ref 107	Zwanzig	LRA	GA	BH ^{ext}
E _{RED}	0.255	0.559	1.118	-0.038	1.672
E _{OX}		-0.016	-0.811	0.469	
E _{AVG}		0.272	0.153	0.216	

The failure of the BH^{ext} method is likely due poor agreement between the MM forcefield and the DFT description of the heme. Errors in the MM description of the heme geometry which induce a comparable error in the oxidized and reduced energies evaluated at the DFT level are immediately cancelled when using vertical energy gap methods. In contrast, the BH^{ext} method incorporates the energetic contributions of all geometrical fluctuations. If the change in redox state alters the erroneous fluctuations at the MM level, they are preserved. We decomposed the potential computed with BH^{ext} into its conformational and solvation components which revealed the average over the heme conformations in the gas-phase only differed by 38 mV between the oxidized and reduced states. Therefore, we conclude that the energies we computed are dominated by erroneous fluctuations.

Therefore, our calculations demonstrate that when the MM forcefield provides a geometrical description, consistent with the QM method employed, the BH^{ext} method provides a very accurate reduction potential estimates. Otherwise, vertical energy gap methods, in particular those with fewer approximations, such as the Zwanzig equation, provide the best estimates. In the next section, we apply the BH^{ext} method to interrogate PCET mechanisms in α_3W .

3.4.3. Tryptophan oxidation significantly decreases the pK_a of glutamate

PCET reactions can occur by three different modes: electron transfer followed by proton transfer (ETPT), proton transfer followed by electron transfer (PTET), or concerted electron and proton transfer (CEPT). The mode used by a particular system is strongly influenced by the

available proton transfer pathways. When the proton acceptor is weak, the kinetics of oxidation can outpace the kinetics of proton transfer (PT) and the reaction occurs in a stepwise fashion (ETPT). When a strong proton acceptor is available, the reaction is more likely to occur by CEPT. Glover and coworkers concluded that oxidation of W34 in α_3 W most likely occurs by ETPT, based on an analysis of oxidation kinetics and the assumption that the proton is transferred to bulk water. Our discovery of the role of E15 in setting the reduction potential of W34 inspired us to revisit the mechanism. The driving force for proton transfer (PT) is given by,

$$\Delta(\Delta G_a) = \frac{2k_B T}{\log_{10}(e)} \Delta pK_a \quad (3.19)$$

The pK_{OX} of tryptophan is approximately 3.4, whereas bulk water has a pK_a of 0.0. Therefore, proton dissociation into water is energetically unfavorable with a free energy change of +0.402 eV. In contrast, PT to glutamic acid, which has a textbook pK_a of 4.25, is energetically favored with a free energy change of -0.101 eV. While W34 and E15 are separated by a water bridge, and they only directly hydrogen bond with each other for 8% of our simulation, we hypothesized that the water bridge could support PT to E15 via a Grotthuss mechanism.

We evaluated our hypothesis by running a potential energy scan (PES). We split the scan into two components. In the first scan, we pulled the indole N-H proton away from the indole nitrogen. Then, leaving the indole N-H proton dissociated from the tryptophan, we ran a second scan in which we pulled a proton from the closest water to E15 toward the carboxylate of E15. We found that forcing the proton to associate with E15 did trigger a Grotthuss-like PT event

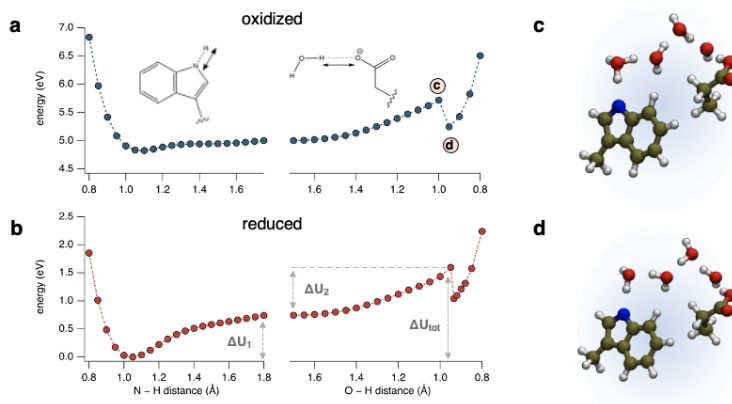


Figure 3.4: PES to determine barrier for PT to E15.

(a) PES scan with W34 in an oxidized state. Proton dissociation from W34 is on the left and proton association with E15 is on the right. **(b)** PES scan with W34 in a reduced state. **(c)** Structure of W34, E15, and water molecules involved in PT to E15. Corresponding energy is labeled with **c** in panel (a). **(d)** Structure from (c) following PT to E15. Corresponding energy is labeled with **d** in panel (a).

Table 3.3: Potential energy barriers to PT from W34 to E15

	Potential Energy Difference (eV)	
	W34 _(OX)	W34 _(RED)
ΔU_1	0.178	0.740
ΔU_2	0.699	0.847
ΔU_{tot}	0.877	1.587

(Figure 3.4). However, while oxidation of the tryptophan reduced the energetic barrier for PT, the total energetic cost was still prohibitively large (Table 3.3).

Therefore, we conclude that it is unlikely that the PCET reaction in $\alpha_3\text{W}$ proceeds via protonation of E15, consistent with the conclusions of Glover et al¹⁰⁵.

This result was somewhat surprising. The PT state (labeled **d** in Figure 3.4a) is still higher in energy than the local minimum following W34 oxidation (minimum in Figure 3.4a). This suggests either the pK_{OX} of W34 is higher than previously estimated, or oxidation of W34 causes the pK_a of E15 to decrease. To evaluate the effect of tryptophan oxidation on the pK_a of E15, we constructed a thermodynamic cycle relating the oxidation of W34 to proton dissociation from E15 (Figure 3.5). We can split the thermodynamic cycle along the diagonal, using the intramolecular PCET (I-PCET) reaction to establish a relationship between the two proton dissociation reactions. When this is done, we obtain an expression which depends only on the PCET reactions, for which we have already established a method for accurate evaluation of free energies,

$$\Delta(\Delta G_a) = \Delta G_{a(\text{ox})} - \Delta G_{a(\text{red})} = \Delta G_{\text{PCET}(E)} - \Delta G_{\text{PCET}(EH)} \quad (3.20)$$

We simulated $\alpha_3\text{W}$ with E15 protonated and reevaluated the proton coupled reduction potential. Protonation of E15 increased the reduction potential of W34 by 305 mV. Equating Equation 3.20 with Equation 3.19, we determined that oxidation of tryptophan causes the pK_a of E15 to decrease by 2.58 pH units. This is a fairly large pK_a shift, which has very interesting implications regarding the mechanism of PCET in this model system. Our analysis predicts that when the pH of the system is set such that it is between the two pK_a values of E15, oxidation of W34 will occur via a one electron two proton transfer (E2PT) mechanism. The E2PT mechanism

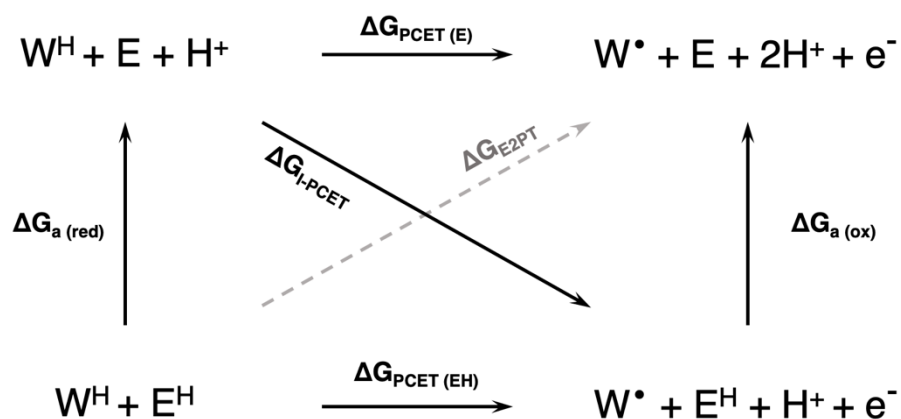


Figure 3.5: Thermodynamic cycle relating oxidation of W34 to proton dissociation from E15. The superscript “H” indicates the species is protonated.

is relevant to the oxidation of tyrosine-Z in photosystem II. There have been recent efforts to design suitable model systems to study the mechanism^{109,110}. Our results suggest that α_3W may enable the study of E2PT mechanisms in a protein environment.

To estimate the pH range for the E2PT regime, we computed the I-PCET reduction potential. Using our calculation of the potential of the α_3Y cation radical as an internal reference, we determined that the I-PCET reaction has a reduction potential of 1.416 V. Therefore, when W34 is reduced, E15 has a pK_a of 3.32, which decreases to 0.74 upon oxidation of W34. This pH range is quite low and not very experimentally tractable. However, our work provides the theoretical framework for the rational design of α_3W derivatives which shift the E2PT range toward neutral pH.

3.5 Discussion

The development of theoretical methods to accurately predict reduction potentials in protein environments is important for future studies of ET and PCET reactions in biological systems. The rates of ET and PCET between redox centers depends exponentially on the square of the reaction free energy. Therefore, errors in free energy calculations are amplified, and computed rates cannot be trusted. We have demonstrated that subtractive schemes increase

computational accuracy and can enable mechanistic studies of systems whose function depends on small potential differences (< 0.1 V).

Based on our results, we conclude that, when using vertical energy gap methods, the LRA be used cautiously. The LRA can capture relative potential shifts quite accurately when paired with an internal reference¹⁰⁷. However, it is unclear how this solution will scale as the characteristics of the molecule of interest diverge from the reference. Reinhardt et al. reported a mean unsigned error of 24 mV for calculations of reduction potential shifts for fluorotyrosine derivatives of α_3Y . However, the error increased with increasing chemical complexity. The MUE of disubstituted fluorotyrosine residues was only 5.0 mV but the MUE of trisubstituted fluorotyrosine residues is 43 mV. When we computed the reduction potential shift of α_3W relative to α_3Y , using the LRA, we overestimated by 276 mV (Table 3.1), consistent with the trend. The Zwanzig equation reduced the error to 164 mV, and the BH^{ext} method further reduced the error to 19 mV. While BH^{ext} does not work for all systems, our results suggest it is the best available method for computing proton coupled reduction potentials in protein environments.

While this project started as a method development project, our calculations revealed an interesting relationship between the reduction potential of tryptophan and the pK_a of a nearby glutamate. Our calculations of the shift in the pK_a of E15 predicted that there exists a pH range in which oxidation of tryptophan triggers a E2PT reaction. Our theoretical framework provides the means to rationally design mutations in α_3W which could allow for experimental investigations of E2PT kinetics.

3.6 Methods

3.6.1. Molecular dynamics

We built our models of the α_3Y and α_3W proteins using the NMR structures from Tommos and coworkers (α_3Y PDB ID: 2MI7; α_3W PDB ID: 1LQ7). Cytochrome-c was built from the 1.9 Å crystal structure from Brayer and coworkers (PDB ID: 1HRC). We set the protonation state of

ionizable residues based on their textbook pK_a values such that our simulation was run at neutral pH (pH = 7.0). Using VMD⁹⁸, We added a water box using the TIP3P water model, such that the protein was padded by 15 Å in each dimension. We added chloride ions to neutralize the net charge of the system. For oxidized tyrosine and tryptophan residues, we adjusted the partial charges to match the oxidation induced change in the electronic dipole as determined by DFT calculations. The partial charged used in our simulations are given in Table 2.1 to Table 2.4.

Simulations were run with the NAMD¹¹¹ software package using the CHARMM36⁷⁵ force field. First we ran an energy minimization for 5,000 steps. We then ran a simulation of the water box in the NPT ensemble, keeping the atoms of the protein fixed in their minimum energy configuration. We then equilibrated the simulation, increasing the temperature from 0 K to 310 K over 30 ps in the NVT ensemble. The simulation was held at 310 K for an additional 3.5 ns to ensure sufficient equilibration. The production trajectory was run for 100 ns in the NPT ensemble.

Subsequent calculations were run on snapshots obtained from our production trajectory. We performed RMSD analysis to determine a 40 ns window for which the RMSD was stable. If no window was available, the production trajectory was extended for an additional 100 ns. Once the 40 ns window was identified, we selected 400 equally spaced snapshots (100 ps spacing).

3.6.2. *QM/MM calculations*

QM/MM calculations were performed on the 400 snapshots selected from our MD trajectory. We used the Janus model in Q-Chem⁷⁷ to implement an electronic embedding scheme. The Janus model allows the QM self-consistent field calculations to be influenced by the electrostatic potential of the surrounding MM layer, thus explicitly including the electrostatic interaction energy in the QM calculation. We also computed the van der Waals interaction energy between the QM and MM layers, which cannot be done when using the simpler “\$external_charges” electronic embedding scheme implemented in Q-Chem. For the results presented in the main text,

we described the QM layer with the B3LYP functional and the cc-pVDZ basis set. This level of theory was determined to provide the best reduction potential estimates across all three systems studied. This was ascertained by benchmarking a set of 11 different functional/basis set combinations for the α_3Y and α_3W systems (Supplementary Table 3.1 and Supplementary Table 3.2) and 4 different functional/basis set combinations for cytochrome c (Supplementary Table 3.3 and Supplementary Table 3.4).

The QM layer by default was limited to the protein residue or cofactor which performed the redox reaction. For α_3Y this included tyrosine 34; for α_3W , this included tryptophan 34; for cytochrome c, this included the heme as well as the covalently bound cysteine residues (cysteine 14 and cysteine 17) and the axial ligands (histidine 18 and methionine 80). For our calculations of α_3W , we also performed calculations with an expanded QM layer. This expanded layer, termed QM2, included glutamate 15 as well as the 15 closest waters to tryptophan 34 and glutamate 15.

The MM layer of the QM/MM calculations was described by the CHARMM36 force field. This force field is not built in to Q-Chem, so we used a custom Python script to reformat our CHARMM parameter files and insert the parameters into the “\$force_field_params” section of the Q-Chem input file. For all single point calculations, we only imported the electrostatic and Lennard-Jones parameters. From the output files, we extracted only the QM + QM/MM energy, which is the sum of the QM SCF energy and the QM/MM van der Waals interaction energy. We recomputed the MM energy using the NAMD interaction energy function. This allowed us to utilize periodic boundary conditions and PME electrostatics to avoid finite system artifacts. Additionally, it allowed us to sample many more MM energies. For most simulations, we obtained 36,000 MM energies from the last 90 ns of our simulations. We determined the net internal energy of our system by adding the averages of the QM+QM/MM energies and the MM energies.

3.7 Supplementary Information

Supplementary Table 3.1: DFT benchmarking for calculations of the reduction potential of α_3Y and α_3W using the Zwanzig equation

		Reduction potential (V vs. SHE) @ pH 7.0					
Functional	Basis set	α_3Y	(err) ^a	α_3W (QM1) ^b	(err) ^a	α_3W (QM2) ^c	(err) ^a
B3LYP	cc-pVDZ	0.918	-0.067	1.190	0.094	1.237	0.142
PBE	cc-pVDZ	0.427	-0.559	0.838	-0.257	0.828	-0.267
PBE0	cc-pVDZ	0.953	-0.033	1.207	0.112	1.253	0.158
PBE50	cc-pVDZ	1.217	0.231	1.474	0.379	1.512	0.417
ω B97X-D	cc-pVDZ	1.220	0.234	1.450	0.355	1.548	0.453
B3LYP	VDZ	0.943	-0.043	1.399	0.304	1.827	0.732
B3LYP	cc-pVTZ	1.051	0.065	1.323	0.228	1.344	0.249
B3LYP	aug-cc-pVDZ	0.973	-0.013	1.230	0.135	1.220	0.125
B3LYP	6-31G(d,p)	0.970	-0.016	1.255	0.160	1.293	0.197
PBE0	6-31G(d,p)	1.156	0.170	1.429	0.334	1.468	0.373
B3LYP	6-311++G(2d,2p)	1.030	0.044	1.293	0.198	1.268	0.173

^a Error is evaluated as the difference between the computed value and the experimentally measured value. ^b QM1 indicates that these values were computed using QM/MM calculations in which only Trp34 was included in the QM layer. ^c QM2 indicates that these values were computed using QM/MM calculations in which the QM layer was expanded to include Glu15 as well as the 15 closest water molecules.

Supplementary Table 3.2: DFT benchmarking for calculations of the reduction potential of α_3Y and α_3W using the extended Born-Haber method

		Reduction potential (V vs. SHE) @ pH 7.0					
Functional	Basis set	α_3Y	(err) ^a	α_3W (QM1) ^b	(err) ^a	α_3W (QM2) ^c	(err) ^a
B3LYP	cc-pVDZ	1.000	0.014	1.289	0.194	1.090	-0.005
PBE	cc-pVDZ	0.869	-0.116	--	--	0.714	-0.381
PBE0	cc-pVDZ	0.961	-0.025	--	--	1.113	0.018
PBE50	cc-pVDZ	1.121	0.135	--	--	0.359	0.264
ω B97X-D	cc-pVDZ	1.112	0.126	--	--	1.363	0.268
B3LYP	VDZ	0.902	-0.084	--	--	1.511	0.416
B3LYP	cc-pVTZ	1.059	0.073	--	--	0.852	-0.243
B3LYP	aug-cc-pVDZ	1.042	0.056	--	--	0.911	-0.184
B3LYP	6-31G(d,p)	1.047	0.061	--	--	1.081	-0.014
PBE0	6-31G(d,p)	1.158	0.172	--	--	1.266	0.171
B3LYP	6-311++G(2d,2p)	1.045	0.059	--	--	1.119	0.024

^a Error is evaluated as the difference between the computed value and the experimentally measured value. ^b QM1 indicates that these values were computed using QM/MM calculations in which only Trp34 was included in the QM layer. QM1 was not evaluated for all levels of theory. ^c QM2 indicates that these values were computed using QM/MM calculations in which the QM layer was expanded to include Glu15 as well as the 15 closest water molecules.

Supplementary Table 3.3: DFT benchmarking for calculations of the reduction potential of cytochrome-c using the Zwanzig equation

Functional	Basis set	Reduction potential (V vs. SHE ^a)			
		cytochrome-c WT	(err) ^a	cytochrome-c M80H	(err) ^a
B3LYP	cc-pVDZ	0.272	0.017	-0.367	-0.408
PBE0	cc-pVDZ	0.338	0.083	-0.274	-0.315
ω B97X-D	cc-pVDZ	0.464	0.209	0.077	0.036
B3LYP	6-31G(d,p)	0.166	-0.089	-0.339	-0.380

^a Computed reduction potentials were shifted by the empirically determined value for the absolute potential of the standard hydrogen electrode given by Trasatti ($E_{\text{abs}}(\text{SHE}) = 4.44 \text{ V}$)

Supplementary Table 3.4: DFT benchmarking for calculations of the reduction potential of cytochrome-c using the gaussian approximation

Functional	Basis set	Reduction potential (V vs. SHE ^a)			
		cytochrome-c WT	(err) ^a	cytochrome-c M80H	(err) ^a
B3LYP	cc-pVDZ	0.216	-0.039	-0.401	-0.442
PBE0	cc-pVDZ	0.161	-0.094	-0.344	-0.385
ω B97X-D	cc-pVDZ	0.381	0.126	0.003	-0.039
B3LYP	6-31G(d,p)	0.302	0.047	-0.382	-0.423

^a Computed reduction potentials were shifted by the empirically determined value for the absolute potential of the standard hydrogen electrode given by Trasatti ($E_{\text{abs}}(\text{SHE}) = 4.44 \text{ V}$)

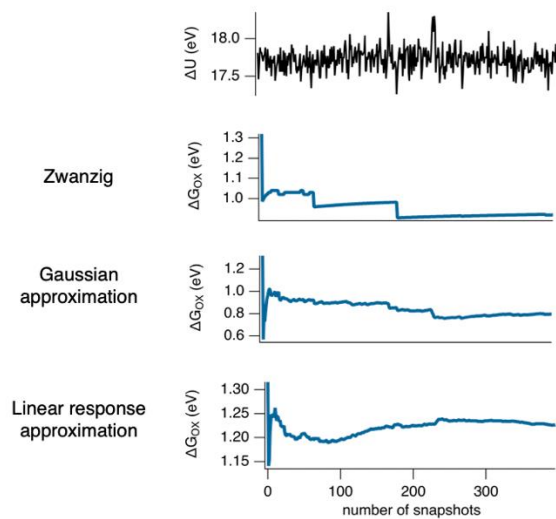
Supplementary Table 3.5: DFT benchmarking for the calculations of the reduction potential of cytochrome-c using the linear response approximation

Functional	Basis set	Reduction potential (V vs. SHE ^a)			
		cytochrome-c WT	(err) ^a	cytochrome-c M80H	(err) ^a
B3LYP	cc-pVDZ	0.153	-0.102	-0.287	-0.328
PBE0	cc-pVDZ	0.143	-0.112	-0.296	-0.337
ω B97X-D	cc-pVDZ	0.425	0.170	-0.081	-0.123
B3LYP	6-31G(d,p)	0.071	-0.184	-0.372	-0.413

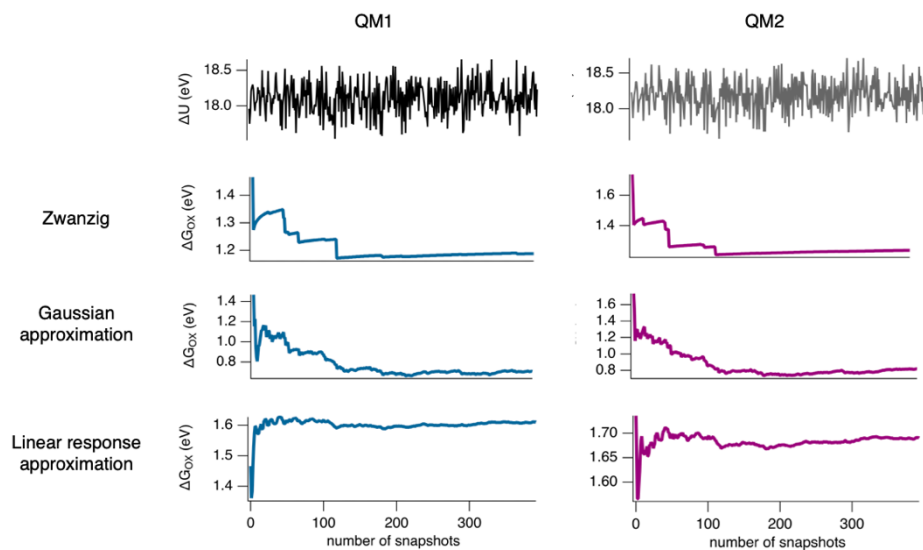
^a Computed reduction potentials were shifted by the empirically determined value for the absolute potential of the standard hydrogen electrode given by Trasatti ($E_{\text{abs}}(\text{SHE}) = 4.44 \text{ V}$)

Supplementary Table 3.6: Computed reduction potential of $\alpha_3\text{W}$ for increasing size of QM layer

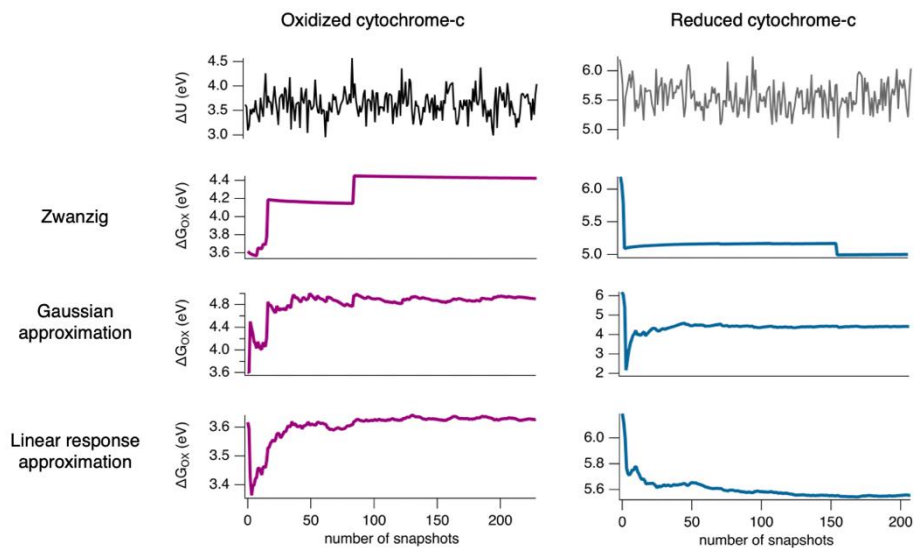
Reduction potential (V vs. SHE) @ pH 7.0				
QM Layer	BH ^{ext}	Zwanzig	GA	LRA
W34	1.289	1.191	0.707	1.611
W34 + E15	1.374	1.185	0.713	1.604
W34 + H ₂ O	1.307	1.300	0.869	1.705
W34 + E15 + H ₂ O	1.090	1.238	0.817	1.690



Supplementary Figure 3.1: Convergence of reduction potential of $\alpha_3\text{Y}$ computed with vertical energy gaps.



Supplementary Figure 3.2: Convergence of reduction potential of α_3W computed with vertical energy gaps.



Supplementary Figure 3.3: Convergence of reduction potential of cytochrome-c computed with vertical energy gaps.

4. Mechanism of charge transport in OmcS nanowires

A 300-fold conductivity increase in microbial cytochrome nanowires due to temperature-induced restructuring of hydrogen bonding networks

Peter J. Dahl, Sophia M. Yi, Yangqi Gu, Atanu Acharya, Catharine Shipps, Jens Neu, J. Patrick O'Brien, Uriel N. Morzan, Subhajyoti Chaudhuri, Matthew J. Guberman-Pfeffer, Dennis Vu, Sibel Ebru Yalcin, Victor S. Batista, Nikhil S. Malvankar

This chapter is a modified version of a published paper⁴⁴.

DOI: <https://doi.org/10.1126/sciadv.abm7193>

4.1 Author contributions

P.J.D. performed MD and QM/MM electronic structure calculations and 2-probe temperature-dependent conductance measurements on the nanowires as well as deuteration and Raman spectroscopy experiments. S.M.Y. performed 4-probe temperature-dependent conductance measurements on the nanowires and 2-probe conductance measurements of individual nanowires under conditions used to solve the atomic structure. Y.G. performed length-dependent conductance measurements of individual nanowires and TEM imaging of nanowire-producing cells. C.S. performed conductance measurements of reduced nanowires. Y.G., J. N., and D.V. prepared nanoelectrodes used for both temperature- and length-dependent conductance studies. A.A. performed initial MD and QM/MM electronic structure calculations. J.N. helped with the temperature-dependent UV-vis and Raman spectroscopy. P.J.D., C.S., J.N., and J.P.O. grew cells and purified nanowires used for conductance measurements. P.J.D. and U.N.M. performed the DFTB electronic structure calculations. P.J.D. and S.C. performed the electronic coupling calculations. P.J.D., A.A., and U.N.M. wrote the code for kinetic Monte Carlo

simulations and job control. M.J.G.-P. suggested normal coordinate structural decomposition, partitioning of conformational and electrostatic influences, and dynamical simulations at lower temperatures. N.S.M. and V.S.B. supervised the project with inputs from S.E.Y. N.S.M. and P.J.D. wrote the manuscript with input from all the authors.

4.2 Summary

Although proteins are considered as non-conductors that transfer electrons only up to 1-2 nanometers via tunneling, *Geobacter sulfurreducens* transport respiratory electrons over micrometers, to insoluble acceptors or syntrophic partner cells, via nanowires composed of polymerized cytochrome OmcS. However, the mechanism enabling this long-range conduction is unclear. Here we demonstrate that individual nanowires exhibit theoretically-predicted hopping conductance, at rate ($>10^{10} \text{ s}^{-1}$) comparable to synthetic molecular wires, with negligible carrier loss over micrometers. Surprisingly, nanowires show 300-fold increase in their intrinsic conductance upon cooling, which vanishes upon deuteration. Computations show that cooling causes a massive rearrangement of hydrogen bonding networks in nanowires. Cooling makes hemes more planar, as revealed by Raman spectroscopy and simulations, and lowers their reduction potential. We find that the protein surrounding the hemes acts as a temperature-sensitive switch which controls charge transport by sensing environmental perturbations. Rational engineering of heme environments could enable systematic tuning of extracellular respiration.

4.3 Introduction

Electron flow between cofactors in proteins is central to many life processes such as respiration, photosynthesis and nitrogen fixation⁷⁸. The protein architecture between cofactors has long been considered a passive tunneling bridge resulting in transport that decays exponentially with distance, thus limiting transport to 1-2 nanometers⁷⁸. Some proteins can conduct over distances up to 20 nm¹. Long-distance ($> 20 \text{ nm}$) charge transport is usually achieved via a redox potential gradient generated by distinct redox enzymes which provides an energetic driving force

for the transport of charge toward the terminal acceptor¹¹². However, the common soil bacterium *Geobacter sulfurreducens* transports electrons extracellularly over micrometer distances via “microbial nanowires”. These micrometer-long filaments are homopolymers of cytochromes OmcS (Figure 4.1)^{43,55} or OmcZ^{45,60}, which contrasts with multiple distinct cytochromes used by other bacteria for extracellular electron transfer up to nanometers³⁹. This extracellular electron transfer is important in global biogeochemical cycling of carbon, nutrients and metals as well as in regulating the bacterial release of methane to the atmosphere³⁹.

The atomic structure of OmcS nanowires revealed seamless stacking of heme cofactors, which provide a continuous path for electron flow (Figure 4.1B, C)^{43,55}. Prior theoretical studies of multiheme cytochromes have assumed that charges hop between heme cofactors⁹⁰, with the heme-to-heme hopping rates determined by the reduction potentials of the individual hemes and the electronic coupling between each pair. However, each protomer in OmcS must have a similar midpoint redox potential. Therefore, while there may exist a redox potential gradient within a protomer, there remain questions regarding how *G. sulfurreducens* generates high enough current through such a structure to meet its respiratory needs.

Prior computational studies on OmcS nanowires suggested multiple mechanisms such as hopping⁶³ quantum transport¹¹³, and coherence-assisted transport⁶⁴ to explain the experimentally-measured conductivity⁴³. However, experimental evidence supporting a particular mechanism is lacking.

In this work, we measure the intrinsic (contact-free) conductivity of individual OmcS nanowires as a function of nanowire-length, voltage, temperature, and pH, which reveal a surprisingly high hopping rate ($> 10^{10} \text{ s}^{-1}$), comparable to synthetic molecular wires, with negligible carrier loss over micrometers. We also find a 300-fold increase in nanowire conductance upon cooling that vanishes upon deuteration. Computations show that cooling causes

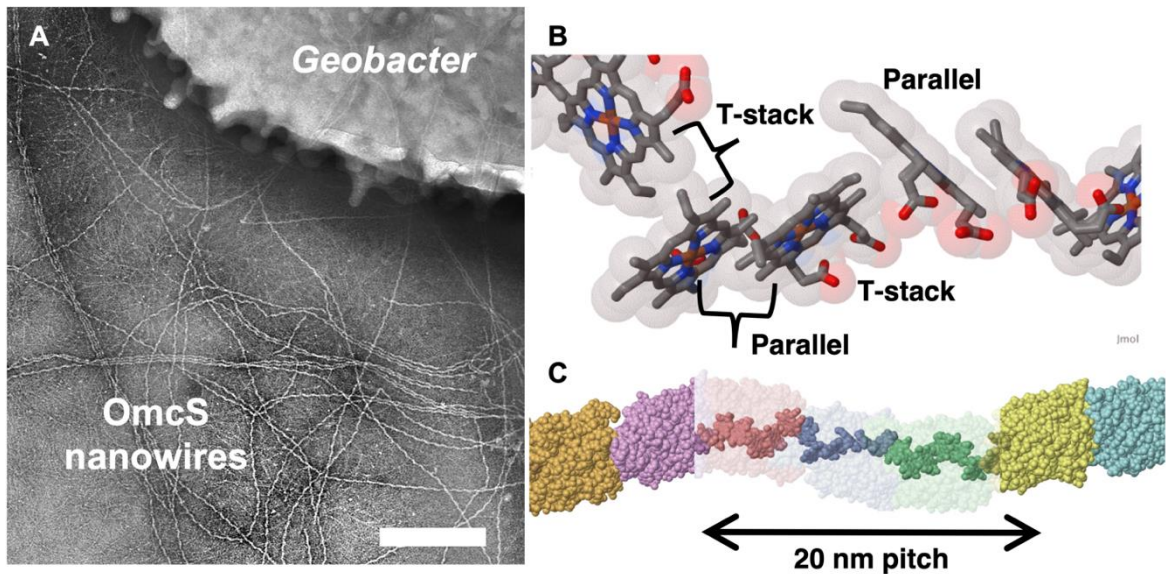


Figure 4.1: Closely-stacked hemes in OmcS nanowires provide a continuous path for extracellular electron transport over micrometers.

(A) Transmission electron microscopy image showing a *G. sulfurreducens* producing OmcS nanowires. Scale bar is 200 nm. Image levels were adjusted selectively in different areas to show the most information. (B) Each pair of parallel-stacked hemes is perpendicular to the next pair in a T-shaped geometry. (C) Upon polymerization, the hemes align to stack along the entire length of the OmcS filament with a 20-nm helical pitch. Each OmcS monomer and corresponding hemes are highlighted in different colors.

a massive rearrangement of hydrogen bonding networks, making hemes more planar, thus lowering their reduction potential, and increasing conductivity.

4.4 Results

4.4.1. Correlating nanowire structure with function using conductivity measurements under conditions used to solve the atomic structure

To correlate nanowire structure with conductivity, we performed measurements of individual nanowires in the same alkaline (pH 10.5) buffer used to solve the atomic structure, rather than pH 7 used previously for conductivity measurements⁴³. Using atomic force microscopy, we identified OmcS nanowires bridging gold electrodes via the distinct height and helical pitch of OmcS nanowires (Figure 4.2). The nanowires showed high conductance over 300 nanometers at physiologically relevant potentials⁶² (Figure 4.2D, Figure 4.3B). This finding contrasts with most proteins that can transfer electrons only up to 1–2 nanometers, due to the exponential decay of current with distance, characteristic of the tunneling mechanism⁷⁸.

Conductance in non-cytochrome proteins has been limited to 20 nm^1 . In contrast, conductance of OmcS nanowires is more comparable to synthetic molecular systems^{3,10,114-117}, for which the transport mechanism has been observed to transition from tunneling to hopping for molecular lengths greater than 4 nm^{116} .

4.4.2. Intrinsic conductivity measurements reveal hopping transport with negligible carrier loss

To test whether OmcS transports electrons via hopping, we measured DC conductance as a function of nanowire length using conducting-probe atomic force microscopy (CP-AFM) at physiological pH⁴⁵. We deposited nanowires across a gold/SiO₂ interface (Figure 4.3A), and electrically contacted the nanowires at varying distances away from the gold electrode with a conductive AFM tip to measure the electrical resistance (Figure 4.3B). We found that the nanowire resistance increased linearly with length (Figure 4.3C). Such a linear dependence of resistance on length is consistent with a multistep hopping mechanism¹¹⁷. These length-dependent measurements also helped to determine the contact resistance ($R_C \sim 1.2 \text{ G}\Omega$), yielding the intrinsic conductivity of OmcS nanowires ($\sim 24 \text{ mS/cm}$) (Figure 4.3C), comparable to prior studies^{43,45}.

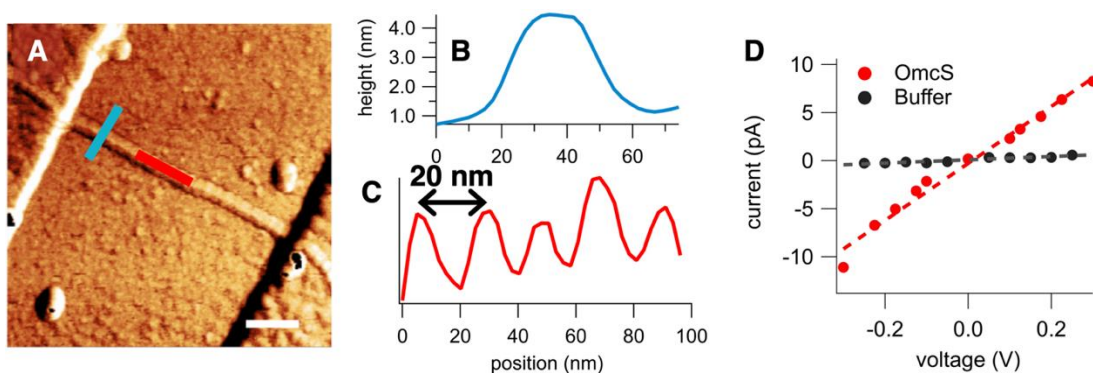


Figure 4.2: Correlating nanowire structure with conductivity by measurement under conditions used to solve the atomic structure.

(A) AFM image of a nanowire bridging the gap between nano-electrodes. Scale bar, 100 nm. (B) Nanowire height and (C) pitch measured at locations shown in A. (D) Current-voltage profile for a single nanowire hydrated in the buffer, compared to the buffer alone, measured at $\sim 290\text{K}$, and at pH 10.5 used to solve the OmcS structure.

To further understand the hopping conductivity, we analyzed our data using an expression for hopping flux (J) of the form $J = (k_{hop}/N)e^{-\alpha N}$, where k_{hop} is the hopping rate, α is related to carrier decay, and N is the number of heme-to-heme hopping steps¹¹⁷. Using the bias of 0.1 V and the rise-per-protomer of 4.67 nm (axial distance between protomers), we converted the measured resistance versus distance into flux (J) versus $1/N$ (Figure 4.3D) ($J = 0.1 V/(R \cdot e)$; $N = (d/4.67 \text{ nm}) \cdot (6 - 1)$ hemes). Remarkably, our measurements showed that α is close to zero, suggesting negligible loss of charge carriers over micrometer distances (Figure 4.3E). Furthermore, the measured hopping rate in nanowires ($3.2 \times 10^{10} \text{ s}^{-1}$) is comparable to that in synthetic porphyrin wires¹¹⁸. Such high hopping rate and negligible carrier loss in nanowires explains unique ability of *G. sulfurreducens* to transport electrons efficiently over micrometers.

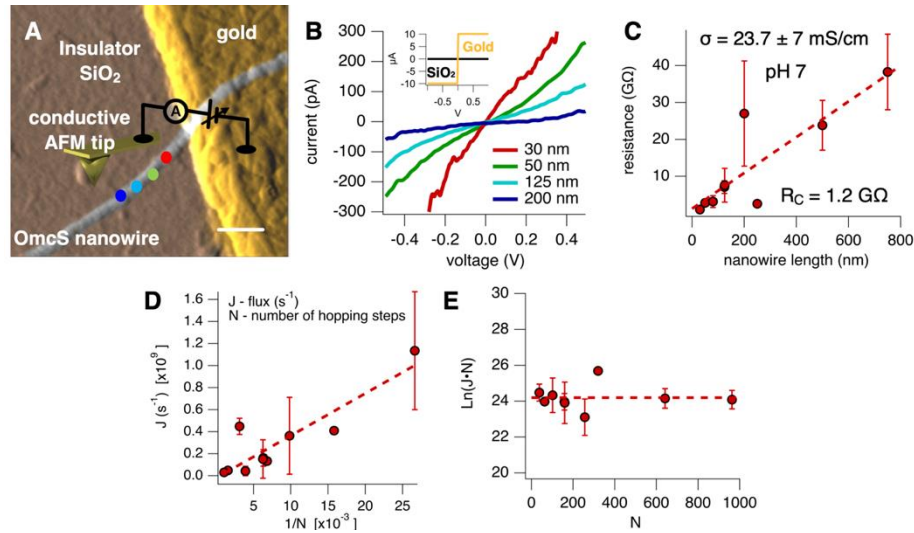


Figure 4.3: Identification of hopping conductivity in nanowires.

(A) Measurement strategy for the length-dependence of the single nanowire resistance, at 300K and at pH 7, using conducting probe (CP)-AFM. The current is measured between the gold electrode and AFM tip as the tip contacts the nanowire at varying distances away from the electrode. Scale bar is 100 nm. (B) Representative current – voltage curves along a nanowire at various distances. Inset, current – voltage collected on the gold electrode and the insulating SiO₂ substrate (black). (C) Resistance vs. nanowire length. Dashed red line is a linear fit ($R^2 = 0.74$). (D) CP-AFM data plotted as flux (at 0.1 V) vs. the inverse of the number of hopping steps. Dashed red line is a linear fit ($R^2 = 0.80$). (E) The product of the charge flux and the number of hopping steps plotted against the number of hopping steps. The slope of the linear fit (α) indicates the rate of carrier loss. All error bars represent s.e.m. $n=9$.

4.4.3. A 300-fold increase in nanowire conductivity upon cooling

Further insight into the conduction mechanism was obtained by measuring the intrinsic conductivity of individual nanowires as a function of temperature, at pH 10.5. To eliminate artifacts due to contacts or electrode polarization, we used a four-point probe (4-probe) configuration³. Upon cooling from room temperature (300 K), the conductivity of the nanowires initially increased exponentially by approximately 300-fold, followed by a transition to exponentially decreasing conductivity (Figure 4.4A). Notably, this behavior was reversible and did not show hysteresis. This finding is surprising because instead of increasing, hopping conductivity decreases exponentially upon cooling, known as Arrhenius behavior. Thus, individual OmcS nanowires showed a temperature dependence of conductance similar to living biofilms of a *G. sulfurreducens* strain CL1⁴⁶ engineered to overexpress OmcS¹¹⁹.

Measurements of nanowire films in a 2-probe configuration also showed the non-Arrhenius temperature dependence, albeit with a deviation from the trend between 280 K and 300 K, likely due to contact resistance (Figure 4.4B). Notably, the non-Arrhenius trend vanished upon deuterating the nanowires (Figure 4.4B). The conductivity was weakly dependent on temperature and showed a sharp transition around 220 K, likely due to the protein glass transition¹²⁰. Therefore, this low-temperature transition is distinct from the conductivity increase near physiological temperatures. The deviation from the trend at higher temperatures can likely be explained by the difference in zero-point energy for hydrogen and deuterium bonds. Deuterium substitution is known to change the strength of H-bonds, with weaker hydrogen (H)-bonds transitioning to stronger deuterium (D)-bonds¹²¹⁻¹²³. Stronger H-bonds experience a smaller increase in strength upon deuterium substitution than weaker H-bonds¹²¹. This change in bond strength results in a smoother free energy landscape¹²⁴. The vanishing of the increase in conductivity upon cooling after deuterium exchange suggests an important role for hydrogen bonding in nanowire conductivity, as we reported for amyloid proteins³.

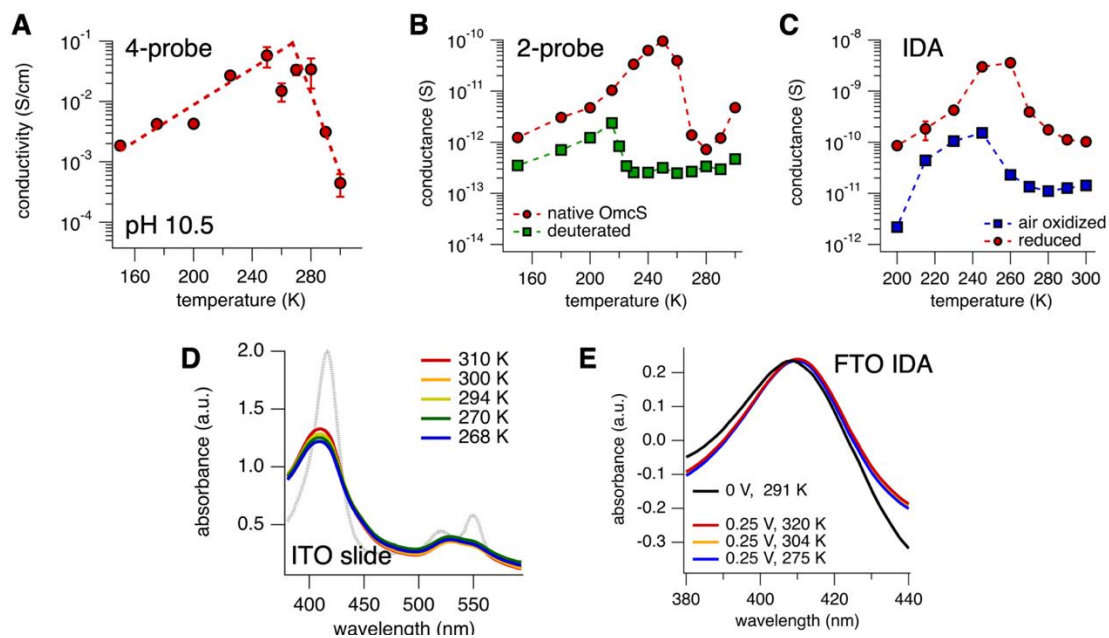


Figure 4.4: OmcS demonstrates a non-Arrhenius temperature dependence.

(A) Temperature dependence of the conductivity of OmcS nanowires determined experimentally, by four-probe measurements on nano-electrodes, at pH 10.5 used to solve the OmcS structure. The red dashed lines are exponential fits to the data. Error bars represent s.d. The data are representative of four independent measurements. (B) Temperature dependence of the conductance of a film of deuterated OmcS nanowires. The measurements were performed in a two-probe configuration on nanoelectrodes with 300 nm spacing. (C) Temperature dependence of the conductance of a film of air-oxidized and chemically reduced OmcS nanowires. The film was measured on a gold interdigitated array with 5 μm spacing. (D) UV-Visible spectra of OmcS nanowires at varying temperature. The spectrum of chemically reduced hemes is displayed in grey for reference. (E) Temperature dependence of the UV-Visible spectrum of OmcS nanowires under bias on a transparent FTO interdigitated array with 5 μm spacing.

Our findings contrast with previous temperature-dependent conductivity measurements of proteins where deuteration shows a stronger temperature dependence due to dominant electron transport through hydrogen bonds and the increased rigidity of the mostly β -sheet protein, which increases the reorganization energy¹²⁵. OmcS contains a very small number of β -strands (< 6%), suggesting a novel role of H-bonding in modulating protein conductivity.

Our findings also contrast previous reports of non-Arrhenius temperature dependence in films of cytochrome c3 and hydrogenase¹²⁶ where the conductivity increase upon cooling was due to an increased tendency of hydrogenase to reduce cytochrome c3 at lower temperatures. In contrast, the UV-Visible spectrum of air-oxidized OmcS nanowires did not change upon cooling (Figure 4.4D), suggesting an absence of substantial change in the redox state of OmcS. Although reduced films showed higher conductance (Figure 4.4C; Figure 4.5E), both reduced films and

air-oxidized films showed a non-Arrhenius trend (Figure 4.4C). Even under current carrying conditions, only a small, reduced population was evident (Figure 4.4E). Therefore, the cooling-induced increase in conductivity is intrinsic to OmcS, and not due to a change in the redox state of the hemes.

4.4.4. Computational modelling captures experimentally-measured conductivity

To obtain a molecular level description of the OmcS charge transport mechanism, we complemented our experimental results with computational modeling. Using the near-atomic resolution cryo-electron microscopy structure of OmcS nanowires⁴³ as a starting structure, we used the CHARMM36⁷⁵ force field to build 12-heme (dimer) models of OmcS under fully oxidized (electron transfer regime) and fully reduced (hole transfer regime) conditions

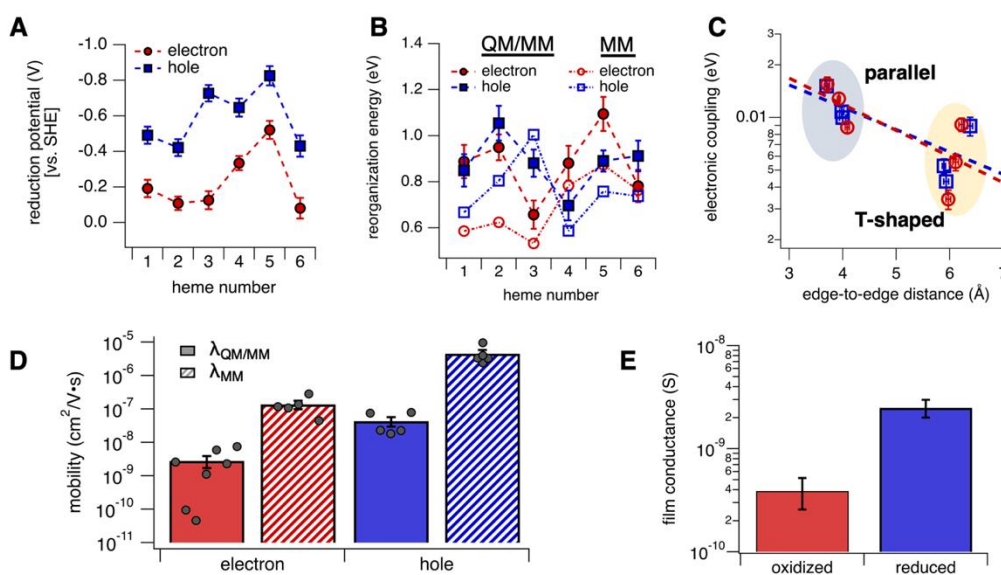


Figure 4.5: Computations and experiments reveal facile hole transport in OmcS.

(A) Free energy landscape vs. SHE for electron and hole transfer in OmcS obtained by QM/MM electronic structure calculations. Error bars are s.e.m. (B) Reorganization energies for electron and hole transfer models of OmcS. Solid markers were computed using QM/MM derived energies. Hollow markers were computed from molecular mechanics derived energies. Error bars are s.e.m. (C) Electronic coupling between heme pairs as a function of minimum edge-to-edge distance. The dotted lines are exponential fits to the data. The shaded areas differentiate the electronic coupling values corresponding to the parallel stacked heme pairs and the T-shaped heme pairs. Error bars are s.e.m. (D) Computed charge mobility and conductivity. Solid bars were computed using QM/MM derived reorganization energies and striped bars were computed using MM derived reorganization energies. (E) Conductance comparison of an air-oxidized vs. chemically reduced film of OmcS nanowires reveals higher hole conductivity. Error bars are s.e.m.

(Supplementary Figure 4.1). Molecular dynamics simulations of these models at 310 K provided sampling of thermally accessible configurations of OmcS. We used hybrid quantum/classical (QM/MM) calculations on an ensemble of these configurations to compute heme ionization energies (details in Methods). From these energies, we estimated the reduction potential of each heme.

We found that the six hemes in OmcS have a wide range of reduction potentials (Figure 4.5A; Supplementary Table 4.1, Supplementary Table 4.2), similar to QM/MM studies of other multi-heme cytochromes¹²⁷. Our results differ from prior theoretical estimates of differences in heme potentials in OmcS⁶³, which predicted a more narrow range of values using continuum electrostatics calculations on an energy minimized conformation. When we replaced the explicit protein/solvent environment with a polarizable dielectric continuum model, the range of computed reduction potentials was diminished and resulted in a distinct free energy landscape (Supplementary Figure 4.2). This result demonstrates the importance of the protein electrostatics in tuning the reduction potentials of c-type hemes. This result also suggests that our methodology may be particularly sensitive to polarization of the electron density in response to the protein environment.

We used the same ionization energies from our QM/MM calculations to estimate reorganization energies (Figure 4.5B). We also computed reorganization energies from molecular mechanics (MM) derived energies, using a framework which was designed to address non-ergodic protein dynamics, or conformational sampling which occurs on timescales slower than the electron transfer reaction¹⁵ (Figure 4.5B). Given substantial debate within the literature regarding the necessity of this approach^{17,87}, we present our results as a direct comparison to experiments. In general, the MM-derived reorganization energies were smaller, and thus give rise to greater charge transfer rates (Supplementary Table 4.5 and Supplementary Table 4.6) and higher mobility estimates (Figure 4.5D). These values are closer to experimental values.

Therefore, further comparisons between computed and experimentally determined conductivity will use the MM computed reorganization energies.

Calculations of the electronic coupling between adjacent heme pairs demonstrated that coupling is much less than the reorganization energy (Figure 4.5B,C; Supplementary Table 4.3 and Supplementary Table 4.4). Therefore, the electron transfer reactions are non-adiabatic and can be described by Marcus theory⁷⁸. The values we obtained for the coupling were higher for the parallel-stacked heme pairs than for the T-shaped heme pairs (Figure 4.5C). This is expected as the parallel orientation of the porphyrin rings allows closer distances between hemes and increases overlap between the pi-orbitals. An exponential fit for the donor-acceptor coupling (H_{AD}) of the form $|H_{AD}| = A \exp[-\beta(r - r_0)/2]$ (where β is the distance decay constant, r is the minimum edge-to-edge distance between donor and acceptor, r_0 is the van der Waals distance of 3.4 Å, and A is a pre-exponential factor) yielded distance decay factors of $0.69 \pm 0.3 \text{ \AA}^{-1}$ and $0.59 \pm 0.3 \text{ \AA}^{-1}$ for electron transfer and hole transfer couplings, respectively. These decay constants are smaller than previously reported values for multiheme cytochromes¹²⁸, due to the high coupling between T-stacked hemes 1 and 2 (9.1 meV), likely due to the proximity of Cysteine 12 to heme 2 (Supplementary Figure 4.3)¹²⁹.

Using these computed reduction potentials, reorganization energies, and electronic couplings in Marcus theory, we computed charge transfer rates between each hemes using the hopping model¹³⁰ (Supplementary Table 4.5 and Supplementary Table 4.6). From these values, we estimated electron and hole mobilities (μ) using kinetic Monte Carlo simulations (Figure 4.5D). Our modelling predicted the hole conductivity to be approximately an order of magnitude higher than electron conductivity (Fig. 3D). This result is consistent with prior studies¹²⁶ as well as our finding that a chemically reduced film of OmcS nanowires had ~ 6-fold higher conductance than air-oxidized nanowires (Figure 4.5E, Figure 4.4C). The increased conductivity under reduced conditions may have physiological implications for the anoxic growth

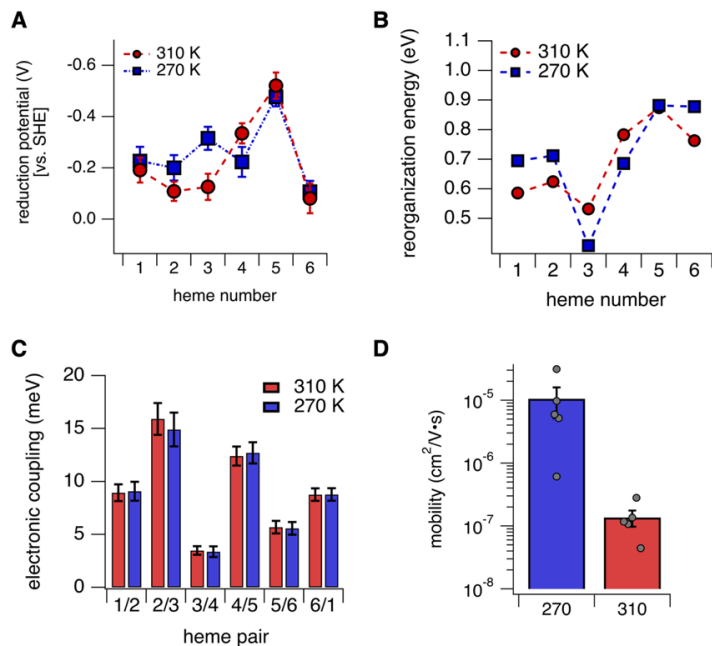


Figure 4.6: Temperature induced increase in reduction potentials enhances nanowire conductivity. (A) Computed free energy landscape for electron transfer at 310 K and 270 K. (B) Computed reorganization energies for OmcS models at 310 K and 270 K. (C) Computed electronic coupling between heme pairs at 310 K and 270 K. (D) Computed temperature dependence of charge mobility and conductivity in OmcS.

environment of *G. sulfurreducens*, allowing rapid extracellular transport of hole carriers to meet metabolic needs.

4.4.5. Cooling decreases heme reduction potentials which could explain increased conductivity

Non-Arrhenius hopping conductivity suggests a temperature-dependent activation energy, indicating a dynamic, temperature-sensitive, free energy landscape for OmcS nanowires. To determine the effect of cooling on the reduction potentials of OmcS, we re-computed heme reduction potentials and reorganization energies for electron transfer using an ensemble of configurations from MD simulations at 270 K. We found that cooling decreased reduction potentials for hemes 1, 2, and 3, with heme 3 showing the largest shift in potential (Figure 4.6A; Supplementary Table 4.7). Changes in reorganization energy were relatively small (< 0.1 eV) (Figure 4.6A,B; Supplementary Table 4.1 and Supplementary Table 4.7), and the electronic coupling did not change with temperature (Figure 4.6C). Thus, the reduction potentials dominate the temperature dependence of the activation energy in OmcS. The computed charge mobility was ~ 77 -fold higher at 270 K (Figure 4.6D), in quantitative agreement with the experiments (Figure 4.3A), validating our computational methodology.

4.4.6. Cooling massively restructures hydrogen bonding network in OmcS nanowires

We next performed a comparative study of our two models at 310 K and 270 K, with the goal of identifying the features of OmcS which allow its conductivity to be tuned over such a large range. The loss of the non-Arrhenius temperature dependence in response to deuterium exchange (Figure 4.4B) indicated the role of hydrogen bonding network in nanowire conductivity. Temperature is reported to influence the strength of hydrogen bonds¹³¹. We evaluated if the temperature alters H-bonds within OmcS which could modify protein conformation as well as the electronic structure of hemes¹³²⁻¹³⁴.

On average, our OmcS dimer model has 6.2 % more H-bonds at 270 K relative to 310 K (Figure 4.7A). However, this value alone fails to capture the change in composition of the H-bond network (i.e., the distribution of donor-acceptor pairs). To quantify the difference in composition, we computed a H-bonding frequency matrix whose elements $A(i,j)$ described the frequency an H-bond was realized between residues i and j . From this matrix, we use the norm of the matrix to define the characteristic H-bond frequency (CHF). When applied to the H-bond frequency matrix of a particular simulation, this metric provides information regarding the number of H-bonds present at any point in time. Therefore, the CHF for the simulation at 270 K is larger than the CHF for the simulation at 310 K (Figure 4.7B). We also applied this analysis to the difference matrix, whose elements are composed of the differences of the of the matrix elements computed at 270 K and those computed at 310 K. Each difference matrix element provides a direct measure of how prevalent a particular H-bonding interaction is at each temperature. The difference CHF therefore provides a quantification of the difference in H-bonding structure at the two temperatures.

We found that the difference CHF was large, as its value was more than half the CHF of the individual models and larger than the difference between the CHF values computed at 270 K and 310 K (Figure 4.7B). This is indicative of a massive restructuring of the H-bond network

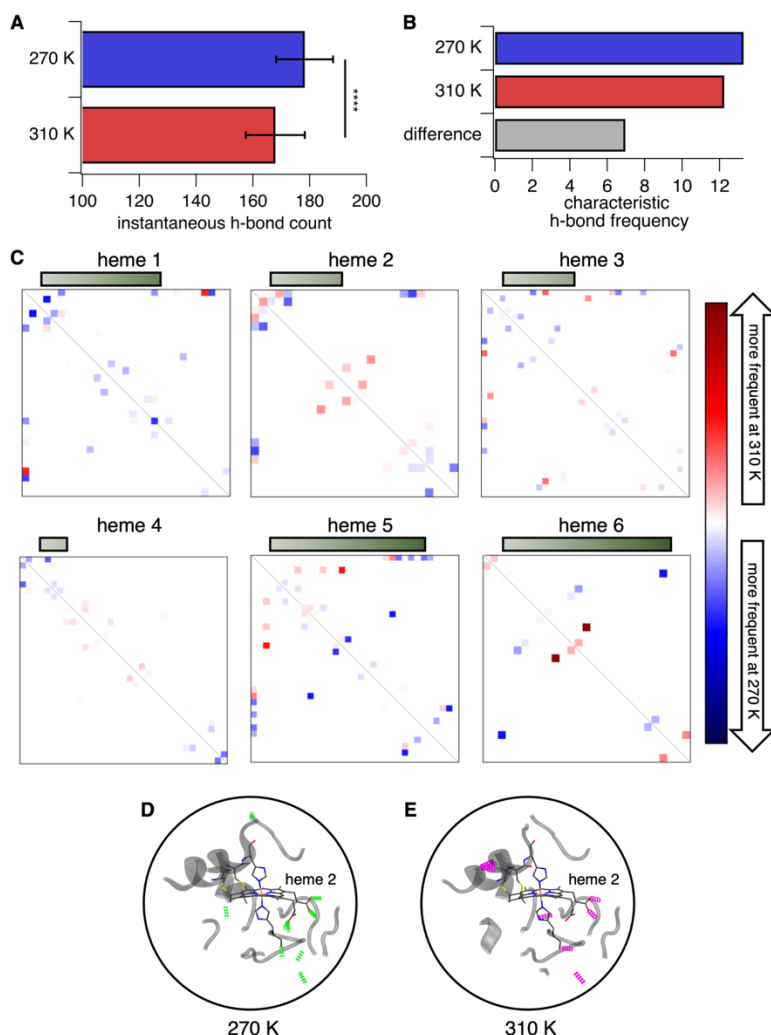


Figure 4.7: Temperature induces restructuring of hydrogen bonds.

(A) Average number of H-bonds in a selection of 200 snapshots from MD simulations of an OmcS dimer model. (B) Characteristic H-bonding frequency (norm of the H-bonding frequency matrix) for the h-bonding frequency matrices computed at 310 K and 270 K. (C) H-bonding frequency difference matrices for the hemes and protein within 5 Å of each heme. Green bars represent the difference CHF for the displayed matrices. Representative H-bonds are shown in the vicinity of heme 2 at (D) 270 K and (E) 310 K.

upon cooling. Decomposition of the individual H-bond interactions revealed that only 7 % of these interactions were unique to a particular temperature. Rather, 59 % of the interactions were more frequent at 270 K (Supplementary Figure 4.4). Thus, the H-bonding structure of OmcS is dominated by a different set of donor-acceptor pairs at lower temperatures. This result suggests there exist distinct states of the H-bonding network, defined by local minima in the H-bonding free energy landscape. This interpretation is consistent with the weak temperature dependence we observed with deuterated OmcS (Figure 4.4B). Deuteration creates a smoother free energy landscape. Therefore, the preference for particular H-bonding states will be less defined, resulting in less contrast between the H-bonding networks at high and low temperatures. The increase in H-bonding frequency upon cooling that we observe in our model is typical of secondary structures

such as α -helices and β -sheets¹³¹. However, OmcS has no β -sheets and only 13% of helices⁴³. Therefore, the restructuring of the H-bonding network and its role in nanowire conductivity may be unique to OmcS.

Changes to the H-bonding structure local to the hemes will have the largest effect on heme reduction potentials. To focus attention on the H-bonding interactions most likely to alter heme energetics, we computed the frequency difference matrices for residues within 5 Å of each heme (Figure 4.7C). Notably, the H-bond network around heme 4, whose predicted reduction potential remained unchanged at 270 K, was most robust under changing temperature. The remainder of the hemes experienced various changes to the H-bond network in their vicinity. For example, an additional H-bond with the propionate group of heme 2 is realized at 270 K (Figure 4.7D,E). However, the complexity of the H-bond networks surrounding the hemes make it difficult to assign shifts in reduction potential to individual H-bond interactions. Therefore, we analyzed how H-bonding-induced changes in the protein structure surrounding the hemes affected heme conformation and electrostatics.

4.4.7. Cooling makes hemes more planar, as revealed by Raman spectroscopy and simulations

Heme conformation, and in particular heme ruffling (Figure 4.8A), has been demonstrated to affect heme reduction potential^{93,95}, with increased ruffling corresponding to lower reduction potentials. Ruffling distortions are induced by the structure of the protein surrounding the hemes^{96,135}, and are therefore readily influenced by the H-bond network. Quantification of the ruffling distortion from our MD simulations revealed that, on average, the ruffling distortion was lower at 270 K than at 310 K (Figure 4.8B). This can readily be explained by the thermal depopulation of the heme ruffling mode. However, the cooling-induced shift toward heme planarity was not uniform, as hemes 2, 3, and 6 did not exhibit decreased ruffling. Therefore, in addition to thermal depopulation, changes to the structure of the protein surrounding

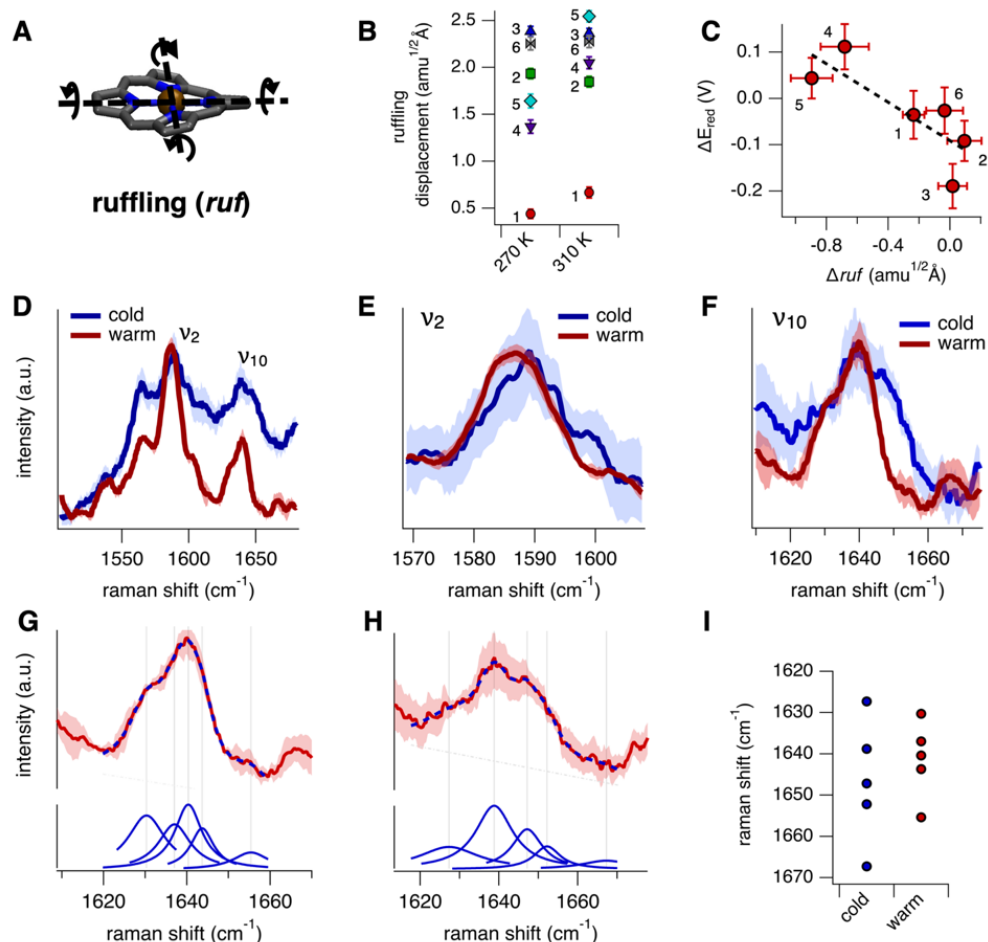


Figure 4.8: Hemes become more planar upon cooling.

(A) Illustration of the heme ruffling distortion. (B) Computed ruffling component of the out-of-plane distortion of the six hemes in OmcS from our models simulated at 270 K and 310 K. Error bars are s.e.m. Data are from an ensemble of 200 snapshots from our MD trajectory. (C) Computed cooling-induced shifts in the reduction potentials and ruffling distortions plotted against each other. Points are labeled to indicate heme identity. Error bars are s.e.m. Dashed line is a linear fit to the data ($R^2=0.65$). (D) Raman spectra of OmcS nanowires. Data were collected under warm (~ 296 K) and cooled (~ 280 K) conditions. (E) Magnification of the ν_2 peak from the Raman spectra in (D). (F) Magnification of the ν_{10} peak from the Raman spectra in (D). (G) Lorentzian decomposition of the ν_{10} peak of the Raman spectrum collected under warm (~ 296 K) conditions. Blue dashed line is the multipeak fit to the data. (H) Lorentzian decomposition of the ν_{10} peak of the Raman spectrum collected under cold (~ 280 K) conditions. Blue dashed line is the multipeak fit to the data. (I) Peak positions corresponding to the Lorentzian fit to the ν_{10} peak of the Raman spectra in (G) and (H).

the hemes appear to have altered heme ruffling. Notably, the computed shifts in ruffling correlated with the computed shifts in reduction potential (Figure 4.8C; $R^2=0.65$).

We further probed heme ruffling experimentally with Raman spectroscopy. The ν_2 , ν_3 , and ν_{10} modes have been associated with heme out-of-plane distortions^{93,94}, and have been directly correlated with ruffling. We collected the Raman spectra at room temperature (~ 296 K)

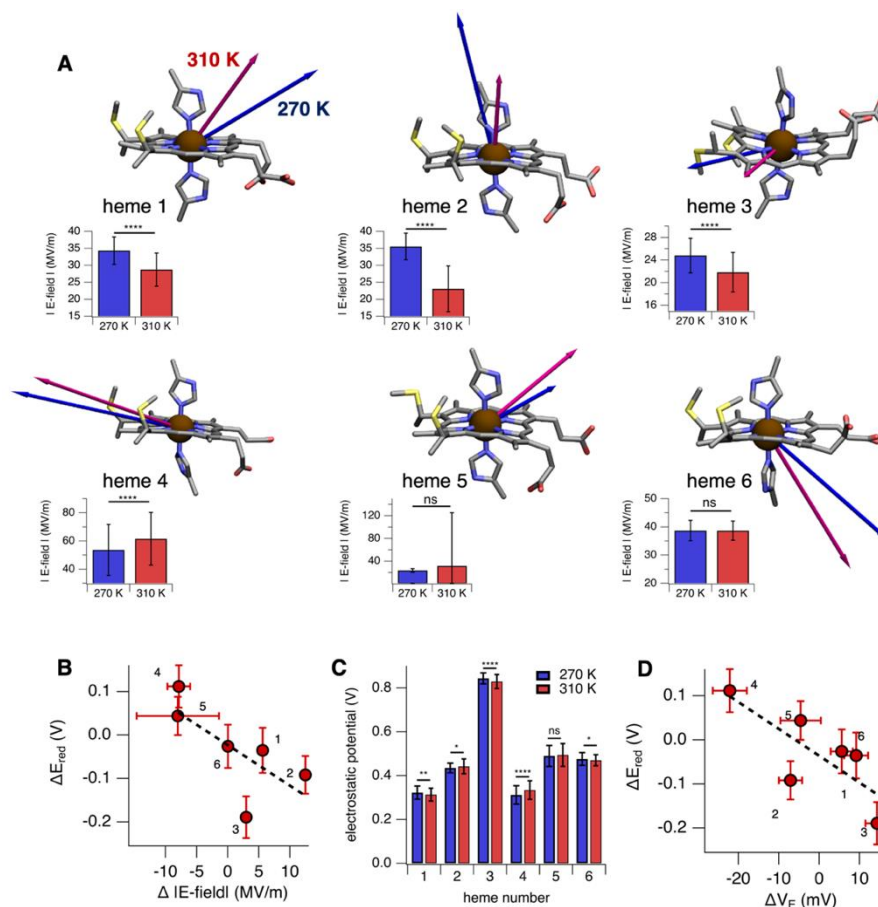


Figure 4.9: Temperature induced changes in protein structure alter the electric field at the heme iron atoms.

(A) Illustrations of the vectors representing the electric field at the iron atoms of the hemes in OmcS. Vectors displayed in blue were computed from our simulation at 270 K and the vectors displayed in red were computed from our simulation at 310 K. Insets plot the magnitude of the electric field for the simulations run at 270 K and 310 K. Error bars are standard deviation. (B) Cooling-induced shifts in heme reduction potentials and electric field magnitudes plotted against each other. Points are labeled to indicate heme identity. Error bars are s.e.m. Dashed line is a linear fit to the data ($R^2=0.51$). (C) Electrostatic potential at each heme site, computed from our simulations at 270 K and 310 K. Error bars are standard deviation. (D) Cooling-induced shifts in heme reduction potentials and electrostatic potentials plotted against each other. Points are labeled to indicate heme identity. Dashed line is a linear fit to the data ($R^2=0.60$).

and under cooled conditions ($T \sim 280\text{K}$) (Figure 4.8D). Both the ν_2 and ν_{10} peaks showed a shift toward higher frequency (Figure 4.8E,F), consistent with a decrease in ruffling^{93,94}. The ν_3 peak was too noisy under cooled conditions therefore could not be included in our analysis. Of the ν_2 and ν_{10} peaks, ν_{10} is the most sensitive to nonplanar distortions of the hemes^{93,94}. We performed Lorentzian decomposition analysis on the ν_{10} peak to extract information regarding the ruffling of individual hemes (Figure 4.8G,H). Comparison of the decomposition analysis with the computed

ruffling distortions revealed agreement between experiment (Figure 4.8B) and simulation (Figure 4.8I), further suggesting the role of heme distortions in modulating nanowire conductivity.

4.4.8. Cooling increases the electric field at the heme iron, lowering reduction potential

In addition to change in heme distortions upon cooling, we also examined the effect of temperature on electrostatic potential of hemes and protein-induced electric field at the heme iron centers. We found that the direction of these fields was altered upon changing the temperature from 310 K (red arrow) to 270 K (blue arrow) (Figure 4.9A). We also found that cooling increased the magnitude of heme electric field, thereby decreasing its reduction potential, in agreement with prior studies using external electric fields^{136,137}. We observed a negative correlation between the computed shift in the electric field magnitude and the computed shift in reduction potential (Figure 4.9B; $R^2=0.51$). In contrast, the hemes experienced relatively small (< 20 mV) shifts in electrostatic potential (Figure 4.9C), which did not correlate with the shifts in reduction potential as expected (Figure 4.9D). This finding suggests that the change in H-bonding structure altered the orientation of charged residues without significantly changing their distance from the hemes. Therefore, we conclude that a combination of heme ruffling and protein-induced electric field are responsible for the predicted shifts in heme reduction potentials and thus the non-Arrhenius temperature dependence.

4.5 Discussion

Electron transfer via *c*-type cytochrome plays a central role in many chemical and biological processes. However, cytochromes were long considered monomeric, limiting transfer to over a few nanometers. Here we show that common soil bacteria *Geobacter* can transport electrons over micrometers, via polymerized cytochrome nanowires with negligible electron loss. Combining theory with measurements of intrinsic, contact-free, conductivity measurements of

individual nanowires as a function of nanowire length, voltage and temperature, we find that a hopping mechanism explains the surprising length and temperature dependence of nanowire conductivity. This was previously reported only in synthetic nanowires and non-redox proteins where it was limited to distances less than 20 nm^{1,10}.

Alternative models based on quantum transport have introduced the possibility that such a mechanism has a role in OmcS^{64,113}. To date, all studies of quantum transport in OmcS have not incorporated the effect of the protein environment. Such a heterogeneous environment with thermal fluctuations would greatly impact the stability of delocalized electronic states. Our calculations suggest the protein has an important role in curating unique environments for each heme. Further studies are required to evaluate quantum transport in OmcS nanowires.

Protein environment controls the reduction potentials of c-type hemes⁹⁵. We demonstrate that this protein control of reduction potentials allows nanowire conductivity to be tuned over a remarkable range. Heme 3 showed a remarkable ability to be tuned in response to a changing environment. Thus, the OmcS nanowires are a new class of metalloproteins with highly tunable electronic properties. Our studies can help guide systematically fine-tuning the conductivity of nanowires by modulating protein-induced heme distortions. Using a suite of complementary experiments to measure the conductivity of individual nanowires as a function of molecular length and temperature and combining with computational studies using molecular dynamics and QM/MM electronic structure calculations, here we show that the thermally-activated vibrations induce out-of-plane heme distortions that modulate activation energy to enhance conductivity by 300-fold. We thus present a novel strategy to induce cooperative and large-scale conformational changes that modulate heme distortions, which were previously thought to have only local influence.

Our findings have consequences for the physiology of *G. sulfurreducens*¹³⁸. OmcS is essential for the reduction of iron oxides, an important electron acceptor in the native environment of *G. sulfurreducens*, as well during the early growth stages of electricity-producing

biofilms in bioelectrochemical systems¹³⁸. In addition, artificially expressing cytochrome OmcS in photosynthetic cyanobacteria, increased catalytic performance in a diversity of processes such as an increase in photocurrent by 9-fold¹³⁹, increased nitrogen fixation by 13-fold¹⁴⁰ and improved photosynthesis by increasing 60 % biomass¹⁴¹ compared to the wild-type cyanobacteria. These studies highlight the important role of OmcS in light-driven biocatalysis

Therefore, improving the conductivity of OmcS could help to control bacterial physiology and ecology as well as improve biocatalysis efficiency. The increased nanowire conductivity upon cooling could also help bacteria to compensate for the loss of metabolic rate at cold environments. Furthermore, protein structure and heme geometries can significantly differ after binding to substrates⁹⁵ such as minerals or anodes of microbial fuel cells, potentially enhancing the coupling between the nanowires and their electron acceptors .

Our discovery also has implications in the rational design of protein nanowires^{3,45,52}. Our mechanistic studies of OmcS nanowires provides a new framework for rational design of nanowire structures with tunable conductivity by modulating the redox potential of hemes as well as heme distortions by leveraging changes in the hydrogen bonding.

4.6 Materials and Methods

This section contains descriptions of the experimental methods used to collect the data described in this chapter. Detailed descriptions of the computational methods can be found in Chapter 2.

4.6.1. Bacterial strains and culture conditions.

Geobacter sulfurreducens wild-type (WT) strain PCA (designated DL-1) (ATCC 51573) was obtained from our laboratory culture collection. The cultures were maintained at 30 °C or at 25 °C under strictly anaerobic conditions in growth medium supplemented with acetate (10 mM) as the electron donor and fumarate (40 mM) as the electron acceptor¹⁴². These strains were grown

under electron acceptor limiting conditions that induces nanowire expression. Nanowires were purified via centrifugation as described previously⁴³.

4.6.2. Nanoelectrode design and fabrication

Gold electrodes separated by a 300 nm nonconductive gap were designed using electron-beam lithography. Silicon wafers with 300 nm of thermally grown oxide were used as substrates. The electrodes were first patterned by electron-beam lithography on an electron beam resist layer and developed in a solution of cooled isopropyl alcohol. A 30 nm thick gold film, deposited on top of a 5 nm thick titanium adhesion layer was thermally evaporated on the lithographically patterned wafer. The electron beam resist was removed with N-Methyl(1-2)pyrrolidone, resulting in gold nanoelectrodes separated by a 300 nm gap, followed by sequential rinsing with acetone, methanol, and isopropanol to remove any residue. Before usage, the device was washed with distilled water and then rinsed with isopropanol to remove contaminants on the surface. The device was further plasma cleaned for 1 min and dried with nitrogen flow, yielding a hydrophilic surface. In addition to electron beam lithography, nanoimprinting was used to fabricate electrodes. The devices were further inspected with optical and scanning electron microscopy to ensure that the gap was well separated, and resistance measurements were used to confirm that the electrodes are well insulated from each other ($R_{\text{gap}} > 1 \text{ T}\Omega$).

4.6.3. Nanowire sample preparation

Cell-free nanowire preparations were imaged with negative-staining transmission electron microscopy to ensure sample quality. Dilute 5 μl solutions containing OmcS nanowires were placed on gold nanoelectrodes to achieve individual filaments bridging the electrodes (Fig 2A). Nanowires on the electrodes were imaged with AFM under air-dried conditions, and height measurements were performed to confirm the presence of individual filaments. A comparison of the nanowire diameter to the atomic structure of OmcS allowed confirmation of nanowire

identity. Samples were maintained under hydrated buffer environments (150 mM ethanolamine) and pH of the buffer was equilibrated using HCl. Samples were air dried prior to data acquisition.

Nanowire reduction was achieved via the addition of 50-fold molar excess (vs. hemes) of sodium dithionite to a nanowire suspension. Reduction was confirmed by UV-Visible spectroscopy. To form films, 0.5 μl drops of reduced nanowires were deposited on interdigitated electrodes and were allowed to dry overnight in an anaerobic chamber.

4.6.4. Deuterium Exchange

Deuterium exchange was performed by drying 10 μl of 30 μM OmcS nanowires suspended in 20 mM Ethanolamine pH 10.5 under vacuum (at least 3 hours) followed by 5 minutes under N_2 flow. The nanowire film was resuspended in pure deuterium oxide (D_2O). This process was repeated twice. For the “native OmcS” control, the same process was repeated using Milli-Q[®] water rather than D_2O .

4.6.5. Electrical (dc) Conductivity measurements

As described previously³, all dc conductivity measurements were performed in either a 2-electrode or 4-electrode configuration using semiconductor parameter analyzer (Keithley 4200A-SCS) equipped with preamplifiers, allowing 0.1 fA current resolution and 0.5 μV voltage resolution. For 2-electrode conductance measurements, a fixed potential was applied across the electrodes and the current was measured for a minimum of 120 seconds in sampling mode until the steady state current was reached. For 4-electrode conductance measurements, a fixed current was applied between the two outer electrodes and the potential difference between two inner electrodes was measured over a period of minimum 120 seconds in sampling mode until the steady state was reached. Each current was adjusted to keep voltage difference close to 100 mV to eliminate artifacts due to hot carrier injection. The validity of the 4-probe measurements was checked by reversing the polarity of the input current. Forward and reverse currents yielded similar conductivity values, verifying the ohmic contact of the junction. The linearity of the I - V

characteristics was maintained by applying an appropriate low current and the slope of I - V curve was used to determine the conductance ($G=I/R$). All analysis was performed using Igor Pro software (WaveMetrics Inc.).

4.6.6. Conducting-probe atomic force microscopy (CP-AFM) measurements

As described previously⁴⁵, To measure the distance dependence of conductance using CP-AFM, 5 μ l of buffer solution containing OmcS nanowires was deposited on gold electrodes patterned with electron-beam lithography on a silicon wafer grown with 300 nm silicon dioxide similar to those used for 4-electrode measurements. The excess buffer was absorbed with filter paper. The sample was air-dried and was mounted on a metal puck. It was further transferred to a heater-cooler sample stage inside AFM (Oxford Instrument Co., Cypher ES), which enables temperature control over the sample.

AFM and subsequent CP-AFM experiments were performed using soft cantilevers (ASYELEC-01, Oxford Instrument Co.) with a nominal force constant of 2 N/m and resonance frequencies of 70 KHz. The tip was coated with Pt/Ir, altering the tip radius from 7-10 nm to 40-60 nm. The free-air amplitude of the tip was calibrated with the Asylum Research software and the spring constant was captured by thermal vibration method. For CP-AFM experiments, the dual gain ORCA holder was used (Asylum Research) to record both low and high current values. The sample was imaged with a Cypher ES scanner using intermittent tapping (AC-air topography) mode. AFM showed that gold electrodes were partially covered with nanowires to facilitate CP-AFM measurements (Fig. 3A).

After identifying nanowires across the electrodes and the substrate, the tip was withdrawn and brought into contact with the nanowire by switching on the contact mode. Points along the length of the nanowire were selected based on the AFM image (Fig. 3A) and the corresponding distance from the gold electrode to the AFM tip was measured with Asylum Research Software that was used to operate AFM. With partially gold-coated substrate as the first electrode and a

metal-coated AFM tip used as a second mobile electrode, the uncovered parts of the nanowire were contacted, measuring the current-voltage (I - V) characteristics as a function of the distance between the tip and the fixed electrode by applying a bias ramp in the range -1 V to +1 V (Fig. 3B) and the tip was withdrawn to the next point. To verify proper electrical contact during the measurements, the tip was frequently brought into contact with either gold or SiO₂ substrate (Fig. 3B, inset). The resistance vs. length curve $R(L)$ was determined along the nanowire by fitting a straight line to the linear regime (-0.2 V to 0.2 V) of the I - V data. A loading force of 10 nN was used to obtain stable current and the same force was used for all experiments reported in this manuscript. The I - V characteristics were captured in the software and the analysis was performed in Igor Pro software (Wavemetrics Inc.). For each point, at least 8 repeats were recorded to demonstrate statistical significance.

The linear regime of the I - V characteristics was used for the resistance calculation. I - V curves were processed using 75 points Savitzky-Golay smoothing function prior to fitting using IGOR Pro software (Wavemetrics Inc.). The resistance (G) was calculated using the equation: $R=V/I$. The resistance from different points was plotted as a function of distance, and the data were fit by linear regression. The y-intercept revealed a contact resistance of $1.25 \pm 3.6 \text{ G}\Omega$ which was about 10-fold lower than the nanowire resistance.

4.6.7. Temperature variation conductivity experiments.

As described previously³, a Physical Property Measurement System (DynaCool, Quantum Design) was used to vary the temperature of a sample stage with an electrode of size 1 cm x 1.25 cm. Each sample stage included pre-mapped pads for three sets of current and voltage channels. Electrical contacts between the sample and the specific channel input pads were made by creating wire bonds between the electrodes and pads using the operator-guided wedge-wedge wire bonder (West Bond), which uses ultrasonic energy to attach aluminum wire to contact pads. The sample-to-sample stage wiring connections were tested using either a resistance meter

(Fluke) or a source meter (Keithley 2400) before inserting into the system. The dissipative power was kept under 10^{-6} W to eliminate self-heating effects. All conductance measurements were performed under ambient atmospheric pressure.

4.6.8. Raman Spectroscopy

A Horiba LabRAM HR Evolution Confocal Raman Microscope was used to collect the Raman spectra of an OmcS film, dried on a glass coverslip. The Raman spectra was acquired with a 532 nm laser focused on the protein film with a 100X objective over a 30 second exposure. Temperature control was achieved with a thermoelectric cooling stage we built by coupling a pair of thermoelectric Peltier-elements to a copper bar. Heat dissipation was achieved via heat sinks and fans attached to the Peltier device. The temperature of the sample was measured with a solid-state thermometer placed on the glass coverslip, adjacent to the protein film. To generate the cool sample spectrum, the sample was cooled to approximately 280 K during spectrum acquisition. The warm spectrum was acquired at an ambient temperature of 296 K. On each film, at least 8 spectra were collected under both warm and cooled conditions. The spectra for each condition were then aligned with each other, smoothed with a 31-point Savitzky-Golay filter, and averaged. We measured a total of three OmcS films.

The Lorentzian decomposition of the ν_{10} peak between 1610 and 1670 cm^{-1} was performed with the Igor Pro Multippeak Fit tool. We used a linear baseline, and we constrained the fit such that all peaks should have roughly the same area. We aimed to fit 6 peaks corresponding to the 6 hemes. However, the program was only able to fit 5.

4.6.9. UV-Visible Spectroscopy

We collected the UV-Visible spectrum of an OmcS film deposited on an interdigitated FTO electrode using an Avantes UV-Vis spectrometer. A blank FTO electrode was used to measure the background FTO spectrum. The spectrum of OmcS was measured under changing bias and temperature. Temperature was controlled with the thermoelectric Peltier device

described above. Bias was applied using a Gamry potentiostat whose leads were clipped to wires which were attached to the FTO electrode with silver epoxy. The estimation of charge density from UV-Visible spectra is described below in the section “Charge mobility calculations”.

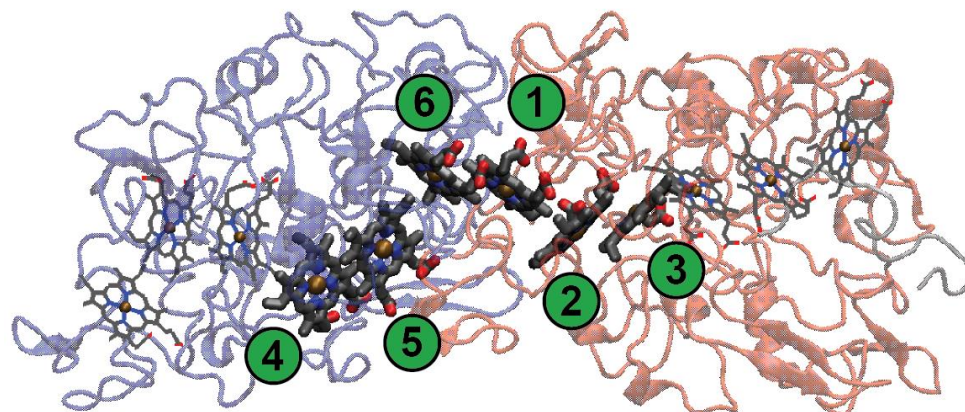
4.6.10. Calculation of electrostatic potential and electric field

We calculated the protein-induced electrostatic potential and electric field using the Delphi program. The point charges of the heme of interest were set to zero and a site calculation was used to compute the potential and electric field components at each atom site. The reported electrostatic potential was computed as the average potential over all heme atoms. The reported electric field magnitude was taken from the site of the heme iron atom.

4.6.11. Calculation of hydrogen bonding structure

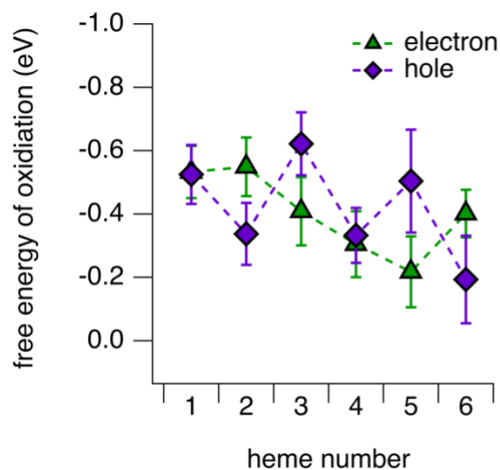
The hydrogen bonding structure of OmcS was calculated with the VMD⁹⁸ HBonds plugin, applied to the fully oxidized OmcS MD simulation. The instantaneous hydrogen bonding count was extracted from the default output file, while the characteristic hydrogen bonding frequency (CHF) was calculated from the detailed output file. We used a custom Python script to generate a hydrogen bonding matrix whose entries $A(i,j)$ described the frequency at which a hydrogen bond was observed between residue i and residue j in our MD simulations. The CHF was calculated as the Frobenius norm of the matrix. The difference CHF was calculated as the Frobenius norm of the difference between the matrices corresponding to 310 K and 270 K.

4.7 Supplementary Information



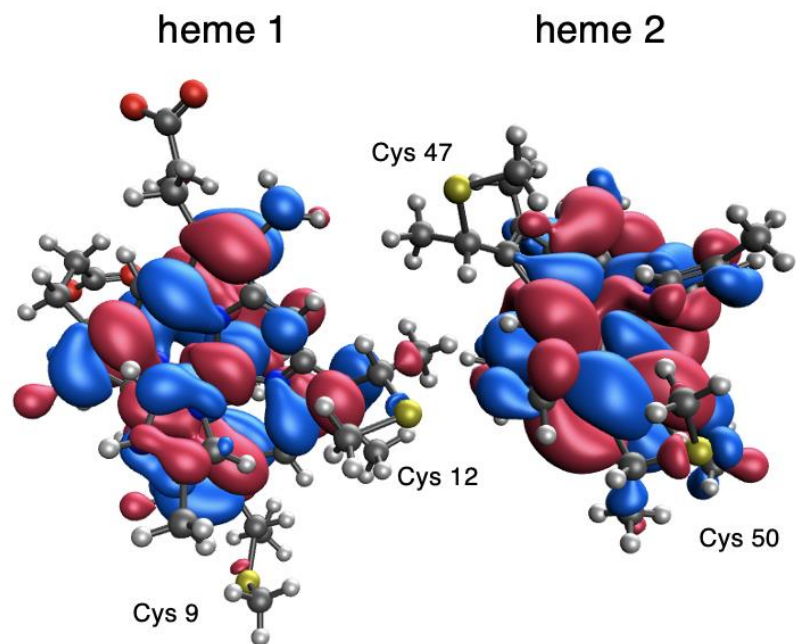
Supplementary Figure 4.1: Computational model of an OmcS dimer.

Model system used for all computational characterization. Two full protein chains as well as the first 20 residues from a third chain are included in the model. The additional 20 residues from the third chain are included to satisfy coordination of heme 5 with Histidine 16 of the next protein chain. Our electronic structure calculations, electronic coupling calculations, distance analysis, and essential dynamics analysis were performed on the central six hemes highlighted here. The hemes closest to the edges of the system were excluded from our analysis to limit the potential influence of heme solvation.

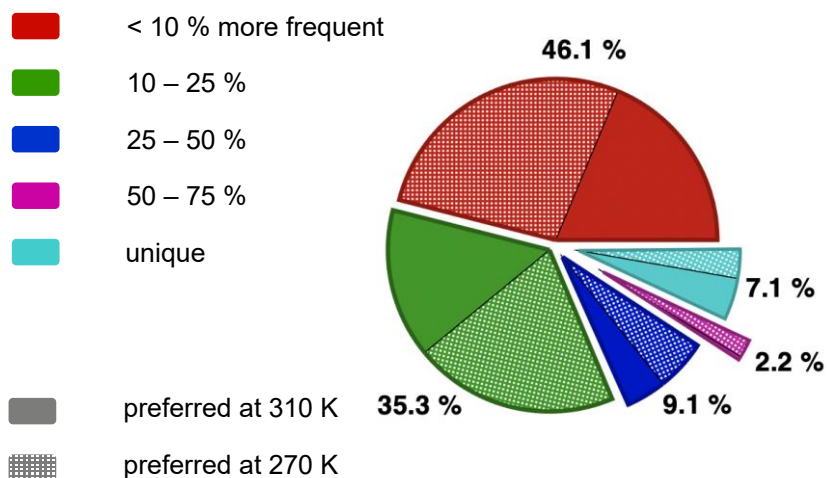


Supplementary Figure 4.2: Free energy landscape of OmcS in a uniform dielectric environment.

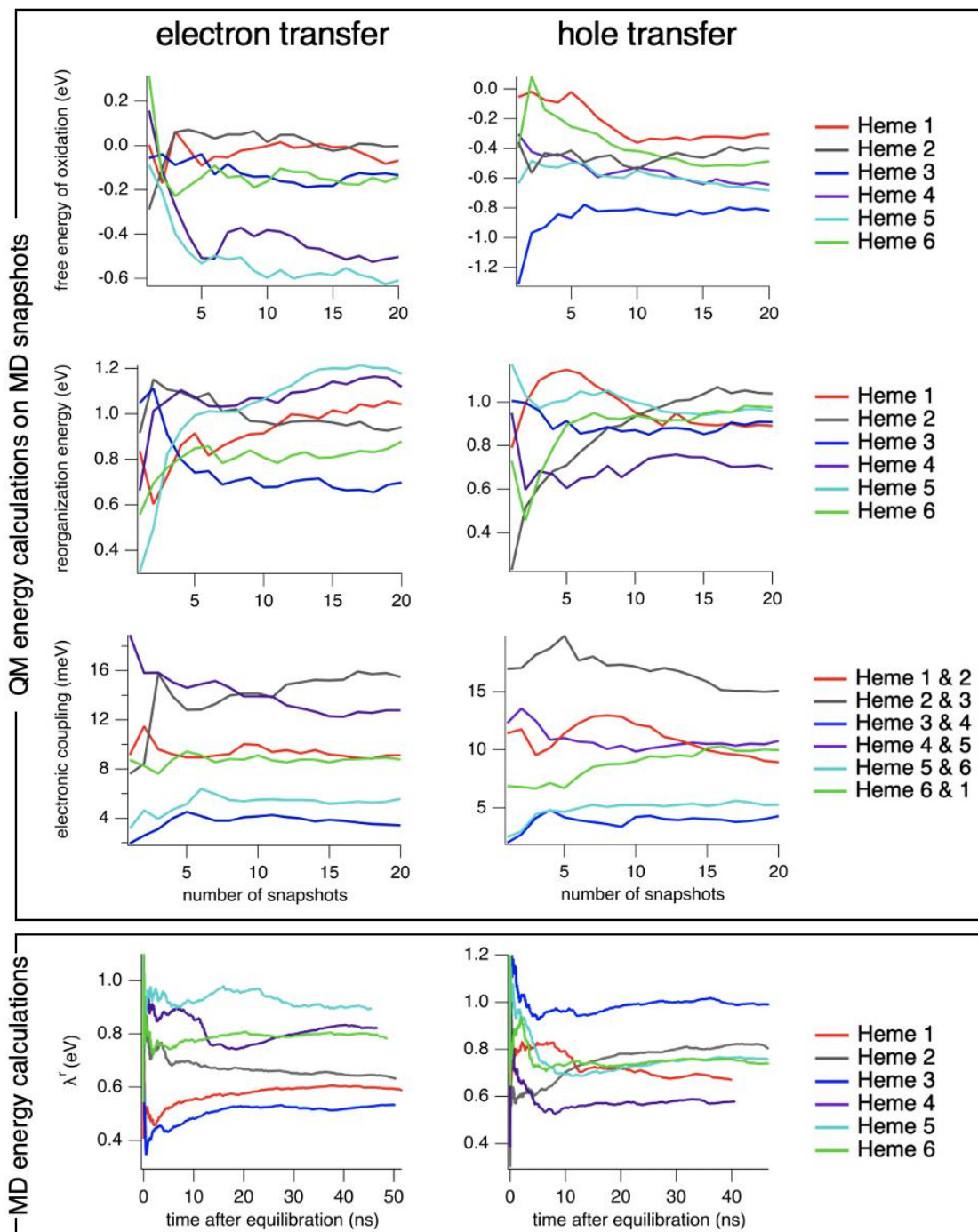
Redox potentials computed using the same ensemble of heme configurations that were used to generate Fig. 3A. For this calculation, the protein electrostatics were replaced with a dielectric continuum model. We used a dielectric constant of 4.7113 corresponding to chloroform to model a protein environment.



Supplementary Figure 4.3: Proximity of Cysteine 12 to heme 2 contributes to increased coupling between hemes 1 and 2.
 HOMO orbitals of reduced heme 1 and oxidized heme 2. This is a representative configuration. Orbitals are displayed using an isovalue of 0.01.

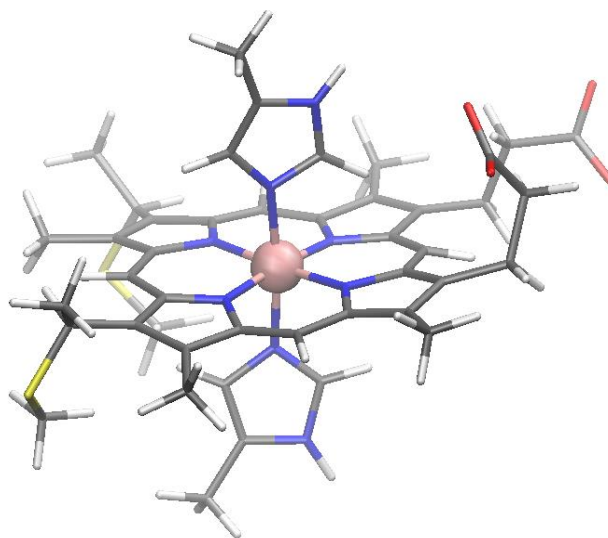


Supplementary Figure 4.4: The hydrogen bonding network of OmcS changes significantly upon cooling.
 Analysis of the preference of the hydrogen bonding interactions at 310 K and 270 K



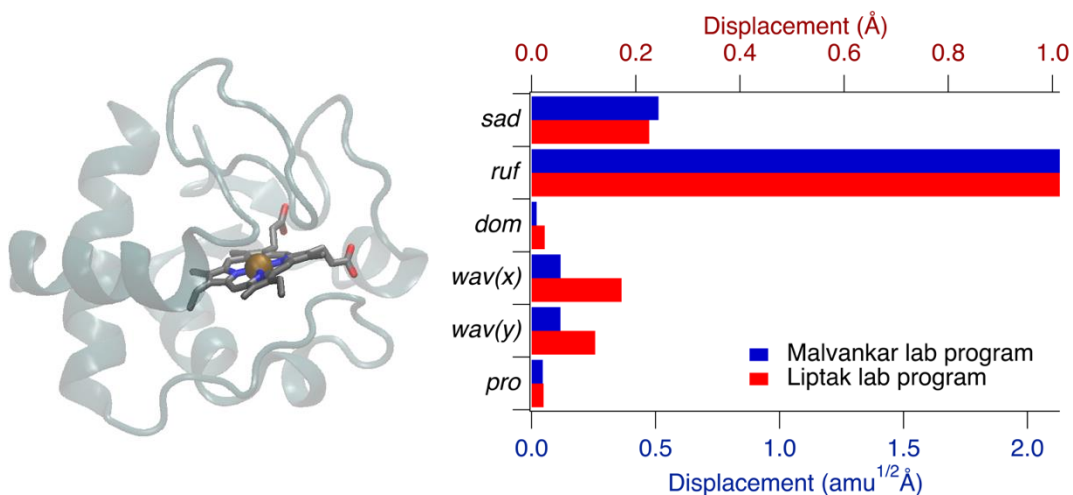
Supplementary Figure 4.5: Convergence of the free energy of oxidation, reorganization energy, and electronic coupling.

The free energy of oxidation, reorganization energy, and electronic coupling plotted as a function of the number of snapshots included in the calculation. Left column: Oxidized hemes Right Column: reduced hemes.



Supplementary Figure 4.6: QM region for electronic structure calculations.

The QM region for the electronic structure calculations included the heme (porphyrin ring, iron center, propionate substituents) as well as the covalently bound cysteine and histidine amino acids. The amino acids were truncated at their C_β atom and a hydrogen were inserted to satisfy the C_β valency.



Supplementary Figure 4.7: Benchmarking NSD program with analysis of heme distortion in horse heart cytochrome c.

(A) Structure of horse heart cytochrome c (PDB ID: 1HRC) showing the distorted heme geometry. (B) NSD analysis of the heme distortions in horse heart cytochrome c using our program (blue) and the program described by Graves and colleagues².

Supplementary Table 4.1: Free energies of oxidation and reorganization energies for electron transfer half reaction at 310 K

Heme Number	Free energy of oxidation (eV)	Reorganization energy (eV) [LRA]	Reorganization energy (eV) [MD]
1	-0.191 ± 0.05	0.888 ± 0.05	0.586
2	-0.108 ± 0.04	0.949 ± 0.04	0.624
3	-0.126 ± 0.05	0.657 ± 0.05	0.532
4	-0.334 ± 0.04	0.881 ± 0.04	0.783
5	-0.521 ± 0.05	1.094 ± 0.05	0.874
6	-0.080 ± 0.06	0.781 ± 0.06	0.763

Supplementary Table 4.2: Free energies of oxidation and reorganization energies for hole transfer half reaction at 310 K

Heme Number	Free energy of oxidation (eV)	Reorganization energy (eV) [LRA]	Reorganization energy (eV) [MD]
1	-0.491 ± 0.05	0.849 ± 0.05	0.667
2	-0.421 ± 0.05	1.054 ± 0.05	0.804
3	-0.727 ± 0.05	0.881 ± 0.05	1.004
4	-0.647 ± 0.05	0.697 ± 0.05	0.587
5	-0.826 ± 0.05	0.890 ± 0.05	0.758
6	-0.431 ± 0.06	0.912 ± 0.06	0.737

Supplementary Table 4.3: Gibbs free energy, reaction reorganization energy, and electronic coupling for heme-to-heme electron transfer at 310 K

Heme Pair	Gibbs Free Energy (eV)	Reorganization energy (eV)		Electronic coupling (meV)
		LRA	MD	
1 – 2	-0.083	0.918	0.605	8.93 ± 0.8
2 – 3	0.018	0.803	0.578	15.9 ± 1.5
3 – 4	0.209	0.769	0.658	3.48 ± 0.4
4 – 5	0.186	0.987	0.829	12.4 ± 0.9
5 – 6	-0.440	0.938	0.819	5.68 ± 0.6
6 – 1	0.111	0.835	0.675	8.76 ± 0.6

Supplementary Table 4.4: Gibbs free energy, reaction reorganization energy, and electronic coupling for heme-to-heme hole transfer at 310 K

Heme Pair	Gibbs Free Energy (eV)	Reorganization energy (eV)		Electronic coupling (meV)
		LRA	MD	
1 – 2	0.070	0.952	0.736	8.93 ± 1.1
2 – 3	-0.305	0.968	0.904	15.1 ± 1.1
3 – 4	0.080	0.789	0.795	4.31 ± 0.7
4 – 5	-0.179	0.793	0.672	10.8 ± 0.7
5 – 6	0.395	0.901	0.748	5.28 ± 0.5
6 – 1	-0.061	0.880	0.702	9.99 ± 0.9

Supplementary Table 4.5: Electron transfer rates at 310 K

Heme numbers	LRA reorganization energy		MD reorganization energy	
	forward rate (s ⁻¹)	reverse rate (s ⁻¹)	forward rate (s ⁻¹)	reverse rate (s ⁻¹)
1 – 2	1.12 x 10 ⁹	4.98 x 10 ⁷	2.50 x 10 ¹⁰	1.11 x 10 ⁹
2 – 3	1.81 x 10 ⁹	3.50 x 10 ⁹	1.76 x 10 ¹⁰	3.39 x 10 ¹⁰
3 – 4	2.02 x 10 ⁶	5.02 x 10 ⁹	5.64 x 10 ⁶	1.40 x 10 ¹⁰
4 – 5	5.46 x 10 ⁶	5.83 x 10 ⁹	2.46 x 10 ⁷	2.63 x 10 ¹⁰
5 – 6	4.65 x 10 ¹⁰	3.22 x 10 ³	1.14 x 10 ¹¹	7.91 x 10 ³
6 – 1	6.13 x 10 ⁷	3.89 x 10 ⁹	2.94 x 10 ⁸	1.87 x 10 ¹⁰

Supplementary Table 4.6: Hole transfer rates at 310 K

Heme numbers	LRA reorganization energy		MD reorganization energy	
	forward rate (s ⁻¹)	reverse rate (s ⁻¹)	forward rate (s ⁻¹)	reverse rate (s ⁻¹)
1 – 2	4.71 x 10 ⁷	6.42 x 10 ⁸	3.98 x 10 ⁸	5.42 x 10 ⁹
2 – 3	5.49 x 10 ¹⁰	5.97 x 10 ⁵	9.66 x 10 ¹⁰	1.05 x 10 ⁶
3 – 4	4.45 x 10 ⁷	8.88 x 10 ⁸	4.18 x 10 ⁷	8.36 x 10 ⁸
4 – 5	2.50 x 10 ¹⁰	3.12 x 10 ⁷	7.90 x 10 ¹⁰	9.86 x 10 ⁷
5 – 6	1.20 x 10 ⁴	3.48 x 10 ¹⁰	3.95 x 10 ⁴	1.14 x 10 ¹¹
6 – 1	1.43 x 10 ⁸	1.38 x 10 ⁹	8.43 x 10 ⁸	8.15 x 10 ⁹

Supplementary Table 4.7: Free energies of oxidation and reorganization energies for electron transfer half reaction at 270 K

Heme Number	Free energy of oxidation (eV)	Reorganization energy (eV) [LRA]	Reorganization energy (eV) [MD]
1	-0.227 ± 0.06	1.016 ± 0.06	0.695
2	-0.200 ± 0.05	1.012 ± 0.05	0.712
3	-0.315 ± 0.04	0.962 ± 0.04	0.408
4	-0.221 ± 0.06	0.882 ± 0.06	0.686
5	-0.477 ± 0.04	0.988 ± 0.04	0.882
6	-0.107 ± 0.04	0.954 ± 0.04	0.878

Supplementary Table 4.8: Gibbs free energy, reaction reorganization energy, and electronic coupling for heme-to-heme hole transfer at 270 K

Heme Pair	Gibbs Free Energy (eV)	Reorganization energy (eV)		Electronic coupling (meV)
		LRA	MD	
1 – 2	-0.027	1.014	0.704	9.07 ± 0.9
2 – 3	0.115	0.987	0.560	14.9 ± 1.6
3 – 4	-0.092	0.922	0.547	3.37 ± 0.5
4 – 5	0.254	0.935	0.784	12.7 ± 1.0
5 – 6	-0.370	0.971	0.880	5.56 ± 0.6
6 – 1	0.120	0.954	0.787	8.77 ± 0.6

Supplementary Table 4.9: Electron transfer rates at 270 K

Heme numbers	LRA reorganization energy		MD reorganization energy	
	forward rate (s ⁻¹)	reverse rate (s ⁻¹)	forward rate (s ⁻¹)	reverse rate (s ⁻¹)
1 – 2	4.74 x 10 ⁷	1.49 x 10 ⁷	1.58 x 10 ⁹	4.98 x 10 ⁸
2 – 3	7.12 x 10 ⁶	1.00 x 10 ⁹	8.34 x 10 ⁸	1.17 x 10 ¹¹
3 – 4	6.80 x 10 ⁷	1.30 x 10 ⁶	4.64 x 10 ⁹	8.90 x 10 ⁷
4 – 5	2.57 x 10 ⁵	1.43 x 10 ¹⁰	1.24 x 10 ⁶	6.85 x 10 ¹⁰
5 – 6	8.50 x 10 ⁹	1.87 x 10 ³	2.05 x 10 ¹⁰	4.51 x 10 ³
6 – 1	2.25 x 10 ⁶	3.92 x 10 ⁸	2.02 x 10 ⁷	3.53 x 10 ⁹

Supplementary Table 4.10: MM reorganization energy parameters for electron transfer at 310 K

Heme Number	λ^{St} (eV)	λ (eV)	κ_{G} (eV)
1	0.782	1.045	1.34
2	0.811	1.055	1.30
3	0.587	0.648	1.10
4	0.840	0.900	1.07
5	1.021	1.192	1.17
6	0.857	0.962	1.12

Supplementary Table 4.11: MM reorganization energies for hole transfer at 310 K

Heme Number	λ^{St} (eV)	λ (eV)	κ_{G} (eV)
1	0.880	1.162	1.32
2	0.932	1.082	1.16
3	0.806	0.648	0.80
4	0.738	0.929	1.26
5	0.852	0.957	1.12
6	0.887	1.067	1.20

Supplementary Table 4.12: MM reorganization energies for electron transfer at 270 K

Heme Number	λ^{St} (eV)	λ (eV)	κ_{G} (eV)
1	0.825	0.980	1.19
2	0.789	0.876	1.11
3	0.532	0.693	1.30
4	0.808	0.952	1.18
5	0.933	0.987	1.06
6	0.917	0.958	1.04

5. Homogenous OmcZ films conduct via a mixed ionic-electronic transport mechanism

High proton mobility in OmcZ nanowire films catalyzes power generation from ambient humidity

Peter J Dahl, Jens Neu, Yangqi Gu, Catharine Shipp, Victor S. Batista, and Nikhil S. Malvankar

This chapter is a modified version of a paper that has been submitted for publication.

5.1 Author Contributions

P.J.D. performed all conductivity measurements, KIE measurements, electrochemical impedance spectroscopy, back gating measurements of electron and proton mobility, power density measurements, and measurements of proton gradient reequilibration. J.N. prepared nanoelectrode devices. Y.G. and C.S. purified OmcZ nanowires. N.S.M. and V.S.B. supervised the project. P.J.D. and N.S.M. wrote the manuscript with input from all authors.

5.2 Summary

We report measurements of the intrinsic conductivity of protein films composed of the filamentous octa-heme cytochrome OmcZ. Our results demonstrate that OmcZ filaments form homogenous films whose conductivity can be tuned over 4-orders of magnitude by varying relative humidity. Electrochemical impedance spectroscopy revealed that the humidity dependence of protein film conductivity results from a mixed protonic-electronic ambipolar transport mechanism. Field-effect measurements of charge mobility and the temperature dependence of film conductivity revealed a percolation-limited transition in the mechanism of proton transport, with increased water content or decreased temperature supporting high proton mobility via a Grotthuss mechanism. We find that the transport properties are anisotropic, with 1000-fold lower proton mobility across the thickness of the film. This observation is important in understanding the mechanism of power generation from ambient humidity. Our experiments demonstrate proton gradients within nanowire

films generate 0.5 V potentials which are maintained via reversible oxidation of the c-type hemes by atmospheric O₂.

5.3 Introduction

Biomaterials capable of long-range charge transport have been investigated for use in a new generation of biocompatible and biodegradable electronic devices¹⁴³. Proteins are particularly interesting because their properties can be so easily tuned through site-directed mutagenesis. This was demonstrated for electron transport in the pili filaments of *E. coli*⁵² as well as proton transport in amyloid peptides¹⁴⁴. Additional electronic functionality can be introduced to protein systems by incorporating metal-containing sites such as gold nanoparticles⁵² or heme molecules¹⁴⁵.

Cytochrome nanowires, a class of biological materials produced by soil bacteria, have emerged as promising candidates for protein-based electronics. One particularly promising application is in the field of hygroelectric power generation, in which clean energy is produced from ambient humidity. Films of crude nanowire extracts have been demonstrated to produce a continuous power density of 0.23 $\mu\text{W}/\text{cm}^2$ ¹⁴⁶. However, the biochemical composition of these nanowire films as well as the mechanism by which the nanowires promote power generation remain open questions. With this current study, we address these questions via a mechanistic assessment the transport properties of purified nanowire films, followed by an assessment of their power generation capacity.

The nanowires composed of proteins OmcS⁴³, OmcZ^{45,59,60}, and OmcE⁵⁸ from the bacterium *Geobacter sulfurreducens* naturally use stacked heme cofactors to export respiratory electrons from the organism, and are involved in current production in microbial fuel cells^{147,148}. They appear to have evolved to efficiently transport electrons over micrometer distances, using well conserved stacking arrangements for their heme cofactors^{58,59}. The OmcZ nanowire, the

primary subject of this study, demonstrates the highest conductivity (~ 30 S/cm) reported thus far, 1000-fold higher than the OmcS nanowire^{44,45}.

The conductivity values currently available in the literature are restricted to single filament measurements, and conductance measurements of films formed from purified nanowires are restricted to two-probe measurements, subject to high contact resistances. Here, we present measurements of the intrinsic conductivity of OmcZ nanowire networks. While single-filament measurements are ideal for comparisons between nanowires and structure-function studies, such measurements are technically challenging and rely on incorporation into nano-scale circuits. Furthermore, OmcZ forms aggregated networks on the periphery of the secretory cell (Figure 5.1a), suggesting OmcZ networks to be most relevant to bacterial physiology. Therefore, characterization of the bulk properties of nanowire films will be an important contribution toward the further development of nanowire-based electronics as well as a greater understanding of the physiological relevance of these materials.

5.4 Results

5.4.1. Increased humidity drives a 30,000-fold increase in OmcZ conductivity

To obtain the intrinsic conductivity of OmcZ nanowire films, we performed DC four-probe measurements in a van der Pauw geometry (Figure 5.1c). Under ambient conditions, the films demonstrated an ohmic response under low bias and revealed a conductivity of $18.4 \mu\text{S/cm}$. The conductivity was independent of the size of the gap between electrodes (Figure 5.1d), which led us to conclude that OmcZ networks, deposited in a thin film (~ 300 nm), act as a homogenous material, a prerequisite of the van der Pauw method¹⁴⁹. In contrast, we could not measure film conductivity of OmcS nanowires, as OmcS films were incapable of supporting measurable current over even the smallest device with a gap size of $250 \mu\text{m}$. We attribute the ability of OmcZ nanowires to efficiently transport charge through networks to its unique structure. OmcZ contains 8 heme cofactors which stack to form a diverging charge transport pathway (Figure 5.1b), with

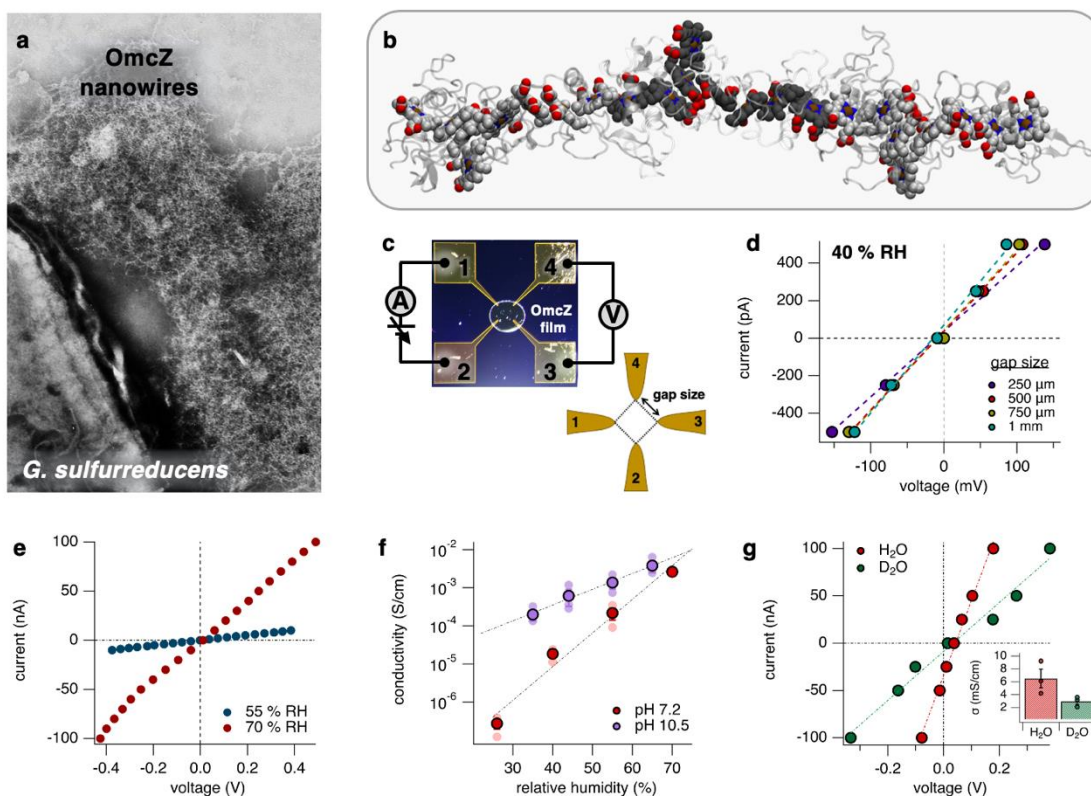


Figure 5.1: Conductivity of OmcZ nanowire films increased 30,000-fold with increased humidity. (a) *G. sulfurreducens* cell surrounded by a network of OmcZ nanowires. (b) Structure of an OmcZ trimer. The color of the haems from each subunit alternate between silver and black. (c) Image of a van der Pauw electrode with the four leads contacting the edges of an OmcZ nanowire film. On the lower right of the panel, the equidistant spacing of the four leads is illustrated. (d) Current-voltage curves for OmcZ nanowire films measured across gap sizes ranging from 250 μm to 1 mm. (e) Current-voltage curves for an OmcZ nanowire film, measured at 55 % RH and 70 % RH. (f) Conductivity of OmcZ nanowire films prepared at pH 7.2 and pH 10.5, measured under varied humidity. (g) Current-voltage curves and conductivity (inset) under humidity composed of water and deuterium oxide, demonstrating a kinetic isotope effect.

the heme furthest from the central heme chain almost entirely exposed to solvent (SASA = 343 \AA^2), which likely results in increased interfilamentous electron transfer rates.

The conductivity of biomolecules is known to be influenced by their level of hydration^{144,150,151}, similar to other conductive soft materials such as conducting polymers¹⁵², or even crystalline semiconductors such as lead-halide perovskites¹⁵³. OmcZ nanowire films are no exception. We used a humidity chamber to regulate the relative humidity (RH) over a range of 25 % RH to 70 % RH. The conductivity of nanowire films prepared at neutral pH increased exponentially with RH covering 4 orders of magnitude, resulting in maximum observed conductivity of 2.6 mS/cm (Figure 5.1e-f). Films prepared at basic pH (see Methods)

demonstrated a similar maximum conductivity (3.8 mS/cm) but displayed a much weaker dependence on humidity (Figure 5.1f). We interpret this result to indicate an important role for protons in the conduction mechanism. Consistent with this, we measured a kinetic isotope effect of 2.21 ± 0.4 (Figure 5.1g), a signature of protonic conductivity¹⁵⁴ or a mixed protonic-electronic conductor.

5.4.2. *OmcZ* films are mixed ionic-electronic conductors

To separate protonic and electronic contributions to the film conductivity, we used electrochemical impedance spectroscopy (EIS) in both a 2-probe and 4-probe configuration. For our 2-probe measurements, we used electrodes with a gap size of 707 μm . The 4-probe measurements were performed in the same configuration as the DC measurements, with a gap size of 500 μm . We treated the electronic and protonic components of the conductivity to be two parallel circuit elements, with the resistor representing the protonic component in series with a capacitor representing the electric double layer (EDL) capacitance at the interface between the film and the electrode. An additional capacitor representing the bulk dielectric of the hydrated nanowire film was also included in parallel with the electronic and protonic resistance elements (Figure 5.2a).

The EIS spectra were consistent with a mixed conductor. The impedance showed two plateaus on the Bode plot (Figure 5.2b,c; Supplementary Figure 5.1), and the Nyquist plot showed two semicircles (Figure 5.2d-g), consistent with our model circuit (Figure 5.2b). Humidity had the largest effect on the high frequency contribution to the impedance (Figure 5.2c) (impedance plateau at ~ 10 Hz on Bode plot; low impedance semicircle on Nyquist plot). We fit our data to the equivalent circuit and extracted values for each element at varying humidity. The bulk material dielectric remains largely unchanged, but there is a weak exponential increase with increased humidity (Figure 5.2h), consistent with an increase in water content. The

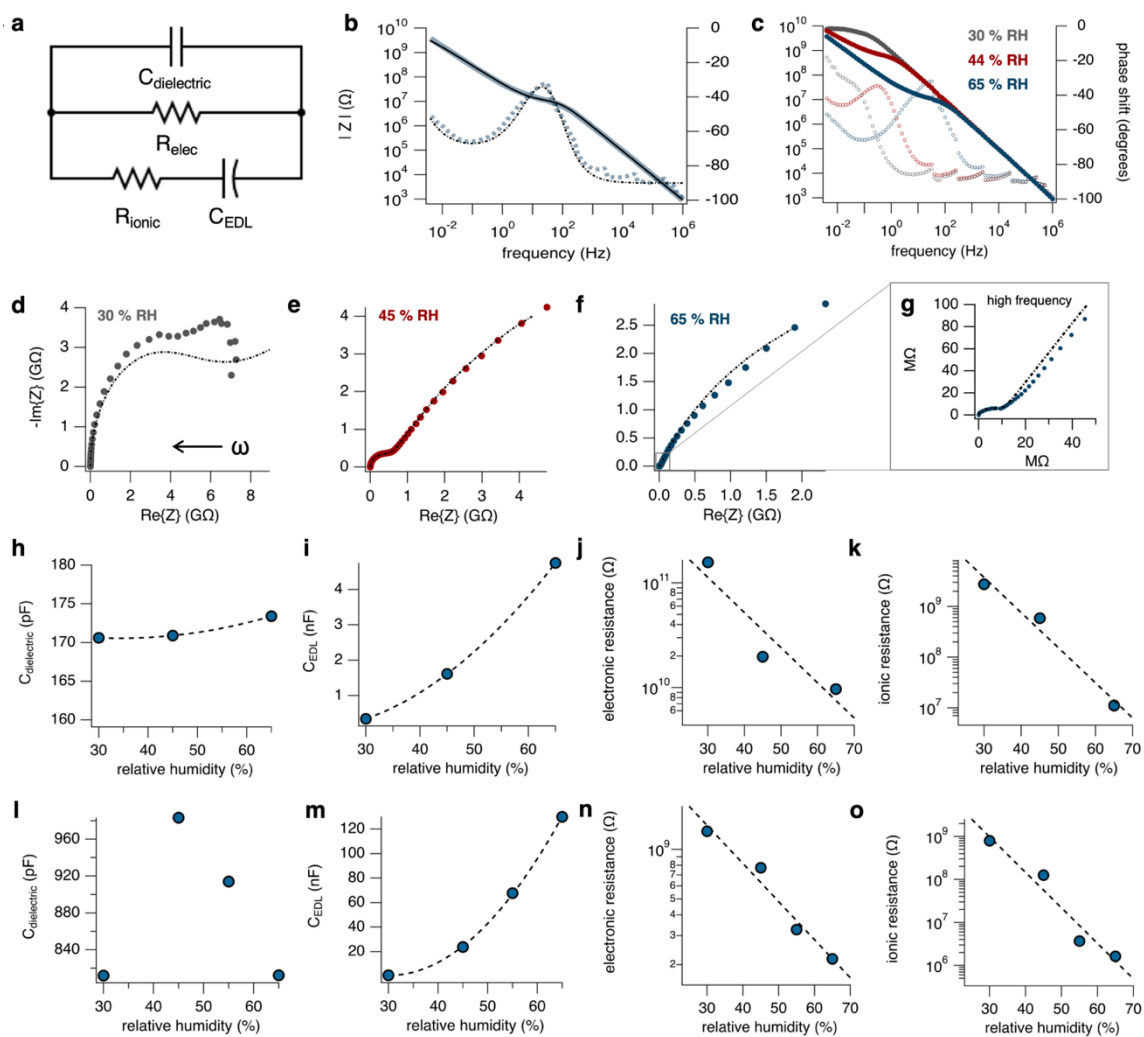


Figure 5.2: Electrochemical impedance spectroscopy revealed a mixed ionic-electronic ambipolar transport mechanism.

(a) Diagram of the model circuit used to analyze the EIS data. The parallel resistors describe the impedance of two separate charge species. (b) Example Bode plot (cyan line) with the fit to the model circuit (black line). (c) Bode plots for OmcZ nanowire films measured in a 2-probe configuration. Measurements were performed at 30 % RH, 44 % RH, and 65 % RH. (d) Nyquist plot measured in a 2-probe configuration at 30 % RH. (e) Nyquist plot measured in a 2-probe configuration at 45 % RH. (f) Nyquist plot measured in a 2-probe configuration at 65 % RH. (g) High frequency region of the Nyquist plot measured at 65 % RH. (h) Capacitance of the OmcZ film, extracted from the fit to the 2-probe impedance data for varying humidity. The black dashed line is an exponential fit to the data. (i) Electric double layer capacitance extracted from the fit to the 2-probe impedance data for varying humidity. The black dashed line is an exponential fit to the data. (j) Electronic resistance extracted from the fit to the 2-probe impedance data for varying humidity. The black dashed line is an exponential fit to the data. (k) Protonic resistance extracted from the fit to the 2-probe impedance data for varying humidity. The black line is an exponential fit to the data. (l) Capacitance of the OmcZ film, extracted from the fit to the 4-probe impedance data for varying humidity. (m) Electric double layer capacitance extracted from the fit to the 4-probe impedance data for varying humidity. The black dashed line is an exponential fit to the data. (n) Electronic resistance extracted from the fit to the 4-probe impedance data for varying humidity. The black dashed line is an exponential fit to the data. (o) Protonic resistance extracted from the fit to the 4-probe impedance data for varying humidity. The black line is an exponential fit to the data.

the van der Pauw configuration is not an optimal geometry to measure capacitance. The double layer capacitance increased exponentially for both 2-probe (Figure 5.2i) and 4-probe (Figure 5.2m) measurements. This result suggests an increase in the mobility of the ionic species in the diffuse layer of the EDL. These results for the humidity dependence of the capacitive elements indicate an increase in the water content of the nanowire film and may also indicate increased percolation of the water network.

Both the electronic resistance and the protonic resistance decreased exponentially with increased humidity (Figure 5.2j-k,n-o). However, the protonic resistance showed a much stronger response (Figure 5.2k,o), spanning 3-4 orders of magnitude, consistent with the DC conductivity data (Figure 5.1f). Our 4-probe data revealed that, at low humidity, the electronic resistance was comparable to the protonic resistance (Figure 5.2n). But the weak humidity dependence of the electronic component led to a massive difference between protonic and electronic resistance at high humidity. Therefore, the protonic contribution grows as the humidity increases, as was observed for peptide fibrils¹⁵⁰.

When comparing AC measurements (EIS results) to DC conductivity measurements, we must be cautious. It is tempting to conclude from the EIS data that OmcZ nanowire films are primarily protonic conductors. However, due to the rapid switching in bias, the electronic carriers are not uniformly distributed through the sample resulting in elevated resistance. Therefore, the EIS measurements likely underestimate the electronic contribution to the conductivity. In contrast, DC measurements may underestimate the protonic contribution due to the ionically blocking nature of gold electrodes¹⁵⁰.

Nonetheless, our results have revealed that both protons and electrons contribute to the conductivity of OmcZ nanowire films. Such ambipolar transport minimizes internal electric fields which arise from unidirectional drift of charged particles. This mechanism also implies that the

mobility of each charge species be linked, with the lower mobility species setting a limit for the mobility of its counter charge.

5.4.3. High proton mobility is associated with a transition to a Grotthuss mechanism

To directly measure charge mobility, we performed back-gated field effect transistor measurements on OmcZ nanowire films deposited on the van der Pauw electrodes (Figure 5.3a). We measured the sheet conductance of OmcZ films for gate voltages ranging from -10 to 10 V. The data showed a gating response for both electrons and protons, evidenced by increased conductance for both positive and negative gate voltages (Figure 5.3b; Supplementary Figure 5.2). We extracted the mobility using the relation $\mu = \frac{1}{C_i} \frac{dG}{dV_G}$, where C_i is the specific capacitance of the oxide layer (1.121 F/m² for 300 nm SiO₂), G is the sheet conductance of the nanowire film,

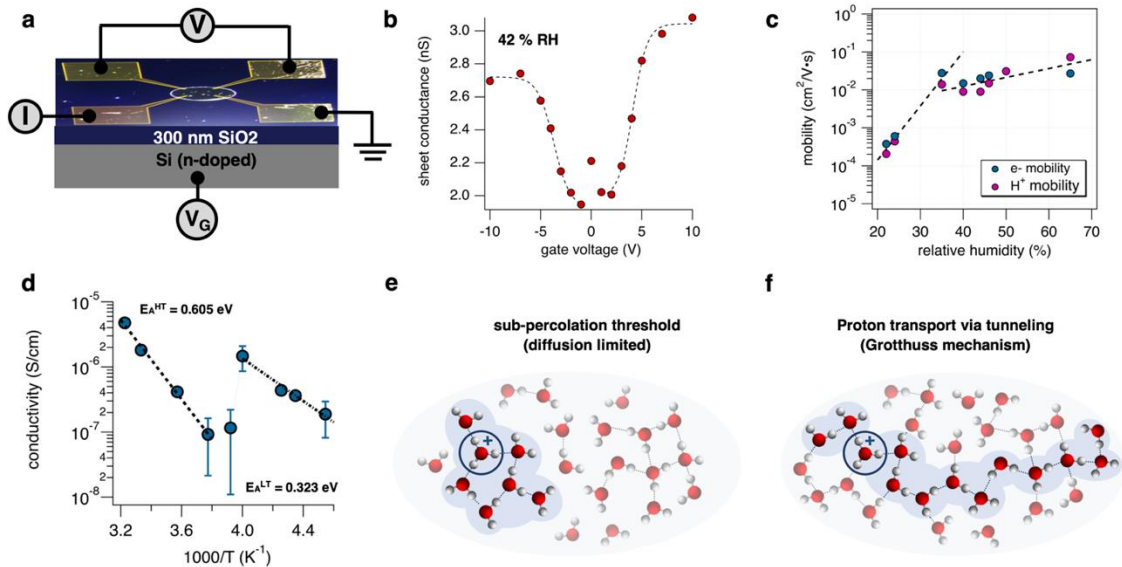


Figure 5.3: A transition to a Grotthuss mechanism supports high proton mobility.

(a) Schematic of the field-effect transistor device we used to measure charge mobility. (b) Sheet conductance of the OmcZ nanowire film, measured under varying gate voltage. These data were measured at 42 % RH. The data obtained under all other humidity conditions is shown in Supplementary Figure 5.2. The black dashed lines are sigmoidal fits to the data. (c) Humidity dependence of the mobility of electrons and protons extracted from our gating data. The black dashed lines are two separate exponential fits to the data. (d) Temperature dependence of OmcZ film conductivity. The black dashed lines are exponential fits to the low temperature (LT) and high temperature (HT) regimes of the data. The corresponding activation energies are indicated on the graph. (e) Representation of diffusion limited proton transport where the H-bond network is below the percolation threshold. (f) Representation of proton transport by a hopping mechanism, where a highly connected H-bond network supports exchange of the proton between water molecules.

and V_G is the gate voltage. Apart from two measurements at high humidity (>50 % RH), electron mobility was higher than proton mobility. For the six data points for which this held true, electron mobility was 1.78 ± 0.1 (mean \pm s.e.m.) times higher than proton mobility.

The mobility of both electron and proton increased exponentially with increased RH, with two distinct exponential regimes apparent (Figure 5.3c). As proton transport is rate limiting, apparent from the lower proton mobility, this result is suggestive of a change in proton transport mechanism. A change in mechanism is supported by measurements of the temperature dependence of an OmcZ film conductivity under low RH conditions. Two regimes are observed on an Arrhenius plot of conductivity, each characterized by a distinct activation energy (Figure 5.3d). At high temperature, we measured an activation energy of 0.605 ± 0.024 eV, consistent with diffusion limited transport of ions^{153,155}. At a critical temperature around 255 K, conductivity increased on cooling before decaying with an activation energy of 0.323 ± 0.032 eV. Such a significant decrease in activation energy suggests a transition to a more efficient transport mechanism.

Increased water content in protein films has been proposed to induce a percolation-like transition from diffusion limited transport to a proton hopping (Grotthuss) mechanism¹⁵⁶. Under sub-percolation threshold conditions (low water content), solvated protons exist in hydronium ion water clusters locally connected via a network of hydrogen bonds (H-bonds) (Figure 5.3e). Mobility of the proton is limited by thermally activated diffusion of the water cluster and exchange of H-bonds. Our data support a model in which a transition to a spatially extended H-bonding network can be stabilized with increased water content or decreased temperature (Figure 5.3f), leading to rapid proton transport via shuttling of the proton between water molecules.

5.4.4. Proton mobility enables power generation from ambient humidity

We have found that our discovery of a mixed ionic-electronic ambipolar transport mechanism in OmcZ nanowire films has direct relevance to the observation of power generation from

ambient humidity. Liu and coworkers demonstrated this phenomenon using nanowire films prepared from *Geobacter sulfurreducens* grown in microbial fuel cells¹⁴⁶. In this initial work, the nanowire preparations were crude and of unknown identity. However, based on our labs own work, we know that both OmcS and OmcZ are produced when *G. sulfurreducens* is grown on electrodes in microbial fuel cells, with OmcZ production being upregulated in response to the applied electric field⁴⁵.

To separately assess the ability of OmcS and OmcZ nanowires to catalyze power generation, we formed thick (~9 μm) films on 9 mm^2 gold electrodes (Supplementary Figure 5.3a-b). We contacted the top of the film with a thin strip of aluminum foil, sandwiching the nanowire film between electrodes (Figure 5.4a; Supplementary Figure 5.3a). We connected the top and bottom electrodes to a load resistor with a resistance of 220 $\text{k}\Omega$, and we measured the voltage drop across the resistor from which we computed the power density of the device (see Methods for details). Both OmcS and OmcZ devices showed exponentially increased power density with increased RH (Figure 5.4b-c). However, the power density from OmcZ devices was approximately 10-fold higher than the power density from OmcS devices (Figure 5.4c).

Moisture based power generation relies on the formation of ion gradients which provide the potential required to drive current through a load. In cytochrome nanowire batteries, this is proposed to occur via mobile protons, solvated in a gradient of moisture spanning the thickness of the film¹⁴⁶. This is consistent with our observation of high proton mobilities in OmcZ nanowire films. The existence of a proton gradient is further supported by the current-voltage response of the films.

To measure the current-voltage response, we bypassed the load resistor and measured the current through the device as a function of the applied bias. The resulting curves were non-linear, with a change in slope centered around the open-circuit potential (OCP), which was consistently around 0.5 V (Figure 5.4d, Supplementary Figure 5.3c-f). Decreased slope and thus increased

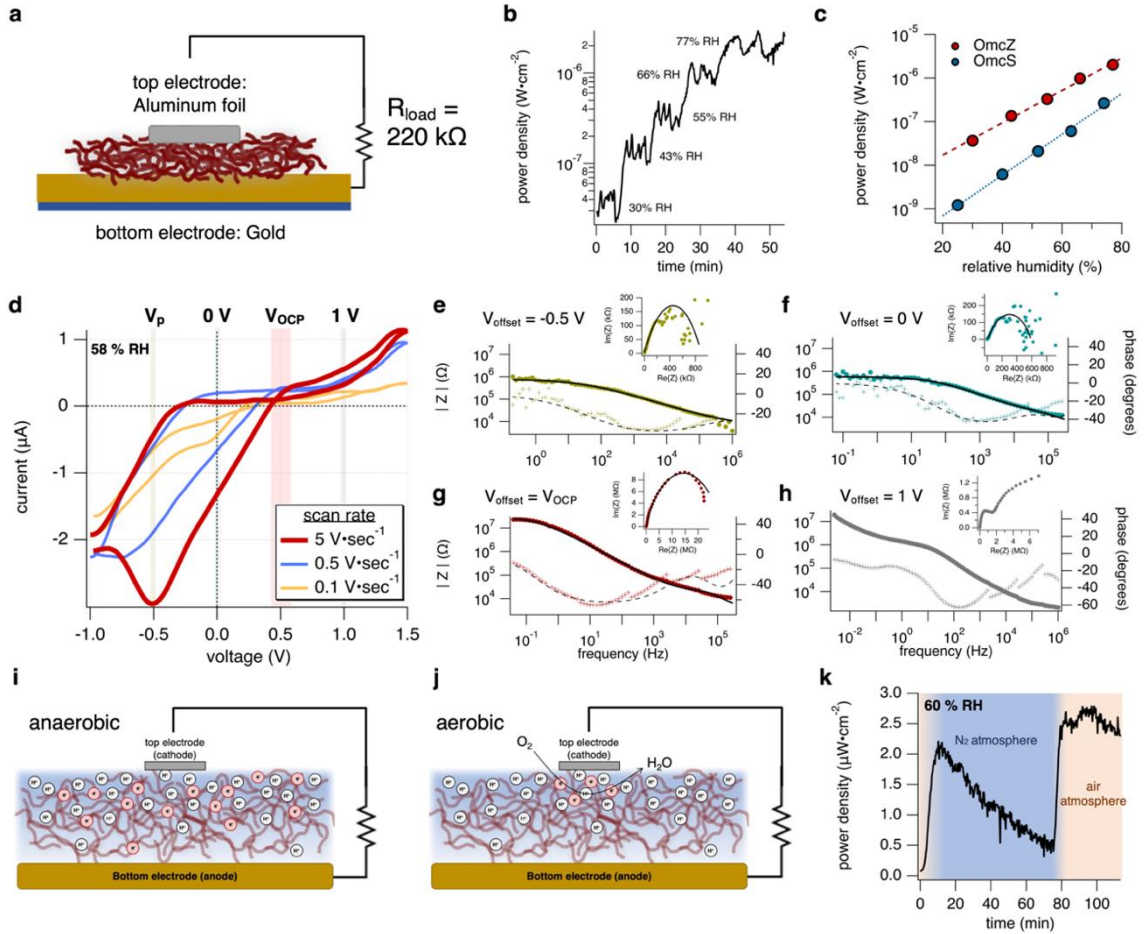


Figure 5.4: Cytochrome nanowire films produce power by using a proton gradient to couple electron transfer to oxygen reduction.

(a) Cartoon representation of the OmcZ-based hygroelectric device. A micrometre thick nanowire film is sandwiched between a gold substrate (bottom electrode) and a strip of aluminum foil (top electrode). The top and bottom electrodes are then connected to a load resistor. (b) Power density measured over an hour as the humidity was ramped up from 30 % RH to 80 % RH. (c) Power density for hygroelectric devices composed of OmcZ and OmcS nanowires, plotted against relative humidity. The dashed lines are exponential fits to the data. (d) Current-voltage response measured across the thickness of the OmcZ film. The data were collected at various scan rates. (e-h) EIS Bode plot of the OmcZ film, measured across the film thickness. The films were measured at DC offsets of (e) -0.5 V, (f) 0 V, (g) OCP of 0.5 V, and (h) 1 V. Insets are the Nyquist plots. Black lines are fits to the model circuit in Fig. 2a. (i) Cartoon model of nanowire film, connected to a load resistor, under anaerobic conditions. There is a buildup of reduced hemes (electrons), neutralizing the proton gradient. (j) Cartoon model of the nanowire film, connected to a load resistor, under aerobic conditions. Oxygen is reduced to water, maintaining all hemes in an oxidized state. (k) Power density, measured over 2 hours, under anaerobic conditions from 10 min to 80 min and aerobic conditions from 80 min to the end.

resistance at voltages greater than the OCP indicates we are driving current against an internal gradient. The aerobic ambient environment precludes a gradient of reduced hemes, and films are prepared in a non-ionic buffer, therefore, the gradient is most likely composed of protons.

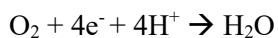
At high scan rates, we observed hysteresis between anodic (increasing bias) and cathodic (decreasing bias) scans. Notably, at the highest scan rates (> 1 V/sec), there was a peak in the anodic scan (Figure 5.4d). EIS revealed that this is the result of restructuring of the internal gradient. When performed with a DC voltage offset less than the OCP, the films behaved like a pure electronic resistor (Figure 5.4e-f). At the OCP, the film still behaved like an electronic resistor, but with an increased impedance. However, when EIS was performed at a DC voltage offset greater than the OCP, we observed ambipolar characteristics, similar to our measurements along the bottom of the films (Figure 5.2). These data demonstrate that when an external bias greater than the OCP is applied, protons migrate against their gradient to offset the charge of the mobile electrons.

At sufficiently high scan rates, a full cathodic scan can be performed before the proton gradient re-equilibrates. We therefore attribute the peak in the anodic scan of the 5 V/sec current-voltage curve to the re-equilibration of the proton gradient, with the peak position indicating the timescale of this process. We used this information to calculate the proton mobility required to support re-equilibration of the gradient (Supplementary Figure 5.4; see Methods for details) and obtained a value of $2.97 \times 10^{-5} \pm 3.9 \times 10^{-6}$ cm²/V·s (mean \pm s.e.m.). This contrasts with the mobility obtained from back-gating (Figure 5.3c), likely due to the de-coupling of the electrons and protons when measuring in this configuration.

Our evidence of the existence of a proton gradient as well as the high proton mobility within the films demonstrates the mechanism by which cytochrome nanowire can generate power under ambient humidity. However, as batteries discharge, the gradient driving the current is expected to break down, resulting in a decay of power with time. Nanowire hygroelectric devices are no exception. In a closed system, when the device is sealed from the environment, power density decays¹⁴⁶. This is likely due to reduction of hemes by the top electrode (cathode) (Figure 5.4i) which would neutralize the proton gradient. Under open conditions, with an air atmosphere, the

hemes would be oxidized by atmospheric oxygen (O₂), thus maintaining the gradient (Figure 5.4j). To test this, we measured power density under an N₂ atmosphere, with a constant supply of gas (Figure 5.4k). As the chamber was deoxygenated, power density decayed continuously over the course of 65 minutes. We then replaced the N₂ atmosphere with air and observed a rapid rise in power density followed by a steady power output for the duration of the experiment. These data strongly support a central role of atmospheric oxygen in maintaining the potential of the nanowire device.

The reduction of oxygen by the c-type hemes of OmcZ likely proceeds via the 4-electron reaction in which 4 moles of electrons and 4 moles of protons are consumed per mole of O₂, to produce one mole of water:



The steady-state power output measured at 60 % RH corresponds to the flow of 457 nA of current. This corresponds to the consumption of 1.18 pmol of O₂ per second, and 4.7 pmol of protons per second. Assuming all O₂ and H⁺ adsorbed into the film are consumed, we estimate oxygen and protons are replaced at a rate of 0.13 mmol/sec and 0.94 nmol/sec, respectively (see Methods for details). Therefore, we conclude that regeneration of the potential is limited by proton availability. These mechanistic details outline key principles as well as the limitations underlying moisture-based power generation using cytochrome nanowires. We have demonstrated a direct link between transport properties and power generation, establishing a platform for rational design of the next generation of protein-based electronics.

5.5 Materials and Methods

5.5.1. Nanowire sample preparation

OmcZ and OmcS nanowire samples were prepared as described^{43,60}. To adjust the pH of the nanowire preparation to pH 10.5, the nanowires were dialyzed against 20 mM ethanolamine pH 10.5 overnight.

For transport measurements, 0.5 μl of sample was dropped on the center of the van der Pauw electrodes and allowed to dry overnight in a desiccator. Cytochrome nanowire hygroelectric devices were prepared as described¹⁴⁶. Briefly, a polydimethylsiloxane (PDMS) well with a radius of 2 mm was fixed to an IDA electrode. The electrode was placed on a hot plate at 60 °C. A total of 12 μl of OmcZ (at 4 μM concentration) or OmcS (at 25 μM concentration) was deposited in two 6 μl drops in the PDMS well and allowed to dry.

5.5.2. Electrode design and fabrication

Two types of electrodes were used in this study. All transport measurements were performed using gold van der Pauw electrodes, while the hygroelectric power experiments were performed using gold interdigitated array (IDA) electrodes. The IDA electrodes had spacings of either 3 μm or 5 μm . However, since these electrodes were being used as a simple gold surface, all connections were shorted together.

Both types of electrodes were prepared as described previously¹⁵⁷. Briefly, the electrodes were fabricated using UV-Lithography on thermally oxidized Silicon wafers. This resulted in a 300 nm silicon dioxide layer, which served as the insulation between the van der Pauw contacts as well as the dielectric for the back-gating experiments. The gold contacts were fabricated by spin coating a double resist, which was then exposed to UV radiation through a shadow mask and developed for 2 minutes. The photoresists were metalized using 5 nm Ti or Cr and 30-60 nm of gold. Finally, a lift-off in 80-120° C NMP removed the metalized resists. A protective coating was spin coated onto the devices, which was washed off with acetone prior to use.

5.5.3. Humidity variation

For the DC conductivity, EIS, charge mobility, and humidity dependence of power density measurements relative humidity was varied by pumping humid air into a glovebox (Coy Lab) using compressed air. RH was monitored using a hygrometer (Fisherbrand).

For the anaerobic power generation measurement, a solution of saturated sodium chloride was sparged with N₂ gas for 3 hours prior to moving the solution into the glove box. The solution was constantly bubbled with N₂ or air throughout the measurements. This generated an environment with 60 % RH. The humidity was stable for the duration of the experiment.

5.5.4. Electrical (DC) conductivity measurements

DC electrical conductivity measurements were performed in a four-probe, van der Pauw electrode geometry using a semiconductor Parameter Analyzer (Kiethley 4200A-SCS), providing 0.1 fA current resolution and 0.5 μ V voltage resolution. Measurements were conducted according to the van der Pauw method¹⁴⁹. Briefly, current was driven across one side of the device while the voltage difference between the two electrodes on the other side of the device was measured. The voltage was allowed to settle over 1-3 minutes. Current-voltage curves were assembled with at least four points including both positive and negative currents. This was repeated for each of the four orientations of the electrode. The sheet resistance was determined by solving the van der Pauw equation,

$$e^{\frac{-\pi R_{vertical}}{R_{sheet}}} + e^{\frac{-\pi R_{horizontal}}{R_{sheet}}} = 1 \quad (5.1)$$

where, $R_{vertical}$ is the average of the resistance measured between contacts 1 and 2, and contacts 3 and 4 and $R_{horizontal}$ is the resistance measured between contacts 2 and 3 and contacts 1 and 4 (Fig. 1c). The van der Pauw equation was solved using the bisection method, implemented in a custom Python script. The sheet resistance was converted to conductivity using the equation,

$$\sigma = \frac{1}{R_{sheet}d} \quad (5.2)$$

where, d is the film thickness, measured using optical profilometry. For all DC conductivity measurements, at least 3 samples were measured.

For the kinetic isotope effect measurements, van der Pauw electrodes were placed on a sample puck and inserted into a sample wiring test station (QuantumDesign). Electrical contact

with the van der Pauw electrode were made by creating wire bonds between the electrode contacts and the sample puck using the operator-guided wedge-wedge wire bonded (West Bond), which uses ultrasonic energy to attach aluminum wire to metal contacts. A custom, small humidity chamber was made from PDMS and fitted to the sample wiring test station. 1 ml of Milli-Q water (Millipore) or deuterium oxide (Cambridge Isotope Labs) was placed in the chamber. The sample was allowed to sit for 30 minutes to allow humidity to fill the chamber. Conductivity was measured by connecting the Parameter Analyzer to the sample wiring test station using triax-to-banana cable adapters.

The chamber was too small to fit our hygrometer, so we do not know the exact RH during the KIE measurements. However, based on the magnitude of the conductivity we measured, we estimate the humidity was close to 75 % to 80 % RH.

5.5.5. Charge mobility measurements

Field effect transistor devices were fabricated by scratching the back of the van der Pauw electrode wafers with a diamond scrubber. Electrical connection to the n-doped silicon of the van der Pauw electrode wafer was achieved by adhering a plain gold electrode to the wafer using silver epoxy.

Measurements were performed using a semiconductor Parameter Analyzer (Kiethley 4200A-SCS). Since we only have four preamplifiers for our Parameter Analyzer, the current drain was replaced with the ground unit. We measured a current voltage curve using the ground unit as the current drain and compared to a current voltage curve measured with the current drain held at 0 V to assure this would provide comparable results. The now free, fourth preamplifier channel was used to control the gate voltage. The gate current was monitored throughout the experiment to make sure the 300 nm SiO₂ layer did not breakdown or there was not significant leakage current.

We measured current-voltage curves at each gate voltage, providing 90 seconds for the measured voltage drop at each current value to settle. The sheet conductance of the device was determined as described under “Electrical (DC) Conductivity Measurements” and was plotted against gate voltage. The mobility was determined using the equation

$$\mu = \frac{1}{C_i} \frac{dG_S}{dV_G} \quad (5.3)$$

where, C_i is the specific capacitance of the 300 nm SiO₂ oxide layer, G_S is the sheet conductance, and V_G is the gate voltage. The specific capacitance was calculated using the equation $C_i = \epsilon\epsilon_0/d$, where ϵ is the dielectric of SiO₂ ($\epsilon = 3.8$), ϵ_0 is the permittivity of free space ($\epsilon_0 = 8.85$ pF/m), and d is the thickness of the oxide layer. The slope of the sheet conductance (dG_S/dV_G) was determined by fitting a line to the steepest part of the sigmoidal dependence of the conductance on the gate voltage. This analysis was performed using Igor Pro software (WaveMetrics Inc.).

5.5.6. Temperature variation conductivity measurements

As described previously³, we used a Physical Property Measurement System (PPMS) (DynaCool, Quantum Design) to vary the temperature of a sample stage. Electrical contacts between the van der Pauw electrode and the sample stage were made by creating wire bonds between the electrodes and the pads of the sample stage using the operator guided wedge-wedge wire bonder (West Bonder). After loading the sample to the PPMS the chamber was purged three times, maintaining a minimal RH. All measurements were performed under ambient atmospheric pressure.

5.5.7. Electrochemical impedance spectroscopy

Electrochemical impedance spectroscopy (EIS) and fast scan rate current voltage curves were obtained with a Gamry Potentiostat (Gamry Instruments). For EIS, the frequency of the AC

signal was scanned from 1 MHz to 5 mHz. For the two electrode measurements, the working and working source connections were connected to one electrode contact and the reference and counter connections were connected to the other. For the four electrode measurements, the current source and current drain were connected to the working and counter connections, respectively. The working source and reference served as the voltmeter. Fitting of the equivalent circuit to the data was achieved using the Gamry Echem Analyst™ software.

5.5.8. Hygroelectric power experiments

Thick cytochrome nanowire films ($>1 \mu\text{m}$) were sandwiched between the gold IDA electrodes, upon which the films were deposited, and a 1 mm strip of aluminum foil. The open circuit potential was determined by obtaining a current voltage curve using a semiconductor Parameter Analyzer (Kiethley 4200A-SCS). The two electrodes were then attached to a 220 k Ω load resistor. We used the parameter analyzer to measure the voltage drop across the resistor. The power density was computed using the equation

$$Pd = \frac{V_{OCP}V_{drop}}{R_{load}A} \quad (5.4)$$

where, V_{OCP} is the open circuit potential, V_{drop} is the voltage drop across the load resistor, R_{load} is the resistance of the load resistor, and A is the area of the bottom electrode, coated by nanowires. The area of our IDA electrodes is 3 mm x 3 mm = 9 mm².

5.5.9. Calculation of proton mobility from high scan rate current-voltage response

The current voltage response of the thick OmcZ films in the hygroelectric devices, measured from top to bottom, demonstrated hysteresis when measured in cycles at high scan rates. Notably, the anodic (scanning from negative to positive) and cathodic (scanning from positive to negative) curves converged at a potential close to the open circuit potential of the device. The hysteresis was asymmetric around this point with potentials less than the OCP

displaying a much larger difference between anodic and cathodic current. Also, for sufficiently high scan rates (approx. ≥ 1 V/s) we observed a peak in the anodic scan at negative potentials.

EIS data collected at potentials greater than the OCP revealed a restructuring of the proton gradient (Figure 5.4h). Therefore, we attribute the increased hysteresis at potentials less than OCP to the migration of protons within the device. This is consistent with the observation of a negative shifted OCP for the cathodic scan (x-intercept). The peak in current in the anodic scan corresponds to the time at which the proton gradient equilibrates to its resting state, thus maximizing the internal driving force for electrons traversing the device.

We have identified three data points within our scans, which we have used to extract the proton mobility. 1) The OCP of the device, measured in the anodic scan (V_{OCP}^A). 2) The OCP of the device, measured in the cathodic scan (V_{OCP}^C). 3) The potential at which we observe the peak in the anodic scan (V_p). We then used Fick's law,

$$J = -D \frac{dc}{dx} \quad (5.5)$$

to extract the proton mobility, as follows:

The concentration gradient which drives proton re-equilibration comes from the hydration gradient in the film. This can be estimated using V_{OCP}^A . We can use a Boltzmann distribution to determine the ratio of the number of protons in the top and bottom halves of the device:

$$\frac{[H_{top}^+]}{[H_{bottom}^+]} = \exp\left(\frac{V_{OCP}^A}{k_B T}\right) \quad (5.6)$$

The concentration gradient can then be computed as the difference between the number of protons in the bottom and top of the film divided by the thickness of the film:

$$\frac{dc}{dx} = \frac{[H_{bottom}^+] - [H_{top}^+]}{dx} \quad (5.7)$$

where, dx is the thickness of the film, measured by optical profilometry ($\sim 9 \mu\text{m}$). The restructuring of the proton gradient can be computed by plugging V_{OCP}^C into Equation (5.6). To compute the proton flux, we need the number of protons which migrate across the device to re-equilibrate the OCP, and we need the time required for this process to occur. The number of migrating protons is given by the difference in the number of moles at the bottom of the device obtained from the two OCP values. The re-equilibration time is given by

$$\tau = \frac{|(V_{lim}^{neg} - V_{OCP}^C) + (V_{lim}^{neg} - V_P)|}{\nu} \quad (5.8)$$

where, V_{lim}^{neg} is the negative limit of the voltage scan (-1 V for our experiments) and ν is the scan rate.

When we divide the flux by the concentration gradient, we obtain an expression for the diffusion coefficient which depends only on the proton ratios computed from Equation (5.6), the thickness of the film, and the re-equilibration time:

$$D = -\frac{(dx)^2}{\tau} \frac{r_A + r_C}{(1 - r_A)(1 + r_C)} \quad (5.9)$$

where, r_A and r_C are the ratios of protons in the top and bottom of the film computed from Eq. (6) using V_{OCP}^A and V_{OCP}^C , respectively. Finally, after plugging the flux and concentration gradient into Equation (5.5), we can convert the diffusion coefficient (D) into proton mobility.

$$\mu = \frac{eD}{k_B T} \quad (5.10)$$

where, e is the elementary charge, k_B is the Boltzmann constant, and T is the temperature at which the experiment was conducted (293 K).

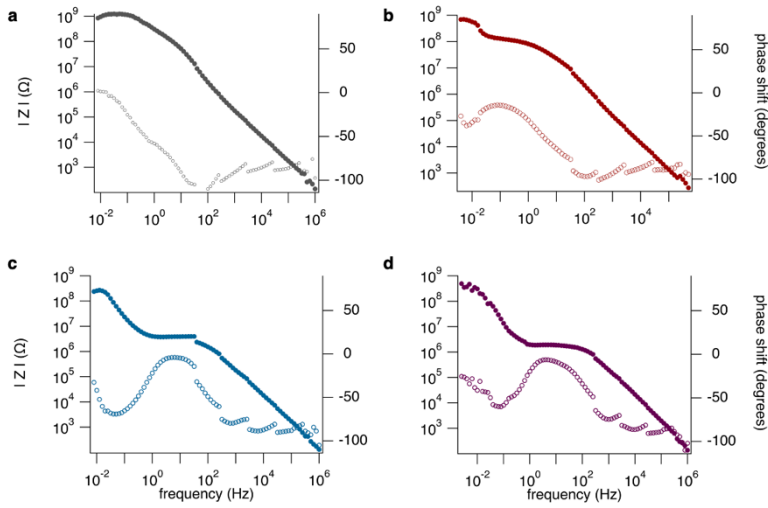
This analysis can only be performed on data which show a peak in the anodic scan. For the OmcZ nanowire films, we observed a peak for scan rates greater than 1 V/s . It is also important to minimize the effect of capacitive current, which increases with increasing scan rate. Notably, we observe a linear increase in the computed mobility with scan rate (Extended Data Fig. 4), which we attribute to capacitive effects. Capacitive contributions are minimal at a scan

rate of 1 V/s, which is highlighted by the minimal hysteresis between anodic and cathodic scans for potentials greater than the OCP (Supplementary Figure 5.4a).

5.5.10. Calculation of consumption rate for O₂ and H⁺

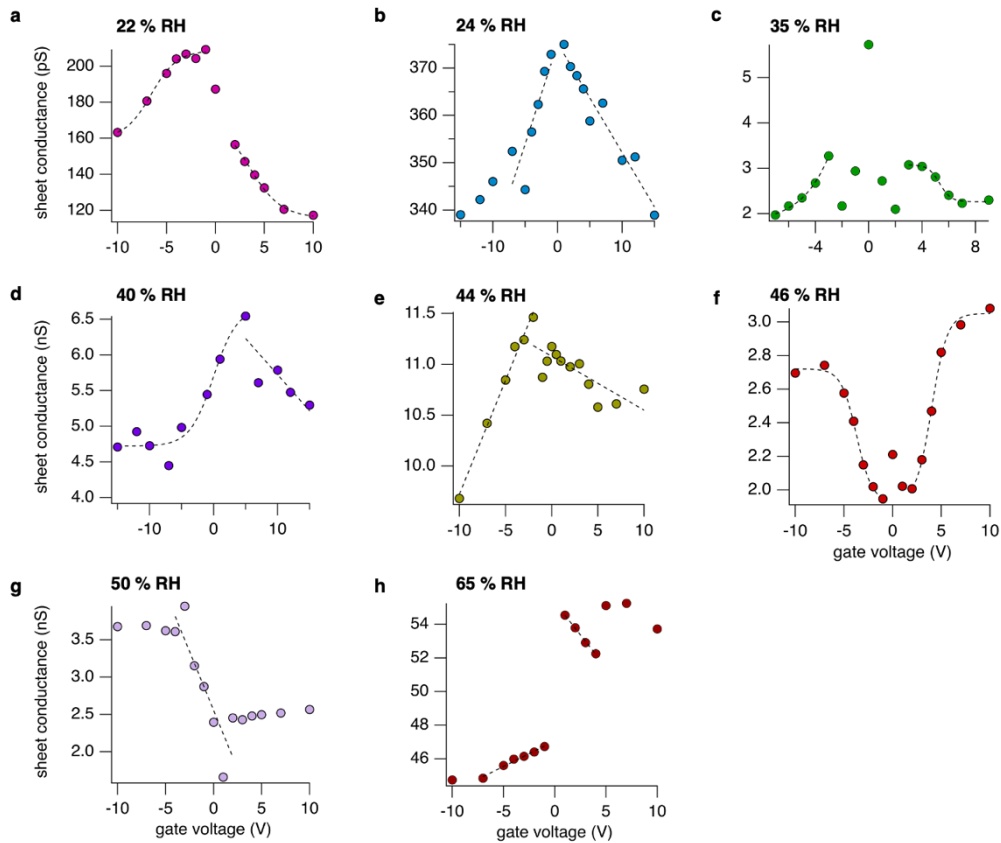
To obtain an estimate of the rate at which protons and atmospheric oxygen are replaced within the protein film, we used Equation 5.5 to compute flux. At room temperature, the diffusion constant of gasses in air is approximately 0.2 cm²/s. The concentration of O₂ is approximately 8.048 mM and the concentration of protons (at 60 % RH) is approximately 60 nM. Assuming the concentration of O₂ and H⁺ is zero at the bottom of the film, we calculate the concentration gradient by dividing the concentrations in air by the thickness of the film. We multiply these values by the diffusion constant and obtain a flux. We multiply the flux by the area of the film to obtain the rate at which protons and O₂ are replaced.

5.6 Supplementary Information



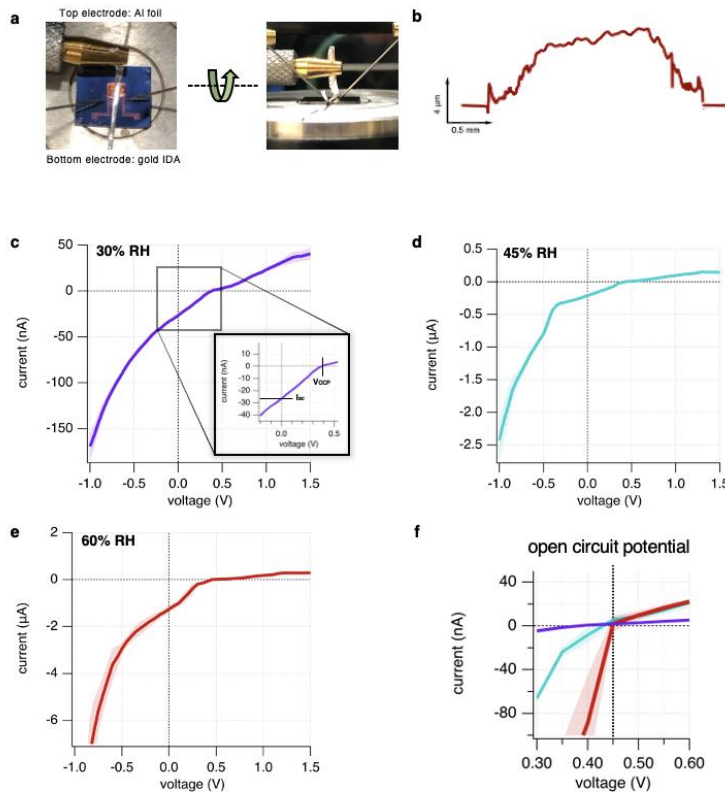
Supplementary Figure 5.1: 4-probe EIS Bode plots.

(a-d) Bode plot for OmcZ measured in a 4-probe configuration on a van der Pauw electrode with 500 μm electrode spacing. Measurements were performed at (a) 30 %, (b) 45 %, (c) 55 %, and (d) 65 % RH.



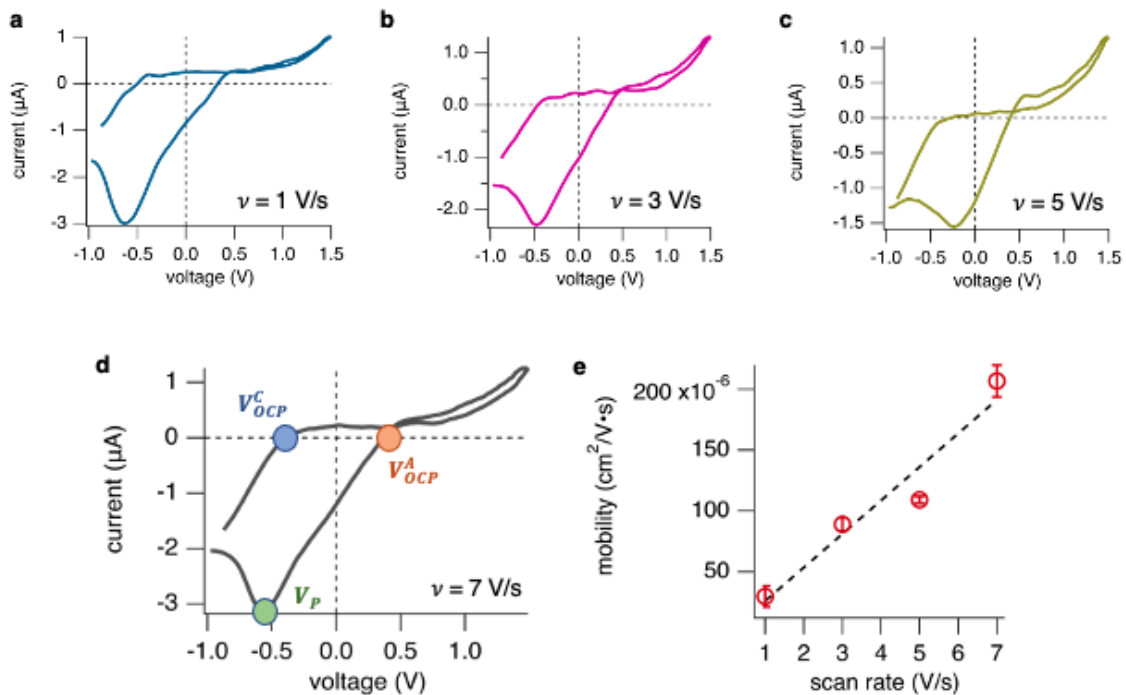
Supplementary Figure 5.2: Field-effect back gating repeats.

(a-h) Sheet conductance of OmcZ films measured at gate voltages ranging from -10 to 10 V. The plots are labeled with the relative humidity at which they were measured.



Supplementary Figure 5.4: Hydroelectric power device characterization.

(a) Photo of hydroelectric power device with an OmcZ film sandwiched between a gold interdigitated electrode and a strip of aluminum foil. (b) Optical profile of an OmcZ film, used to determine the thickness of the films. (c-e) Current-voltage response of the OmcZ film, measured across its thickness, measured at (c) 30 %, (d) 45 %, and (e) 60 % RH. Inset of panel (c) highlights the open circuit potential (V_{OCP}) and the short-circuit current (I_{sc}). (f) Zoom in on the open circuit potential for all three humidity conditions.



Supplementary Figure 5.3: High scan-rate current voltage response.

(a-d) Cyclic current-voltage response of OmcZ measured across the film thickness, measured at (a) 1 V/s, (b) 3 V/s, (c) 5 V/s, (d) 7 V/s. Panel (d) highlights the positions at which the three variables which are used to compute mobility are extracted. (e) Mobility calculated from the current-voltage response at varying scan rates.

6. Mechanism of charge transport in non-cytochrome proteins

This chapter will examine charge transport in protein systems beyond cytochrome nanowires. I will cover the charge transport properties of synthetic amyloid peptide crystals, consensus tetratricopeptide repeat (CTPR) proteins, and bacterial pili filaments, all of which use aromatic amino acids, such as tyrosine and tryptophan as redox centers to mediate successive donor-acceptor charge transfer reactions. In contrast to the heme-based cytochrome nanowires discussed in the previous chapters, oxidation of tyrosine or tryptophan creates unstable radicals. I will present evidence that hydrogen bonds in local protein environments as well as coupling between aromatics via the peptide backbone stabilize these radicals, enabling charges to be transported over long distances without be lost to the solvent.

6.1 Amyloid crystals with stacked tyrosines conduct via hole hopping coupled to proton rocking

Intrinsic electronic conductivity of individual atomically resolved amyloid crystals reveals micrometer-long hole hopping via tyrosines

Catharine Shippo, H. Ray Kelly, Peter J. Dahl, Sophia M. Yi, Dennis Vu, David Boyer, Calina Glynn, Machael R. Sawaya, David Eisenberg, Victor S. Batista, and Nikhil S. Malvankar

This section is adapted from a paper published in The Proceedings of the National Academy of Sciences (PNAS)³.

DOI: <https://doi.org/10.1073/pnas.2014139118>

6.1.1. Author contributions

C.S, V.B, and N.M designed research; C.S., H.R.K, P.D., and S.Y. performed research; M.S., D.B., C.G, and D.E. contributed new reagents/analytical tools; C.S., H.R.K., P.D., and N. M. analyzed data; and C.S. and N.M. wrote the paper.

6.1.2. Introduction

The field of biological charge transport has long treated proteins as insulating, requiring the binding of transition metal complexes to engage in redox processes and long-range charge transport. In the absence of redox centers, where charges can be transiently localized during transport, charge transport is limited to approximately 25 Å allowed by single step tunneling¹⁵⁸. The amino acids tyrosine and tryptophan have been demonstrated to serve as redox centers for charge transport in systems such as Photosystem II and ribonucleotide reductase^{158,159}. Therefore, it follows that an extended system of stacked tyrosine or tryptophan residues should be capable of supporting long-range charge transport in a manner similar to that of cytochrome nanowires⁴⁴. To test this hypothesis, my colleagues Catharine Shipps and Sophia Yi performed measurements of the electrical conductivity of amyloid peptide crystals which contained stacked tyrosine residues along their long-axis. Their experiments demonstrated that the crystals required stacked tyrosines as well as a Zn^{2+} ion to support electrical conductivity³. In the following section I will describe how I used molecular dynamics simulations to elucidate the role of Zn^{2+} and the resulting mechanism of charge transport in amyloid crystals.

6.1.3. Results

Electrical conductivities were measured for four amyloid peptide crystals, each defined by a unique peptide sequence: X1 – NNQQNY w/ Zn^{2+} ; X2 – GNNQQNY; X3 – GGVLVN w/ Zn^{2+} ; and X4 – KVQIINKKL. High resolution structures have been determined for all four crystals, allowing for interrogation of the structure-function relationship using molecular modelling. The conductivity measurements were performed in a 4-probe configuration in which current is applied to the two outer electrodes, and the two inner electrodes are used to measure the voltage drop. In this configuration, the intrinsic conductivity of the sample can be measured, free from artifacts caused by electrode polarization or contact resistance¹⁶⁰. These measurements revealed that the X1 crystal had the highest conductivity ($\sim 3.5 \mu S/cm$). The X2 crystal also demonstrated some

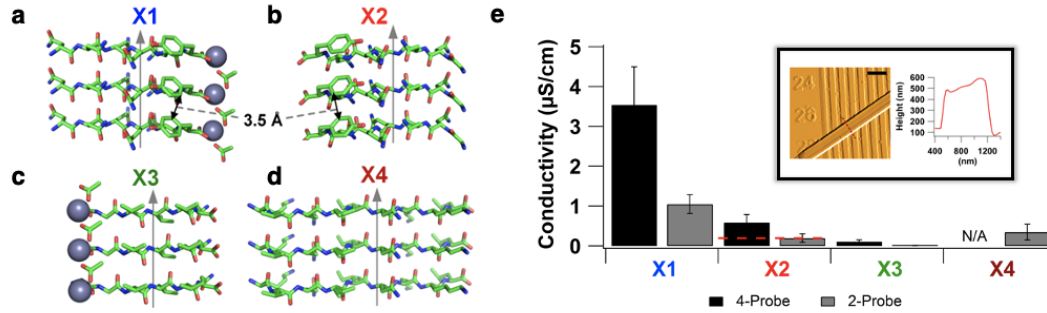


Figure 6.1: Stacked tyrosines and coordinating Zn^{2+} ions are required for conductivity. (a) Model of the X1 crystal structure with sequence NNQQNY. The Zn^{2+} ions are shown as grey spheres. The arrow indicates the fibril axis. (b) Model of the X2 crystal structure with sequence GNNQQNY. The arrow indicates the fibril axis. (c) Model of the X3 crystal structure with sequence GGVLVN. The Zn^{2+} ions are shown as grey spheres. The arrow indicates the fibril axis. (d) Model of the X4 crystal structure with sequence KVQIINKKL. The arrow indicates the fibril axis. (e) Electrical conductivity of the X1 – X4 amyloid peptide crystals, measured in both a 4-probe and 2-probe geometry. The inset is an AFM image of X1 crystal spanning a nanoelectrode device and the height profile of that crystal. This figure is adapted from Figures 1 and 2 from Shipps et al. *Proc. Nat. Acad. Sci.* (2021)³.

conductivity ($\sim 0.8 \mu\text{S/cm}$), however, the X3 and X4 crystals, which lacked tyrosine residues, showed very low conductivity ($< 0.1 \mu\text{S/cm}$) (Figure 6.1). This result demonstrates the necessity of tyrosine in conferring conductivity, but also raises an important question. What role does Zn^{2+} , an ion which lacks redox activity, serve in promoting a 4-fold increase in the conductivity of the X1 crystal, relative to X2.

To address this question, I ran molecular dynamics simulations of the X1 and X2 crystals. Since the rate of charge transfer is largely determined by the electronic coupling, a term which is exponentially dependent on the distance between donor and acceptor ($(|H_{AB}|^2)^{1/2} = A \exp\left(-\frac{\beta}{2}(r - r_0)\right)$)¹²⁸, I analyzed the distribution of the distances between stacked tyrosines. The analysis revealed a wider range of distances for the X2 crystal than for X1. This suggests that in the X1 crystal, the Zn^{2+} ion stabilizes the structure of the crystal, and keeps the tyrosine residues stacked within van der Waals contact.

I also analyzed the distances between the hydroxyl oxygen of the tyrosine and the amide oxygen and nitrogen atoms of a neighboring glutamine residue. Electron transfer via tyrosine

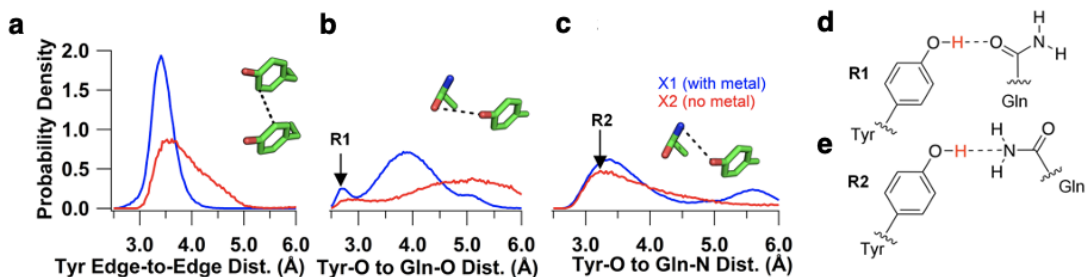


Figure 6.2: The Zn^{2+} ion stabilizes the X1 structure.

(a) Histogram of the nearest-atom distances between stacked tyrosines. The tyrosines in the X1 crystal, which has a Zn^{2+} ion, are closer together and do not drift apart. In contrast the distribution for the the X2 crystal is skewed demonstrating that the structure can fluctuate away from an ideal stacking geometry. (b) Histogram of distances between the tyrosine hydroxyl oxygen and the glutamine amide-oxygen. The X1 crystal has a population of configurations in which the amide-oxygen is in hydrogen bonding distance of the tyrosine (R1 configuration). (c) Histogram of distances between the tyrosine hydroxyl oxygen and the glutamine amide-nitrogen. There is a peak showing a population of configurations in which the amide-nitrogen is in hydrogen bonding distance from the tyrosine (R2 configuration). (d) Chemical representation of the R1 configuration. (e) Chemical representation of the R2 configuration. This figure is adapted from Figures 3 from Shipps et al. *Proc. Nat. Acad. Sci.* (2021)³.

necessarily occurs via proton coupled electron transfer (PCET). This is because tyrosine, in its oxidized form, has a pKa around -2, about 12 pKa units lower than in its pKa when reduced¹⁶¹. The presence of hydrogen bond acceptors in the direct vicinity of the stacked tyrosine chain is a strong indicator that a PCET reaction is occurring. The distance analysis revealed that there existed a population of states in which the amide oxygen of the glutamine was 2.7 Å from the tyrosine hydroxyl oxygen, putting the tyrosine and glutamine in an ideal hydrogen bonding configuration (Figure 6.2). This was labeled the rotamer 1 (R1) state. This population was not clearly present in the X2 crystal, further supporting the structural role of the Zn^{2+} ion. The amide nitrogen also formed hydrogen bonds with the tyrosine. This was labeled the rotamer 2 (R2) state. However, the distance between the tyrosine hydroxyl oxygen and the amide nitrogen of the glutamine was greater than for the R1 state, which suggests that the R1 state is preferred for the PCET reaction. This was further supported by DFT calculations which revealed barrierless proton transfer in the oxidized R1 state of the system.

PCET reactions can occur by three different reaction mechanisms. 1) electron transfer followed by proton transfer (ETPT); 2) proton transfer followed by electron transfer (PTET); or concerted electron-proton transfer (CEPT). Discerning which mechanism is utilized by a

particular system can be challenging, and often requires measurement of the kinetic isotope effect. However, the PTET mechanism can be immediately disregarded as the pKa of reduced tyrosine would prohibit proton dissociation at neutral pH. To distinguish between the remaining two mechanisms, the conductivity of the X1 crystal was measured under varying temperature.

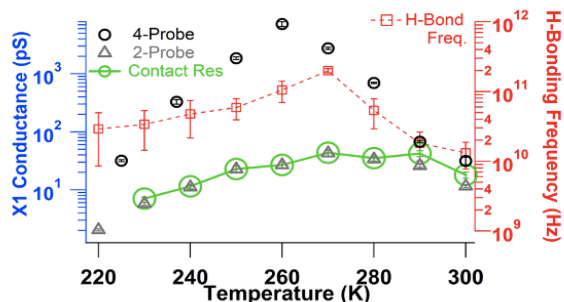


Figure 6.3: Conductivity in X1 is limited by proton acceptor availability.

Temperature dependence of the conductivity of the X1 crystal measured in the 4-probe and 2-probe configurations. The red points are the frequencies of an R1 hydrogen bond being formed at various temperatures. These data show that the temperature dependence of the R1 geometry follows the same trend as the conductivity. This figure was adapted from Figure 6 from Shipp's et al. *Proc Nat Acad Sci* (2021)³.

The data revealed that upon cooling from 300 K, the conductivity increased exponentially until the temperature reached 260 K. Upon further cooling, the conductivity decreased exponentially (Figure 6.3). Molecular dynamics simulations, run at various temperatures, revealed that the frequency at which a hydrogen bond was formed between the tyrosine hydroxyl oxygen and the amide oxygen followed the same trend as the conductivity (Figure 6.3). From these data, we concluded that electron transport along the stacked tyrosines is limited by proton availability. Therefore, charge transfer between tyrosines likely occurs via a CEPT mechanism where the oxidation of tyrosine is coupled to the rocking of its proton between its hydroxyl oxygen and its hydrogen bond acceptor. This is further supported by a DFT potential energy scan (performed by H. Ray Kelly) which demonstrated barrierless proton transfer to the amide oxygen of the neighboring glutamine when the tyrosine was in its oxidized state.

6.1.4. Discussion

This work demonstrated that stacked aromatic amino acids can confer long-range conductivity and provided convincing evidence that charge transport along stacked tyrosines occurs by a hole-hopping mechanism with proton rocking. However, in comparison to heme-

based nanowires, the conductivity of amyloid crystals is very low (>1000 fold lower than the OmcS nanowire)^{43,44}. The close stacking arrangement of the tyrosines should optimize the electronic coupling between sites. The low conductivity suggests this coupling is lower than anticipated, or there is a high reorganization energy for hole transfer between sites.

During my time at Yale, several papers from the lab of Stuart Lindsay^{1,71,72}, as well as one from our own lab⁵² have shown high conductance in non-heme protein systems. In these systems, charge transport is assumed to occur via aromatic amino acids, but their structures lack aromatic stacking within 3-4 Å. In the next two sections, I will discuss these systems along with some results of my own which suggest that the peptide backbone of the protein enhances coupling between aromatics.

6.2 Electronic coupling is enhanced by through-bond tunnelling pathways

6.2.1. Introduction

The consensus tetratricopeptide repeats (CTPR) protein system has emerged as a useful model system for understanding the conductivity of non-heme protein nanowires. CTPR proteins are composed of repeated helix-turn-helix motifs which stack on each other. By increasing the number of repeats, the length of the protein can be tuned. Zhang et al.¹ generated a series of these repeats including 4, 8, 12, 16, or 20 helix-turn-helix motifs and measured their conductance using the scanning tunneling microscopy (STM) break-junction technique¹. They revealed conductance values ranging from ~1.3 nS for the shortest protein containing 4 motifs (CTPR4) to ~3.7 nS for the longest protein containing 20 motifs (CTPR20). The length dependence of the resistance of the proteins could be fit to either an exponential or a square-law dependence. For the square-law dependence, which describes diffusive hopping under low bias, the resistance can be fit to $R(L) = R_0 + aL^2$, where R_0 is the resistance at zero length, L is the length of the protein wire, and a is related to the hopping rate¹⁶².

A computational study of this system attributed the high conductance measured by experiment to low reorganization energies, a product of non-ergodic sampling of the conformational space of the protein¹². This study also concludes that for many pairs of aromatic residues the electron transfer rate is independent of the electronic coupling, and that the distance dependence of the measured resistance is a result of the diffusion of charges along multiple paths under weak bias. However, this conclusion was made without directly computing electronic coupling. Furthermore, measurements on other non-cytochrome protein systems have demonstrated that conductivity can be strongly influenced by decreasing the distance between aromatic sites⁵², a perturbation which has the strongest effect on the electronic coupling. To address the contribution of the electronic coupling in the electron transfer rate in CTPR proteins, I used DFT to compute electronic coupling values in CTPR8 and evaluated the ability of the non-adiabatic Marcus ET rate explain the experimentally measured conductance.

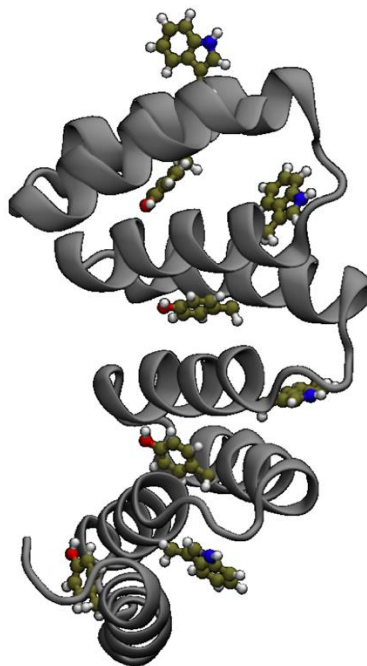


Figure 6.4: CTPR proteins use tyrosine and tryptophan residues to transport charge.

Image of CTPR8 with the tyrosine and tryptophan residues which have intra-protein hydrogen bonding partners displayed as ball-and-stick models.

6.2.2. Results

Electron transport along CTPR proteins is proposed to occur via a series of hops between tyrosine and tryptophan residues. Our prior work on charge transport in amyloid crystals demonstrated that charge transport via aromatics, such as tyrosine, is limited by the availability of hydrogen bond acceptors³. The hydrogen bond enables a concerted proton coupled electron transfer mechanism, which stabilizes the oxidized state of the tyrosine or tryptophan. In its absence, tyrosine or tryptophan oxidation results in either a high potential cation radical with a

low pKa ($pK_{OX}^Y = -2$; $pK_{OX}^W = 3$) or the proton is transferred to water. When transferred to water, the reaction can be very slow¹⁰⁵, which would prohibit rapid electron exchange.

To model charge transport in CTPR8, we ran molecular dynamics simulations under the NPT ensemble at 310 K to sample configurations. We used the VMD H-Bonds plugin to identify the tyrosine and tryptophan residues which formed hydrogen bonds within the protein. From this analysis we obtained only two residues, a tyrosine and tryptophan, which formed any hydrogen bonds with other amino acid residues: Tyrosine 58 formed a hydrogen bond with asparagine 43 for 71 % of the 200 ns simulation, and tryptophan 72 formed a hydrogen bond with the backbone of proline 66 for 40 % of the simulation. To simulate the oxidized state of tyrosine or tryptophan, we used modified partial charges for the cation radical state of the residue.

We used QM/MM calculations with electrostatic embedding to compute reduction potentials for tyrosine 58 and tryptophan 72. A selection of 400 snapshots were chosen and calculations were set up such that the hydrogen bonding partner for each residue was included in the QM layer. The system was then optimized, with relaxed tolerances such that the protons could relax. In the absence of an optimization, proton transfer in response to oxidation would not be able to occur, as the MM force field does not allow for bonds to break. The reduction potentials were then computed in the linear response regime (See Chapter 2).

Our calculations predicted a reduction potential of 798 mV vs. SHE for tyrosine 58 and 855 mV vs SHE for tryptophan 72. Using the QM/MM energies we also computed reorganization energies. Oxidation of tyrosine 58 had a reorganization energy of 0.634 eV, and oxidation of tryptophan 72 had a reorganization energy of 0.776 eV. These values are considerably higher than those computed by Krishnan et al¹². However, it is notable that our sampling was limited to 400 snapshots from a 200 ns simulation whereas Krishnan et al. sampled over 750 ns. Since the work of Matyushov has demonstrated that reorganization energy can be heavily influenced by the amount of sampling^{11,12,15,87}, we will use a value of 0.3 eV, consistent with the value obtained by Krishnan et al¹².

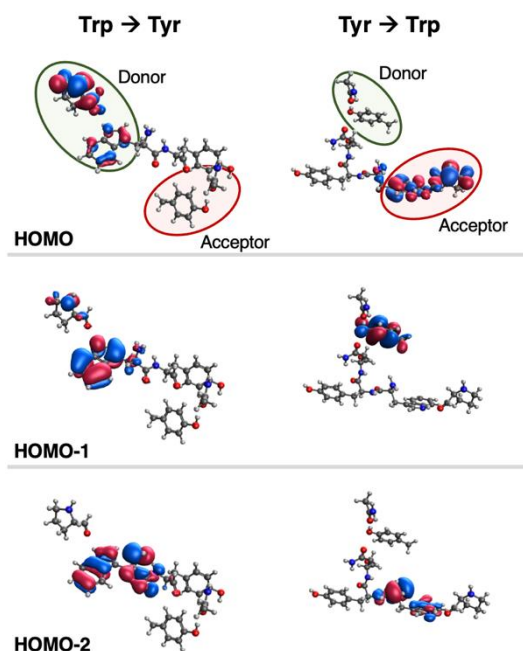


Figure 6.5: Mixing of frontier orbitals supports high electronic coupling.

The electronic coupling was computed using the CDFT-CI method in the Q-Chem software package. Rather than isolating the tyrosine and tryptophan residues for the coupling calculation, we used the VMD pathways¹⁶³ plugin to identify the most likely ET path connecting the residues. All residues identified by the pathways analysis were included in the coupling calculation. The results of the coupling calculation revealed that, when a tunneling pathway was present, hole transfer from tyrosine 58 to tryptophan 72 has a root mean squared coupling of 4.60 ± 0.2 meV

(error is s.e.m.), and hole transfer from tryptophan 72 to tyrosine 92 (equivalent to Tyr58 in next repeat) has a root mean squared coupling of 5.01 ± 0.08 meV. Notably, these “through-bond” coupling values are comparable to the through-space coupling for c-type hemes in a T-shaped (perpendicular) geometry. In contrast, if the tunneling pathway is excluded, the coupling between tyrosine 58 and tryptophan 72 is 0.015 ± 0.03 meV. This value is comparable to that which is obtained if using

the Hopfield equation to estimate coupling. Tyr 58 and Trp 72 are approximately 10 Å apart.

Using the parameterized expression for coupling,

$$|H_{AB}| = \frac{2.7 \text{ eV}}{\sqrt{N_D N_A}} \exp(-0.77 \text{ \AA}^{-1} \cdot R_{DA}) \quad (6.1)$$

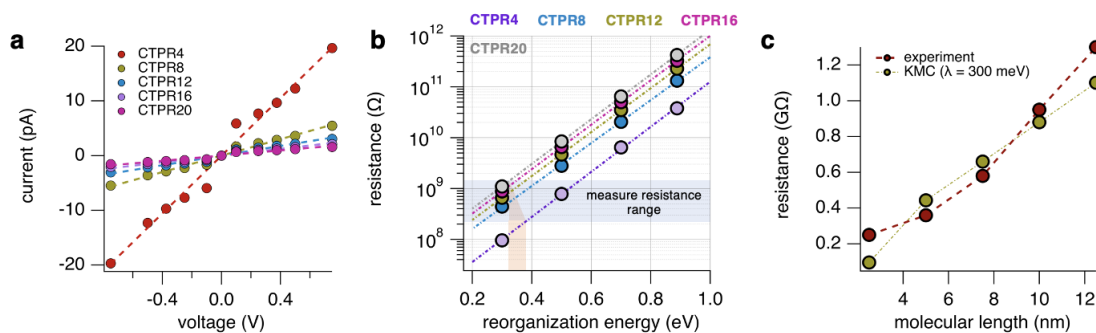
where, N_D and N_A are the number of atoms in the donor and acceptor, respectively, and R_{DA} is the nearest atom distance between donor and acceptor, the coupling is computed to be 0.15 meV, about 40 – 50-fold lower than the value computed using the CDFT-CI method.

Table 6.1: Hole transfer parameters for CTPR8

ET step	ΔG^0 (eV)	λ (eV) (this work)	λ (eV) (estimate)	$\sqrt{\langle H_{AB} ^2 \rangle}$ (meV)	k_{ET} (s ⁻¹)
Tyr → Trp	0.057 ± 0.04	0.705	0.3	4.60 ± 0.2	7.545×10^{10}
Trp → Tyr	-0.057 ± 0.04	0.705	0.3	5.01 ± 0.08	6.378×10^{12}

The electronic coupling is probably enhanced by the peptide backbone due to mixing of the HOMO through HOMO-2 orbitals. When these are visualized, we see that the HOMO-2 is localized on the peptide backbone (Figure 6.5). The additional orbital overlap offered by the HOMO-2 can provide a bridge from donor to acceptor. This type of coupling enhancement cannot be captured by orbital based methods such as fragment orbital DFT (FODFT) or projection operator diabaticization (POD), as those methods can only compute through-space coupling via calculation of the overlap between the donor and acceptor orbitals. To test this, I ran a test calculation using the POD method which returned a coupling value of 0.1 meV, about 50-fold than the CDFT-CI method.

We used Marcus theory^{5,130} to compute the non-adiabatic electron transfer rates (Table 6.1). Plugging these rates into a repeating 2-site kinetic Monte Carlo (KMC) simulation, we computed current-voltage curves and estimated of the length dependence of the resistance of CTPR4, CTPR8, CTPR12, CTPR16, and CTPR20. We computed the resistance using reorganization

**Figure 6.6: Computed resistance of CTPR proteins.**

(a) Computed current voltage curves of CTPR proteins containing 4, 8, 12, 16, or 20 repeats. (b) Computed resistance for the CTPR proteins computed using different values for the reorganization energy. The range of experimentally measured resistance values is highlighted in blue. Its projection to the x-axis is shown in orange. (c) Comparison of the computed length dependence of the resistance to the experimental values.

energies ranging from 0.3 eV to 0.9 eV. The computed resistance values matched the experimentally determined range when we used a low reorganization energy of 0.35 eV, in agreement with the value computed by Krishnan et al¹². While our simulation could match the measured magnitude of the resistance, we were unable to capture the length dependence. This is unsurprising, as our KMC model of charge transport via hopping through protein is expected to return a linear length dependence¹¹⁷, and the KMC model employed assumed that the fraction of the applied voltage dropped across the protein was independent of protein length. It is likely that the length dependence could be corrected by expressing the injection and ejection rates as a function of molecular length, in a manner similar to that of Krishnan et al¹².

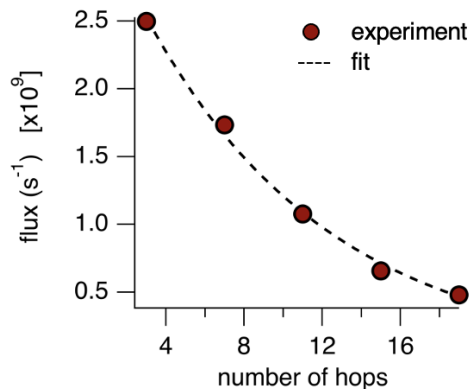
There are now two potential interpretations of the length dependence of CTPR resistance. The first, offered by Zhang et al¹, is that charge transport in CTPR proteins is diffusive and non-directional, and results from a weak driving force (i.e. low voltage bias)^{1,12}. The second, implicates the length dependence of the fraction of the applied bias dropped across the protein system¹². While these are possible and even supported by modelling¹², I would like to offer an alternative interpretation. Segal et al.¹⁶⁴ proposes that the flux of charge carriers through a molecule via intermediate-range steady-state hopping be described by,

$$J = (k_{inj}^{-1} + k_{hop}^{-1}N)^{-1} e^{-\alpha N} \quad (6.2)$$

where, k_{inj} is the rate at which charge carriers are injected from the electrode into the molecule, k_{hop} is the hopping rate between sites within the molecule, N is the number of sites, and α describes the loss of charge carriers to the environment¹⁶⁴. For molecules with a stable oxidized and reduced state, the α term is close to zero, and the exponential dependence vanishes⁴⁴.

However, for tyrosine and tryptophan, it is reasonable to believe that the high potential radical formed when the residue is oxidized may result in carrier loss.

We converted the experimentally measured resistance⁻¹ data from Zhang et al.¹ into flux converted the molecular length to the number of hopping steps assuming only tyrosine 58 and



$$J \propto (k_{in}^{-1} + k_{hop}^{-1}N)^{-1} e^{-\alpha N}$$

Parameter	value
k_{in}	$3.467 \times 10^9 \text{ s}^{-1}$
k_{hop}	$2.374 \times 10^{12} \text{ s}^{-1}$
α	0.104

Figure 6.7: Fitting reveals hopping mechanism with competing carrier loss.

The experimental data from Zhang et al.¹ were converted to flux and fit with the equation for intermediate-range steady-state hopping. The table to the right contains the fit parameters.

tryptophan 72 are in the charge transport pathway. We fit these data with Equation 6.2 and received a very good fit to the data. The parameters obtained from the fit revealed an injection rate of $3.467 \times 10^9 \text{ s}^{-1}$, a hopping rate of $2.374 \times 10^{12} \text{ s}^{-1}$, and a decay parameter (α) of 0.104. The hopping rate is in good agreement with the non-adiabatic ET rate computed in this work, suggesting that non-adiabatic electron transfer theory may be sufficient to explain charge transport in CTPR proteins.

6.2.3. Discussion

The work on CTPR proteins, performed by Zhang et al.¹, Krishnan et al.¹², and myself, has demonstrated that non-cytochrome proteins can transport charges very efficiently. At short distances, the conductance values are comparable to those measured for OmcS nanowires. However, it is unclear how such a protein system will conduct over long distances. The loss of carriers, giving rise to a non-linear length dependence of the conductance, would lead to divergence of the resistance of cytochrome and non-cytochrome nanowires. To evaluate this, we must compare the resistance of cytochrome nanowires to non-cytochrome proteins measured over longer distances.

The amyloid crystals presented in the previous section of this chapter provide a comparison to the CTPR proteins. The crystals measured in this study allowed for measurements over lengths

of 50 – 300 nm. When extrapolating to the lengths measured for the CTPR proteins, the resistance of the amyloid crystals is about 7-fold higher than CTPR20. However, at 270 K, when the computed hydrogen bonding frequency between the tyrosine and glutamine in the amyloid crystal was comparable to that of tyrosine 58 in CTPR8 (70 % of the simulation corresponds to a frequency of 2.8×10^{11} Hz), the resistance of the amyloid crystal was $0.3 \text{ G}\Omega$ (Figure 6.3), in close agreement with the measurements on CTPR4. Therefore, these studies lead to the conclusion that non-cytochrome proteins can support long-range charge transport which rivals the OmcS cytochrome nanowire, so long as the structure of the protein surrounding the aromatic amino acids provides proton acceptors to support tyrosine and tryptophan oxidation.

It is important to note that the comparisons between non-cytochrome protein nanowires and cytochrome nanowires have been limited to OmcS. To date, there have not been any measurements on non-cytochrome proteins which have demonstrated conductivity values close to those of the OmcZ nanowire. However, this does not preclude biological relevance of non-cytochrome protein conductivity (see next chapter), or biotechnological applications of conductive proteins⁶⁵.

7. Protein conductivity promotes bacterial adhesion to host-cell surfaces

Extracellular electron transfer via pili promotes host-pathogen adhesion

Peter J. Dahl, Sibel Ebru Yalcin, Paul Kennouche, Dennis Vu, Uriel N. Morzan, Atanu Acharya, Vishok Srikanth, Vaishakh Kedambaimoole, Neelotpala Kumar, Konandur Rajanna, Deji Akinwande, Victor S. Batista, Lisa Craig, Guillaume Dumenil, and Nikhil S. Malvankar

This chapter is a modified version of a paper that has been submitted for publication.

7.1 Author Contributions

P.J.D. performed modelling, conductivity, EFM measurements of pili, biofilm voltammetry, and single-cell force spectroscopy (SCFS) measurements. S.E.Y. performed EFM experiments and helped with data analysis and interpretation. P.K., under the guidance of G. D., generated *N. meningitidis* mutant pili and performed adhesion experiments on host-cell surfaces. D. V. fabricated nanoelectrodes. U.N.M. and A.A. helped with modelling under the guidance of V.S.B. V.S. modelled *Bifidobacterium pilus*. N.K. prepared GO under the guidance of A.K. L.C. provided *N. gonorrhoeae* and *V. cholerae* pili. P.J.D. and N.S.M. wrote the manuscript with substantial input from all authors.

7.2 Summary

The first step in most infections is bacterial adhesion to host-cell surfaces, or to other bacteria, to form biofilms that account for >80% infections¹⁶⁵. This adhesion occurs despite electrostatic repulsion between negatively-charged bacterial and host-cell surfaces, first identified >50 years ago¹⁶⁶. Diverse bacteria use filamentous appendages called Type 4 pili (T4P) to

overcome this repulsion¹⁶⁷, but the underlying mechanism is unclear. Non-pathogenic bacteria use haem-based extracellular electron transfer (EET) to respire in anoxic environments, but the existence and mechanism of other direct-contact EETs remains unknown. Combining single-cell and electrostatic force spectroscopy with EET measurements through individual T4P and biofilms, we show that diverse *Neisseria* and *Pseudomonas* species use T4P for EET to facilitate adhesion. Adhesion is enhanced by increased T4P conductivity, likely due to improved stacking of aromatic residues in pilus, by introduction of aromatic residues or by reducing pH found at many infection sites, such as cystic fibrosis lungs¹⁶⁸. Suppression of EET decreases bacterial adhesion. We therefore show that changes in bacterial metabolism drives host-cell adhesion. As T4P are key virulence factors for anti-bacterial therapeutics, targeting microbe-to-microbe and microbe-to-host EET via T4P at the adhesion stage of infection may offer a novel strategy for preventing and treating bacterial infections.

7.3 Introduction

Metabolism releases excess electrons that every bacterial species must jettison to successfully replicate inside its host and to ensure its own survival. In harsh environments that lack soluble, membrane-permeable electron acceptors such as oxygen, diverse non-pathogenic bacteria respire by attaching to minerals in the soil to carry out extracellular electron transfer (EET) – transfer of electrons across the outer membrane and to an extracellular substrate⁴⁵ (Fig. 1a). However, this contact-based EET requires *c*-type cytochromes either embedded in the outer-membrane or forming polymerized filaments⁴⁵. It was hypothesized that EET in soil microbes was performed via T4P, but recent studies show that the extracellular conductive filaments responsible for this process are in fact cytochrome filaments and not T4P^{42,43,45}.

Similar to these soil bacteria, pathogens also attach to the diverse host surfaces and survive in harsh environments in which electron acceptors are scarce¹⁶⁹. So far, the only mode of EET by gut and lung pathogens is via diffusion of soluble redox molecules, such as flavins or phenazines,

as redox-active shuttles^{170,171} (Figure 7.1a). However, such non-contact EET via diffusive shuttles becomes inefficient in the highly dynamic environments like the gut and lung with high fluid flow¹⁷². The mechanism of EET in such turbulent environments is not known.

T4P are used by diverse Gram-negative and Gram-positive pathogens for initial colonization of various organs such as lung, brain and urogenital tracts¹⁷³. Bacterial colonization thus begins with pilus-mediated adhesion at a distance, owing to the micrometre-long pili¹⁶⁷. This initial contact is followed by retraction of the T4P and ultimately, intimate adhesion of the bacterium to the surface of the host cell based on the strength of the interaction between receptor molecules on the host cell membrane and bacterial surface ligands¹⁶⁷.

Problematically, the surfaces of both the bacterial and host cells are negatively charged and repel each other as these cells are brought together, despite shielding of surface charges by ions in the solution¹⁶⁶ (Figure 7.1b). This electrostatic barrier repels approaching motile bacteria to deter their adhesion; this repulsion can be overcome in some cases by increased swimming speed¹⁷⁴. Prior experiments have shown that bacteria use pili to eliminate this repulsion and colonize host¹⁷⁵. However, the role and mechanism of pili-mediated host-pathogen electrical interactions for initiation of infections have remained unclear. Here, we show that diverse pathogens use EET via T4P to transfer metabolic electrons to underlying surfaces. We further show that the pathogen colonization is enhanced by this electron transfer, altering the charge of the underlying surface which diminishes electrostatic repulsion (Figure 7.1c).

7.4 Results

7.4.1. Pathogens perform EET in high fluid flow

To evaluate the ability of pathogens to survive in dynamic environments via direct-contact EET, we grew *P. aeruginosa* anaerobically on electrodes in bioelectrochemical systems and monitored electrical current generated due to metabolism. In contrast to microbes that use non-contact EET via shuttles¹⁷⁶, we observed no loss in current production of *P. aeruginosa* upon

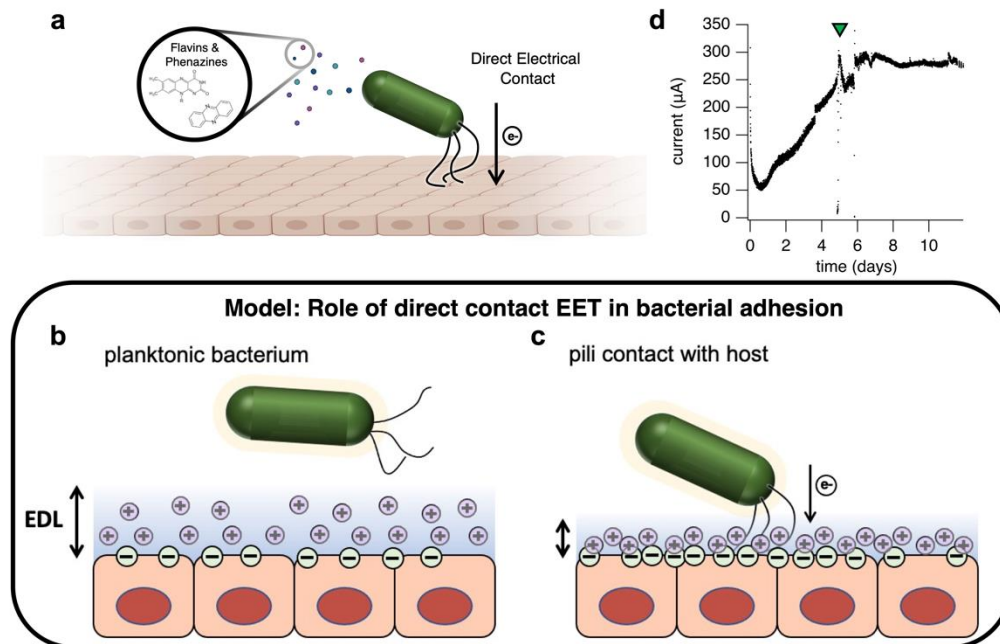


Figure 7.1: EET via direct contact enables charge redistribution on host surfaces.

(a) Schematic of a bacterium on epithelial cells using extracellular electron transfer. **(b)** Cartoon representation of a planktonic bacterium approaching a negatively charged epithelium. **(c)** Direct contact EET redistributes charges and results in a more compact EDL, diminishing repulsion. **(d)** Current produced by *P. aeruginosa* grown in a microbial fuel cell. The green arrow indicates the time at which flow-through mode was initiated.

switching to high-fluid-flow conditions that would remove soluble shuttles (Figure 7.1d). These results sharply contrast with complete loss of current by shuttle-producing bacteria¹⁷⁶. Such ability to maintain EET under high-fluid-flow conditions has been observed only in bacteria capable of direct-contact EET¹⁴⁸. These experiments suggest that *P. aeruginosa* is capable of direct-contact EET.

Our finding of pathogen capable of generating current under high-fluid-flow is consistent with our previous demonstration that gut bacteria can also generate electricity and form biofilms with four-times more conductivity than the soil bacteria capable of performing direct-contact EET¹⁴⁸. In these studies, fluid flow shifted the gut bacterial community into more conductive biofilms. However, the components conferring such high conductivity to biofilms is not known.

7.4.2. Pathogens use T4P to dissipate electrons

To directly visualize and quantify EET by pathogens and to identify the components and pathways involved in EET, we used electrostatic force microscopy (EFM) charge mapping of *P. aeruginosa* on a graphene oxide (GO) surface as an electron acceptor (Figure 7.2a-b). In its pristine state, GO is a negatively charged non-conductor with a surface charge density similar to that of epithelial host surfaces^{175,177-180}. When electrons are transferred to the GO surface, it is locally reduced (rGO) and becomes an electrical conductor, allowing injected electrons to propagate through the reduced surface¹⁸¹ (Figure 7.2b). Non-pathogenic bacteria have been shown to reduce GO via direct-contact EET^{182,183}. We have previously established the ability of EFM to image the electron transfer in bacterial filaments¹⁸⁴ as well as the visualize changes in the conductivity of GO upon electron transfer by quantifying the increase in the EFM phase shift due to electron transfer¹⁸¹. Here we use EFM to directly visualize the EET by adherent pathogens by mapping the conductive regions of rGO due to EET by pathogens.

We found regions of conductive rGO, distant from *P. aeruginosa* cells, but only in the regions where T4P contacted the GO surface, as evidenced by an increase in the EFM phase shift (Figure 7.2c-d,g). The bare GO surface was not reduced substantially in the absence of T4P contact or without T4P-expressing bacteria (Figure 7.2e-g). These results suggest that *P. aeruginosa* use T4P as a conduit for direct-contact EET to the underlying surface during adhesion.

To evaluate the role of bacterial metabolism in the observed EET to the surface, we performed EFM with *P. aeruginosa* cells treated with either pyocyanin (PYO) or sodium azide (NaN₃). PYO is a phenazine redox shuttle used by *P. aeruginosa* for EET, and diverts respiratory electrons from the surface by serving as an alternate electron acceptor¹⁸⁵ whereas sodium azide is a known inhibitor of respiration which blocks production of respiratory electrons¹⁸⁶. Both PYO and sodium azide inhibited direct-contact EET, even in the absence of any fluid flow, as shown

by the quantification of charge density of the rGO surface upon EET (Figure 7.2h). This result demonstrates that *P. aeruginosa* uses T4P for direct-contact EET to transfer respiratory electrons to surfaces.

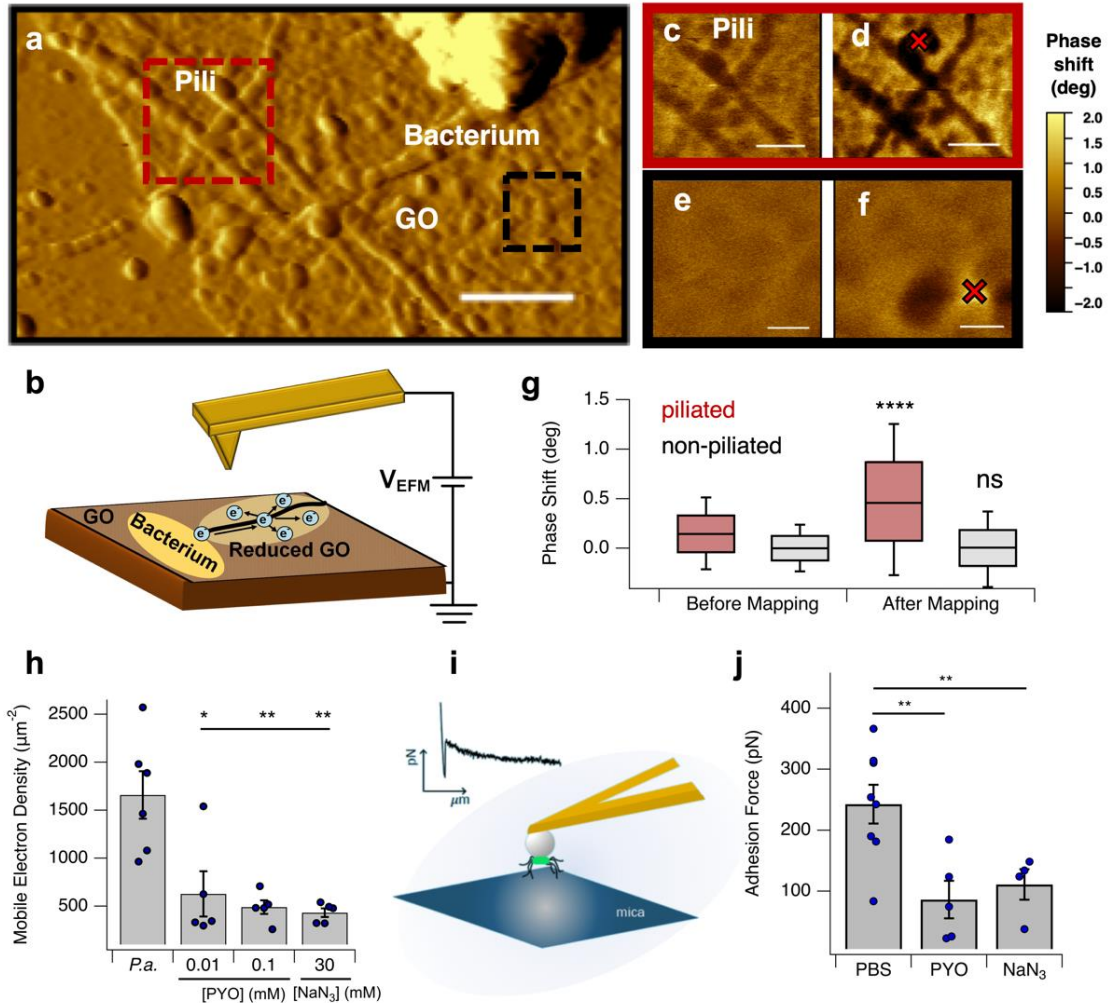


Figure 7.2: *P. aeruginosa* uses T4P for direct contact EET.

(a) AFM image of a piliated *P. aeruginosa* deposited on a graphene oxide (GO) surface. Scale bar is 250 nm. (b) Schematic of the EFM charge mapping experiment on a GO surface. (c) EFM phase image of pili before conductivity mapping at boxed region shown in a. Scale bar is 100 nm. (d) EFM phase image of pili after charge was injected into the GO at the site marked with the “X” to map the conductive region. The bright area on the GO surface is the conductive region. Scale bar is 100 nm. (e) EFM phase image of GO with no bound pili before conductivity mapping at the black boxed region shown in a. Scale bar is 30 nm. (f) EFM phase image after charge was injected into the GO at the site marked with the “X” to map the conductive region. Scale bar is 30 nm. (g) Change in EFM phase during conductivity represented as a box plot. The box for the plot was defined as 25 % and 75 % of the phase shift. The center line is the median and whiskers are the 10-th and 90-th percentile of the data. (h) Quantification of the density of mobile electrons injected into the GO surface following treatment with pyocyanin (PYO) and azide. This value is proportional to the area of rGO. (i) Schematic of the single cell force spectroscopy setup. (j) Adhesion force of *P. aeruginosa* PA103 cells treated with PYO and sodium azide compared to untreated cells, measured with SCFS. ($n \geq 5$ cells).

7.4.3. EET via pili enhances bacterial adhesion

The electrostatic repulsion between bacterial and host surfaces results from both having a net negative surface charge due to the presence of charged proteins, carbohydrates, and lipids. The ions in solution coat a charged surface, creating an electric double layer (EDL) that shields the charge (Figure 7.1b). However, close apposition of bacterial and host surfaces results in overlap of the two EDLs and a return to electrostatic repulsion¹⁶⁶. Non-piliated bacteria can overcome this repulsion only when they approach within van der Waals radii of the surface which is at an energetic minimum¹⁸⁷. This phenomena has been demonstrated experimentally via manipulation of EDL thickness¹⁶⁶ as well as manipulation of the surface properties of bacteria and substrate¹⁸⁷. Due to a difference in the surface charge densities of bacterium¹⁸⁸ and host¹⁷⁵, there also exists a large potential gradient (>200 mV) between the surfaces. The observation of direct-contact EET by *P. aeruginosa* upon adhesion suggest the ability of the bacterium to manipulate the surface charge of its host. As host surfaces are almost ubiquitously insulating, respiratory electrons deposited by the bacterium will remain localized, locally increasing the magnitude of the host surface charge density (Figure 7.1c). This increase in the magnitude of surface charge decreases the EDL thickness¹⁸⁹. Previous experiments have shown that the decrease in the EDL thickness increases the bacterial adhesion¹⁶⁶, however the underlying mechanism is unclear.

To directly quantify how EET affects bacterial adhesion, we used single cell force spectroscopy (SCFS), with individual *P. aeruginosa* cells immobilized on a bead at the end of an AFM probe, to measure the adhesion forces between a bacterium and a mica surface (Figure 7.2i). In this setup, bacteria remain viable and attached to the bead, allowing direct measurements of the forces between the bacterium and host-cell surfaces^{190,191}. Importantly, mica has a surface charge density that mimics the negative surface charge of the host cell¹⁷⁵. Force curves revealed sudden rupture features consistent with the nanospring properties of individual pili^{190,191} as well as features characteristic of desorption, where cells and pili are released from the mica

(Supplementary Figure 7.1). After measuring cells in phosphate buffered saline (PBS) we treated the same cells with PYO or sodium azide to remove respiratory electrons. Treatment with both PYO and sodium azide resulted in a significantly lower adhesion force than untreated cells (Figure 7.1j). This result indicates that the change in bacterial metabolism to pili-mediated direct-contact EET drives their adhesion.

7.4.4. Pili lower barrier for electron transfer

To further characterize bacterial electron transfer to the underlying surface, we complemented our EFM measurements with electrochemical measurements of *P. aeruginosa* cultures on a gold electrode (Figure 7.3). Cyclic voltammograms showed a peak at -250 mV (vs. Ag/AgCl reference electrode) in agreement with phenazines¹⁹² (Figure 7.3b). The current at this peak also showed scan rate dependence consistent with diffusive behaviour of phenazines (Figure 7.3c). However, in addition to phenazines, we observed another peak at 64 mV vs. Ag/AgCl. This peak is consistent with cytochrome c reductase of respiratory complex III which was shown to be necessary for metabolic activity and EET by *Pseudomonas* species¹⁸⁶. The scan rate dependence of this peak current was linear, consistent with bacteria-bound redox species¹⁷¹ (Figure 7.3c). Our finding is also consistent with previous reports of this peak EET by *P. aeruginosa* upon adhesion¹⁹².

To further evaluate the ability of bacteria to use pili for electron transfer to a surface corresponding to this potential, we performed electrochemical impedance spectroscopy on *P. aeruginosa* wild-type and $\Delta pilA$ cells adsorbed on the surfaces. Using this method, we obtained a direct measurement of the barrier for electron transfer between the bacterium and the surface, indicated as electron transfer resistance, at the surface potential at which we observed electron transfer by the cells (Figure 7.1i). We found that piliated, wild-type *P. aeruginosa* demonstrated a ~3-fold lower barrier for electron transfer than $\Delta pilA$ strain (Figure 7.3f; Supplementary

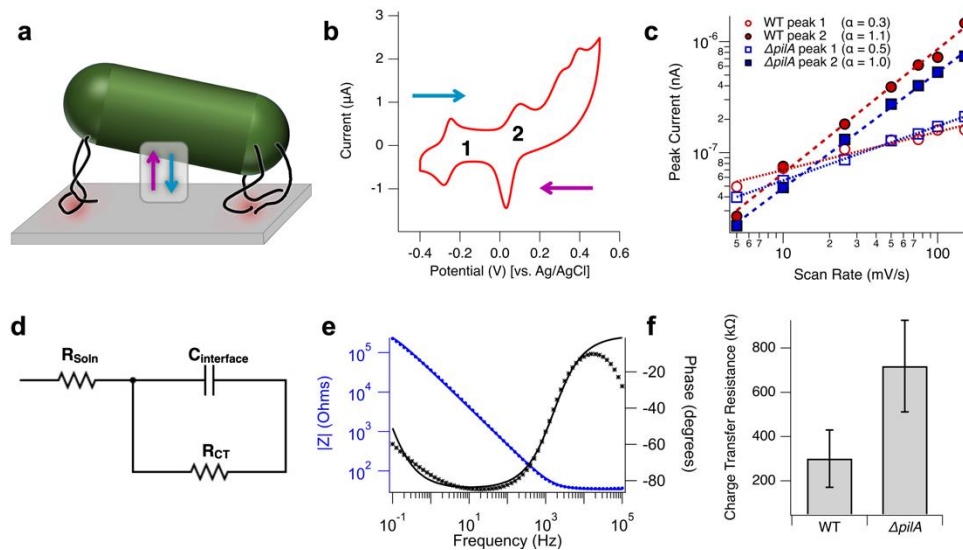


Figure 7.3: Pili reduce the barrier for direct contact EET.

(a) Cartoon representation of a bacteria attached to an electrode. The cyan and magenta arrows indicate the direction of electron transfer corresponding to the anodic (negative to positive) and cathodic (positive to negative) scans in **(b)**. **(b)** Cyclic voltammogram of wild-type *P. aeruginosa* cells attached to a gold electrode. The numbers identify the two peak systems we observed. The arrows indicate the scanning direction. **(c)** Scan rate dependence of the peak current observed at the oxidative (anodic) peaks for peak system 1 and peak system 2 for both wild-type and $\Delta pilA$ cells. The slope of the dashed lines are indicative of the mode of charge transport (diffusive or direct contact) for the specified peak system. **(d)** Diagram of the circuit used to extract the charge transfer resistance between the bacteria and the surface. R_{soln} is the resistance of the solution (PBS), $C_{interface}$ is the capacitance due to the EDL, and R_{CT} is the charge transfer resistance. **(e)** Example electrochemical impedance spectrum (markers) fit with the model in **(d)**. **(f)** Charge transfer resistance for WT and $\Delta pilA$ cells attached to the electrode surface. Error bars are s.e.m.

Figure 7.2), further demonstrating that pili provide a direct electrical connection between bacteria and surfaces.

7.4.5. Pathogenic T4P are electrically conductive

The observation of direct-contact EET via T4P (Figure 7.2 and Figure 7.3) suggests that pathogenic T4P are electrically conductive. Previous studies failed to find substantial conductivity in T4P because the measurements were either made only across the T4P diameter⁴¹, or along networks of T4P¹⁹³ that were affected by inter-filament contact resistance³. We and others had previously hypothesized that non-pathogenic soil bacteria *Geobacter* use T4P to transfer electrons to extracellular acceptors during metabolism¹⁹⁴. However, multiple studies have

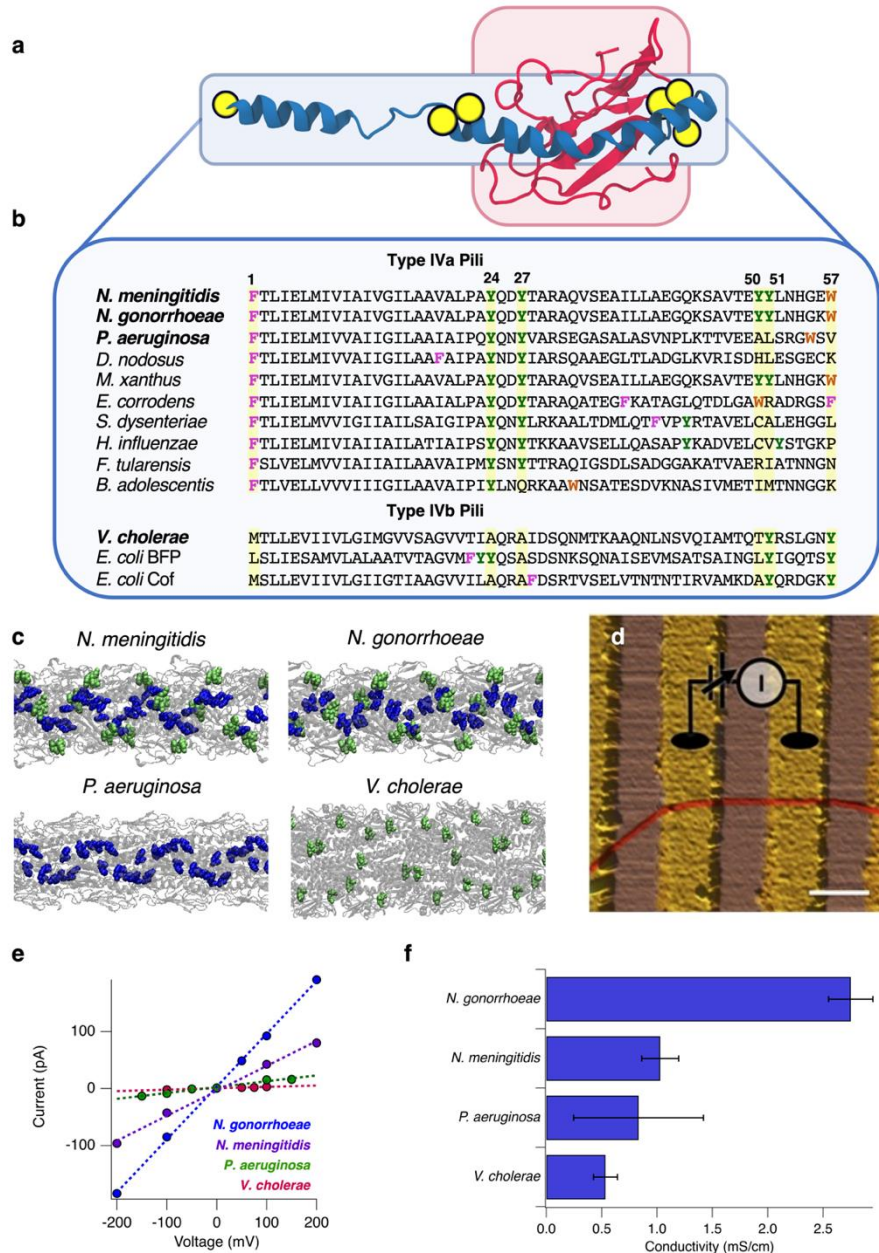


Figure 7.4: Electrical conductivity of pili in diverse pathogens correlates with abundance of aromatic amino acids in $\alpha 1$ of the major pilin protein.

(a) Structure of the *N. meningitidis* major pilin monomer (PDB ID: 5kua). The location of aromatic amino acids that form the electron transfer path are shown as yellow circles. The helical N-terminal helix, $\alpha 1$ is in blue and the globular C-terminus domain is in pink. (b) Sequence alignment of the N-terminal region of the pilus of several pathogens. Aromatic residues are highly conserved at positions 1, 24, and 27 in T4aP but not T4bP. (c) Cryo-EM reconstructions of the *N. meningitidis* (PDB ID: 5KUA), *N. gonorrhoeae* (5VXX) and *P. aeruginosa* (5VXY) T4aP and negative stain reconstruction of *V. cholerae* T4bP (EMDB-1954). Aromatic residues in positions 1, 24, and 27 (blue) are stacked closely in the T4a pili but not in the T4bP. Aromatic residues at other positions are coloured green. (d) Conductivity measurement schematic with AFM image of the nanoelectrodes coloured for clarity. A pilus filament is red. Yellow bars are gold; darker bars are non-conductive gaps. Scale bar, 300 nm. (e) Current-voltage curves and f, conductivity of the individual pili. (Error bars represent s.e.m.; $n \geq 6$)

failed to find any T4P on *Geobacter* surface, and EET was recently shown to occur via

cytochrome nanowires⁴⁵.

We have recently found that incorporating aromatic amino acids render conductivity to *E-coli* pili³⁴. We have also found that overlapping π -orbitals, from closely-stacked aromatic residues, such as phenylalanine and tyrosine, enable micrometre-long electron transfer in amyloid proteins³. Aromatic residues are highly conserved and stacked in the N-terminal α -helix of T4aP¹⁷³. Therefore, we hypothesized that electron conduction occurs via these evolutionary-conserved aromatic residues in the T4aP (Figure 7.4a-c).

To directly evaluate electron transfer in T4P, we used atomic force microscopy (AFM) to locate an individual pilus bridging the non-conductive 300-nm gap on gold nanoelectrodes and measured conductivity of a single pilus by measuring the current-voltage response (Figure 7.5d), similar to our measurements of bacterial⁴³ and synthetic³ protein nanowires (Figure 7.5e). We found that T4aP of *Neisseria meningitidis*, *Neisseria gonorrhoeae* and *P. aeruginosa* were 1000-fold more conductive than synthetic protein nanowires³ (Figure 7.5f). The T4bP of *Vibrio cholerae*, which lack stacked aromatic residues in the N-terminal α -helix (Supplementary Figure 7.3), showed lowest conductivity (Figure 7.5f). The presence of aromatic residues in the filament core may also explain the greater stability of T4aP relative to T4bP¹⁷³. Higher stability, combined with higher conductivity may allow bacterial pathogens to colonize harsh environments such as the urethra for *N. gonorrhoeae* and the acidic CF lung for *P. aeruginosa*. Our finding of conductive T4P in diverse pathogens could explain how pathogens can perform EET by forming highly conductive biofilms¹⁹⁵.

7.4.6. T4P conductivity correlates with cell adhesion

To directly evaluate whether pili conductivity is involved in the adhesion of pathogens to host-cells, we assessed conduction in pili produced by various *N. meningitidis* mutants and used a host-cell adhesion assay to correlate T4P conductivity to bacterial adhesion. We selected mutants in which the distribution of the aromatic residues in the major pilin N-terminus was altered by

introducing an aromatic residue where there was none, or by replacing an aromatic residue with a non-aromatic one (Figure 7.5a). Prior work has shown that these mutations had no discernible effect on pilus assembly or surface display as assessed by a immunofluorescence assay for piliation¹⁹⁶.

We first evaluated the effect of these alterations on pilus conductivity *in silico* by performing molecular dynamics simulations of the pilus variants. Electron transfer rates are expected to decrease with the distance between aromatics³. Therefore, we studied the change in inter-aromatic-residue distances as well as the resulting number of independent conduction paths formed by the mutations (see Methods section). We found that these amino acid changes modulate both the mean electron transfer distance as well as the number of conduction paths (Figure 7.5b), suggesting that they would significantly affect the conductivity of pili. For example, our simulations predicted larger distances between remaining aromatic residues in the Y27A and Y50C variants would result in lower conductivity in the corresponding pili (Figure 7.5b). On the other hand, decreased distances between aromatic residues and increased number of conduction paths in Y51W and S34Y, respectively, were predicted to increased conductivity (Figure 7.5b). Experimentally measured conductivities of individual Y51W and S34Y pili showed higher conductivity than WT (Figure 7.5c). We find that the experimentally measured conductivities for each mutant, normalized by the corresponding computed number of paths, is exponentially dependent on the computed distances between aromatics (Extended Data Fig. 4). This suggests that pili conduction is limited by electron tunnelling of the charge between aromatic sites³.

As electron transfer can potentially reduce electrostatic repulsion between bacterial and host surfaces, allowing intimate interaction upon pilus retraction, we next evaluated the link between pilus conductivity and bacterial adhesion to host-cell surfaces using human umbilical vein endothelial cells (HUVEC). With the exception of Y27A, our host-cell adhesion assay showed

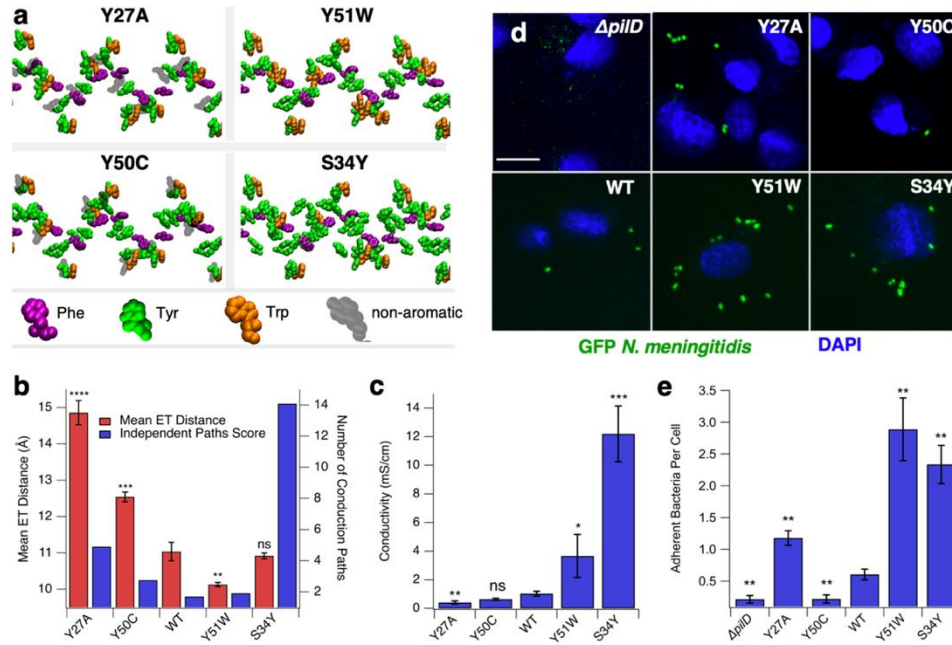


Figure 7.5: Bacterial adhesion increases with higher conductivity of *N. meningitidis* T4P. (a) Aromatic stacking in the *N. meningitidis* T4P mutants. Grey indicates an aromatic residue substituted with a non-aromatic one. (b) Maximum distances between aromatic residues involved in electron transfer (ET) paths as determined via shortest path calculations on molecular dynamics trajectories of each *N. meningitidis* pilus variant (red) and corresponding number of independent conduction paths (blue). (Error bars represent s.e.m.; $n \geq 8$) (c) Conductivity of purified *N. meningitidis* T4P mutants. (Error bars represent s.e.m.; $n \geq 8$). (d) Adherent *N. meningitidis* (GFP) on human umbilical vein endothelial cells (HUVEC) with fluorescently labelled DNA. Scale bar is 30 μm . (e) Quantification of *N. meningitidis* adhesion to HUVEC. The non-piliated $\Delta pilD$ strain is included as a negative control. (Error bars represent s.e.m.; $n = 16$ fields of view across 6 independent experiments containing HUVEC cells). Results of Student's t-tests are shown by * ($P \leq 0.05$), ** ($P \leq 0.01$), *** ($P \leq 0.001$), and **** ($P < 0.0001$).

that the bacteria with more conductive Y51W and S34Y pilus variants adhere in greater numbers to HUVECs relative to the WT strain whereas the poorly conductive Y50C variant showed reduced adherence, comparable to that of a strain lacking pili ($\Delta pilD$) (Figure 7.2e,f; Supplementary Figure 7.5). These results further demonstrate that EET via pili facilitates host cell adhesion.

7.4.7. pH regulates conductivity and adhesion

We also assessed the role of environment in pilus conduction and *P. aeruginosa* adhesion, by varying pH. We found that increased acidity resulted in up to a 20% decrease in pilus diameter (Figure 7.6a; Supplementary Figure 7.6), likely due to dehydration that can cause proteins and other polymers to adopt a more compact structure at lower pH⁴⁵. The

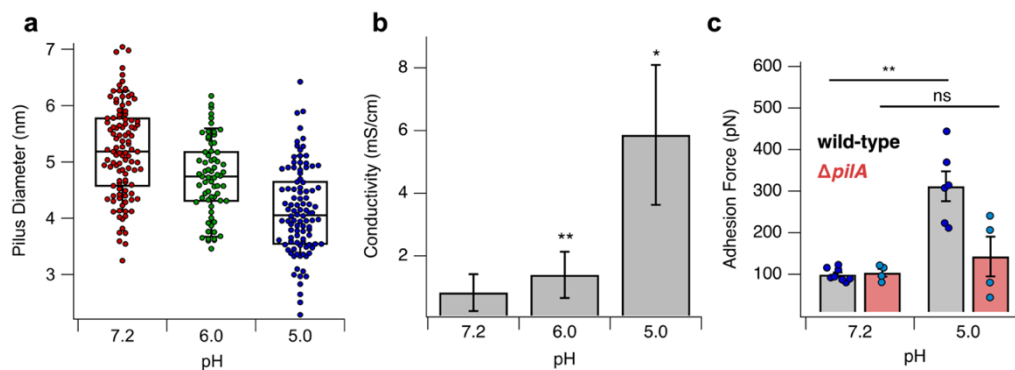


Figure 7.6: pH regulates *P. aeruginosa* pili conductivity and adhesion.

(a) Pilus diameter at pH 7.2, 6.0 and 5.0 represented by boxplots. The box was defined as 25 and 75% with centre line as median and the whiskers as 10 and 90%. ($n \geq 67$ distinct pili). (b) Conductivity of individual *P. aeruginosa* pili under varied pH conditions (error bars represent s.e.m; $n=8$). (c) Adhesion force of wild-type and $\Delta pilA$ *P. aeruginosa* PAO1 cells at pH 7.2 and 5.0 ($n \geq 4$ cells).

decreased diameter was accompanied by a 7-fold increase in pilus conductivity (Figure 7.6b). In contrast, low pH did not increase the background conductivity of the buffer, nor that of the poorly conductive *V. cholerae* pili, which only possess aromatic residues at the C-terminus of $\alpha 1$ (Supplementary Figure 7.7a-b). Thus, we attribute the increased conductivity of the *P. aeruginosa* T4P at low pH to its decreased diameter, which may result in closer packing of the stacked aromatic side chains in a manner similar to hemes in *G. sulfurreducens* nanowires⁴⁵.

SCFS measurements demonstrated that piliated cells adhered to mica 5-fold more strongly at pH 5.0 than at pH 7.2 (Figure 7.6c). In contrast, $\Delta pilA$ cells (Figure 7.6c), and bare AFM probes without cells (Supplementary Figure 7.7c), did not show a substantial increase in adhesion force at pH 5. Therefore, these single-cell measurements suggest that the low-pH-induced increase in bacterial adhesion is due to an increase in the T4P conductivity and not due to a change in the protonation state of the bacterial cell or the underlying surface.

7.5 Discussion

Prior EET studies on pathogens have been focused on diffusive, redox-active shuttle molecules, such as flavins and phenazines, which are used by diverse pathogens for EET¹⁷⁰, and are washed away in high-flow environments¹⁷². Therefore, the change in the charge redistribution

across the host/pathogen interface is unlikely to occur by diffusion of such small molecules, given the fluid flow that occurs in the blood vessels, urogenital tracts, and catheters. In fact, our results show that diffusive redox shuttles (PYO) inhibit EET (Figure 7.2h) and reduce bacterial adhesion (Figure 7.2j). The T4P provide a direct electrical contact between the well-separated bacterium and host cell surface even in a high-flow environment, thus providing an additional competitive advantage to pathogens with T4P for efficient attachment to host cells via redistributing surface charges even in high-flow environments.

The low pH conditions used to modulate *P. aeruginosa* pilus conductivity have direct relevance to the cystic fibrosis (CF) disease state. The pH of the airway surface liquid (ASL) in the lungs decreases from ca.7.5 in healthy people to as low as 2.9 in CF patients¹⁶⁹. Several mechanisms have been proposed for increased bacterial viability in CF lung infections such as loss of anti-microbial activity of the ASL¹⁶⁸, defective glycosylation of CF lung epithelial cells¹⁹⁷ or mucin changes in the host cell¹⁹⁸. The results of our experiments offer an additional explanation for increased *P. aeruginosa* colonization in an acidic environment. Bacterial colonization of lung epithelial cells at normal pH in healthy people is restricted, likely due to a repulsive interaction between host and pathogens. However, at the low pH in the CF lung¹⁶⁹, increased pilus conductivity would enable *P. aeruginosa* to transfer electrons to the lung surface, reducing the electrostatic repulsion and promoting attachment. The prevalence of *P. aeruginosa* in the acidic, anoxic sputum of cystic fibrosis lungs, during early stages of infection, could be due to a competitive advantage conferred by pili with increased conductivity under acidic environments.

In addition to promoting adhesion, our finding of diverse bacteria capable of direct-contact EET suggests that pathogen growth could be accelerated by electron transfer via pili to host-produced molecules. In nearly half of known gut bacteria, pili are essential for diverse functions such as adhesion and biofilm formation but their exact function is not known¹⁹⁹. The ability of

pathogens to perform EET via shuttles has been shown to provide a competitive advantage by promoting growth and colonization via controlling redox balance²⁰⁰ and enhancing nutrient access²⁰¹ under closed environment of bacterial microcompartments. In contrast, direct-contact EET could provide growth advantage in open environments despite large fluid flow. Notably, common commensal gut bacteria *Bifidobacterium adolescentis* express T4aP in response to increased starch content²⁰². Our model of these pili showed structure similar to those of the *Pseudomonas* and *Neisseria* species (Supplementary Figure 7.8), suggesting *B. adolescentis* pili could be also conductive and these bacteria could be capable of direct-contact EET to survive in dynamic and turbulent gut environments. Thus, increasing abundance of conductivity pili could promote the growth of commensals. A greater understanding of the role of EET may lead to novel strategies for accelerating the growth and colonization of probiotic microbes.

In addition to promoting commensal growth, understanding pili-mediated EET could lead to a new class of pili-intercalating compounds designed to inhibit pathogen colonization and growth. Such a new generation of therapeutics might be transformative, because to overcome this unique aspect of bacterial survival via EET may exceed the ability of bacteria to adapt. To date, there is limited success for current methods that target adhesive pili²⁰³, such as carbohydrate derivatives of host receptors to block pili adhesion²⁰⁴. Because a large number of pilin variants can arise from phage and antigenic variation²⁰⁴, an effective antibody response is extremely challenging against pathogens and repeated infections occur. The electron transfer in stacked aromatic molecules can be manipulated by a diversity of mechanisms. For example, a variety of small molecules, such as Rhodium complexes, can selectively intercalate between base stacking of aromatic molecules²⁰⁵ to interrupt stacking and block electron transfer. Such small molecules could serve as potential drugs to suppress pilus-mediated adhesion.

In summary, our finding of EET via conductive T4P resolves a long-standing puzzle about how pathogens overcome host repulsion. Our finding suggests that targeting microbe-to-microbe and microbe-to-host EET via T4P at the adhesion stage of infection may offer a novel strategy for

preventing and treating bacterial infections. Suppressing colonization and growth of pathogens and promoting colonization and growth of commensals could help optimize the composition of microbial communities to prevent dysbiosis without causing the harmful side effects of current anti-inflammatory and immunoresponsive therapies²⁰⁶.

7.6 Materials and Methods

This section contains descriptions of the experimental methods used to collect the data described in this chapter. Detailed descriptions of the computational methods can be found in Chapter 2.

7.6.1. Bacterial strains and culture conditions

N. gonorrhoeae strain MS11 and *V. cholerae* strain RT4225 were obtained from the Craig lab culture collection. *P. aeruginosa* strains PAO1 and PA103 were obtained from Barbara Kazmierczak (Yale University School of Medicine). *N. meningitidis* strains belong to the Dumenil lab culture collection, derived from the 8013 serogroup C strain. Generation of *N. meningitidis pilE* point mutants was described previously^{196,207}.

7.6.2. *N. gonorrhoeae* pilus purification

T4P from *N. gonorrhoeae* were purified as previously described²⁰⁸. Briefly, *N. gonorrhoeae* strain MS11 cells were grown on GCB agar plates containing Kellogg's supplements in a moist atmosphere at 37 °C with 5% CO₂. Cells were collected and vortexed to shear the pili from the cells, and cells were removed by centrifugation at 4,000 x g for 30 min at 4 °C. The pili in the supernatant were resuspended in 50 mM CHES buffer, pH 9.5 and purified by precipitation in pilus buffer [50 mM Tris (pH 7.5), 150 mM NaCl, 0.02% NaN₃ and 1 mM dithiothreitol]. The sample was incubated for 2 hr on ice followed by centrifugation at 15,000 x g, 30 min. The pellet containing the pili was resuspended in CHES buffer.

7.6.3. *N. meningitidis* pilus purification

Pili were prepared as described previously²⁰⁹. Briefly, *N. meningitidis* was grown on GCB agar plates containing Kellogg's supplements in a moist atmosphere containing 5% CO₂ at 37 °C. Bacteria from 10–12 plates were harvested in 5 mL of 150 mM ethanolamine at pH 10.5. Pili were sheared by vortexing for 1 min. Bacteria were pelleted by centrifugation at 4,000 x g for 30 min at 4 °C. The resulting supernatant was further centrifuged at 15,000 x g, 30 min, ambient temperature to remove residual cells. The pili were then precipitated from the supernatant by the addition of 10% (mass/vol) ammonium sulfate saturated in 150 mM ethanolamine buffer at pH 10.5 and allowed to stand for 1 h. The aggregated pili were pelleted by centrifugation at 4,000 x g for 1 h at 20 °C.

7.6.4. *P. aeruginosa* pilus purification

P. aeruginosa T4P were prepared from strain PA103 cells grown on LB agar plates. The cells were suspended TPM buffer (10 mM Tris HCl, 1 mM KPO₄, and 8 mM MgSO₄, pH 7.5) and vortexed for 3 minutes to shear the pili from the cells. The cells were pelleted by 8,000 x g for 5 minutes at room temperature. Pili were precipitated from the supernatant by adding MgCl₂ to a final concentration of 100 mM. The sample was incubated on ice for 4 hours. The sample was then centrifuged at 24,000 x g for 15 minutes to pellet the pili. The pellet was resuspended in 150 mM ethanolamine, pH 10.5.

7.6.5. *V. cholerae* pilus purification

V. cholerae T4bP were expressed and purified as previously described¹⁷³. Briefly, *V. cholerae* classical strain RT4225 was grown in 800 ml LB [1% tryptone, 0.5% yeast extract and 86 mM NaCl (pH 6.5)]-streptomycin/ampicillin/IPTG for 16 h at 30 °C, in a rotating drum. The RT4225 strain has a mutation encoding a H161A substitution in the *tcpA* gene which causes the pili to fall off the cells into the cell culture. Overnight cultures were centrifuged to remove cells, and TCP were precipitated from the supernatant using 30% ammonium sulphate, in PBS. Pili were pelleted

by centrifugation and the pellet was resuspended in ethanolamine buffer, pH 10.5. The resuspended pili sample was dialyzed in the same buffer to remove residual ammonium sulphate. All purification steps were performed on ice or at 4 °C.

7.6.6. Nanoelectrode design and fabrication

Gold electrodes separated by a 300-nm non-conductive gap were designed using electron beam lithography. Si wafer with 300 nm thermally grown oxide was used as a substrate. The electrodes were first patterned by electron-beam lithography on a photoresist layer. A 30-nm-thick gold film on top of a 5-nm-thick titanium adhesion layer was thermally evaporated on lithographically patterned wafer. The photoresist was removed with acetone and rinsed with methanol and isopropanol, resulting in gold nanoelectrodes with a 300-nm gap. Before usage, the device was washed with distilled water and then rinsed with isopropanol to remove contaminants on the surface. The device was further plasma cleaned for 1 min and dried with nitrogen flow, yielding a hydrophilic surface.

7.6.7. Preparation of pili for conductivity measurements

Cell-free pilus preparations were imaged with transmission electron microscopy to ensure sample quality. Dilute 5 µl solutions containing pili were placed on gold nanoelectrodes to achieve individual filaments bridging two electrodes (Fig. 1d). Pili were imaged with AFM and height measurements were performed to confirm the presence of individual filaments. Samples were maintained under hydrated buffer environments (150 mM ethanolamine) and pH of the buffer was equilibrated using HCl.

7.6.8. Electrical (DC) conductivity measurements

All DC conductivity measurements were performed in a 2-electrode configuration using a semiconductor parameter analyser (Keithly 4200A-SCS) equipped with preamplifiers, allowing 0.1 fA current resolution and 0.5 µV voltage resolution. A fixed potential was applied between

the two electrodes and the current through the sample was measured over a period of 180 seconds (minimum) in sampling mode until the steady state was reached. The magnitude of the potential bias was kept below 200 mV to avoid thermally activated current contributions and to remain in the ohmic conductance regime. The slope of I - V curve was used to determine the conductance ($G=I/R$). All analysis was performed using Igor Pro software (Wavemetrics Inc.).

7.6.9. Conductivity calculations

The conductivity (σ) of pili filaments was calculated using the relation $\sigma = G (L/A)$ where G is the conductance, L is the length of the pili and $A = \pi r^2$ is the area of cross section of pili with $2r$ as the height of the pilus measured using AFM.

7.6.10. Single Cell Force Spectroscopy (SCFS)

AFM probes for single cell force spectroscopy methods were prepared as described previously^{190,191}. Briefly, silica microspheres (SS06N, Bangs Laboratories) of diameter 6.46 μm were fixed to tipless AFM cantilevers (PNP-TR-TL-Au, NanoWorld) using UV curable optical adhesive (NOA 61, Norland Products). The probes were immersed in 10 mM Tris buffer (pH 8.5) containing 4 mg/ml Dopamine hydrochloride (H8502, Sigma Aldrich) for 1 hour after which the probes were rinsed with Milli-Q and dried with N_2 .

P. aeruginosa PAO1 cells were grown overnight on LB agar. Individual colonies were scraped from the plate and resuspended in phosphate buffered saline, pH 7.2 (PBS). Cells were labelled using the LIVE/DEAD[®] BacLight viability kit (L7012, Thermo Fisher Scientific). Labelled cells were drop cast on freshly cleaved muscovite mica (71855-01, Electron Microscopy Sciences). Using a Cypher ES atomic force microscope (Asylum Corporation, Oxford Instruments), individual cells were attached to the polydopamine coated AFM probe. Specifically, the probe was lowered in the cell-containing phosphate buffered saline (PBS) until stable contact with the mica surface was detected. Contact was held for 3 minutes before withdrawing. Bacterial

attachment was verified after the experiment by placing the probe on a glass coverslip and imaged on a fluorescence microscope.

Force spectroscopy was performed at 30 °C using an Asylum Cypher ES atomic force microscope. Probe calibration and spring constant determination was achieved via the thermal noise method. Experiments were performed on freshly cleaved muscovite mica in PBS, pH adjusted to either pH 7.2 or 5.0. At each pH, force-distance curves were generated at 5 positions on the substrate, with at least 100 curves being collected at each position. Curves were generated using a constant approach and retraction velocity of 950 nm/s. Retraction was triggered upon an application of a force ranging from 0.7 – 2 nN with no dwell time. This process was performed for each cell at pH 7.2 and was then immediately repeated at pH 5.0. For wild-type cells, we collected 809 force curves at pH 7.2 and 505 force curves at pH 5.0. For $\Delta pilA$ cells, we collected 220 force curves at pH 7.2 and 235 force curves at pH 5.0. At pH 7.2, only 81 force curves from $\Delta pilA$ cells showed a clear adhesion event. Control experiments were performed on probes upon which no cells were attached, which showed no change in adhesion force between the two pH conditions. A Student's t-test was performed on the adhesion force data using Igor Pro software (Wavemetrics Inc), which returned a p-value of 7.6×10^{-77} for the comparison between the adhesion of wild-type cells at pH 7.2 and pH 5.0.

To test the effect of EET on adhesion, the experiment was repeated in PBS to which we added 10 – 100 μ M pyocyanin or 30 mM sodium azide. The tip attached cells were immediately submerged in the pyocyanin or azide suspension and measurements were performed.

7.6.11. Bacterial adhesion Assay

Human umbilical vein endothelial cells (HUVEC - PromoCell) were used between passages 1 and 8 and grown in Human Endothelial-SFM (Gibco) supplemented with 10% heat-inactivated fetal bovine serum (PAA Laboratories) and 40 μ g/ml of endothelial cell growth supplement (Sigma-Aldrich) and passed every 2-3 days. HUVEC cells were incubated with GFP-expressing

N. meningitidis cells bearing pili with the same aromatic amino acid changes as those used in the conductivity and pilus adhesion measurements. Cells were washed, fixed, and imaged by fluorescence microscopy to quantify the number of adherent *N. meningitidis* cells. For early adhesion assays, 3.5×10^4 cells were seeded in Cellstar[®] 96 well plates (Greiner) the day before infection. On the next day, cells were rinsed once. Hoechst was added to the medium at a final concentration of 1 $\mu\text{g/ml}$ and cells were infected with midlog-phase GFP-bacteria (multiplicity of infection, 500) for 30 minutes at 37 °C - 5% CO₂. Wells were rinsed 3 times and then fixed with 4% formaldehyde for 30 min at room temperature. Wells were rinsed 3 times with PBS and then imaged with a 40x objective. Each infection was run in duplicate, and 16 images were taken per well. A homemade macro in Fiji was used to count the number of bacteria and nuclei per field of view. These values were summed for each well and a ratio of the total number of bacteria over the total number of nuclei was used to evaluate the number of bacteria per cell.

7.6.12. *Electrostatic Force Microscopy (EFM) on graphene oxide (GO)*

The sample was prepared by depositing graphene oxide (GO) flakes suspended in deionized water on a freshly cleaved mica surface. After washing thrice with deionized water to remove large GO particles, plate-grown *P. aeruginosa* PA103 cells, suspended in deionized water, were deposited and allowed to settle on the surface for 30 minutes. Extraneous cells and debris were washed away with deionized water and the sample was allowed to air dry. Before performing EFM, bacteria adhered to the GO flakes were localized by imaging the sample topography with AFM in AC mode. To inhibit EET, 10 – 100 μM pyocyanin or 30 mM sodium azide was added to the cell suspension prior to drop-casting cells on the GO surface.

EFM experiments were performed with an Asylum Cypher ES atomic force microscope following a previously described procedure^{210,211}. Qualitative EFM images were acquired before and after charge injection on the GO surface using tip voltages of ± 3 V. Charge injection was achieved via a series of approach-retract curves while biasing the EFM cantilever with an

injection voltage of +10 V with respect to the substrate. During the approach-retract curves, 150 nN of force was applied to the surface for 2 s, followed by a dwell of 5 s above the surface. This was repeated over the course of a minute.

Quantification of mobile charge density was performed by collecting the EFM phase image at tip voltages (V_{EFM}) varying from -7 V to +7 V in 1 V increments. The average phase over the GO surface at each tip voltage was fit to the expression $\Delta\Phi = \Delta\Phi_Q + \Delta\Phi_C = AV_{EFM} + BV_{EFM}^2$ where $\Delta\Phi_Q$ and $\Delta\Phi_C$ are the Coulombic and capacitive contributions to the measured phase shift, respectively.

The ratio of the fitting parameters was used to extract the surface charge density using the equation

$$\frac{A}{B} = -\frac{g \sigma \times e \times z}{\alpha \epsilon_R \times \epsilon_0} \quad (7.1)$$

where z is the distance between the tip and the substrate (20 nm), e is the elementary charge (1.602×10^{-19} C), ϵ_R is the dielectric constant for the GO surface (equal to 3 for GO), ϵ_0 is vacuum permittivity, α is the tip shape factor (1.5 for a conical tip), g is the sample shape factor (equal to 5 for planar GO), and σ is the surface charge density.

7.6.13. Current generation in a microbial fuel cell (MFC)

P. aeruginosa PA103 cells were grown in anaerobic LB media in the anode of a microbial fuel cell with graphite electrodes. The anode was held at a potential of 300 mV vs. Ag/AgCl, and current was monitored with a Gamry potentiostat. The cells were grown in batch mode (no flow) and constantly bubbled with a CO₂/H₂ gas mix to maintain anaerobic conditions. After 5 days, the cell suspension was drained and replaced with fresh anaerobic LB media leaving only cells adhered to the graphite electrode. Fresh media was constantly supplied at a flow rate of 0.5 ml/min (flow-through mode). The current output was observed for up to a week following the media exchange.

7.6.14. Bacterial biofilm voltammetry

P. aeruginosa PAO1 cells (wild-type or $\Delta pilA$) grown on LB agar plates overnight were scraped and resuspended in anaerobic PBS (sparged with N_2) at an OD_{600} of 0.6. In an N_2 environment, 100 μ l of cell suspension was deposited on a planar gold electrode in a circular polydimethylsiloxane (PDMS) chamber with a radius of 3 mm. The electrochemical circuit was connected in the canonical 3-electrode configuration using a platinum counter electrode and an Ag/AgCl (3.5 M KCl) reference electrode. The planar gold electrode served as the working electrode. Cyclic voltammetry and differential pulse voltammetry experiments were performed over potentials ranging from -0.7 V vs. Ag/AgCl to 0.7 V vs. Ag/AgCl using a potentiostat (Gamry Corp.). A scan rate dependence of the peak current from the cyclic voltammetry was performed to identify diffusive vs. bound redox species. The peak current was extracted from the oxidation peaks corresponding to the peak systems at midpoint redox potentials of -250 mV and 64 mV vs. Ag/AgCl using the multipeak fitting plugin in the Igor Pro software. The data was fit with the equation,

$$I_p \propto Av^\alpha \quad (7.2)$$

to extract alpha (slope of the log-log plot in Fig. 3c), which informs on the mode of charge mobility. A value of $\alpha = 1$ indicates direct contact between the electrode and the redox species, whereas a value of $\alpha = 0.5$ indicates a diffusive species.

Electrochemical impedance spectroscopy was performed in the same configuration as the voltammetry experiments. The frequency of the AC signal was scanned from 10^5 Hz to 0.1 Hz. This was repeated at DC voltage offsets ranging from -250 mV to 250 mV. The charge transfer resistance between the bacteria and working electrode was extracted by fitting with the equivalent circuit in Figure 7.3d using the Gamry Echem AnalystTM software.

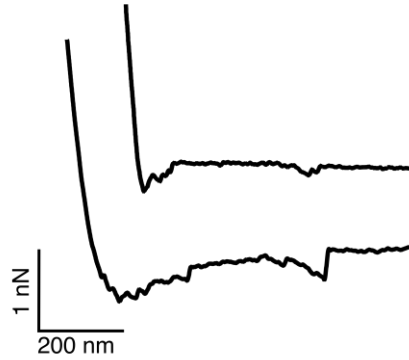
7.6.15. Molecular dynamics (MD) simulations.

The atomic structure for the T4P of *N. meningitidis* was obtained from the protein data bank (PDB ID: 5KUA). Ten protein chains from the original structures were included for each pilus structure used. Point mutations were introduced using the VMD⁹⁸ Mutate Residue plugin. All structures were hydrated in a TIP3P water box and ionized with Na⁺ or Cl⁻ to neutralize the charge of the system using VMD. MD simulations were performed with NAMD¹¹¹ using CHARMM36⁷⁵ force-field parameters with periodic boundary conditions. First, hydrated and ionized systems were minimized, followed by a 500 ps simulation of the water box with fixed protein conformation. Then, each system was gradually heated to 310 K and equilibrated under NVT conditions for a total of 3.5 ns. During the equilibration, different restraints were imposed on the protein backbone and side-chain atoms. Finally, the production simulation was run for 100 ns (all *N. meningitidis* models) without any restraints under NPT conditions using Langevin dynamics with 2-fs timestep at 310 K and 1 atm. Snapshots were collected in 2.5 ns interval resulting in a total of 40,000 frames for subsequent analysis. Structure of the *B. adolescentis* type IVa pilus was modelled using AlphaFold²¹².

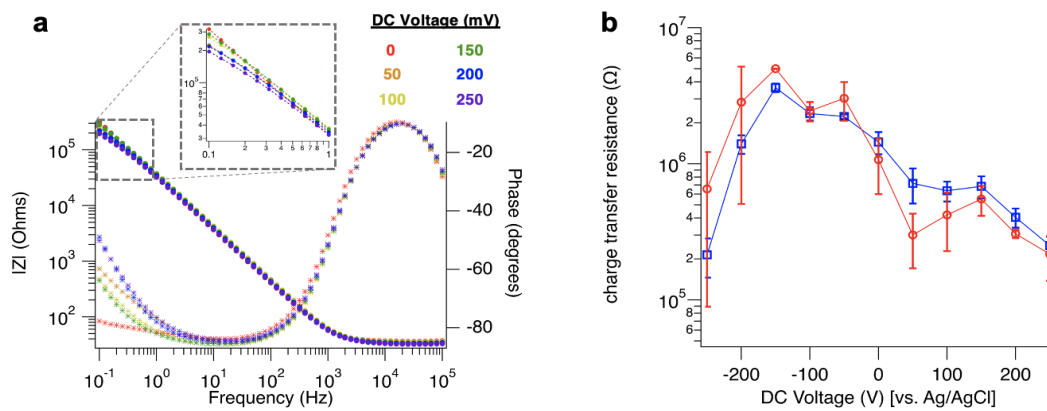
7.6.16. Analysis of optimal charge transfer pathways.

We truncated the end of the pilus from each snapshot to avoid edge artefacts in pathway analysis. A network of aromatic residues was analysed, where each aromatic residue in the model serves as a node of the network. A distance matrix was populated with the mean distance between each pair of aromatic residues. To compute the shortest paths along the pilus, we employed a Dijkstra algorithm to determine the optimal path between each set of designated aromatic donor and acceptor residues²¹³ for a set of 5 to 6 donor residues and 5 to 6 acceptor residues placed in opposing extremes of the truncated pilus. For each path calculated, we computed the mean of the distances between adjacent residues and averaged that metric over all frames. We have termed this the mean electron transfer distance (Fig. 3b).

7.7 Supplementary Information

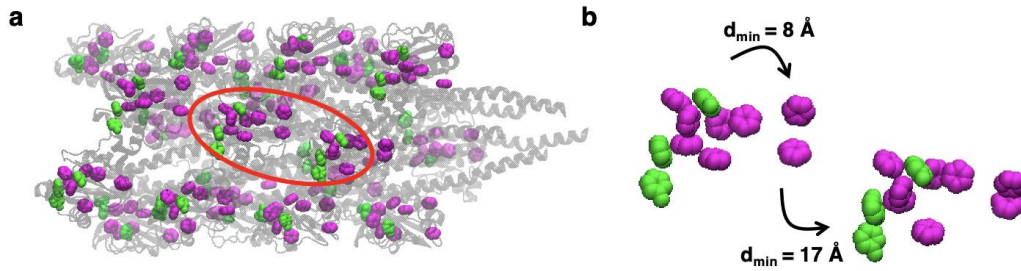


Supplementary Figure 7.1: Example force curves from single cell force spectroscopy.



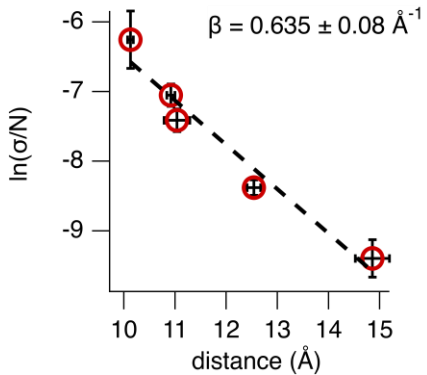
Supplementary Figure 7.2: Pili reduce the charge transfer resistance between *Pseudomonas aeruginosa* and a planar surface

(a) Impedance spectra and (b) charge transfer resistance at various DC voltages. WT (red) and $\Delta pilA$ (blue).



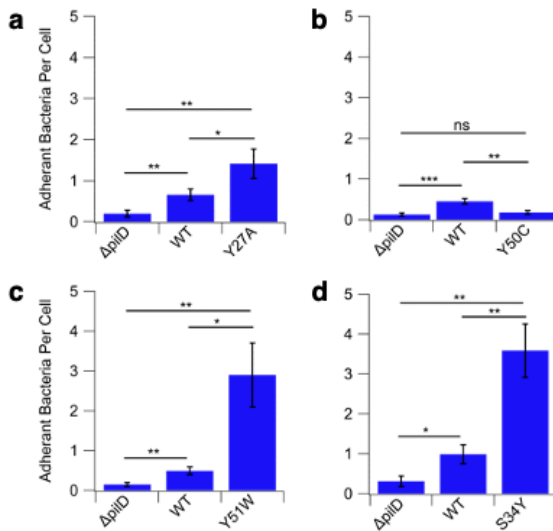
Supplementary Figure 7.3: Aromatic residues in *Vibrio cholerae* T4bP are too far apart to confer high conductivity.

(a) Depiction of the *V. cholerae* T4bP model, highlighting the positions of the aromatic amino acids. Phenylalanine residues are shown in magenta and tyrosine residues are shown in green. (b) Magnified cluster of aromatic residues on the C-terminal globular domains of the pilin subunits with the minimum distances (d_{\min}) between aromatic clusters.



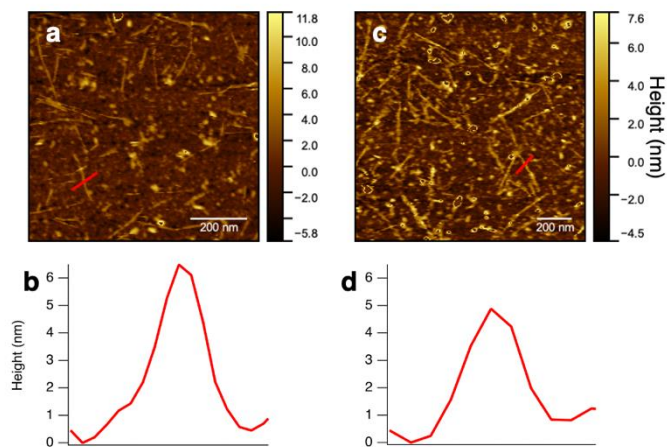
Supplementary Figure 7.4: Conductivity of *Neisseria meningitidis* T4P is exponentially dependent on distance.

Natural log of the experimentally measured conductivity normalized by the computed number of electron transfer paths plotted against the computed distance between aromatics. These data are fit by linear regression with an r-squared of 0.95.



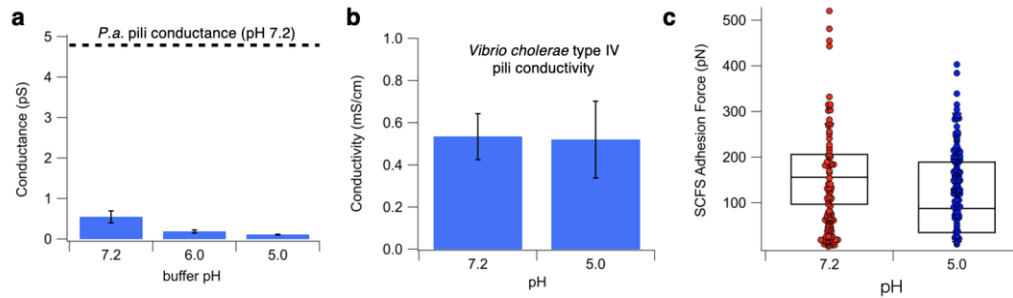
Supplementary Figure 7.5: Adhesion of *N. meningitidis* to HUVEC cells increases with the conductivity of the pilus expressed by the bacteria.

Each graph represents the quantification of *N. meningitidis* adhesion to HUVEC cells for non-piliated (Δ pilD) bacteria, wild-type (WT) bacteria, and bacteria expressing a pilus variant, all three of which were measured in parallel. The pilus variants measured include **a**, Y27A (Error bars represent s.e.m.; n=16), **b**, Y50C (Error bars represent s.e.m.; n=12), **c**, Y51W (Error bars represent s.e.m.; n=9), and **d**, S34Y (Error bars represent s.e.m.; n=9).



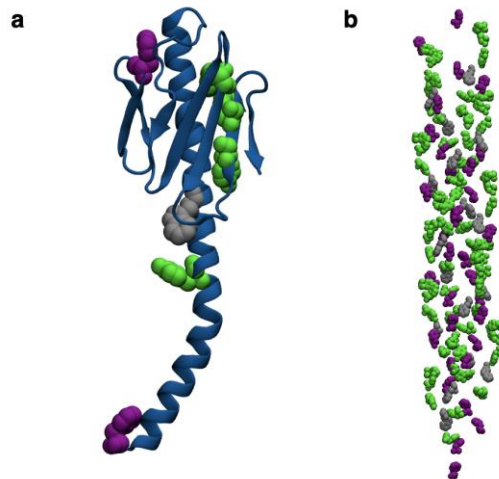
Supplementary Figure 7.6: Lowering the pH reduces the diameter of *P. aeruginosa* pili.

(a) AFM image of *P. aeruginosa* T4P at pH 7. **(b)** Representative height profile from a pilus at pH 7. The red line in (a) indicates the location from which the height trace was obtained. **(c)** AFM image of *P. aeruginosa* T4P at pH 5. **(d)** Representative height profile from a pilus at pH 5 at a location shown in (c).



Supplementary Figure 7.7: The lack of pH dependent conductivity increase in the buffer and *Vibrio cholerae* T4bP.

(a) pH dependence of the conductance of pH-adjusted buffer. The dashed line show the conductance of *P.aeruginosa* T4aP at pH 7.2. (Error bars represent s.e.m.; n=4). pH dependence of *V. cholerae* T4bP (b) conductivity (Error bars represent s.e.m.; n=6) and (c) adhesion (Error bars represent s.e.m.; n≥3). (d) Adhesion force of AFM tip used for pilus adhesion measurements against air dried mica prepared at pH 10.5, 7.0, and 6.0 (Error bars represent s.e.m.; n=3). (e) pH dependence of the single cell force spectroscopy adhesion force of *P. aeruginosa* $\Delta pilA$ cells on mica. Data are represented as a boxplot overlaid with a scatter dot plot. The box was defined as 25 and 75% with center line as median and the whiskers as 10 and 90% (n≥80 force curves). (f) pH dependence of the adhesion force between the single cell force spectroscopy probe and the mica substrate. Data is represented as a boxplot overlaid with a scatter dot plot. The box was defined as 25 and 75% with center line as median and the whiskers as 10 and 90%. (n≥101 force curves).



Supplementary Figure 7.8: Predicted structure of the *B. adolescentis* Type IVa pilus.

(a) AlphaFold predicted structure of the type IVa major pilin from *B. adolescentis*. (b) Arrangement of aromatic residues in a filament composed of the predicted pilin structure in (a). Phenylalanine is shown in purple, tyrosine is shown in green, and tryptophan is shown in grey.

8. Conclusions and Future Directions

When I started my dissertation research the ability of multiheme cytochromes to polymerize was unknown. I started by measuring the electrical conductivities of the type IV pili of the pathogens *Pseudomonas aeruginosa*, *Neisseria meningitidis*, and *Vibrio cholerae*. While the conductivities I measured were lower than the reported values for the protein nanowires of *G. sulfurreducens*, my results appeared to support the hypothesis that *G. sulfurreducens* had conductive type IV pili. The discovery of the OmcS cytochrome nanowire came as quite a surprise. The discovery bred confusion and created more questions than it answered. The hypothesis of conductive pili in *G. sulfurreducens* was wrong, and *G. sulfurreducens* does not even produce type IV pili. How should we interpret our results on the pili of pathogens? Can non-cytochrome proteins support long-range charge transport at all? I consider myself very fortunate to have been able to witness the discovery of cytochrome nanowires. The discovery gave structure to my thesis, allowing me to compare the mechanisms of charge transport in cytochromes as well as in non-cytochrome proteins. While there are still many questions regarding charge transport in protein nanowires, I am proud to have contributed to our understanding of the mechanisms of long-range charge transport in biology.

A common theme throughout my dissertation research is the incredible tunability of protein nanowire conductivity. The conductivity of amyloid crystals with stacked tyrosine residues increased 200-fold with a decrease in temperature of 30 degrees (Chapter 6). The same effect was observed in OmcS nanowires, which contain hemes rather than tyrosines (Chapter 4). The most remarkable result was a 30,000-fold increase in the conductivity of OmcZ nanowires in response to increased relative humidity (Chapter 5). While the specifics of the mechanisms of the conductivity increased were unique to each system, there was a commonality. All mechanisms were dependent on protons. The amyloid crystals depended on a PCET mechanism, and required a hydrogen bond be formed with the tyrosine before it could transfer an electron; OmcS experienced a global change in its hydrogen bonding network, which influenced the secondary

coordination sphere of the hemes; and OmcZ utilizes a mixed protonic-electronic conduction mechanism, in which the mobility of protons limits the mobility of electrons.

The discovery of these mechanisms highlights a unique characteristic of biological electron transport: In proteins, electrons cannot escape protons. This relates back to the electron transport chain in eukaryotic mitochondria, in which electron transport down a redox gradient drives proton transfer across the inner membrane. This process enables production of ATP to support cellular function. In protein nanowires, there is no redox gradient, therefore, they cannot pump protons. However, the sensitivity of the electron transport mechanism to protons may serve a biological function. The sensitivity of the hydrogen bonding networks to environmental perturbations, and their effect on conductivity suggests the nanowires may regulate bacterial metabolism in response to environmental stress.

Protein nanowires can also be tuned through site-directed mutagenesis. Shapiro et al. demonstrated that the addition of non-standard amino acids increased the conductivity of *E. coli* type I pili 170-fold⁵². In collaboration with Paul Kennouche from the Dumenil lab (Pasteur Institute) we demonstrated that point mutations in the type IV pili of *N. meningitidis* could also increase pilus conductivity (Chapter 7). These results indicate that the tools of molecular biology will be able to create nanowires with user-defined conductivities. And in this case of the *N. meningitidis* pili, we demonstrated that increased conductivity of pili led to increased bacterial attachment, a critical first step in many infectious diseases. Therefore, this result also demonstrates a direct relevance to human health.

As our understanding of the mechanisms of charge transport in protein nanowires improves, new technologies will emerge. OmcZ has already shown utility in the generation of clean energy (Chapter 5), and devices utilizing a similar power generation strategy have been shown to be capable of powering wearable electronics²¹⁴. However, there is work to be done toward understanding the high conductivity of the OmcZ nanowire. Our current computational models can identify factors which increase or decrease conductivity of a nanowire, but still result in large

underestimates of the conductivity value. Now that the structure of the OmcZ nanowires has been published, the greater electron transfer field can begin modeling efforts. Whether the truth behind protein nanowire conductivity fits within the biological electron transfer paradigm or new mechanisms need to be invoked is yet to be seen.

9. References

1. Zhang, B., Ryan, E., Wang, X., Song, W. & Lindsay, S. Electronic transport in molecular wires of precisely controlled length built from modular proteins. *ACS Nano* **16**, 1671-1680, (2022).
2. Graves, A. B., Graves, M. T. & Liptak, M. D. Measurement of heme ruffling changes in MhuD using UV-vis spectroscopy. *The Journal of Physical Chemistry B* **120**, 3844-3853, (2016).
3. Shipps, C., Kelly, H. R., Dahl, P. J., Yi, S. M., Vu, D., Boyer, D., Glynn, C., Sawaya, M. R., Eisenberg, D., Batista, V. S. & Malvankar, N. S. Intrinsic electronic conductivity of individual atomically resolved amyloid crystals reveals micrometer-long hole hopping via tyrosines. *Proceedings of the National Academy of Sciences* **118**, e2014139118, (2021).
4. Hartree, E. F. The discovery of cytochrome. *Biochemical Education* **1**, 69-71, (1973).
5. Marcus, R. A. On the theory of oxidation-reduction reactions involving electron transfer. *The Journal of Chemical Physics* **24**, 966-978, (1956).
6. Moser, C. C., Keske, J. M., Warncke, K., Farid, R. S. & Dutton, P. L. Nature of biological electron transfer. *Nature* **355**, 796-802, (1992).
7. Gray, H. B. & Winkler, J. R. Electron transfer in proteins. *Annual Review of Biochemistry* **65**, 537-561, (1996).
8. Beratan, D. N., Betts, J. N. & Onuchic, J. N. Protein electron transfer rates set by the bridging secondary and tertiary structure. *Science* **252**, 1285-1288, (1991).
9. Onuchic, J. N., Beratan, D. N., Winkler, J. R. & Gray, H. B. Pathway analysis of protein electron-transfer reactions. *Annual review of biophysics and biomolecular structure* **21**, 349-377, (1992).
10. Ho Choi, S., Kim, B. & Frisbie, C. D. Electrical resistance of long conjugated molecular wires. *Science* **320**, 1482-1486, (2008).
11. Ghorai, P. K. & Matyushov, D. V. Reorganization energy of electron transfer in viscous solvents above the glass transition. *The Journal of Physical Chemistry B* **110**, 1866-1871, (2006).

12. Krishnan, S., Aksimentiev, A., Lindsay, S. & Matyushov, D. Long-range hopping conductivity in proteins. *bioRxiv*, 2022.2010.2027.514097, (2022).
13. LeBard, D. N. & Matyushov, D. V. Protein–water electrostatics and principles of bioenergetics. *Physical Chemistry Chemical Physics* **12**, 15335-15348, (2010).
14. Martin, D. R. & Matyushov, D. V. Electron-transfer chain in respiratory complex I. *Scientific Reports* **7**, 5495, (2017).
15. Seyedi, S. S., Waskasi, M. M. & Matyushov, D. V. Theory and electrochemistry of cytochrome c. *The Journal of Physical Chemistry B* **121**, 4958-4967, (2017).
16. Martin, D. R., Dinpajoo, M. & Matyushov, D. V. Polarizability of the active site in enzymatic catalysis: cytochrome c. *The Journal of Physical Chemistry B* **123**, 10691-10699, (2019).
17. Jiang, X., Futera, Z. & Blumberger, J. Ergodicity-breaking in thermal biological electron transfer? Cytochrome c revisited. *The Journal of Physical Chemistry B* **123**, 7588-7598, (2019).
18. Wei, J. J., Liu, H., Niki, K., Margoliash, E. & Waldeck, D. H. Probing electron tunneling pathways: electrochemical study of rat heart cytochrome c and its mutant on pyridine-terminated SAMs. *The Journal of Physical Chemistry B* **108**, 16912-16917, (2004).
19. Monari, S., Battistuzzi, G., Bortolotti, C. A., Yanagisawa, S., Sato, K., Li, C., Salard, I., Kostrz, D., Borsari, M., Ranieri, A., Dennison, C. & Sola, M. Understanding the mechanism of short-range electron transfer using an immobilized cupredoxin. *Journal of the American Chemical Society* **134**, 11848-11851, (2012).
20. Mendez, D. L., Babbitt, S. E., King, J. D., D'Alessandro, J., Watson, M. B., Blankenship, R. E., Mirica, L. M. & Kranz, R. G. Engineered holocytochrome c synthases that biosynthesize new cytochromes c. *Proceedings of the National Academy of Sciences* **114**, 2235-2240, (2017).
21. Davies, A. M., Guillemette, J. G., Smith, M., Greenwood, C., Thurgood, A. G., Mauk, A. G. & Moore, G. R. Redesign of the interior hydrophilic region of mitochondrial cytochrome c by site-directed mutagenesis. *Biochemistry* **32**, 5431-5435, (1993).
22. Kleingardner, J. G. & Bren, K. L. Biological significance and applications of heme c proteins and peptides. *Accounts of Chemical Research* **48**, 1845-1852, (2015).

23. Kleingardner, J. G., Levin, B. D., Zoppellaro, G., Andersson, K. K., Elliott, S. J. & Bren, K. L. Influence of heme c attachment on heme conformation and potential. *JBIC Journal of Biological Inorganic Chemistry* **23**, 1073-1083, (2018).
24. Michel, L. V., Ye, T., Bowman, S. E. J., Levin, B. D., Hahn, M. A., Russell, B. S., Elliott, S. J. & Bren, K. L. Heme attachment motif mobility tunes cytochrome c redox potential. *Biochemistry* **46**, 11753-11760, (2007).
25. Mohamed-Raseek, N., van Galen, C., Stanley, R. & Miller, A.-F. Unusual reactivity of a flavin in a bifurcating electron-transferring flavoprotein leads to flavin modification and a charge-transfer complex. *Journal of Biological Chemistry* **298**, (2022).
26. Battistuzzi, G., Borsari, M., Loschi, L., Menziani, M. C., De Rienzo, F. & Sola, M. Control of metalloprotein reduction potential: The role of electrostatic and solvation effects probed on plastocyanin mutants. *Biochemistry* **40**, 6422-6430, (2001).
27. Shifman, J. M., Gibney, B. R., Sharp, R. E. & Dutton, P. L. Heme redox potential control in *de novo* designed four- α -helix bundle proteins. *Biochemistry* **39**, 14813-14821, (2000).
28. Anraku, Y. Bacterial electron transport chains. *Annual Review of Biochemistry* **57**, 101-132, (1988).
29. Green, J. & Paget, M. S. Bacterial redox sensors. *Nature Reviews Microbiology* **2**, 954-966, (2004).
30. Torrents, E. Ribonucleotide reductases: essential enzymes for bacterial life. *Frontiers in Cellular and Infection Microbiology* **4**, (2014).
31. Caccavo, F., Lonergan, D. J., Lovley, D. R., Davis, M., Stolz, J. F. & McInerney, M. J. *Geobacter sulfurreducens* sp. nov., a hydrogen- and acetate-oxidizing dissimilatory metal-reducing microorganism. *Applied and Environmental Microbiology* **60**, 3752-3759, (1994).
32. Coates, J. D., Phillips, E. J., Lonergan, D. J., Jenter, H. & Lovley, D. R. Isolation of *Geobacter* species from diverse sedimentary environments. *Applied and Environmental Microbiology* **62**, 1531-1536, (1996).
33. Nealson, K. H., Belz, A. & McKee, B. Breathing metals as a way of life: geobiology in action. *Antonie van Leeuwenhoek* **81**, 215-222, (2002).

34. Semprini, L. Strategies for the aerobic co-metabolism of chlorinated solvents. *Current Opinion in Biotechnology* **8**, 296-308, (1997).
35. Bond, D. R. & Lovley, D. R. Electricity production by *Geobacter sulfurreducens* attached to electrodes. *Applied and Environmental Microbiology* **69**, 1548-1555, (2003).
36. Reguera, G., Nevin Kelly, P., Nicoll Julie, S., Covalla Sean, F., Woodard Trevor, L. & Lovley Derek, R. Biofilm and nanowire production leads to increased current in *Geobacter sulfurreducens* fuel cells. *Applied and Environmental Microbiology* **72**, 7345-7348, (2006).
37. Nevin Kelly, P. & Lovley Derek, R. Lack of production of electron-shuttling compounds or solubilization of Fe(III) during reduction of insoluble Fe(III) oxide by *Geobacter metallireducens*. *Applied and Environmental Microbiology* **66**, 2248-2251, (2000).
38. Hernandez, M. E. & Newman, D. K. Extracellular electron transfer. *Cellular and Molecular Life Sciences CMLS* **58**, 1562-1571, (2001).
39. Shi, L., Dong, H., Reguera, G., Beyenal, H., Lu, A., Liu, J., Yu, H.-Q. & Fredrickson, J. K. Extracellular electron transfer mechanisms between microorganisms and minerals. *Nature Reviews Microbiology* **14**, 651-662, (2016).
40. Craig, L., Pique, M. E. & Tainer, J. A. Type IV pilus structure and bacterial pathogenicity. *Nature Reviews Microbiology* **2**, 363-378, (2004).
41. Reguera, G., McCarthy, K. D., Mehta, T., Nicoll, J. S., Tuominen, M. T. & Lovley, D. R. Extracellular electron transfer via microbial nanowires. *Nature* **435**, 1098-1101, (2005).
42. Gu, Y., Srikanth, V., Salazar-Morales, A. I., Jain, R., O'Brien, J. P., Yi, S. M., Soni, R. K., Samatey, F. A., Yalcin, S. E. & Malvankar, N. S. Structure of *Geobacter* pili reveals secretory rather than nanowire behaviour. *Nature* **597**, 430-434, (2021).
43. Wang, F., Gu, Y., O'Brien, J. P., Yi, S. M., Yalcin, S. E., Srikanth, V., Shen, C., Vu, D., Ing, N. L., Hochbaum, A. I., Egelman, E. H. & Malvankar, N. S. Structure of microbial nanowires reveals stacked hemes that transport electrons over micrometers. *Cell* **177**, 361-369.e310, (2019).
44. Dahl, P. J., Yi, S. M., Gu, Y., Acharya, A., Shipps, C., Neu, J., O'Brien, J. P., Morzan, U. N., Chaudhuri, S., Guberman-Pfeffer, M. J., Vu, D., Yalcin, S. E., Batista, V. S. & Malvankar, N. S. A 300-fold conductivity increase in microbial cytochrome nanowires due to temperature-induced restructuring of hydrogen bonding networks. *Science Advances* **8**, eabm7193, (2022).

45. Yalcin, S. E., O'Brien, J. P., Gu, Y., Reiss, K., Yi, S. M., Jain, R., Srikanth, V., Dahl, P. J., Huynh, W., Vu, D., Acharya, A., Chaudhuri, S., Varga, T., Batista, V. S. & Malvankar, N. S. Electric field stimulates production of highly conductive microbial OmcZ nanowires. *Nature Chemical Biology* **16**, 1136-1142, (2020).
46. Malvankar, N. S., Vargas, M., Nevin, K. P., Franks, A. E., Leang, C., Kim, B.-C., Inoue, K., Mester, T., Covalla, S. F., Johnson, J. P., Rotello, V. M., Tuominen, M. T. & Lovley, D. R. Tunable metallic-like conductivity in microbial nanowire networks. *Nature Nanotechnology* **6**, 573-579, (2011).
47. Vargas, M., Malvankar, N. S., Tremblay, P.-L., Leang, C., Smith, J. A., Patel, P., Synoeyenbos-West, O., Nevin, K. P. & Lovley, D. R. Aromatic amino acids required for pili conductivity and long-range extracellular electron transport in *Geobacter sulfurreducens*. *mBio* **4**, e00105-00113, (2013).
48. Xiao, K., Malvankar, N. S., Shu, C., Martz, E., Lovley, D. R. & Sun, X. Low energy atomic models suggesting a pilus structure that could account for electrical conductivity of *Geobacter sulfurreducens* pili. *Scientific Reports* **6**, 23385, (2016).
49. Ru, X., Zhang, P. & Beratan, D. N. Assessing possible mechanisms of micrometer-scale electron transfer in heme-free *Geobacter sulfurreducens* pili. *The Journal of Physical Chemistry B* **123**, 5035-5047, (2019).
50. Polizzi, N. F., Skourtis, S. S. & Beratan, D. N. Physical constraints on charge transport through bacterial nanowires. *Faraday Discussions* **155**, 43-61, (2012).
51. Minnihhan, E. C., Nocera, D. G. & Stubbe, J. Reversible, long-range radical transfer in *E. coli* class Ia Ribonucleotide Reductase. *Accounts of Chemical Research* **46**, 2524-2535, (2013).
52. Shapiro, D. M., Mandava, G., Yalcin, S. E., Arranz-Gibert, P., Dahl, P. J., Shipps, C., Gu, Y., Srikanth, V., Salazar-Morales, A. I., O'Brien, J. P., Vanderschuren, K., Vu, D., Batista, V. S., Malvankar, N. S. & Isaacs, F. J. Protein nanowires with tunable functionality and programmable self-assembly using sequence-controlled synthesis. *Nature Communications* **13**, 829, (2022).
53. Egelman, E. H. A robust algorithm for the reconstruction of helical filaments using single-particle methods. *Ultramicroscopy* **85**, 225-234, (2000).
54. Kühlbrandt, W. The resolution revolution. *Science* **343**, 1443-1444, (2014).

55. Filman, D. J., Marino, S. F., Ward, J. E., Yang, L., Mester, Z., Bullitt, E., Lovley, D. R. & Strauss, M. Cryo-EM reveals the structural basis of long-range electron transport in a cytochrome-based bacterial nanowire. *Communications Biology* **2**, 219, (2019).
56. Mehta, T., Coppi, M. V., Childers, S. E. & Lovley, D. R. Outer membrane c-type cytochromes required for Fe(III) and Mn(IV) oxide reduction in *Geobacter sulfurreducens*. *Applied and Environmental Microbiology* **71**, 8634-8641, (2005).
57. Leang, C., Qian, X., Mester, T. & Lovley, D. R. Alignment of the c-type cytochrome OmcS along pili of *Geobacter sulfurreducens*. *Applied and Environmental Microbiology* **76**, 4080-4084, (2010).
58. Wang, F., Mustafa, K., Suciu, V., Joshi, K., Chan, C. H., Choi, S., Su, Z., Si, D., Hochbaum, A. I., Egelman, E. H. & Bond, D. R. Cryo-EM structure of an extracellular *Geobacter* OmcE cytochrome filament reveals tetrahaem packing. *Nature Microbiology* **7**, 1291-1300, (2022).
59. Wang, F., Chan, C. H., Suciu, V., Mustafa, K., Ammend, M., Si, D., Hochbaum, A. I., Egelman, E. H. & Bond, D. R. Structure of *Geobacter* OmcZ filaments suggests extracellular cytochrome polymers evolved independently multiple times. *eLife* **11**, e81551, (2022).
60. Gu, Y., Guberman-Pfeffer, M. J., Srikanth, V., Shen, C., Giska, F., Gupta, K., Londer, Y., Samatey, F. A., Batista, V. S. & Malvankar, N. S. Structure of *Geobacter* cytochrome OmcZ identifies mechanism of nanowire assembly and conductivity. *Nature Microbiology* **8**, 284-298, (2023).
61. Wang, F., Craig, L., Liu, X., Rensing, C. & Egelman, E. H. Microbial nanowires: type IV pili or cytochrome filaments? *Trends in Microbiology*, (2022).
62. Santos, T. C., Silva, M. A., Morgado, L., Dantas, J. M. & Salgueiro, C. A. Diving into the redox properties of *Geobacter sulfurreducens* cytochromes: a model for extracellular electron transfer. *Dalton Transactions* **44**, 9335-9344, (2015).
63. Jiang, X., van Wonderen, J. H., Butt, J. N., Edwards, M. J., Clarke, T. A. & Blumberger, J. Which multi-heme protein complex transfers electrons more efficiently? comparing MtrCAB from *Shewanella* with OmcS from *Geobacter*. *The Journal of Physical Chemistry Letters* **11**, 9421-9425, (2020).
64. Eshel, Y., Peskin, U. & Amdursky, N. Coherence-assisted electron diffusion across the multi-heme protein-based bacterial nanowire. *Nanotechnology* **31**, 314002, (2020).

65. Zhang, B., Deng, H., Mukherjee, S., Song, W., Wang, X. & Lindsay, S. Engineering an enzyme for direct electrical monitoring of activity. *ACS Nano* **14**, 1360-1368, (2020).
66. Stubbe, J., Nocera, D. G., Yee, C. S. & Chang, M. C. Y. Radical initiation in the class I Ribonucleotide Reductase: Long-range proton-coupled electron transfer? *Chemical Reviews* **103**, 2167-2202, (2003).
67. Migliore, A., Polizzi, N. F., Therien, M. J. & Beratan, D. N. Biochemistry and theory of proton-coupled electron transfer. *Chemical Reviews* **114**, 3381-3465, (2014).
68. Fecenko, C. J., Meyer, T. J. & Thorp, H. H. Electrocatalytic oxidation of tyrosine by parallel rate-limiting proton transfer and multisite electron-proton transfer. *Journal of the American Chemical Society* **128**, 11020-11021, (2006).
69. Zhang, M.-T., Irebo, T., Johansson, O. & Hammarström, L. Proton-coupled electron transfer from tyrosine: A strong rate dependence on intramolecular proton transfer distance. *Journal of the American Chemical Society* **133**, 13224-13227, (2011).
70. Cui, X. D., Primak, A., Zarate, X., Tomfohr, J., Sankey, O. F., Moore, A. L., Moore, T. A., Gust, D., Harris, G. & Lindsay, S. M. Reproducible measurement of single-molecule conductivity. *Science* **294**, 571-574, (2001).
71. Zhang, B., Song, W., Pang, P., Lai, H., Chen, Q., Zhang, P. & Lindsay, S. Role of contacts in long-range protein conductance. *Proceedings of the National Academy of Sciences* **116**, 5886-5891, (2019).
72. Zhang, B. & Lindsay, S. Electronic decay length in a protein molecule. *Nano Letters* **19**, 4017-4022, (2019).
73. Bera, S., Govinda, S., Fereiro, J. A., Pecht, I., Sheves, M. & Cahen, D. Biotin binding hardly affects electron transport efficiency across streptavidin solid-state junctions. *Langmuir* **39**, 1394-1403, (2023).
74. Beratan, D. N., Liu, C., Migliore, A., Polizzi, N. F., Skourtis, S. S., Zhang, P. & Zhang, Y. Charge transfer in dynamical biosystems, or the treachery of (static) images. *Accounts of Chemical Research* **48**, 474-481, (2015).
75. Best, R. B., Zhu, X., Shim, J., Lopes, P. E. M., Mittal, J., Feig, M. & MacKerell, A. D., Jr. Optimization of the additive CHARMM all-atom protein force field targeting improved sampling of the backbone ϕ , ψ and side-chain χ_1 and χ_2 dihedral angles. *Journal of Chemical Theory and Computation* **8**, 3257-3273, (2012).

76. Autenrieth, F., Tajkhorshid, E., Baudry, J. & Luthey-Schulten, Z. Classical force field parameters for the heme prosthetic group of cytochrome c. *Journal of Computational Chemistry* **25**, 1613-1622, (2004).
77. Shao, Y., Gan, Z., Epifanovsky, E., Gilbert, A. T. B., Wormit, M., Kussmann, J., Lange, A. W., Behn, A., Deng, J., Feng, X., Ghosh, D., Goldey, M., Horn, P. R., Jacobson, L. D., Kaliman, I., Khaliullin, R. Z., Kuš, T., Landau, A., Liu, J., Proynov, E. I., Rhee, Y. M., Richard, R. M., Rohrdanz, M. A., Steele, R. P., Sundstrom, E. J., Woodcock, H. L., Zimmerman, P. M., Zuev, D., Albrecht, B., Alguire, E., Austin, B., Beran, G. J. O., Bernard, Y. A., Berquist, E., Brandhorst, K., Bravaya, K. B., Brown, S. T., Casanova, D., Chang, C.-M., Chen, Y., Chien, S. H., Closser, K. D., Crittenden, D. L., Diedenhofen, M., DiStasio, R. A., Do, H., Dutoi, A. D., Edgar, R. G., Fatehi, S., Fusti-Molnar, L., Ghysels, A., Golubeva-Zadorozhnaya, A., Gomes, J., Hanson-Heine, M. W. D., Harbach, P. H. P., Hauser, A. W., Hohenstein, E. G., Holden, Z. C., Jagau, T.-C., Ji, H., Kaduk, B., Khistyayev, K., Kim, J., Kim, J., King, R. A., Klunzinger, P., Kosenkov, D., Kowalczyk, T., Krauter, C. M., Lao, K. U., Laurent, A. D., Lawler, K. V., Levchenko, S. V., Lin, C. Y., Liu, F., Livshits, E., Lochan, R. C., Luenser, A., Manohar, P., Manzer, S. F., Mao, S.-P., Mardirossian, N., Marenich, A. V., Maurer, S. A., Mayhall, N. J., Neuscamman, E., Oana, C. M., Olivares-Amaya, R., O'Neill, D. P., Parkhill, J. A., Perrine, T. M., Peverati, R., Prociuk, A., Rehn, D. R., Rosta, E., Russ, N. J., Sharada, S. M., Sharma, S., Small, D. W., Sodt, A., Stein, T., Stück, D., Su, Y.-C., Thom, A. J. W., Tsuchimochi, T., Vanovschi, V., Vogt, L., Vydrov, O., Wang, T., Watson, M. A., Wenzel, J., White, A., Williams, C. F., Yang, J., Yeganeh, S., Yost, S. R., You, Z.-Q., Zhang, I. Y., Zhang, X., Zhao, Y., Brooks, B. R., Chan, G. K. L., Chipman, D. M., Cramer, C. J., Goddard, W. A., Gordon, M. S., Hehre, W. J., Klamt, A., Schaefer, H. F., Schmidt, M. W., Sherrill, C. D., Truhlar, D. G., Warshel, A., Xu, X., Aspuru-Guzik, A., Baer, R., Bell, A. T., Besley, N. A., Chai, J.-D., Dreuw, A., Dunietz, B. D., Furlani, T. R., Gwaltney, S. R., Hsu, C.-P., Jung, Y., Kong, J., Lambrecht, D. S., Liang, W., Ochsenfeld, C., Rassolov, V. A., Slipchenko, L. V., Subotnik, J. E., Van Voorhis, T., Herbert, J. M., Krylov, A. I., Gill, P. M. W. & Head-Gordon, M. Advances in molecular quantum chemistry contained in the Q-Chem 4 program package. *Molecular Physics* **113**, 184-215, (2015).
78. Edwards, P., Gray, H., Lodge, M. & Williams, R. Electron transfer and electronic conduction through an intervening medium. *Angewandte Chemie (International ed. in English)* **47**, 6758-6765, (2008).
79. Zwanzig, R. W. High-temperature equation of state by a perturbation method. I. Nonpolar gases. *The Journal of Chemical Physics* **22**, 1420-1426, (1954).
80. Ho, J. Are thermodynamic cycles necessary for continuum solvent calculation of pKas and reduction potentials? *Physical Chemistry Chemical Physics* **17**, 2859-2868, (2015).
81. Trasatti, S. The absolute electrode potential: an explanatory note (Recommendations 1986). *Pure and Applied Chemistry* **58**, 955-966, (1986).

82. Kelly, C. P., Cramer, C. J. & Truhlar, D. G. Aqueous solvation free energies of ions and ion-water clusters based on an accurate value for the absolute aqueous solvation free energy of the proton. *The Journal of Physical Chemistry B* **110**, 16066-16081, (2006).
83. Isse, A. A. & Gennaro, A. Absolute potential of the standard hydrogen electrode and the problem of interconversion of potentials in different solvents. *The Journal of Physical Chemistry B* **114**, 7894-7899, (2010).
84. Nørskov, J. K., Rossmeisl, J., Logadottir, A., Lindqvist, L., Kitchin, J. R., Bligaard, T. & Jónsson, H. Origin of the overpotential for oxygen reduction at a fuel-cell cathode. *The Journal of Physical Chemistry B* **108**, 17886-17892, (2004).
85. Peterson, A. A., Abild-Pedersen, F., Studt, F., Rossmeisl, J. & Nørskov, J. K. How copper catalyzes the electroreduction of carbon dioxide into hydrocarbon fuels. *Energy & Environmental Science* **3**, 1311-1315, (2010).
86. Matyushov, D. V. Protein electron transfer: Dynamics and statistics. *The Journal of Chemical Physics* **139**, 025102, (2013).
87. Matyushov, D. V. Protein electron transfer: is biology (thermo)dynamic? *Journal of Physics: Condensed Matter* **27**, (2015).
88. te Velde, G., Bickelhaupt, F. M., Baerends, E. J., Fonseca Guerra, C., van Gisbergen, S. J. A., Snijders, J. G. & Ziegler, T. Chemistry with ADF. *Journal of Computational Chemistry* **22**, 931-967, (2001).
89. Senthilkumar, K., Grozema, F. C., Guerra, C. F., Bickelhaupt, F. M., Lewis, F. D., Berlin, Y. A., Ratner, M. A. & Siebbeles, L. D. A. Absolute rates of hole transfer in DNA. *Journal of the American Chemical Society* **127**, 14894-14903, (2005).
90. Breuer, M., Rosso, K. M. & Blumberger, J. Electron flow in multiheme bacterial cytochromes is a balancing act between heme electronic interaction and redox potentials. *Proceedings of the National Academy of Sciences* **111**, 611, (2014).
91. Kubas, A., Hoffmann, F., Heck, A., Oberhofer, H., Elstner, M. & Blumberger, J. Electronic couplings for molecular charge transfer: Benchmarking CDFT, FODFT, and FODFTB against high-level ab initio calculations. *The Journal of Chemical Physics* **140**, 104105, (2014).
92. Byun, H. S., Pirkadian, S., Nakano, A., Shi, L. & El-Naggar, M. Y. Kinetic Monte Carlo simulations and molecular conductance measurements of the bacterial decaheme cytochrome MtrF. *ChemElectroChem* **1**, 1932-1939, (2014).

93. Ma, J.-G., Laberge, M., Song, X.-Z., Jentzen, W., Jia, S.-L., Zhang, J., Vanderkooi, J. M. & Shelnut, J. A. Protein-induced changes in nonplanarity of the porphyrin in nickel cytochrome c probed by resonance raman spectroscopy. *Biochemistry* **37**, 5118-5128, (1998).
94. Ma, J.-G., Zhang, J., Franco, R., Jia, S.-L., Moura, I., Moura, J. J. G., Kroneck, P. M. H. & Shelnut, J. A. The structural origin of nonplanar heme distortions in tetraheme ferricytochromes c3. *Biochemistry* **37**, 12431-12442, (1998).
95. Sun, Y., Benabbas, A., Zeng, W., Kleingardner, J. G., Bren, K. L. & Champion, P. M. Investigations of heme distortion, low-frequency vibrational excitations, and electron transfer in cytochrome c. *Proceedings of the National Academy of Sciences* **111**, 6570, (2014).
96. Sun, Y., Karunakaran, V. & Champion, P. M. Investigations of the low-frequency spectral density of cytochrome c upon equilibrium unfolding. *The Journal of Physical Chemistry B* **117**, 9615-9625, (2013).
97. Jentzen, W., Song, X.-Z. & Shelnut, J. A. Structural characterization of synthetic and protein-bound porphyrins in terms of the lowest-frequency normal coordinates of the macrocycle. *The Journal of Physical Chemistry B* **101**, 1684-1699, (1997).
98. Humphrey, W., Dalke, A. & Schulten, K. VMD: Visual molecular dynamics. *Journal of Molecular Graphics* **14**, 33-38, (1996).
99. McKechnie, S., Booth, G. H., Cohen, A. J. & Cole, J. M. On the accuracy of density functional theory and wave function methods for calculating vertical ionization energies. *The Journal of chemical physics* **142**, 194114, (2015).
100. Blumberger, J. Free energies for biological electron transfer from QM/MM calculation: method, application and critical assessment. *Physical Chemistry Chemical Physics* **10**, 5651-5667, (2008).
101. Konezny, S. J., Doherty, M. D., Luca, O. R., Crabtree, R. H., Soloveichik, G. L. & Batista, V. S. Reduction of systematic uncertainty in DFT redox potentials of transition-metal complexes. *The Journal of Physical Chemistry C* **116**, 6349-6356, (2012).
102. Rudshteyn, B., Vibbert, H. B., May, R., Wasserman, E., Warnke, I., Hopkins, M. D. & Batista, V. S. Thermodynamic and structural factors that influence the redox potentials of tungsten-alkylidyne complexes. *ACS Catalysis* **7**, 6134-6143, (2017).

103. Jarzynski, C. Nonequilibrium equality for free energy differences. *Physical Review Letters* **78**, 2690-2693, (1997).
104. Gilson, M. K. & Zhou, H.-X. Calculation of protein-ligand binding affinities. *Annual Review of Biophysics and Biomolecular Structure* **36**, 21-42, (2007).
105. Glover, S. D., Tyburski, R., Liang, L., Tommos, C. & Hammarström, L. Pourbaix diagram, proton-coupled electron transfer, and decay kinetics of a protein tryptophan radical: comparing the redox properties of W32• and Y32• generated inside the structurally characterized $\alpha 3W$ and $\alpha 3Y$ proteins. *Journal of the American Chemical Society* **140**, 185-192, (2018).
106. Berry, B. W., Martínez-Rivera, M. C. & Tommos, C. Reversible voltammograms and a Pourbaix diagram for a protein tyrosine radical. *Proceedings of the National Academy of Sciences* **109**, 9739-9743, (2012).
107. Reinhardt, C. R., Sequeira, R., Tommos, C. & Hammes-Schiffer, S. Computing proton-coupled redox potentials of fluorotyrosines in a protein environment. *The Journal of Physical Chemistry B* **125**, 128-136, (2021).
108. Pande, A. & Myer, Y. P. The redox potential of horse heart cytochrome *c*. *Biochemical and Biophysical Research Communications* **85**, 7-13, (1978).
109. Huynh, M. T., Mora, S. J., Villalba, M., Tejada-Ferrari, M. E., Liddell, P. A., Cherry, B. R., Teillout, A.-L., Machan, C. W., Kubiak, C. P., Gust, D., Moore, T. A., Hammes-Schiffer, S. & Moore, A. L. Concerted one-electron two-proton transfer processes in models inspired by the Tyr-His couple of Photosystem II. *ACS Central Science* **3**, 372-380, (2017).
110. Mardis, K. L., Niklas, J., Omodayo, H., Odella, E., Moore, T. A., Moore, A. L. & Poluektov, O. G. One electron multiple proton transfer in model organic donor-acceptor Systems: implications for high-frequency EPR. *Applied Magnetic Resonance* **51**, 977-991, (2020).
111. Phillips, J. C., Braun, R., Wang, W., Gumbart, J., Tajkhorshid, E., Villa, E., Chipot, C., Skeel, R. D., Kalé, L. & Schulten, K. Scalable molecular dynamics with NAMD. *Journal of Computational Chemistry* **26**, 1781-1802, (2005).
112. Firer-Sherwood, M., Pulcu, G. S. & Elliott, S. J. Electrochemical interrogations of the Mtr cytochromes from *Shewanella*: opening a potential window. *JBIC Journal of Biological Inorganic Chemistry* **13**, 849, (2008).

113. Livernois, W. & Anantram, M. P. in *2021 IEEE 16th Nanotechnology Materials and Devices Conference (NMDC)*. 1-5.
114. Tuccitto, N., Ferri, V., Cavazzini, M., Quici, S., Zhavnerko, G., Licciardello, A. & Rampi, M. A. Highly conductive ~40-nm-long molecular wires assembled by stepwise incorporation of metal centres. *Nature Materials* **8**, 41, (2008).
115. Yamada, R., Kumazawa, H., Tanaka, S. & Tada, H. Electrical resistance of long oligothiophene molecules. *Applied Physics Express* **2**, 025002, (2009).
116. Luo, L., Choi, S. H. & Frisbie, C. D. Probing hopping conduction in conjugated molecular wires connected to metal electrodes. *Chemistry of Materials* **23**, 631-645, (2011).
117. Nitzan, A. Electron transmission through molecules and molecular interfaces. *Annual Review of Physical Chemistry* **52**, 681-750, (2001).
118. Sedghi, G., Sawada, K., Esdaile, L. J., Hoffmann, M., Anderson, H. L., Bethell, D., Haiss, W., Higgins, S. J. & Nichols, R. J. Single molecule conductance of porphyrin wires with ultralow attenuation. *Journal of the American Chemical Society* **130**, 8582-8583, (2008).
119. Leang, C., Malvankar, N. S., Franks, A. E., Nevin, K. P. & Lovley, D. R. Engineering *Geobacter sulfurreducens* to produce a highly cohesive conductive matrix with enhanced capacity for current production. *Energy & Environmental Science* **6**, 1901-1908, (2013).
120. Doster, W. The dynamical transition of proteins, concepts and misconceptions. *European Biophysics Journal* **37**, 591-602, (2008).
121. Bellamy, L. J. in *The Infrared Spectra of Complex Molecules: Volume Two Advances in Infrared Group Frequencies* (ed L. J. Bellamy) 240-292 (Springer Netherlands, 1980).
122. Scheiner, S. & Čuma, M. Relative stability of hydrogen and deuterium bonds. *Journal of the American Chemical Society* **118**, 1511-1521, (1996).
123. Li, X.-Z., Walker, B. & Michaelides, A. Quantum nature of the hydrogen bond. *Proceedings of the National Academy of Sciences* **108**, 6369, (2011).
124. Englander, S. W. & Kallenbach, N. R. Hydrogen exchange and structural dynamics of proteins and nucleic acids. *Quarterly Reviews of Biophysics* **16**, 521-655, (1983).

125. Amdursky, N., Pecht, I., Sheves, M. & Cahen, D. Marked changes in electron transport through the blue copper protein azurin in the solid state upon deuteration. *Proceedings of the National Academy of Sciences* **110**, 507-512, (2013).
126. Nakahara, Y., Kimura, K., Inokuchi, H. & Yagi, T. Electrical conductivity of an anhydrous cytochrome c3 film as a function of temperature and ambient pressure. *Chemical Physics Letters* **73**, 31-34, (1980).
127. Barrozo, A., El-Naggar, M. Y. & Krylov, A. I. Distinct electron conductance regimes in bacterial decaheme cytochromes. *Angewandte Chemie International Edition* **57**, 6805-6809, (2018).
128. Jiang, X., Burger, B., Gajdos, F., Bortolotti, C., Futera, Z., Breuer, M. & Blumberger, J. Kinetics of trifurcated electron flow in the decaheme bacterial proteins MtrC and MtrF. *Proceedings of the National Academy of Sciences* **116**, 3425-3430, (2019).
129. Jiang, X., Futera, Z., Ali, M. E., Gajdos, F., von Rudorff, G. F., Carof, A., Breuer, M. & Blumberger, J. Cysteine linkages accelerate electron flow through tetra-heme protein STC. *Journal of the American Chemical Society* **139**, 17237-17240, (2017).
130. Marcus, R. A. Chemical and electrochemical electron-transfer theory. *Annual Review of Physical Chemistry* **15**, 155-196, (1964).
131. Cordier, F. & Grzesiek, S. Temperature-dependence of protein hydrogen bond properties as studied by high-resolution NMR11. *Journal of Molecular Biology* **317**, 739-752, (2002).
132. Guallar, V., Baik, M.-H., Lippard, S. J. & Friesner, R. A. Peripheral heme substituents control the hydrogen-atom abstraction chemistry in cytochromes P450. *Proceedings of the National Academy of Sciences* **100**, 6998, (2003).
133. Douglas, R. G. & Rousseau, D. L. Hydrogen bonding of iron-coordinated histidine in heme proteins. *Journal of Structural Biology* **109**, 13-17, (1992).
134. Kuleta, P., Lasham, J., Sarewicz, M., Ekiert, I., Sharma, V., Ekiert, R. & Osyczka, A. Hydrogen bonding rearrangement by a mitochondrial disease mutation in cytochrome bc1 perturbs heme bH redox potential and spin state. *Proceedings of the National Academy of Sciences* **118**, e2026169118, (2021).
135. Ma, J.-G., Vanderkooi, J. M., Zhang, J., Jia, S.-L. & Shelnut, J. A. Resonance raman investigation of nickel microperoxidase-11. *Biochemistry* **38**, 2787-2795, (1999).

136. Rivas, L., Soares, C. M., Baptista, A. M., Simaan, J., Di Paolo, R. E., Murgida, D. H. & Hildebrandt, P. Electric-field-induced redox potential shifts of tetraheme cytochromes c₃ immobilized on self-assembled monolayers: Surface-enhanced resonance raman spectroscopy and simulation studies. *Biophysical Journal* **88**, 4188-4199, (2005).
137. Murgida, D. H. & Hildebrandt, P. Heterogeneous electron transfer of cytochrome c on coated silver electrodes. Electric field effects on structure and redox potential. *The Journal of Physical Chemistry B* **105**, 1578-1586, (2001).
138. Yalcin, S. E. & Malvankar, N. S. Seeing is believing: Novel imaging methods help identify structure and function of *Geobacter* nanowires in electricity-producing biofilms in Roadmap on emerging concepts in the physical biology of bacterial biofilms: from surface sensing to community formation *Physical Biology* **18**, 051501 (2021).
139. Sekar, N., Jain, R., Yan, Y. & Ramasamy, R. P. Enhanced photo-bioelectrochemical energy conversion by genetically engineered cyanobacteria. *Biotechnology and Bioengineering* **113**, 675-679, (2016).
140. Dong, F., Lee, Y. S., Gaffney, E. M., Liou, W. & Minteer, S. D. Engineering cyanobacterium with transmembrane electron transfer ability for bioelectrochemical nitrogen fixation. *ACS Catalysis* **11**, 13169-13179, (2021).
141. Meng, H., Zhang, W., Zhu, H., Yang, F., Zhang, Y., Zhou, J. & Li, Y. Over-expression of an electron transport protein OmcS provides sufficient NADH for d-lactate production in cyanobacterium. *Biotechnology for Biofuels* **14**, 109, (2021).
142. O'Brien, J. P. & Malvankar, N. S. A simple and low-cost procedure for growing *Geobacter sulfurreducens* cell cultures and biofilms in bioelectrochemical systems. *Current Protocols in Microbiology* **43**, A.4K.1-A.4K.27, (2017).
143. Amdursky, N., Głowacki, E. D. & Meredith, P. Macroscale biomolecular electronics and ionics. *Advanced Materials* **31**, 1802221, (2019).
144. Silberbush, O., Amit, M., Roy, S. & Ashkenasy, N. Significant enhancement of proton transport in bioinspired peptide fibrils by single acidic or basic amino acid mutation. *Advanced Functional Materials* **27**, 1604624, (2017).
145. Amdursky, N., Wang, X., Meredith, P., Riley, D. J., Payne, D. J., Bradley, D. D. C. & Stevens, M. M. Electron hopping across hemin-doped serum albumin mats on centimeter-length scales. *Advanced Materials* **29**, 1700810, (2017).

146. Liu, X., Gao, H., Ward, J. E., Liu, X., Yin, B., Fu, T., Chen, J., Lovley, D. R. & Yao, J. Power generation from ambient humidity using protein nanowires. *Nature* **578**, 550-554, (2020).
147. Inoue, K., Qian, X., Morgado, L., Kim, B.-C., Mester, T., Izallalen, M., Salgueiro, C. A. & Lovley, D. R. Purification and characterization of OmcZ, an outer-surface, octaheme c-type cytochrome essential for optimal current production by *Geobacter sulfurreducens*. *Applied and Environmental Microbiology* **76**, 3999-4007, (2010).
148. Malvankar, N. S., Tuominen, M. T. & Lovley, D. R. Biofilm conductivity is a decisive variable for high-current-density *Geobacter sulfurreducens* microbial fuel cells. *Energy & Environmental Science* **5**, 5790-5797, (2012).
149. van der Pauw, L. J. A method of measuring specific resistivity and hall effect of discs of arbitrary shape. *Phillips Research Reports* **13**, 1-9, (1958).
150. Amit, M., Appel, S., Cohen, R., Cheng, G., Hamley, I. W. & Ashkenasy, N. Hybrid proton and electron transport in peptide fibrils. *Advanced Functional Materials* **24**, 5873-5880, (2014).
151. Silberbush, O., Engel, M., Sivron, I., Roy, S. & Ashkenasy, N. Self-assembled peptide nanotube films with high proton conductivity. *The Journal of Physical Chemistry B* **123**, 9882-9888, (2019).
152. Wieland, M., Dingler, C., Merkle, R., Maier, J. & Ludwigs, S. Humidity-controlled water uptake and conductivities in Ion and electron mixed conducting polythiophene films. *ACS Applied Materials & Interfaces* **12**, 6742-6751, (2020).
153. García-Fernández, A., Moradi, Z., Bermúdez-García, J. M., Sánchez-Andújar, M., Gimeno, V. A., Castro-García, S., Señaris-Rodríguez, M. A., Mas-Marzá, E., Garcia-Belmonte, G. & Fabregat-Santiago, F. Effect of environmental humidity on the electrical properties of lead halide perovskites. *The Journal of Physical Chemistry C* **123**, 2011-2018, (2019).
154. Ordinario, D. D., Phan, L., Walkup Iv, W. G., Jocson, J.-M., Karshalev, E., Hüsken, N. & Gorodetsky, A. A. Bulk protonic conductivity in a cephalopod structural protein. *Nature Chemistry* **6**, 596-602, (2014).
155. Eames, C., Frost, J. M., Barnes, P. R. F., O'Regan, B. C., Walsh, A. & Islam, M. S. Ionic transport in hybrid lead iodide perovskite solar cells. *Nature Communications* **6**, 7497, (2015).

156. Careri, G., Giansanti, A. & Rupley, J. A. Proton percolation on hydrated lysozyme powders. *Proceedings of the National Academy of Sciences* **83**, 6810-6814, (1986).
157. Neu, J., Shipps, C. C., Guberman-Pfeffer, M. J., Shen, C., Srikanth, V., Spies, J. A., Kirchhofer, N. D., Yalcin, S. E., Brudvig, G. W., Batista, V. S. & Malvankar, N. S. Microbial biofilms as living photoconductors due to ultrafast electron transfer in cytochrome OmcS nanowires. *Nature Communications* **13**, 5150, (2022).
158. Dempsey, J. L. & Hartings, M. R. Hop to it. *Biochemistry* **56**, 5623-5624, (2017).
159. Shih, C., Museth, A. K., Abrahamsson, M., Blanco-Rodriguez, A. M., Di Bilio, A. J., Sudhamsu, J., Crane, B. R., Ronayne, K. L., Towrie, M., Vlček, A., Richards, J. H., Winkler, J. R. & Gray, H. B. Tryptophan-accelerated electron flow through proteins. *Science* **320**, 1760-1762, (2008).
160. Bachtold, A., Henny, M., Terrier, C., Strunk, C., Schönenberger, C., Salvétat, J. P., Bonard, J. M. & Forró, L. Contacting carbon nanotubes selectively with low-ohmic contacts for four-probe electric measurements. *Applied Physics Letters* **73**, 274-276, (1998).
161. Warren, J. J., Winkler, J. R. & Gray, H. B. Redox properties of tyrosine and related molecules. *FEBS Letters* **586**, 596-602, (2012).
162. Jortner, J., Bixon, M., Langenbacher, T. & Michel-Beyerle, M. E. Charge transfer and transport in DNA. *Proceedings of the National Academy of Sciences* **95**, 12759-12765, (1998).
163. Balabin, I. A., Hu, X. & Beratan, D. N. Exploring biological electron transfer pathway dynamics with the Pathways Plugin for VMD. *Journal of Computational Chemistry* **33**, 906-910, (2012).
164. Segal, D., Nitzan, A., Davis, W. B., Wasielewski, M. R. & Ratner, M. A. Electron transfer rates in bridged molecular systems 2. A steady-state analysis of coherent tunneling and thermal transitions. *The Journal of Physical Chemistry B* **104**, 3817-3829, (2000).
165. Davies, D. Understanding biofilm resistance to antibacterial agents. *Nature Reviews Drug Discovery* **2**, 114-122, (2003).
166. Marshall, K., Stout, R. & Mitchell, R. Mechanism of the initial events in the sorption of marine bacteria to surfaces. *Microbiology* **68**, 337-348, (1971).

167. Hori, K. & Matsumoto, S. Bacterial adhesion: From mechanism to control. *Biochemical Engineering Journal* **48**, 424-434, (2010).
168. Pezzulo, A. A., Tang, X. X., Hoegger, M. J., Abou Alaiwa, M. H., Ramachandran, S., Moninger, T. O., Karp, P. H., Wohlford-Lenane, C. L., Haagsman, H. P., van Eijk, M., Banfi, B., Horswill, A. R., Stoltz, D. A., McCray, P. B., Welsh, M. J. & Zabner, J. Reduced airway surface pH impairs bacterial killing in the porcine cystic fibrosis lung. *Nature* **487**, 109-113, (2012).
169. Cowley, E. S., Kopf, S. H., LaRiviere, A., Ziebis, W. & Newman, D. K. Pediatric cystic fibrosis sputum can be chemically dynamic, anoxic, and extremely reduced due to hydrogen sulfide formation. *mBio* **6**, e00767-00715, (2015).
170. Light, S. H., Su, L., Rivera-Lugo, R., Cornejo, J. A., Louie, A., Iavarone, A. T., Ajo-Franklin, C. M. & Portnoy, D. A. A flavin-based extracellular electron transfer mechanism in diverse Gram-positive bacteria. *Nature* **562**, 140-144, (2018).
171. Saunders, S. H., Edmund, C., Yates, M. D., Otero, F. J., Trammell, S. A., Stemp, E. D., Barton, J. K., Tender, L. M. & Newman, D. K. Extracellular DNA promotes efficient extracellular electron transfer by pyocyanin in *Pseudomonas aeruginosa* biofilms. *Cell*, (2020).
172. Kim, M. K., Ingremeau, F., Zhao, A., Bassler, B. L. & Stone, H. A. Local and global consequences of flow on bacterial quorum sensing. *Nature Microbiology* **1**, 15005, (2016).
173. Li, J., Egelman, E. H. & Craig, L. Structure of the *Vibrio cholerae* Type IVb pilus and stability comparison with the *Neisseria gonorrhoeae* Type IVa pilus. *Journal of Molecular Biology* **418**, 47-64, (2012).
174. Morisaki, H., Nagai, S., Ohshima, H., Ikemoto, E. & Kogure, K. The effect of motility and cell-surface polymers on bacterial attachment. *Microbiology* **145**, 2797-2802, (1999).
175. Heckels, J., Blackett, B., Everson, J. S. & Ward, M. The influence of surface charge on the attachment of *Neisseria gonorrhoeae* to human cells. *Journal of general microbiology* **96**, 359-364, (1976).
176. Lanthier, M., Gregory, K. B. & Lovley, D. R. Growth with high planktonic biomass in *Shewanella oneidensis* fuel cells. *FEMS microbiology letters* **278**, 29-35, (2008).
177. Tilton, R. D., Blomberg, E. & Claesson, P. M. Effect of anionic surfactant on interactions between lysozyme layers adsorbed on mica. *Langmuir* **9**, 2102-2108, (1993).

178. Heinz, W. F. & Hoh, J. H. Relative surface charge density mapping with the atomic force microscope. *Biophysical Journal* **76**, 528-538, (1999).
179. Mouhat, F., Coudert, F.-X. & Bocquet, M.-L. Structure and chemistry of graphene oxide in liquid water from first principles. *Nature Communications* **11**, 1566, (2020).
180. Ochedowski, O., Bussmann, B. K. & Schleberger, M. Graphene on mica - intercalated water trapped for life. *Scientific Reports* **4**, 6003, (2014).
181. Yalcin, S. E., Galande, C., Kappera, R., Yamaguchi, H., Martinez, U., Velizhanin, K. A., Doorn, S. K., Dattelbaum, A. M., Chhowalla, M., Ajayan, P. M., Gupta, G. & Mohite, A. D. Direct imaging of charge transport in progressively reduced graphene oxide using electrostatic force microscopy. *ACS Nano* **9**, 2981-2988, (2015).
182. Salas, E. C., Sun, Z., Lüttge, A. & Tour, J. M. Reduction of graphene oxide via bacterial respiration. *ACS nano* **4**, 4852-4856, (2010).
183. Kalathil, S., Katuri, K. P., Alazmi, A. S., Pedireddy, S., Kornienko, N., Costa, P. M. F. J. & Saikaly, P. E. Bioinspired synthesis of reduced graphene oxide-wrapped *Geobacter sulfurreducens* as a hybrid electrocatalyst for efficient oxygen evolution reaction. *Chemistry of Materials* **31**, 3686-3693, (2019).
184. Malvankar, N. S., Yalcin, S. E., Tuominen, M. T. & Lovley, D. R. Visualization of charge propagation along individual pili proteins using ambient electrostatic force microscopy. *Nature Nanotechnology* **9**, 1012-1017, (2014).
185. Zhang, S., Wang, L., Wu, L., Li, Z., Yang, B., Hou, Y., Lei, L., Cheng, S. & He, Q. Deciphering single-bacterium adhesion behavior modulated by extracellular electron transfer. *Nano Letters* **21**, 5105-5115, (2021).
186. Lai, B., Bernhardt, P. V. & Krömer, J. O. Cytochrome c reductase is a key enzyme involved in the extracellular electron transfer pathway towards transition metal complexes in *Pseudomonas putida*. *ChemSusChem*, (2020).
187. Rijnaarts, H. H. M., Norde, W., Bouwer, E. J., Lyklema, J. & Zehnder, A. J. B. Reversibility and mechanism of bacterial adhesion. *Colloids and Surfaces B: Biointerfaces* **4**, 5-22, (1995).
188. Poortinga, A. T., Bos, R. & Busscher, H. J. Measurement of charge transfer during bacterial adhesion to an indium tin oxide surface in a parallel plate flow chamber. *Journal of Microbiological Methods* **38**, 183-189, (1999).

189. Saboorian-Jooybari, H. & Chen, Z. Calculation of re-defined electrical double layer thickness in symmetrical electrolyte solutions. *Results in Physics* **15**, 102501, (2019).
190. Beaussart, A., Baker, A. E., Kuchma, S. L., El-Kirat-Chatel, S., O'Toole, G. A. & Dufrêne, Y. F. Nanoscale adhesion forces of *Pseudomonas aeruginosa* type IV pili. *ACS Nano* **8**, 10723-10733, (2014).
191. Beaussart, A., El-Kirat-Chatel, S., Sullan, R. M. A., Alsteens, D., Herman, P., Derclaye, S. & Dufrêne, Y. F. Quantifying the forces guiding microbial cell adhesion using single-cell force spectroscopy. *Nature Protocols* **9**, 1049, (2014).
192. Bosire, E. M. & Rosenbaum, M. A. Electrochemical potential influences phenazine production, electron transfer and consequently electric current generation by *Pseudomonas aeruginosa*. *Frontiers in Microbiology* **8**, (2017).
193. Liu, X., Tremblay, P.-L., Malvankar, N. S., Nevin, K. P., Lovley, D. R. & Vargas, M. A. *Geobacter sulfurreducens* strain expressing *Pseudomonas aeruginosa* type IV pili localizes OmcS on pili but is deficient in Fe(III) oxide reduction and current production. *Applied and Environmental Microbiology* **80**, 1219-1224, (2014).
194. Yalcin, S. E. & Malvankar, N. The blind men and the filament: Understanding structures and functions of microbial nanowires *Current Opinion in Chemical Biology*, (2020).
195. Malvankar, N. S., Lou, J., Nevin, K., Franks, A. E., Tuominen, M. T. & Lovley, D. R. Electrical conductivity in a mixed-species biofilm. *Applied and Environmental Microbiology* **78**, 5967-5971, (2012).
196. Kennouche, P., Charles-Orszag, A., Nishiguchi, D., Goussard, S., Imhaus, A.-F., Dupré, M., Chamot-Rooke, J. & Duménil, G. Deep mutational scanning of the *Neisseria meningitidis* major pilin reveals the importance of pilus tip-mediated adhesion. *The EMBO Journal* **38**, e102145, (2019).
197. Poschet, J. F., Boucher, J. C., Tattersson, L., Skidmore, J., Van Dyke, R. W. & Deretic, V. Molecular basis for defective glycosylation and *Pseudomonas* pathogenesis in cystic fibrosis lung. *PNAS* **98**, 13972-13977, (2001).
198. Henke, M., Renner, A., Huber, R. M., Seeds, M. C. & Rubin, B. K. MUC5AC and MUC5B mucins are decreased in cystic fibrosis airway secretions. *American Journal of Respiratory Cell & Molecular Biology* **31**, 86-91, (2004).
199. Lighthart, K., Belzer, C., De Vos, W. M. & Tytgat, H. L. Bridging bacteria and the gut: functional aspects of type IV pili. *Trends in microbiology* **28**, 340-348, (2020).

200. Rivera-Lugo, R., Deng, D., Anaya-Sanchez, A., Tejedor-Sanz, S., Tang, E., Reyes Ruiz, V. M., Smith, H. B., Titov, D. V., Sauer, J.-D., Skaar, E. P., Ajo-Franklin, C. M., Portnoy, D. A. & Light, S. H. *Listeria monocytogenes* requires cellular respiration for NAD⁺ regeneration and pathogenesis. *eLife* **11**, e75424, (2022).
201. Zeng, Z., Boeren, S., Bhandula, V., Light, S. H., Smid, E. J., Notebaart, R. A., Abee, T. & Laar, T. A. V. Bacterial microcompartments coupled with extracellular electron transfer drive the anaerobic utilization of ethanolamine in *Listeria monocytogenes*. *mSystems* **6**, e01349-01320, (2021).
202. Duranti, S., Turrone, F., Lugli Gabriele, A., Milani, C., Viappiani, A., Mangifesta, M., Gioiosa, L., Palanza, P., van Sinderen, D., Ventura, M. & Björkroth, J. Genomic characterization and transcriptional studies of the starch-utilizing strain *Bifidobacterium adolescentis* 22L. *Applied and Environmental Microbiology* **80**, 6080-6090, (2014).
203. Denis, K., Le Bris, M., Le Guennec, L., Barnier, J.-P., Faure, C., Gouge, A., Bouzinba-Ségard, H., Jamet, A., Euphrasie, D., Durel, B., Barois, N., Pelissier, P., Morand, P. C., Coureuil, M., Lafont, F., Join-Lambert, O., Nassif, X. & Bourdoulous, S. Targeting Type IV pili as an antivirulence strategy against invasive meningococcal disease. *Nature Microbiology* **4**, 972-984, (2019).
204. Wilson, B. A., Salyers, A. A., Whitt, D. D. & Winkler, M. E. Bacterial pathogenesis: a molecular approach. *American Society for Microbiology*, (2011).
205. Zeglis, B. M., Pierre, V. C. & Barton, J. K. Metallointercalators and Metalloinsertors. *Chemical communications (Cambridge, England)*, 4565-4579, (2007).
206. van der Lelie, D., Oka, A., Taghavi, S., Umeno, J., Fan, T.-J., Merrell, K. E., Watson, S. D., Ouellette, L., Liu, B. & Awoniyi, M. Rationally designed bacterial consortia to treat chronic immune-mediated colitis and restore intestinal homeostasis. *Nature communications* **12**, 1-17, (2021).
207. Nassif, X., Lowy, J., Stenberg, P., O'Gaora, P., Ganji, A. & So, M. Antigenic variation of pilin regulates adhesion of *Neisseria meningitidis* to human epithelial cells. *Molecular Microbiology* **8**, 719-725, (1993).
208. Craig, L., Volkmann, N., Arvai, A. S., Pique, M. E., Yeager, M., Egelman, Edward H. & Tainer, J. A. Type IV pilus structure by cryo-electron microscopy and crystallography: implications for pilus assembly and functions. *Molecular Cell* **23**, 651-662, (2006).
209. Melican, K., Michea Veloso, P., Martin, T., Bruneval, P. & Duménil, G. Adhesion of *Neisseria meningitidis* to dermal vessels leads to local vascular damage and *Purpura* in a humanized mouse model. *PLoS Pathog* **9**, e1003139, (2013).

210. Yalcin, S. E., Labastide, J. A., Sowle, D. L. & Barnes, M. D. Spectral properties of multiply charged semiconductor quantum dots. *Nano Letters* **11**, 4425-4430, (2011).
211. Yalcin, S. E., Yang, B., Labastide, J. A. & Barnes, M. D. Electrostatic force microscopy and spectral studies of electron attachment to single quantum dots on indium tin oxide substrates. *The Journal of Physical Chemistry C* **116**, 15847-15853, (2012).
212. Jumper, J., Evans, R., Pritzel, A., Green, T., Figurnov, M., Ronneberger, O., Tunyasuvunakool, K., Bates, R., Židek, A., Potapenko, A., Bridgland, A., Meyer, C., Kohl, S. A. A., Ballard, A. J., Cowie, A., Romera-Paredes, B., Nikolov, S., Jain, R., Adler, J., Back, T., Petersen, S., Reiman, D., Clancy, E., Zielinski, M., Steinegger, M., Pacholska, M., Berghammer, T., Bodenstein, S., Silver, D., Vinyals, O., Senior, A. W., Kavukcuoglu, K., Kohli, P. & Hassabis, D. Highly accurate protein structure prediction with AlphaFold. *Nature* **596**, 583-589, (2021).
213. Dijkstra, E. A note on two problems in connexion with graphs. *Numerische mathematik* **1**, 269-271, (1959).
214. Liu, X., Ueki, T., Gao, H., Woodard, T. L., Nevin, K. P., Fu, T., Fu, S., Sun, L., Lovley, D. R. & Yao, J. Microbial biofilms for electricity generation from water evaporation and power to wearables. *Nature Communications* **13**, 4369, (2022).
215. Zhang, B., Ryan, E., Wang, X., Song, W. & Lindsay, S. Electronic transport in molecular wires of precisely controlled length built from modular proteins. *ACS Nano* **16**, 1671-1680, (2022).
216. Graves, A. B., Graves, M. T. & Liptak, M. D. Measurement of heme ruffling changes in MhuD using UV-vis spectroscopy. *The Journal of Physical Chemistry B* **120**, 3844-3853, (2016).
217. Shipps, C., Kelly, H. R., Dahl, P. J., Yi, S. M., Vu, D., Boyer, D., Glynn, C., Sawaya, M. R., Eisenberg, D., Batista, V. S. & Malvankar, N. S. Intrinsic electronic conductivity of individual atomically resolved amyloid crystals reveals micrometer-long hole hopping via tyrosines. *Proceedings of the National Academy of Sciences* **118**, e2014139118, (2021).